CHARACTERIZATION OF ANISOTROPIC MATERIALS USING A PARTIALLY-FILLED RECTANGULAR WAVEGUIDE

By

Junyan Tang

A DISSERTATION

Submitted to
Michigan State University
in partial fulfillment of the requirements
for the degree of

Electrical Engineering – Doctor of Philosophy

2015

ABSTRACT

CHARACTERIZATION OF ANISOTROPIC MATERIALS USING A PARTIALLY-FILLED RECTANGULAR WAVEGUIDE

By

Junyan Tang

Engineered materials with special electromagnetic properties are gaining an interest for applications where tailored material parameters are needed to meet stringent requirements. As the number of applications and the complexity of the engineered materials increase, there is a growing need for characterization methods that can accurately predict the constitutive parameters of these materials. Rectangular waveguide methods are popular in characterizing isotropic and anisotropic materials for many reasons, such as ease of sample preparation, high signal strength due to field confinement, the ability to control the polarization of the applied electric field, and high transmission efficiency over a broad frequency band. However, most characterization techniques based on rectangular waveguides are implemented by placing the sample against various metallic objects such as irises or posts, or by confining samples in sample holders, which increases the measurement complexity and the extraction uncertainties. In this work, a partially-filled waveguide technique that overcomes the drawbacks of the traditional methods is investigated for the characterization two types of anisotropic materials: biaxial and gyromagnetic.

The first group of materials considered for this characterization method are biaxial materials, which have three nonzero entries in each material tensor, corresponding to six complex material parameters that must be extracted. Typically three different samples are manufactured from the same material and placed into the rectangular waveguide in three orientations in order to interrogate the material along three orthogonal axes. Instead of using three samples, this technique uses a single cubical sample of biaxial material which is placed at the center of a guide and measured under three different rotations, providing the required number of reflection and transmission measurements to determine the six unique constitutive

parameters. The theoretical reflection and transmission coefficients are determined using a modal analysis. The desired complex constitutive parameters can be obtained by minimizing the difference between theoretical and measured data.

The second type of materials considered in this work are gyromagnetic. Gyromagnetic materials have scalar permittivity and anisotropic permeability which can be described by a tensor with three diagonal entries and two off-diagonal entries. Since the cross-sectional dimensions of waveguides become large at low frequencies where the gyromagnetic properties are most pronounced, and sufficiently large samples that can fill the cross-section of the waveguide are typically unavailable, a technique overcomes the limitation of sample size and only requires the sample to fill part of the guide is beneficial. The measured refection and transmission coefficients can be obtained from a gyromagnetic sample under various experimental configurations. The theoretical refection and transmission coefficients are determined using a mode matching technique. A nonlinear least squares method is employed to extract the gyromagnetic material parameters using optimization algorithms in Matlab.

ACKNOWLEDGMENTS

I would first like to thank the professors who are not on my committee. Thank you to Dr. Qi for encouraging and helping me to transfer from Geography to ECE department. Thank you to Dr. Kemple for supporting me at my conference talks and giving me lots of advice during my Ph.D. study. Thank you to Dr. Havrilla for generously letting us use your lab equipments for a long period of time, without which I would not have the measured data for the completion of this work.

Thank you to Dr. Diaz for giving me the opportunity to work with the metamaterial research group and also for his time and effort being my committee member. Thank you to Dr. Chahal for his assistance and help during my transfer to the ECE department, and many useful advice during my job search. Thank you to Dr. Shanker for his support all over the years. I will miss all the classes I had with him.

Many thanks to Dr. Rothwell for accepting me as his student and transforming me in many ways. I really appreciate all his effort over the years for educating, helping and encouraging me. I will always cherish the fun times we had together and remember the interesting stories he told us. He is and always will be my friend and mentor.

Special thanks to Dr. Raoul Ouedraogo and Dr. Benjamin Crowgey who guided me at different stages of my study at MSU. Thank you for helping me through many difficult times in my life. You two are like my big brothers and I know our friendship will never die. Thank you to Korede Akinlabi-Oladimeji for his numerous amount of hours spent on reading my writings and for his unconditional support when I am in trouble. Thank you to Andrew Temme and Joshua Myers for the friendship we established over the years and I will miss your interesting comments on my "Tang-ism". Thank you to Dr. Kazuko Fuchi for being a nice coworker during my study and also being a kind friend in my life. Thank you to Dr. Jose Hejase for believing in me and supporting me many times in my life.

Thank you to my parents for the love and support over the years. No words can express

my gratitude to them for letting me be myself.

Finally I want to thank my girlfriend Ranran Yang who is also going to be my wife in the near future for her love and support. I know that we shall create an extraordinary life together!

TABLE OF CONTENTS

LIST OF TABLES

LIST OF FIGURES

CHAPTER 1

INTRODUCTION AND BACKGROUND

There has been a recent emergence in the development of materials with electromagnetic properties tailored to the demands of different applications. Most materials that exist naturally are found to either exhibit high loss in the microwave region or to have minimal magnetic properties, which make them undesirable for many applications. Similarly, no known natural materials exhibit negative permittivity and permeability simultaneously. Because of the usefulness of these types of properties, there is great emphasis on the development of engineered materials that offer a variety of possibilities to achieve applications that are ordinarily out of reach. One well known example is the development of negative index materials by Dr. Pendry [1], later known as metamaterials. The properties of those types of artificial materials have been studied, and the ability of manipulating material properties through structural design enables applications such as cloaking [2]-[3]. The development of novel antennas is another application that employs such materials [4]-[6]. Composite materials with inclusions of graphene nanoribbons or nano metallic particles are used in many RF applications to obtain desired material properties [7], to miniaturize radio frequency (RF) electronic components [8]-[9], or to create flexible substrates for wearable RF devices

[10]. Engineered materials with 3D structures such as honeycombs are used for broadband microwave absorption [11]-[12], and 3-D printing technology is used to achieve complex 3D objects with artificially controlled effective material properties [13]. As the number of applications and the complexity of the engineered materials increase, there is a growing need for characterization methods that can accurately predict the constitutive parameters of these materials.

Many characterization techniques suitable for measuring EM materials have been developed. The typical procedures for determining the permittivity and permeability involve comparisons of the theoretical data and the measured data. The measured data are usually acquired in a laboratory where the test samples are prepared to accommodate the experimental environment, and a vector network analyzer (VNA) is used to obtain the data. Appropriate algorithms are then used to extract the complex constitutive parameters by minimizing the difference between predicted and measured data. The majority of the existing techniques can be categorized into free space methods, resonant cavity methods, coaxial line methods, and rectangular waveguide methods.

Free space methods have many advantages compared to other methods, such as accurate results over a wide frequency range, ease of sample preparation, and no physical contact between the sample and the test equipment [14]. They also provide characterization using multiple measurements of different incident angles or polarizations [15]-[16] which can be hard to achieve with other methods. However, these types of methods usually require a large and flat test sample, and multiple reflections occur between the interrogating antennas and the surface of the sample. As such, diffraction at the edge of the sample may lead to significant increases in error. In addition to this, in some applications only transmission data S21 is used since S11 is more sensitive to measurement uncertainties [17]-[18]. These disadvantages make free space methods unsuitable for many materials.

Resonant cavity measurements are very accurate in obtaining permittivity and permeability. There are two types of resonant measurements that are commonly adopted. Perturba-

tion methods are suitable for all permittivity measurements, and measurements of magnetic materials with medium to high loss [19]. A low loss measurement method is suitable for measurements on low loss materials with larger sizes [20]. The resonant cavity method offers the ability to measure very small materials samples by using approximate expressions for fields in the sample and cavity. However, this method usually requires high frequency resolution VNAs, accurately machined samples to fit into the cavity, and is generally narrow band. Therefore, characterization of materials over a wide frequency range is difficult using this method.

Coaxial line methods are very popular for characterization of complex permittivity and permeability since they provide broadband measurements using a single test. They are usually easy to implement compared to the resonant cavity methods where special cavities are required [21]-[22], and the required sample size is typically small. However, there are many disadvantages in using these methods. First, samples must be precisely machined so that there is no air gap between the sample and the coaxial line fixture. It is found that even a very small air gap can cause huge errors for samples with high permittivity and corrections have to be made to compensate for the errors caused by air gaps [23]-[24]. Second, coaxial lines lack ruggedness and the thermal expansion or mechanical vibration between the sample fixture and the test samples makes it very difficult to maintain consistent precise measurements [25].

Rectangular waveguides are the most common waveguiding structure and they have several advantages over other characterization methods. Physically, they are more rugged than coaxial lines, making them less sensitive to thermal expansion and vibration. Unlike the free space method, resonant cavity method, or the coaxial lime method, sample preparation for rectangular waveguides is much simpler, since the samples are usually rectangular sheets or blocks and they do not require high precision. The large surface area of waveguides significantly reduces conductor losses that are relatively high in two wire transmission lines and coaxial lines due to small conducting surface and roughness of the copper [26]. Also, at high

frequencies, energy transmission by coaxial cables becomes less efficient due to skin effect while waveguides can still maintain a high transmitted signal strength. Also, the analytical analysis of sample interaction is available [27].

The primary limitations of rectangular waveguides are their cost and physical size. The inside surfaces of waveguides are often plated with silver or gold to reduce losses which make them very expensive in many applications. The width of a waveguide is usually a half wavelength at the frequency of the wave to be transported. For instance, the WR650 L-band waveguide (1.12 GHz-1.7 GHz) has dimensions 6.5 inches by 3.25 inches which makes it very difficult to carry or set up and this makes the use of rectangular waveguide below 1 GHz almost impractical. Limited operating bandwidth is also another drawback of rectangular waveguides compared to other method such as coaxial lines methods. To allow the propagation of a single dominant mode, the lower end of the operating band is usually about 30% higher than the cutoff frequency. The higher end of the band is also chosen be lower than the cutoff frequency of the next higher order mode.

Many characterization techniques based on rectangular waveguide applicators have been developed in which the samples can be placed inside the guide, against an open-ended flange, or placed against various metallic objects such as irises, posts, slots or stubs. One of the most widely used technique is the Nicolson-Ross-Weir (NRW) method [28]-[29] in which a sample is machined to fill the cross-section of the waveguide and the transmission and reflection coefficients are measured. The benefit gained from using this method is its ability to directly solve for the complex μ and ϵ in closed form. However, a closed-form expression is not always available for most anisotropic materials and in some cases it is even difficult to obtain flat test samples which are large enough to fill the entire waveguide cross section. To obtain the parameters of anisotropic materials without a closed form expression, iterative solvers such as Newton's method [30] or least squares approaches [31] are usually used. Several techniques have also been developed to reduce the size requirement of the test sample. In [32], the authors utilize a stepped waveguide aperture to characterize isotropic materials

with small electrical size. This method reduces the cost or producing large, precise samples. However, the extracted results using this method may be sensitive to the propagated error from measurement uncertainties. In [33], the author presents characterization of PEC backed lossy simple media using a waveguide slot aperture, but the extraction process require two measurements of different sample thickness. Techniques that do not require metallic objects such as reduced waveguide apertures or waveguide slots have also been developed to simplify the measurement process. In [34], a dielectric sample is partially loaded in a rectangular waveguide and measured. Newton's method is used to search for a fit between simulated and measured scattering parameters. In [35], the authors present a partially-filled waveguide method that improves the accuracy of the material characterization. A mode-matching technique is developed to accommodate the high order modes excited at the discontinuity of the waveguide and Newton's method is employed to extract the electromagnetic properties of samples with low-loss and high-loss parameters. To the best knowledge of the author, little work has been done to achieve accurate characterization of complex anisotropic materials using only rectangular waveguides. The motivation for this dissertation is to develop characterization methods for different complex anisotropic materials using a partially-filled waveguide technique, which can be a stepping stone toward full tensor characterization.

Two types of anisotropic materials are considered in this work. The first type are biaxial materials which have six nonzero entries in the material tensors, corresponding to six complex material parameters. Several techniques have been previously developed to determine the complex material parameters such as a cavity perturbation technique [36] and a modified free-space method which extracts the dielectric properties of the test samples. Characterization approaches based on rectangular waveguides have also been investigated to determine the complex material parameters. Two issues are usually taken into consideration when characterizing biaxial materials which contain multiple complex parameters. The first is the determination of the total number of measured data which are sufficient for extracting all the constitutive parameters, whether using reflection measurement data, transmission mea-

surement data or both. The second problem is finding the appropriate experimental setup to collect the measured data that introduces few uncertainties.

In [37], the authors demonstrate a technique for the extraction of the six material parameters in a biaxial material. Closed form solutions are derived to solve three material parameters using two different excitations of TE_{10} and TE_{20} mode. By rotating the sample, the other three parameters can be obtained. In order to obtain the measured data under two excitations, a special waveguide fixture is built. However, only the extraction for a non-dispersive material was conducted using two sets of measurements and no measurements of an actual biaxial sample were carried out. Recently a method for characterizing the properties of biaxially anisotropic materials was developed using a reduced-aperture waveguide system [38]. By using a sample holder of cubical shape, a single sample of biaxial material may be measured in three different orientations, providing the required number of reflection and transmission measurements to determine the six unique constitutive parameters. The fields in the sample region are computed analytically, and the mode-matching approach is used to determine the theoretical S-parameters of the cascaded system consisting of the sample holder and the empty waveguide transitions. This technique has the drawback that the sample must fit tightly within the conducting sample holder (to eliminate air gaps), the restricted aperture of the sample holder reduces the energy transmitted through the sample, and a special sample holder must be constructed. To achieve the full characterization of baixial media without requiring an additional sample holder, one work [39] was developed in which the measured data is obtained from multiple independent reflection measurements of samples partially filled in a shorted rectangular waveguide at different orientations. Iterative solvers that compare the difference between FEM simulated results of the S11 characteristics and the measured reflection data are used to determine the parameters. However, this work only shows the characterization of permittivity properties of the biaxial sample and the use of FEM simulations greatly slow down the extraction procedure. To overcome the drawbacks seen in these works, this dissertation introduces a partially filled waveguide technique for full

biaxial material characterization. This approach eliminates the presence of gaps along the sidewalls, reduces reflections from the conducting restriction, and does not require a special sample holder. More importantly, an analytic solution is used instead of FEM simulations, which greatly shortens the extraction time.

The second type of materials considered in this dissertation are gyromagnetic materials. Gyromagnetic materials have scalar permittivity and an anisotropic permeability tensor that contains two identical and one different diagonal entry, and two off-diagonal entries. Gyromagnetic materials are widely used in many applications such as filters, phase shifters, and radar absorbing materials (RAM) and techniques that accurately extract the complex scalar permittivity and permeability tensor components are desired. In [40] and [41] the authors describe a method for measuring the complex scalar permittivity and permeability tensor components of a gyromagnetic material using a partially filled waveguide technique. A sample that partially fills the cross-section of the guide is placed next to a dielectric slab. A mode-matching technique is used to derive the theoretical reflection and transmission coefficients. Two sets of measurements are required to extract the material parameters. The first set is taken when the gyromagnetic material is completely demagnetized to extract the scalar permittivity properties. A second measurement with certain magnetic biasing configuration is used to complete the extract for the permeability tensor. However, the authors failed to demonstrate the accuracy of the extracted parameters and no information was given to validate the extracted results compared to the theoretical values. In addition, this method may suffer from the measurement uncertainties caused by air gaps between the test sample and the dielectric slab, and the use of electromagnets with the assumption of known static magnetic field strength may amplify the uncertainties in the extracted parameters. Recently, a method for characterizing gyromagnetic materials using a reduced-aperture waveguide was developed [42] in which the sample completely fills the cross-section of a narrow waveguide section. This method has several drawbacks, such as the need of a special sample holder, potential for air gaps along four walls, reduced energy transmission due to the restriction of

the narrow guide and no experimental validation is performed. These drawbacks leads to part of the motivation for this work, which is to develop a accurate method for characterizing gyromagnetic materials by placing a narrow sample into a full-aperture waveguide.

CHAPTER 2

Characterization of Biaxial Material Using a Partially-Filled Waveguide

2.1 Introduction

This chapter presents a novel waveguide method for extracting full biaxial tensors using a single sample that is partially filled in a waveguide. This method eliminates the presence of gaps along the sidewalls, reduces reflections from the conducting restriction, and does not require a special sample holder [42]. Since the extraction of material parameters is accomplished through an inverse problem that minimizes the difference between the theoretical reflection and transmission coefficients and the measured S-parameters, a carefully computed forward problem which computes theoretical S-parameters is needed for accurate characterization. The theoretical reflection and transmission coefficients are determined using a mode-matching technique. This method allows the computational error in the forward problem to be controlled by using an appropriate number of modes. Two samples made of stacked layers of substrates were manufactured in the shape of a cube so that multiple measurements can be obtained only from one sample which is inserted with different orientations in the guide. The sample was placed at the center of the cross-section of a waveguide,

and the transmission and reflection coefficients were measured for various orientations. The material parameters were extracted to demonstrate the feasibility of the proposed approach.

2.2 Theoretical Transmission and Reflection Coefficients Using Mode-Matching Analysis

Biaxial materials are anisotropic and have six non-zero complex permittivity and permeability tensor entries along the orthogonal axes A, B, and C. The material properties can be described by the tensors

$$\epsilon = \epsilon_0 \begin{bmatrix} \epsilon_A & 0 & 0 \\ 0 & \epsilon_B & 0 \\ 0 & 0 & \epsilon_C \end{bmatrix} \tag{2.1}$$

and

$$\mu = \mu_0 \begin{bmatrix} \mu_A & 0 & 0 \\ 0 & \mu_B & 0 \\ 0 & 0 & \mu_C \end{bmatrix}, \tag{2.2}$$

where the values ϵ_A, μ_A, etc., are relative parameters, and are complex quantities: $\epsilon_A = \epsilon_{rA} + j\epsilon_{iA}$, $\mu_A = \mu_{rA} + j\mu_{iA}$, etc.

The proposed measurement system is shown in Figure 2.1. A cubical sample of the biaxial material is centered within the cross-section of a rectangular waveguide such that the cross-sectional view is shown in Figure 2.2. The sample is machined into a cube of which the side length d is same as the height of the waveguide aperture b. Moreover, no extra sample holder is required to contain the cubical sample, and the sample can be placed directly into the waveguide extension of the sending end ($z < 0$). The extension serves as a sample holder and the length is properly chosen such that a single TE_{10} mode is incident on the sample from the sending ($z < 0$) extension, and that a single mode appears at the receiving end ($z > d$).

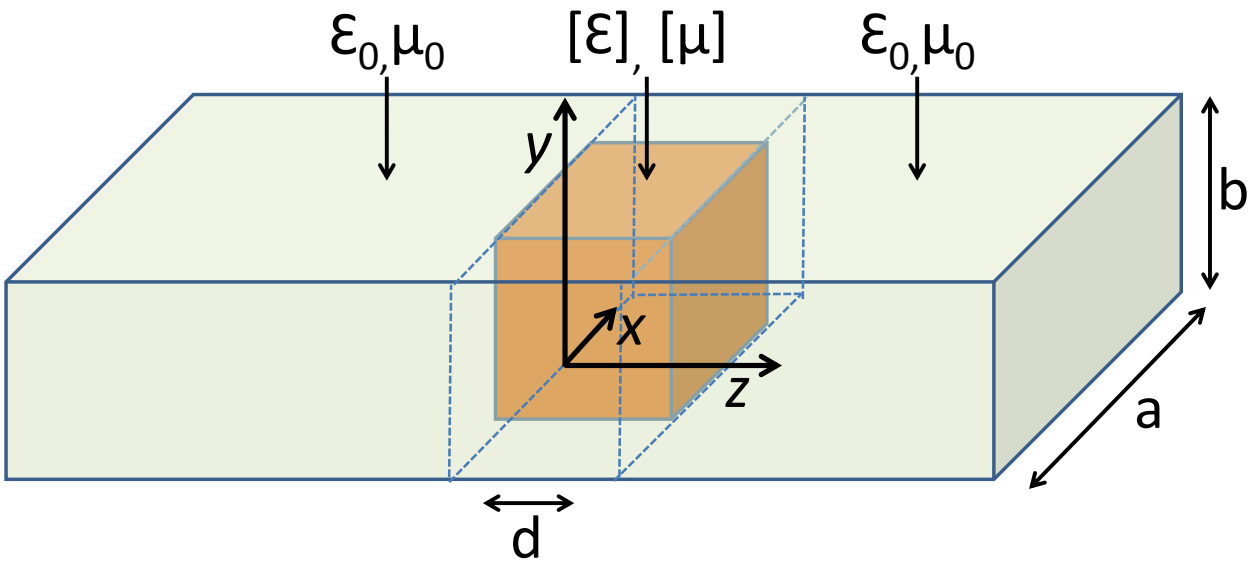

Figure 2.1 Waveguide contains cubical sample.

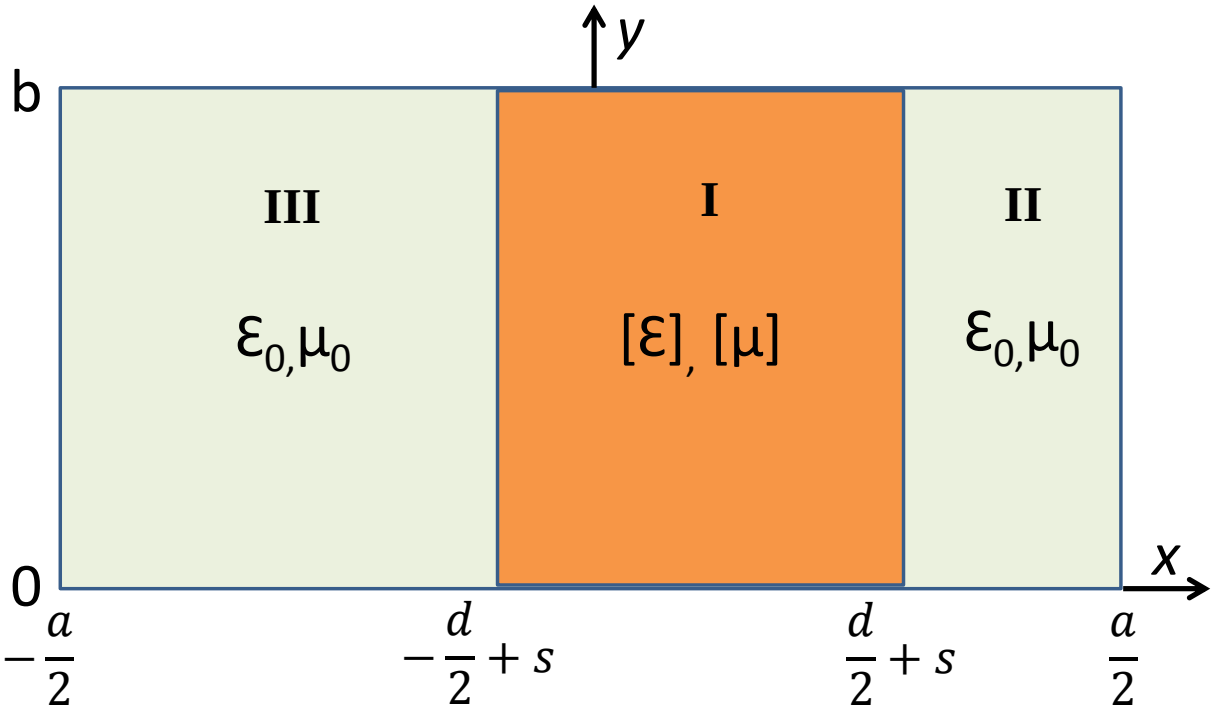

Figure 2.2 Cross-sectional view of the waveguide partially filled with biaxial material.

To solve the inverse problem which requires minimizing the difference between the measured and the theoretical reflection and transmission coefficients, an accurate computation of the S-parameters of the partially-filled waveguide system is desired. This is accomplished by a mode-matching technique, which takes account of the higher order modes excited at the interface between the empty waveguide and the sample region ($0 < z < d$), and allows the computational accuracy to be easily controlled.

A single TE_{10} mode is assumed to be incident upon the sample, as shown in Figure 2.3. Due to the discontinuity at the sample interface, an infinite number of waveguide modes are reflected into the transmitting extension ($z < 0$), while an infinite number of waveguide modes are transmitted into the sample region. The transmitted modal fields are incident on the second sample interface $z = d$, and thus a spectrum of higher order modes is also reflected back into the sample region, and transmitted into the receiving end ($z > d$). However, since the electric field of the incident TE_{10} mode is even about $x = 0$, and the sample placement is also symmetric about $x = 0$, the incident field will only couple to modes with a similar symmetry. Also, the field structure of the empty waveguide is well known [43].Therefore, only TE_{n0} modes with odd values of n are excited in the empty guides, with electric fields that are even about $x = 0$.

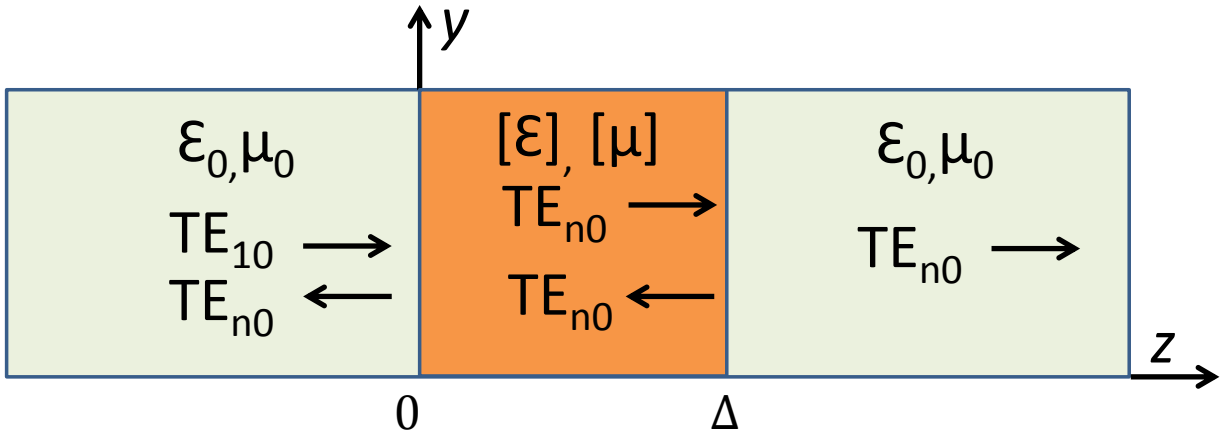

Figure 2.3 Side view of a partially filled waveguide.

2.2.1 Field Structure in a Waveguide Partially Filled with Biaxial Material

The material sample can be placed into the waveguide in various orientations. Assuming that the orientation is chosen such that $\mu_A = \mu x$, $\mu_B = \mu y$ and $\mu_C = \mu z$, etc. As mentioned, only TE_{n0} modes with odd values of n are excited in the empty guides. The field structure of the empty waveguide modes is given by,

$$\bar{E}_n(x,z) = -\frac{j\omega\mu_o}{\bar{k}_{cn}} \sin\left[\bar{k}_{cn}\left(x - \frac{a}{2}\right)\right] e^{\pm j\beta_n z}, \quad \bar{H}_n(x,z) = \frac{E_n(x,z)}{\bar{Z}_n}. \tag{2.3}$$

Here a is the width of the guide, $\bar{k}^s_{cn} = n\pi/a$ is the cutoff wavenumber for the n^{th} TE_{n0} mode ($n = 1, 2, \ldots$), and $\bar{Z}_n = \frac{\omega\mu_o}{\bar{\beta}_n}$ is the TE wave impedance. The real phase constant $\bar{\beta}_n$ of the TE_{n0} mode is given by

$$\bar{\beta}_n = \sqrt{k_0^2 - (\bar{k}_{cn})^2} \tag{2.4}$$

with $k_0 = \omega\sqrt{\mu_0\epsilon_0}$ being the free-space wavenumber.

The field structure of the waveguide modes in the sample region is more complicated and can be found solving the wave equation for a biaxial medium (Section 2.3.3 [42]):

$$\left[\frac{\partial^2}{\partial x^2} + (k_{cn})^2\right] H_z(x,z) = 0 \tag{2.5}$$

where

$$(k_{cn})^2 = \frac{\mu_z}{\mu_x}\left[\omega^2\mu_x\epsilon y - (\beta_n)^2\right] \tag{2.6}$$

is the cutoff wavenumber. The fields are given as

$$H_z^I(x,z) = A^I \sin k_c^I e^{\pm j\beta_n z} \tag{2.7}$$

$$E_y^I(x,z) = \frac{j\omega\mu_z}{k_c^I} A^I \cos k_c^I e^{\pm j\beta_n z}, \tag{2.8}$$

where A^I is the modal amplitude of the transverse field for the biaxial medium, and k_{cn}^I is the cutoff wavenumber shown in (2.6). Note that there is also empty space in the sample region. The field structure for this part is the same as that of the empty waveguide, and thus the fields can be expressed as:

$$H_z^{II}(x,z) = A^{II} \sin k_{cn}^{II} e^{\pm j\beta_n z} \tag{2.9}$$

$$E_y^{II}(x,z) = -\frac{j\omega\mu_0}{k_{cn}^{II}} A^{II} \cos k_c^{II} \left(x - \frac{a}{2}\right) e^{\pm j\beta_n z}, \tag{2.10}$$

where A^{II} is the modal amplitude of the transverse field for the empty part in the sample region, and k_{cn}^{II} is the cutoff wavenumber in the empty part of the sample region.

With the expressions of the fields shown above, the boundary conditions are applied at the interfaces $x = \frac{a}{2}$ and $x = \frac{d}{2}$. The complex propagation constants β are found by solving the transcendental equation,

$$\mu_o k_c^I \sin\left(k_{cn}^I \frac{d}{2}\right) \sin\left(k_{cn}^{II} \frac{a-d}{2}\right) = \mu_z k_{cn}^{II} \cos\left(k_c^I \frac{d}{2}\right) \cos\left(k_{cn}^{II} \frac{a-d}{2}\right) \tag{2.11}$$

where the cutoff wavenumbers are related to the complex propagation constants by

$$\left(k_{cn}^I\right)^2 = \frac{\mu_z}{\mu_x}\left[\omega^2 \mu_x \epsilon_y - (\beta_n)^2\right] \tag{2.12}$$

$$\left(k_c^{II2}\right) = k_0^2 - \beta_n^2. \tag{2.13}$$

Note that the boundary conditions at $x = -\frac{a}{2}$ and $x = -\frac{d}{2}$ are also satisfied due to symmetry.

Different approaches can be used to solve the transcendental equation for β_n. One approach is to start with the solution for β_n under the condition $d = 0$, which is found by equations of the TE_{n0} modes in an empty guide, and then slowly increase the width of the sample, solving for β_n at each step using the previous solution as an initial guess. This approach has been used in [35] for thin samples. However, as the sample width increases, there is an uncertainty of the modal types between propagating and evanescent. Thus, solving

the transcendental equation using previous results as initial guesses becomes problematic. Instead, the following approach is used when the material loss is not too high. First the imaginary parts of the material parameters are set to zero which implies a lossless material. Then the real values of β are found by looking for zero crossings of the transcendental equation (2.11) between $\beta = 0$ and $\beta = \omega\sqrt{\mu_x \epsilon_y}$, and as *beta* exceeds this range, no real roots can be found. These zero crossings represent the propagating modes, and the modal number n is assigned based on the order of the zero crossing. Next the phase constant β in the transcendental equation is replaced by $j\delta$, and real values of δ are found by finding zero crossings starting from $\delta = 0$ and continuing until a desired number of modes have been found. These are the evanescent modes, and they are numbered continuing after the highest order propagating mode. Finally, the imaginary parts of the material parameters and the zero crossing values found earlier for β and δ are used as initial guesses in a root-search method to find the complex propagation constants β_n for both the propagating and the evanescent modes.

With the complex propagation constants β_n found, the modal fields are given for $x > 0$ by

$$E_n(x,z) = \begin{cases} E_n^I(x,z), & 0 \le x \le \frac{d}{2} \\ E_n^{II}(x,z), & \frac{d}{2} < x \le \frac{a}{2} \end{cases} \tag{2.14}$$

$$H_n(x,z) = \begin{cases} H_n^I(x,z), & 0 \le x \le \frac{d}{2} \\ H_n^{II}(x,z), & \frac{d}{2} < x \le \frac{a}{2}, \end{cases} \tag{2.15}$$

where

$$E_n^I(x,z) = \frac{j\omega\mu z}{k_{cn}^I}\cos\left(k_{cn}^I x\right)e^{\pm j\beta_n z}, \tag{2.16}$$

$$E_n^{II}(x,z) = -\frac{j\omega\mu z}{k_{cn}^{II}}\sin\left(k_{cn}^I\frac{d}{2}\right)\frac{\sin\left[k_c^{II}(x-\frac{a}{2})\right]}{\cos\left[k_c^{II}\left(\frac{d-a}{2}\right)\right]}e^{\pm j\beta_n z}, \tag{2.17}$$

$$H_n^I(x) = \frac{E_n^I(x)}{Z^I{}_n}, \quad H_n^{II}(x) = \frac{E_n^{II}(x)}{Z^{II}{}_n}, \tag{2.18}$$

with

$$Z^I{}_n = \frac{\omega\mu x}{\beta_n}, \quad Z^{II}{}_n = \frac{\omega\mu_o}{\beta_n}. \tag{2.19}$$

2.2.2 Solution for S-Parameters Using Modal Expansions

The transverse fields can be expanded as an infinite sum of TE_{n0} modes, with modal amplitudes determined by applying appropriate boundary conditions. For the empty waveguide extension region $z < 0$,

$$E_y(x,z) = a_1^i\bar{E}_1(x)\mathrm{e}^{-j\bar{\beta}1z} + \sum_{\substack{n=1\\ \text{odd}}}^{\infty} a_n^r\bar{E}_n(x)\mathrm{e}^{+j\bar{\beta}nz} \tag{2.20}$$

$$H_z(x,z) = -a_1^i\bar{H}_1(x)\mathrm{e}^{-j\bar{\beta}1z} + \sum_{\substack{n=1\\ \text{odd}}}^{\infty} a_n^r\bar{H}_n(x)\mathrm{e}^{+j\bar{\beta}nz}. \tag{2.21}$$

The modal amplitude a_1^i represents the amplitude of the incident TE_{10} wave, which is assumed to be known. Only odd mode indices are used such that no even mode is taken into

account. In the sample region, $0 < z < d$, the transverse fields are

$$E_y(x,z) = \sum_{\substack{n=1 \\ \text{odd}}}^{\infty} \left[a_n^+ \mathrm{e}^{-j\beta_n z} + a_n^- \mathrm{e}^{+j\beta_n z} \right] E_n(x) \tag{2.22}$$

$$H_x(x,z) = \sum_{\substack{n=1 \\ \text{odd}}}^{\infty} \left[-a_n^+ \mathrm{e}^{-j\beta_n z} + a_n^- \mathrm{e}^{+j\beta_n z} \right] H_n(x). \tag{2.23}$$

Finally, since only transmited fields exist in the waveguide extension for $z > d$, the transverse fields are

$$E_y(x,z) = \sum_{\substack{n=1 \\ \text{odd}}}^{\infty} a_n^t \bar{E}_n(x) \mathrm{e}^{-j\bar{\beta}_n (z-d)} \tag{2.24}$$

$$H_x(x,z) = -\sum_{\substack{n=1 \\ \text{odd}}}^{\infty} a_n^t \bar{H}_n(x) \mathrm{e}^{-j\bar{\beta}_n (z-d)}. \tag{2.25}$$

The unknown modal amplitudes can be determined by applying the boundary conditions on E_y and H_x at the interfaces $z = 0$ and $z = d$,

$$a_1^i \bar{E}_1(x) + \sum_{n=1}^{N} a_n^r \bar{E}_n(x) = \sum_{n=1}^{N} \left[a_n^+ + a_n^- \right] E_n(x), \tag{2.26}$$

$$-a_1^i \bar{H}_1(x) + \sum_{n=1}^{N} a_n^r \bar{H}_n(x) = \sum_{n=1}^{N} \left[-a_n^+ + a_n^- \right] H_n(x), \tag{2.27}$$

$$\sum_{n=1}^{N} \left[a_n^+ \mathrm{e}^{-j\beta_n d} + a_n^- \mathrm{e}^{+j\beta_n d} \right] E_n(x) = \sum_{n=1}^{N} a_n^t \bar{E}_n(x), \tag{2.28}$$

$$\sum_{n=1}^{N} \left[-a_n^+ \mathrm{e}^{-j\beta_n d} + a_n^- \mathrm{e}^{+j\beta_n d} \right] H_n(x) = -\sum_{n=1}^{N} a_n^t \bar{H}_n(x). \tag{2.29}$$

Note the number of modes N used for the empty waveguide is the same as that used for

sample regions. These equations above are a system of functional equations and can be transformed into a system of linear equations by applying the testing operations of empty waveguide modes to the four equations. The linear equations with testing operators are expressed as

$$a_1^i \int_0^{\frac{a}{2}} \bar{E}_1(x)\bar{E}_m(x)dx + \sum_{n=1}^{N} a_n^r \int_0^{\frac{a}{2}} \bar{E}_n(x)\bar{E}_m(x)dx =$$

$$\sum_{n=1}^{N} a_n^+ \int_0^{\frac{a}{2}} E_n(x)\bar{E}_m(x)dx + a_n^- \int_0^{\frac{a}{2}} E_n(x)\bar{E}_m(x)dx, \quad (2.30)$$

$$a_1^i \int_0^{\frac{a}{2}} \bar{H}_1(x)\bar{H}_m(x)dx - \sum_{n=1}^{N} a_n^r \int_0^{\frac{a}{2}} \bar{H}_n(x)\bar{H}_m(x)dx =$$

$$\sum_{n=1}^{N} a_n^+ \int_0^{\frac{a}{2}} H_n(x)\bar{H}_m(x)dx - a_n^- \int_0^{\frac{a}{2}} H_n(x)\bar{H}_m(x)dx, \quad (2.31)$$

$$\sum_{n=1}^{N} a_n^+ \mathrm{e}^{-j\beta_n d} \int_0^{\frac{a}{2}} E_n(x)\bar{E}_m(x)dx + \sum_{n=1}^{N} a_n^- \mathrm{e}^{-j\beta_n d} \int_0^{\frac{a}{2}} E_n(x)\bar{E}_m(x)dx =$$

$$\sum_{n=1}^{N} a_n^t \int_0^{\frac{a}{2}} \bar{E}_n(x)\bar{E}_m(x)dx, \quad (2.32)$$

$$\sum_{n=1}^{N} a_n^+ \mathrm{e}^{-j\beta_n d} \int_0^{\frac{a}{2}} H_n(x)\bar{H}_m(x)dx - \sum_{n=1}^{N} a_n^- \mathrm{e}^{-j\beta_n d} \int_0^{\frac{a}{2}} H_n(x)\bar{H}_m(x)dx =$$

$$\sum_{n=1}^{N} a_n^t \int_0^{\frac{a}{2}} \bar{H}_n(x)\bar{H}_m(x)dx. \quad (2.33)$$

The integrals are defined as,

$$C_{mn} = \int_0^{\frac{a}{2}} \overline{E}_1(x)\overline{E}_m(x)dx \tag{2.34}$$

$$E_{mn} = \int_0^{\frac{a}{2}} \overline{H}_1(x)\overline{H}_m(x)dx \tag{2.35}$$

$$D_{mn} = \int_0^{\frac{a}{2}} \overline{E}_n(x)\overline{E}_m(x)dx \tag{2.36}$$

$$F_{mn} = \int_0^{\frac{a}{2}} \overline{H}_n(x)\overline{H}_m(x)dx. \tag{2.37}$$

The integrals can be computed in closed form and this results in a $4N \times 4N$ system of equations as follows,

$$a_1^i C_{m1}^+ \sum_{n=1}^{N} a_n^r C_{mn} = \sum_{n=1}^{N} a_n^+ D_{mn} + \sum_{n=1}^{N} a_n^- D_{mn} \tag{2.38}$$

$$a_1^i E_{m1} - \sum_{n=1}^{N} a_n^r E_{mn} = \sum_{n=1}^{N} a_n^+ F_{mn} - \sum_{n=1}^{N} a_n^- F_{mn} \tag{2.39}$$

$$\sum_{n=1}^{N} a_n^+ D_{mn} e^{-j\beta_n d} + \sum_{n=1}^{N} a_n^- D_{mn} e^{+j\beta_n d} = \sum_{n=1}^{N} a_n^t C_{mn} \tag{2.40}$$

$$\sum_{n=1}^{N} a_n^+ F_{mn} e^{-j\beta_n d} - \sum_{n=1}^{N} a_n^- F_{mn} e^{+j\beta_n d} = \sum_{n=1}^{N} a_n^t E_{mn}, \tag{2.41}$$

which can be rewritten as a matrix equation,

$$\left[\begin{array}{c|c|c|c} -C_{mn} & D_{mn} & D_{mn} & 0 \\ \hline E_{mn} & F_{mn} & -F_{mn} & 0 \\ \hline 0 & D'_{mn} & -D''_{mn} & -C_{mn} \\ \hline 0 & -F'_{mn} & F''_{mn} & E_{mn} \end{array}\right] \left[\begin{array}{c} a_n^r \\ \hline a_n^+ \\ \hline a_n^- \\ \hline a_n^t \end{array}\right] = a_1^i \left[\begin{array}{c} C_{m1} \\ \hline E_{m1} \\ \hline 0 \\ \hline 0 \end{array}\right] \tag{2.42}$$

where

$$D'_{mn} = D_{mn}e^{-j\beta_n d}, \qquad D''_{mn} = D_{mn}e^{+j\beta_n d} \tag{2.43}$$
$$F'_{mn} = F_{mn}e^{-j\beta_n d}, \qquad F''_{mn} = F_{mn}e^{+j\beta_n d}.$$

Each of the quantities C_{mn} and D_{mn} are NxN submatrices and a_n^r and a_n^t are the unknown modal coefficients. By solving the matrix equation, the modal amplitudes can be found. Since a_1^i is the known amplitude of the incident TE_{10} mode, the theoretical S-parameters (S^{thy}) can be computed from the equations

$$S_{11}^{thy} = \frac{a_1^r}{a_1^i}, \quad S_{21}^{thy} = \frac{a_1^t}{a_1^i}. \tag{2.44}$$

2.2.3 Validation of Theoretical Analysis

It is important to validate the mode-matching technique by comparison to an alternative method before using it for parameter extraction. Ideally, for the mode-matching technique, an infinite number of modes should be taken into consideration in order to compute the theoretical S-parameters with high accuracy. However, it is not necessary to compute the forward problem with a large number of modes all the time. For example, it would be time-consuming and needless to compute the S-parameters with an accuracy of $\pm 0.01\%$ if the percentage error of the measured S-parameters is 1%. Thus, an appropriate number of modes should be chosen so that reasonable accuracy can be achieved without drastically increasing the computational time. One straightforward approach to achieve this is to increase the size of N until the expected accuracy is achieved. This approach might be time consuming since it requires repeatedly solving the matrix equation. One way to accelerate this process as N is increased is to use an iterative matrix solver, with a previous solution as an initial guess [**?**]. For some cases where a large number of iterative computation is required, extrapolation methods such as linear or least squares extrapolation can be used as an alternative to improve

estimation of the S-parameters.

The validation starts with a lossless, isotropic sample of Teflon with a dielectric constant of 2.1. The mode-matching technique was used to compute the S-parameters for the cubical sample placed into an L-band waveguide system with waveguide dimensions of $a = 16.51$ cm and $b = 8.255$ cm. The convergence criteria for computing the S-parameters are 0.01 dB in magnitude, and 0.1° in phase. For this Teflon sample, convergence can be reached within ten modes, and the number of modes is much smaller than the number of modes used in [42] where more than two hundred modes may be required to reach the same convergences. The S-parameters were also computed using the commercial full-wave solver HFSS. The waveguide extensions with length of 12 inches were included in HFSS, and that length was chosen to ensure that only the TE_{10} mode propagates at the waveguide ports. The convergence tolerance (delta S) in HFSS was specified as 0.001, which is the absolute S-parameter difference between two iterations. It can be seen from Figures 2.4 and 2.5 that excellent agreement is obtained between the two methods, validating the proposed mode-matching technique.

A second example, of a fictitious biaxial material with the material parameters shown in Table 2.1, was considered to further validate this technique. The material is placed into the same L-band waveguide as in the first example with an orientation such that the material axes (A, B, C) are aligned with (x, y, z) respectively. The same S-parameter accuracy as the first example was specified and the computed S-parameters are shown in Figure 2.6 and 2.7, along with the results generated from HFSS. The excellent agreement further validates the mode-matching technique with biaxial materials.

Note that the computational time of the mode-matching technique is significantly shorter than that in the HFSS. Therefore, the extraction process using closed form expressions take less time than those approaches using FEM simulated results.

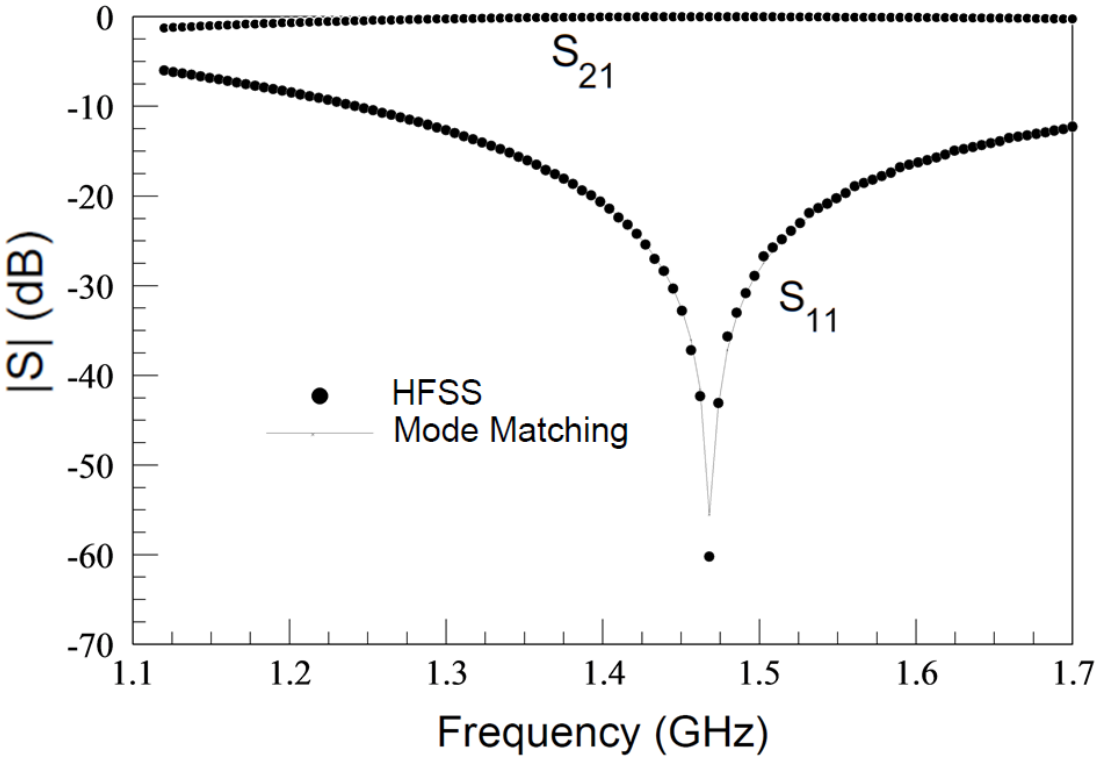

Figure 2.4 S-parameters computed for a Teflon test material.

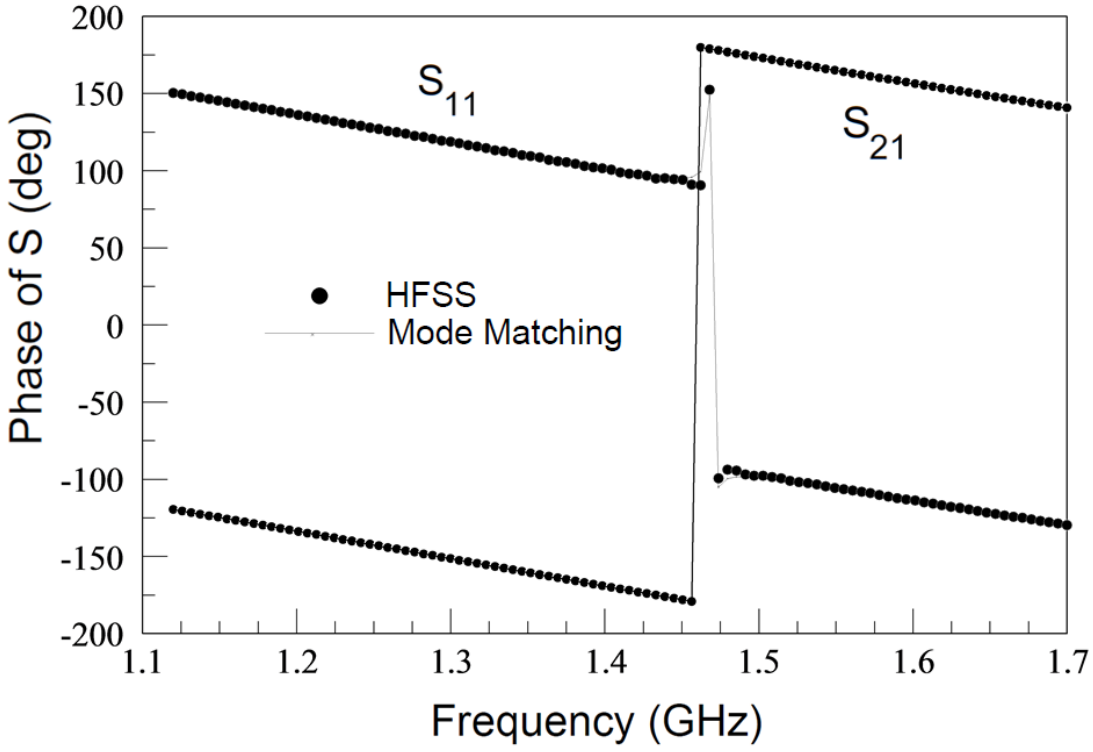

Figure 2.5 S-parameters computed for a Teflon test material.

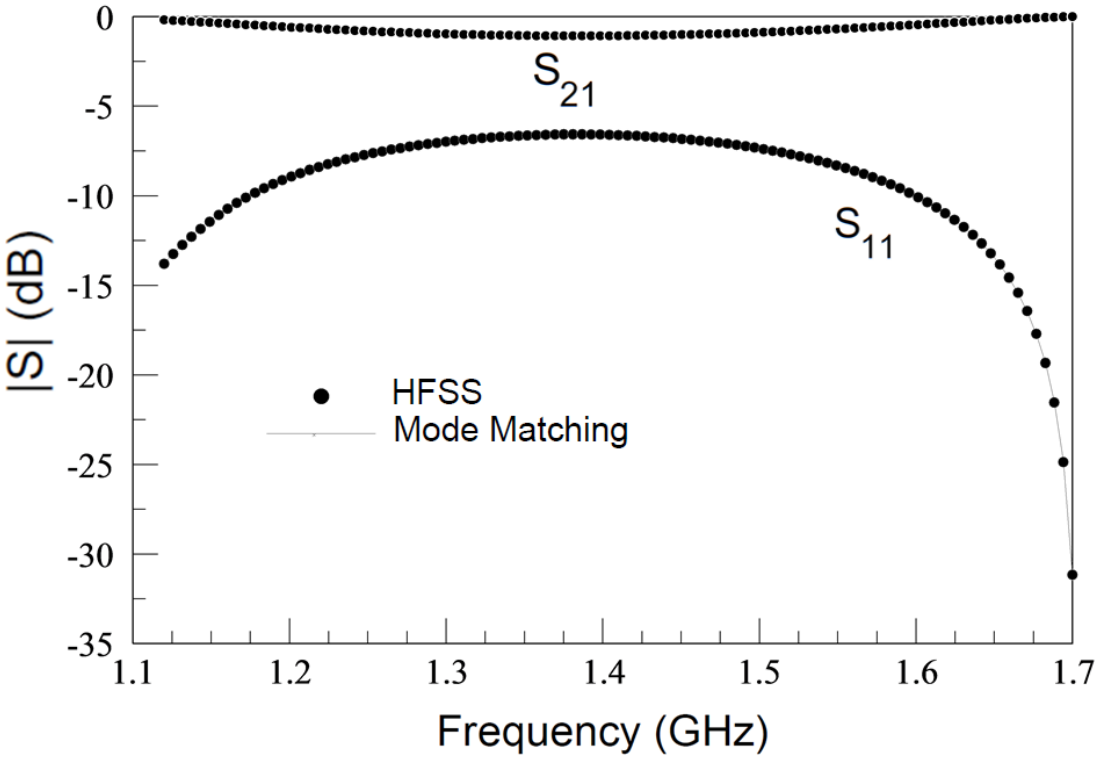

Figure 2.6 S-parameters computed for a biaxial test material with material parameters shown in Table 2.1.

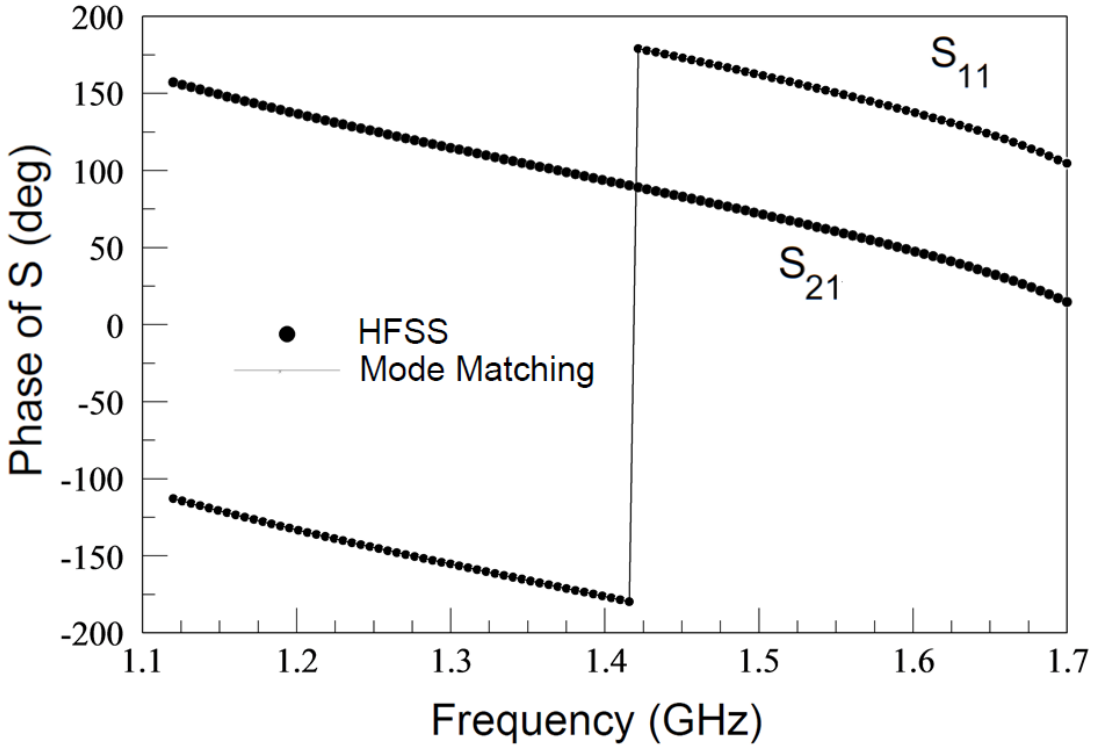

Figure 2.7 S-parameters computed for a biaxial test material with material parameters shown in Table 2.1.

Table 2.1 Material parameters for a fictitious biaxial material.

Parameter	Value
ϵ_A	1.5
ϵ_B	1
ϵ_C	2.0
μ_A	1.0
μ_B	3.0
μ_C	1.0

2.2.4 Extraction Process

Since there are six complex biaxial material parameters $(\epsilon_A, \epsilon_B, \epsilon_C, \mu_A, \mu_B, \mu_C)$ to be determined, a minimum of six independent measurements are required. These measurements can be achieved by measuring S_{11} and S_{21} of a biaxial sample with the material axes A, B, and C aligned along three properly chosen directions. With the following orientations,

$$(A, B, C) \rightarrow (x, y, z) \tag{2.45}$$

$$(A, B, C) \rightarrow (z, x, y) \tag{2.46}$$

$$(A, B, C) \rightarrow (y, z, x) \tag{2.47}$$

S-parameters of $\left(S_{11,1}^{\text{meas}}, S_{21,1}^{\text{meas}}\right)$, $\left(S_{11,2}^{\text{meas}}, S_{21,2}^{\text{meas}}\right)$, and $\left(S_{11,3}^{\text{meas}}, S_{21,3}^{\text{meas}}\right)$ can be obtained, respectively. The material parameters can be determined by solving six nonlinear equations with six complex unknowns,

$$S_{11,n}^{\text{thy}}(\epsilon_A, \epsilon_B, \epsilon_C, \mu_A, \mu_B, \mu_C) - S_{11,n}^{\text{meas}} = 0 \quad n = 1, 2, 3 \tag{2.48}$$

$$S_{21,n}^{\text{thy}}(\epsilon_A, \epsilon_B, \epsilon_C, \mu_A, \mu_B, \mu_C) - S_{21,n}^{\text{meas}} = 0 \quad n = 1, 2, 3. \tag{2.49}$$

However, since standard root-solving methods such as Newton's method typically require accurate initial guesses, it is very difficult to find six proper guesses for this problem. In addition, due to experimental error, one might not be able to find solutions to the system of

equations even with good initial guesses. Therefore, traditional methods are not advisable for solving this problem, and an alternative method needs to be developed. In this work, the six parameters are obtained by separating the system equations into several subsets of system equations. The new subsets of equations contain fewer unknowns and equations. A subset of the material parameters may be found by solving the first set of system equations and then these parameters can be used as known quantities to solve the second set until all parameters are extracted. This approach is feasible because only parameters ϵ_B, μ_A, and μ_C are involved in any orientation.

For a cubical sample, there are 24 different orientations that it can be inserted into the waveguide, and this creates various measurement combinations. A three-step process was developed to obtain the material parameters. First, measurements are implemented with the orientations

$$(A, B, C) \rightarrow (x, y, z) \tag{2.50}$$

$$(A, B, C) \rightarrow (-z, y, x) \tag{2.51}$$

giving the S-parameters $\left(S_{11,1}^{\text{meas}}, S_{21,1}^{\text{meas}}\right)$ and $\left(S_{11,2}^{\text{meas}}, S_{21,2}^{\text{meas}}\right)$ respectively. The initial orientation is shown in Figure 2.8 and labeled 1. Then the sample is rotated by 90° and measured S-parameters are obtained in the orientation labeled 2. These measurements only involve the parameters ϵ_B, μ_A, and μ_C. Using three out of the four complex measurements and Newton's method, the first set of equations with three unknowns,

$$S_{11,n}^{\text{thy}}(\epsilon_B, \mu_A, \mu_C) - S_{11,n}^{\text{meas}} = 0, \ n = 1, \tag{2.52}$$

$$S_{21,n}^{\text{thy}}(\epsilon_B, \mu_A, \mu_C) - S_{21,n}^{\text{meas}} = 0, \ n = 1, 2, \tag{2.53}$$

can be solved. The reason that measurement of $S_{21,2}$ is chosen over $S_{11,2}$ is that it might improve the characterization efficiency and less difficulties are encountered during the root

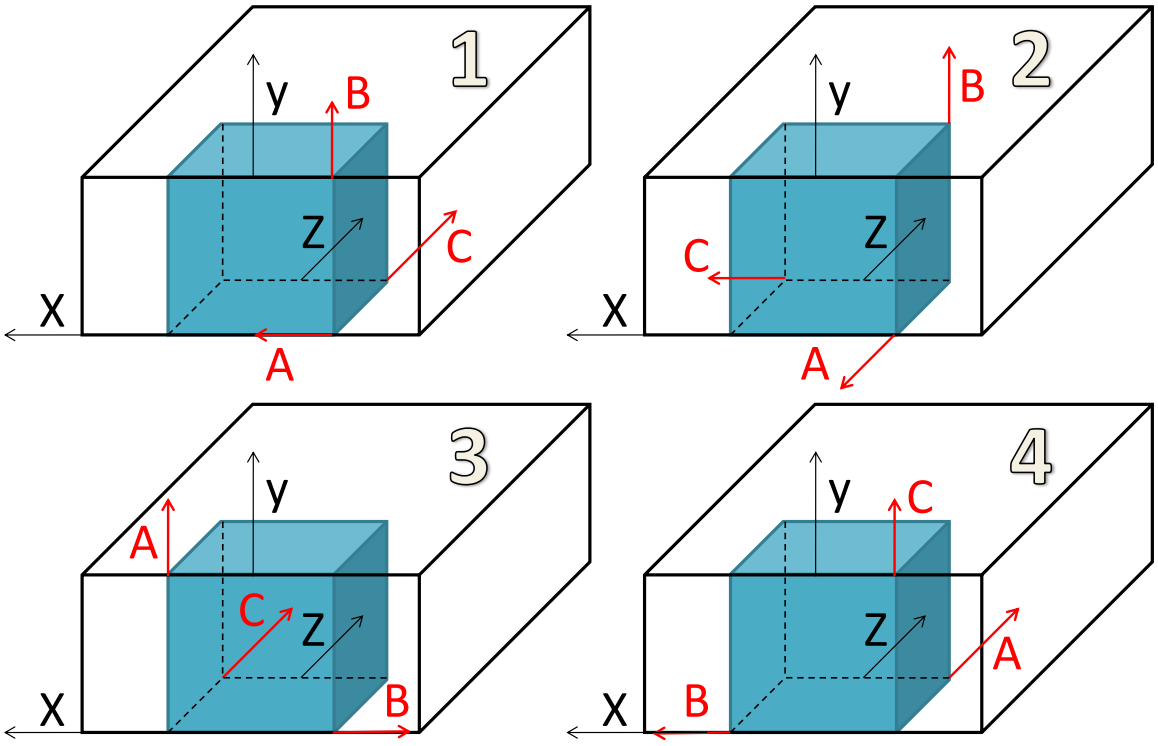

Figure 2.8 Four cube orientations used in the three-step process.

search since S_{21} phase is generally more accurate and it is less sensitive to position error. Next, another measurement is made using orientation 3 in Figure 2.8. This orientation

$$(A, B, C) \rightarrow (y, -x, z) \tag{2.54}$$

gives $\left(S_{11,3}^{\text{meas}}, S_{21,3}^{\text{meas}}\right)$ and this measurement involves ϵ_A, μ_B, and μ_C. However, since μ_C is known, ϵ_A and μ_B can be found by solving the system of equations,

$$S_{11,3}^{\text{thy}}(\epsilon_A, \mu_B) - S_{11,3}^{\text{meas}} = 0, \tag{2.55}$$

$$S_{21,3}^{\text{thy}}(\epsilon_A, \mu_B) - S_{21,3}^{\text{meas}} = 0, \tag{2.56}$$

using Newton's method. Finally, a last measurement is made under orientation 4 in Figure 2.8,

$$(A, B, C) \rightarrow (z, x, y). \tag{2.57}$$

This measurement implicates ϵ_C, μ_A, and μ_B. Since only ϵ_C is unknown, it can be found by solving the single complex equation

$$S_{21,4}^{\text{thy}}(\epsilon_C) - S_{21,4}^{\text{meas}} = 0. \tag{2.58}$$

This process described above is the three-step approach that can be used to extract the six complex material parameters. The drawback of this method is that many measurements are required and since the three-step approach requires using previously solved parameters for the latter two steps, measurement error from the first two steps can influence the extracted results, sometimes leading to amplified errors in the extracted results.

For materials that are unixially anisotropic, where $\epsilon_A = \epsilon_C$ and $\mu_A = \mu_C$, the three-step approach can be modified to reduce the impact of accumulated errors, thus improving the extraction accuracy. The extraction process for uniaxial materials, which have only four complex material parameters, can be reduced to two steps. First, a measurement is made with orientation 1 shown in Figure 2.8. This measurement implicates the parameters ϵ_B, μ_A, and μ_C. Since the value of μ_A is the same as μ_C for unixial material, only two complex measurements are required to solve the following equations using Newton's method:

$$S_{11,1}^{\text{thy}}(\epsilon_B, \mu_C) - S_{11,1}^{\text{meas}} = 0, \tag{2.59}$$

$$S_{21,1}^{\text{thy}}(\epsilon_B, \mu_C) - S_{21,1}^{\text{meas}} = 0, \tag{2.60}$$

Next, another measurement is made using orientation 3 in Figure 2.8 and this measurement implicates ϵ_A, μ_B, and μ_C. However, since μ_C is determined from the previous equations, ϵ_A and μ_B can be found by solving the system of equations

$$S_{11,3}^{\text{thy}}(\epsilon_A, \mu_B) - S_{11,3}^{\text{meas}} = 0, \tag{2.61}$$

$$S_{21,3}^{\text{thy}}(\epsilon_A, \mu_B) - S_{21,3}^{\text{meas}} = 0. \tag{2.62}$$

This approach reduces the number of measurements for characterizing a uniaxial material. Thus the propagation of measurement errors can be reduced, which improves the accuracy of the extracted material parameters.

To validate the proposed technique for characterizing bixial materials, S-parameters were generated using the fictitious material parameters from Table 2.2 with the cubical sample in four orientations. The three-step extraction approach was performed with the convergence of the S-parameters assigned to be 0.01 dB in magnitude, and 0.01° in phase. The results of the characterization are shown in Figure 2.9 and 2.10. Good agreement is achieved between the characterized material parameters and the parameters shown in Table 2.2. Notice that data gaps are seen in the exrtacted parameters over specific ranges of frequency. This is a typical problem inherent to all guided-wave techniques where the sample thickness approaches one half of a guided wavelength, includingthe Nicolson-Ross-Wier closed-form method for isotropic materials [28]-[29]. Experience has shown that a frequency range within approximately $\pm 5\%$ of the half-wavelength frequency should be avoided, and data within that range is not displayed in the figures.

Table 2.2 Material parameters for a fictitious biaxial material.

Parameter	Value
ϵ_A	2.0-0.01j
ϵ_B	4.0-0.02j
ϵ_C	3.0-0.03j
μ_A	1.5-0.02j
μ_B	2.0-0.01j
μ_C	2.5-0.03j

2.2.5 Error and Sensitivity Analysis

There are two types of error that should be taken into consideration during the extraction procedure. The first type of error arises from inaccuracies in the forward problem, and usually these errors in the theoretical reflection and transmission coefficients are introduced from

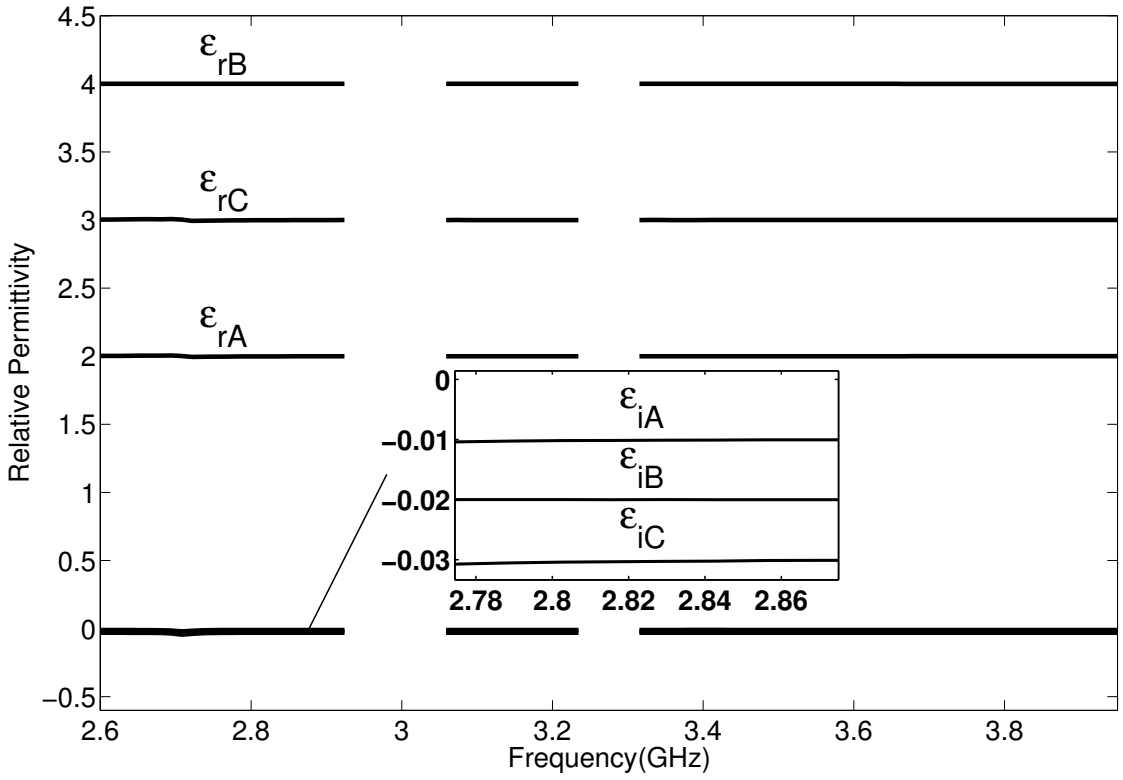

Figure 2.9 Extracted permittivity of the fictitious test material with parameters shown in Table 2.2.

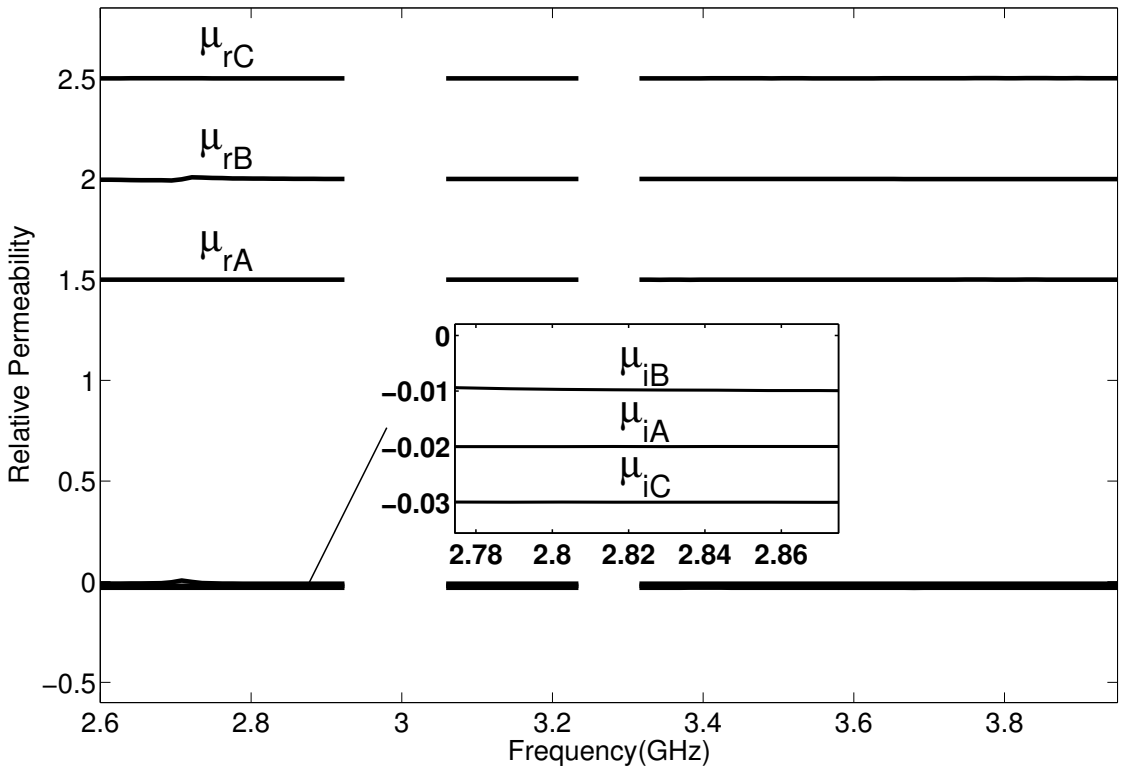

Figure 2.10 Extracted permeability of the fictitious test material with parameters shown in Table 2.2.

errors in the numerical solution or from difficulties in accurately modeling the experiment. The analysis in this section uses closed-form expressions for the prediction of reflection and transmission coefficients and therefore this first type of error is not implicated.

The second type of error is due to measurement inaccuracies and it can be categorized into systematic error and random error. Systematic errors influence the experimental results to cause consistent inaccuracies. They mostly arise from the imperfect construction of the experimental setup or fabricated sample or poorly performing test equipment. An inaccurately machined sample, for example, can produce air gaps between the sample and waveguide walls and cause error between the theoretical S-parameters and the measured S-parameters. Random errors are caused by misalignment of waveguide sections, inaccurate sample positioning in the waveguide which varies from experiment to experiment, and measurement uncertainty inherent in the VNA. It is difficult to model the S-parameter errors caused by inaccurate sample position, due to the analysis assumption that the sample is located at the center of the cross-section of the guide. To reduce random errors in the experiments, accurately machined samples are required along with alignment pins for waveguide sections. In comparison, uncertainties inherent to the VNA can be easily studied using Monte Carlo techniques.

Different S-parameters uncertainties were determined for the extraction of the material parameters of biaxial and uniaxial materials based on the *HP 8510C Specifications & Performance Verification Program* provided by Hewlett Packard. For the HP8510C, a statistical variance of S_{11} is specified linearly in amplitude and phase, with values of $\sigma_{A_{11}} = 0.004$ and $\sigma_{\phi_{11}} = 0.8^{\circ}$, respectivly. Variance of S_{21} is specified logarithmically in amplitude and linearly in phase with values of $\sigma_{A_{21}} = 0.04$ dB and $\sigma_{\phi_{21}} = 2.0^{\circ}$, respectivly. Note that this VNA is an old model and the error level is significantly larger than newer VNA models. Also, these are worst case VNA uncertainties.

A Monte Carlo analysis of the propagation of VNA uncertainty for extraction of a bixial material at S-band (2.6-3.95 GHz) was performed using the fictitious test material with

properties are given in Table 2.2. The cubical sample has a side length of 34.036 mm. The forward problem was computed at 101 frequency points under the four orientations described in Section 2.2.4. White Gaussian noise was introduced at each frequency point of the generated S-parameters and the values of the standard deviations of the Gaussian noise was chosen to be half of the values indicated by the *HP 8510 Specifications & Performance Verification Program*. The data with noise mixed in was then used to extract the material parameters according to the three-step approach. This process was repeated 200 times, and the average values of the material parameters were calculated, along with the standard deviations. Results are shown in Figures 2.11 to 2.14. In these figures, the center black line is the average value of the 200 trials, while the two surrounding lines indicate the 95% confidence interval (2σ). It can be seen that data gaps similar to those displayed in Figures 2.9 and 2.10 appear in the error analysis. In addition, new data gaps at 2.7 GHz and 3.65 GHz are observed. It can be also noticed that the propagation errors for the real part of the material parameters vary significantly with frequency. For example, in Figure 2.11, ϵ_{rB} shows a low error at the lower frequency range of S-band and higher error at the higher frequency ranges, while the opposite occurs for the propagation error of ϵ_{rA}. For the imaginary part of the material parameters, the propagation error is relatively low compared to that of the real part except at 2.75, 3.4 and 3.75 GHz. Considering the overall propagation error level and the corresponding uncertainties introduced, this extraction method for biaxial material is reasonally robust.

A similar Monte Carlo error analysis was undertaken for a fictitious uniaxial material to evaluate the impact of measurement uncertainties for the extraction method for uniaxial material. The material parameters used are shown in Table 2.3. The material parameters are chosen to have larger dielectric loss and magnetic loss compared to the test biaxial sample. The standard deviations used to generate the gaussian noise are one quarter of the values indicated by the *HP 8510 Specifications & Performance Verification Program*. The values are $\sigma_{A_{11}} = 0.001$ and $\sigma_{\phi_{11}} = 0.2^\circ$, $\sigma_{A_{21}} = 0.01$ dB and $\sigma_{\phi_{21}} = 0.5^\circ$. The results are shown

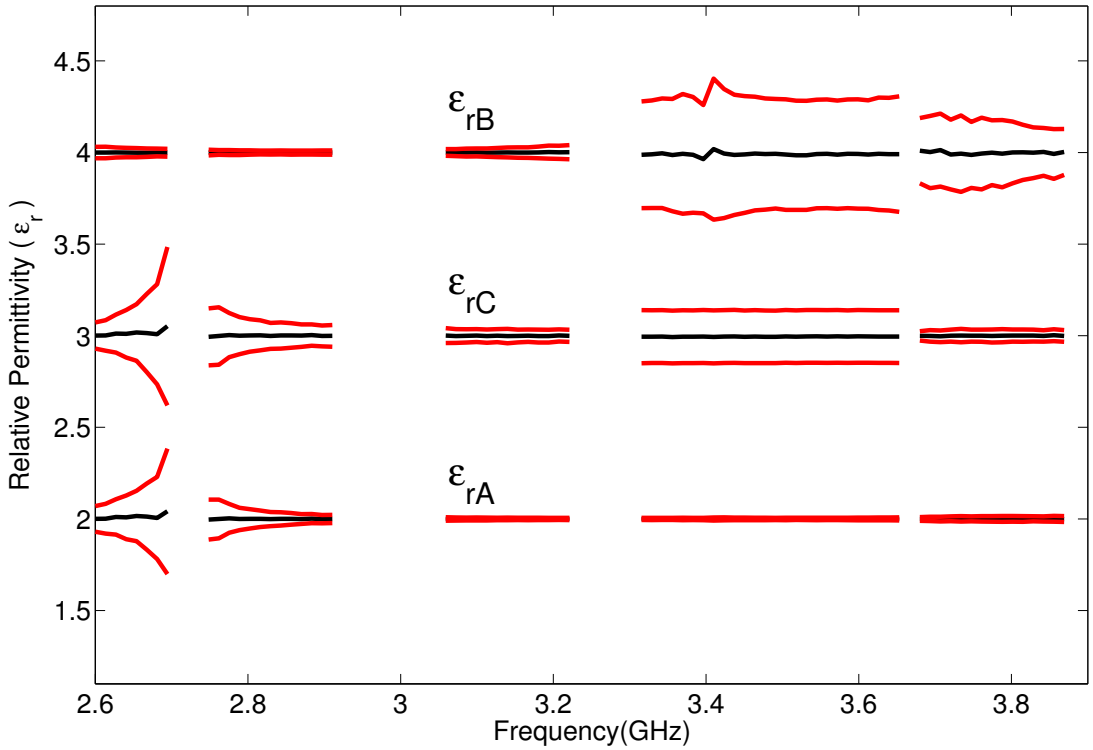

Figure 2.11 Real part of the relative permittivities for a fictitious biaxial material extracted using 200 random trials. Center line is the average of the trials. Upper and lower lines show the 95% confidence interval.

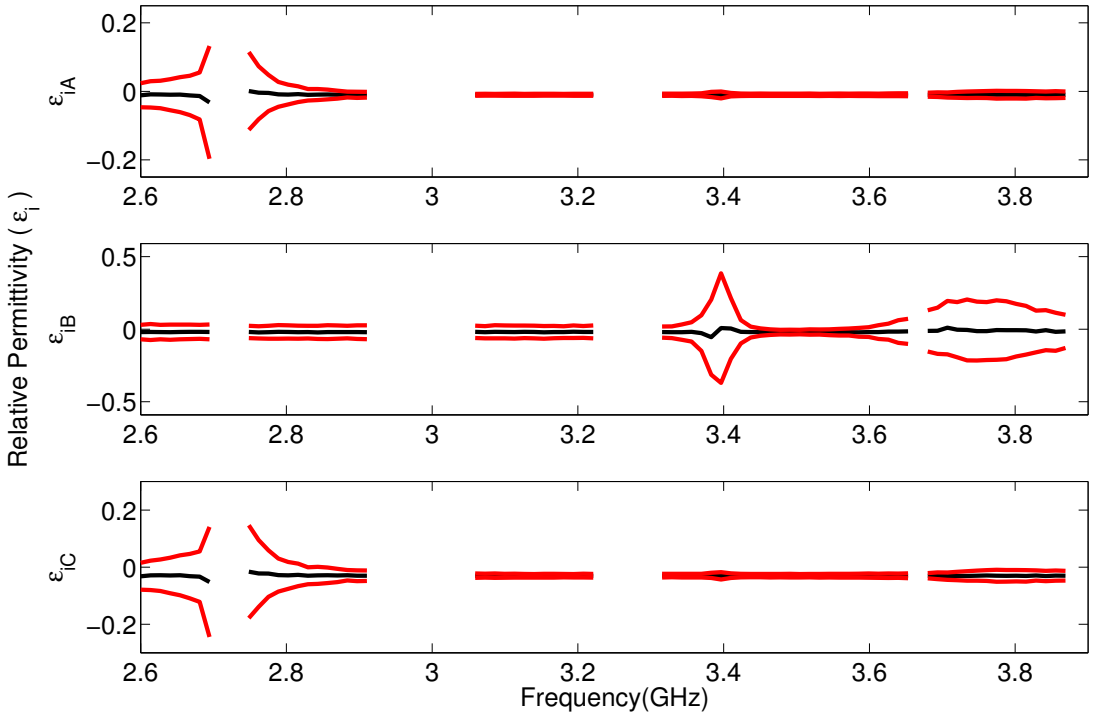

Figure 2.12 Imaginary part of the relative permittivities for a fictitious biaxial material extracted using 200 random trials. Center line is the average of the trials. Upper and lower lines show the 95% confidence interval.

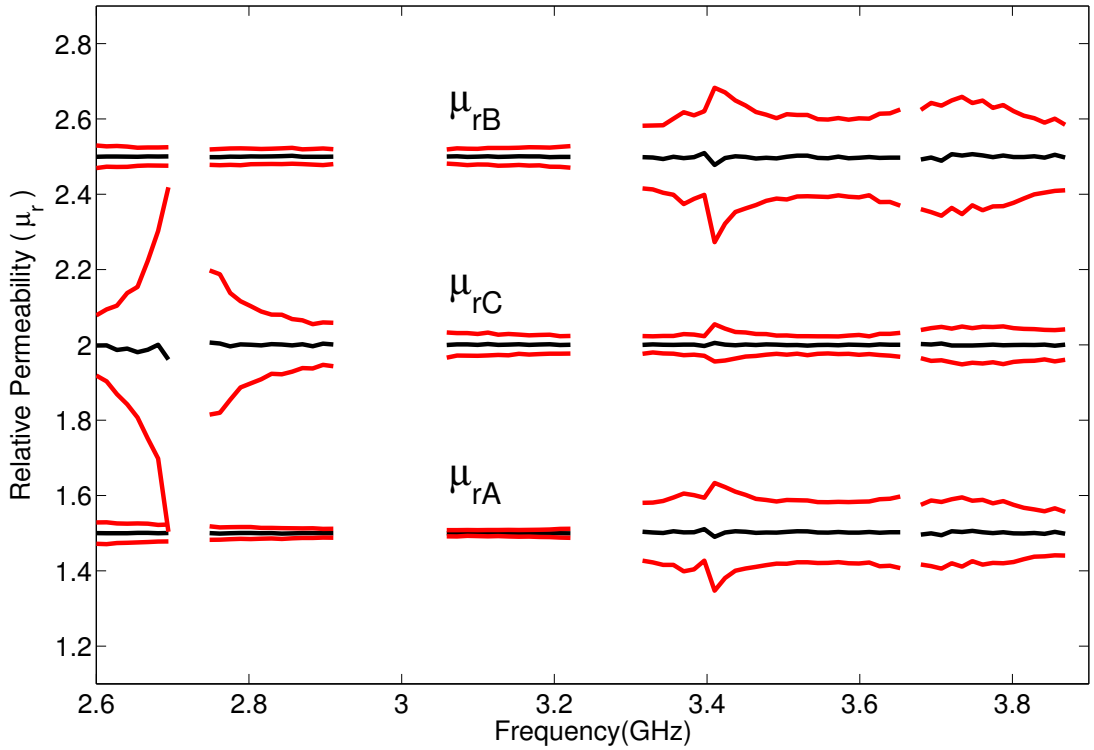

Figure 2.13 Real part of the relative permeabilities for a fictitious biaxial material extracted using 200 random trials. Center line is the average of the trials. Upper and lower lines show the 95% confidence interval.

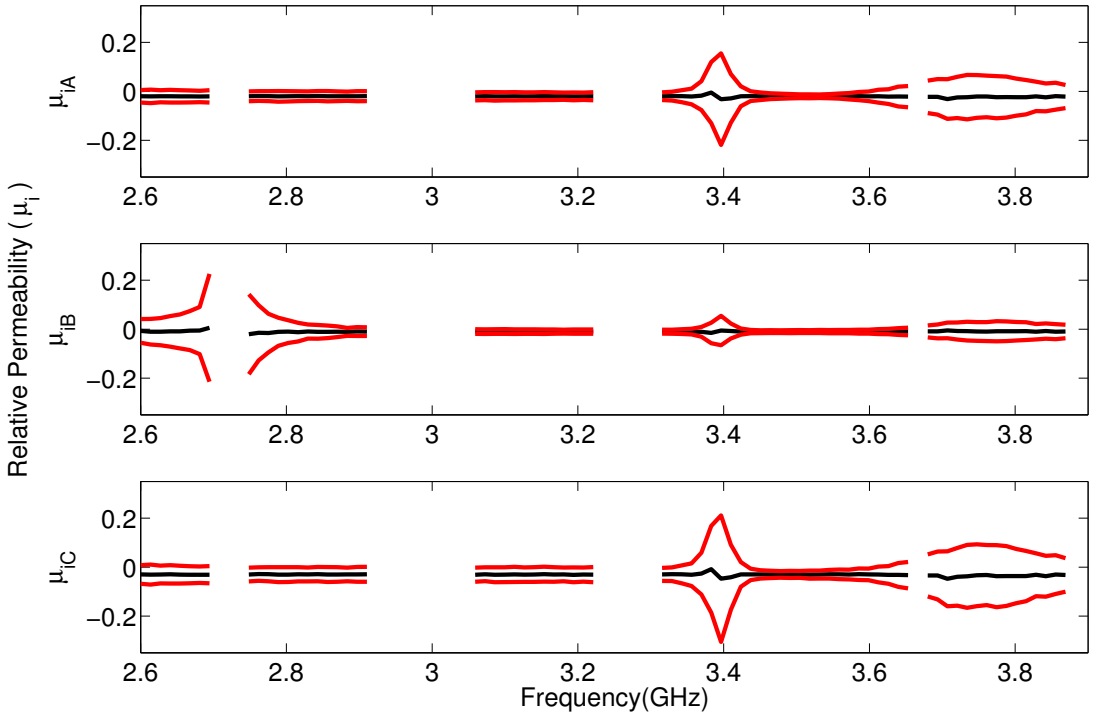

Figure 2.14 Imaginary part of the relative permeabilities for a fictitious biaxial material extracted using 200 random trials. Center line is the average of the trials. Upper and lower lines show the 95% confidence interval.

in Figures 2.11 to 2.14. Since the number of orientations to generate the S-parameters are reduced to two for uniaxial materials, and the number of unknowns under each orientation are also reduced to two, this extraction approach for uniaxial material shows a much lower error due to measurement uncertainties. It can be seen that almost no data gaps exist and the overall error is consistent and small (less than 5% of the actual value). Therefore, this extraction technique is very robust to random measurement errors.

Table 2.3 Material parameters for a fictitious Uniaxial material.

Parameter	Value
ϵ_A	4.0-0.2j
ϵ_B	5.0-0.3j
μ_A	1.2-1.3j
μ_B	1.4-1.1j

2.2.6 Summary

A partially-filled waveguide technique is introduced for measuring the permittivity and permeability of biaxially anisotropic materials. A single cubical sample is required and measured under different orientations in a waveguide to complete the extraction process. The performance of the technique is evaluated using error analysis based on network analyzer uncertainty. It is found that data gaps may occur during the error analysis when the electrical size of the sample approaches a half wavelength. However, the overall performance is still considered to be acceptable. In addition, a simplified method for extracting unixially anisotropic materials is established and this method has shown excellent performance under moderate noise levels.

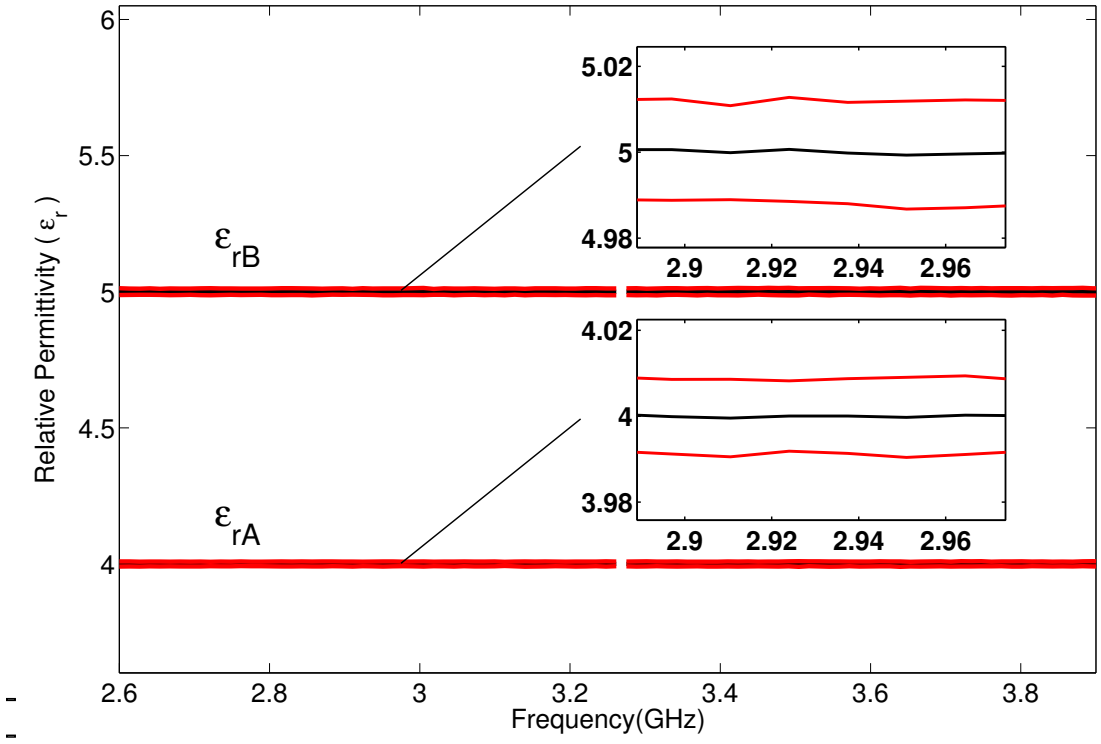

Figure 2.15 Real part of the relative permittivities for a fictitious uniaxial material extracted using 200 random trials. Center line is the average of the trials. Upper and lower lines show the 95% confidence interval.

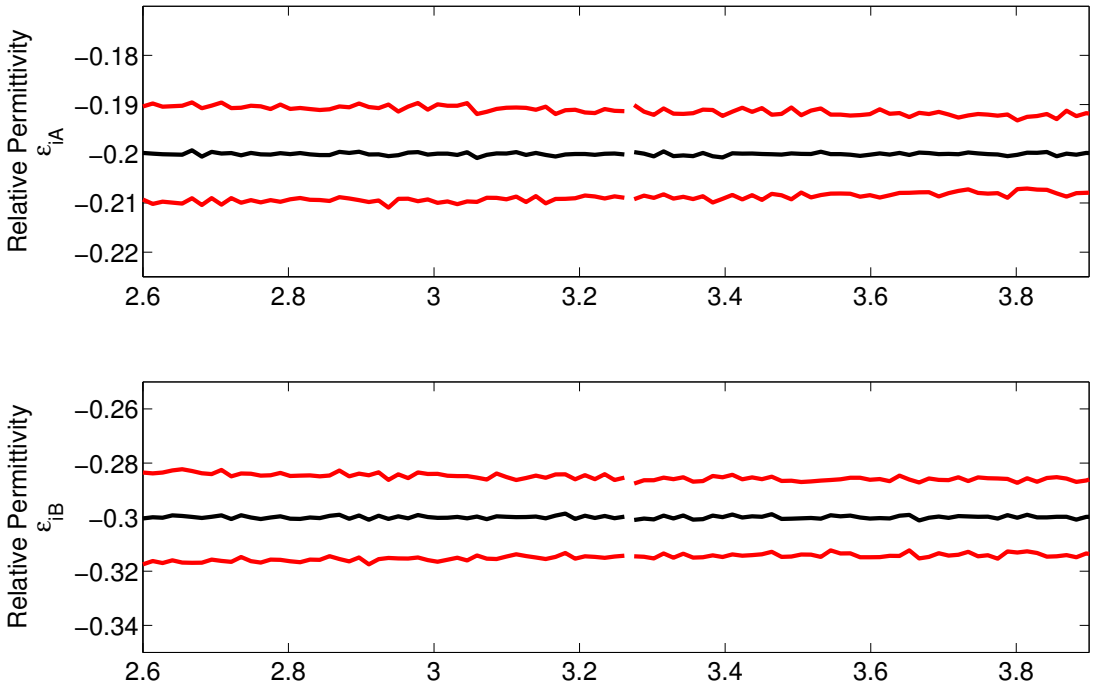

Figure 2.16 Imaginary part of the relative permittivities for a fictitious uniaxial material extracted using 200 random trials. Center line is the average of the trials. Upper and lower lines show the 95% confidence interval.

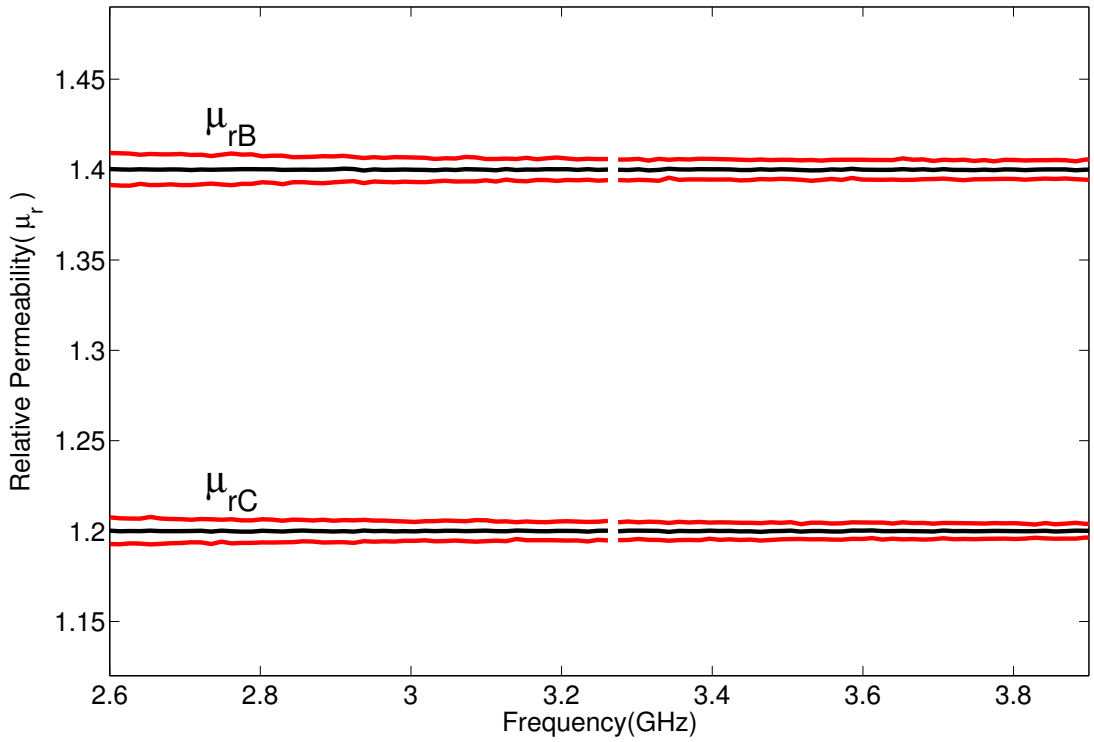

Figure 2.17 Real part of the relative permeabilities for a fictitious material uniaxial extracted using 200 random trials. Center line is the average of the trials. Upper and lower lines show the 95% confidence interval.

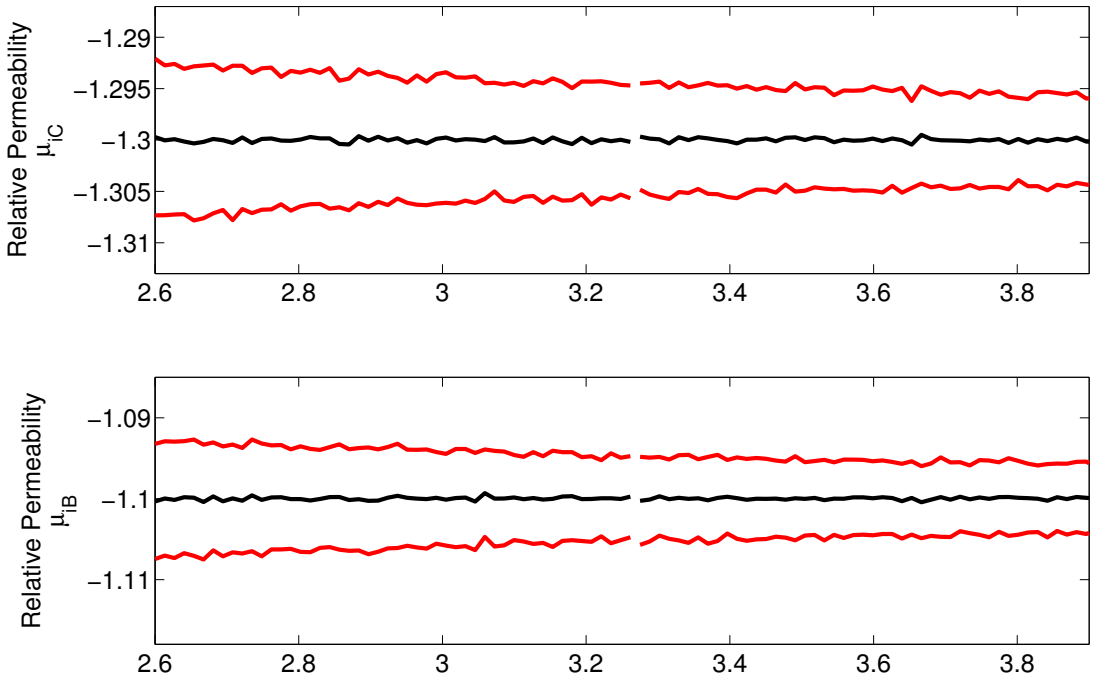

Figure 2.18 Imaginary part of the relative permeabilities for a fictitious uniaxial material extracted using 200 random trials. Center line is the average of the trials. Upper and lower lines show the 95% confidence interval.

CHAPTER 3

Characterization of Gyromagnetic Materials Using a Partially-Filled Waveguide Technique

3.1 Introduction

This chapter presents a technique for characterizing gyromagnetic materials using rectangular waveguides where the sample is magnetized perpendicular to the broad dimension of the guide, and only part of the cross-section of a waveguide is filled. Since the extraction of material parameters is implemented through minimizing the difference between the measured and the theoretically reflection and transmission coefficients, an accurate modeling method is required for material characterization. This is achieved by computing the S-parameters of the waveguide system with the material sample placed at a proper location using a mode-matching technique, which analyzes the behavior of the higher order modes excited at the interface between the sample region and the empty waveguide region. A special case where the material sample is placed at the center of the waveguide is also discussed and analyzed. By using an appropriate number of modes, the theoretical S-parameters for samples under

various measurement conditions can be predicted accurately.

3.2 Theoretical Transmission and Reflection Coefficients Using Mode-Matching Analysis

3.2.1 Characteristics of Gyromagnetic Material

The increased demand for developing new artificial materials has driven more researchers to study the behavior and application of gyromagnetic materials at microwave frequencies. The material parameters of gyromagnetic material can be expressed by the tensors

$$\epsilon = \epsilon_0 \begin{bmatrix} \epsilon_r & 0 & 0 \\ 0 & \epsilon_r & 0 \\ 0 & 0 & \epsilon_r \end{bmatrix} \tag{3.1}$$

and

$$\mu = \mu_0 \begin{bmatrix} \mu_g & 0 & -j\delta \\ 0 & 1 & 0 \\ j\delta & 0 & \mu_g \end{bmatrix}, \tag{3.2}$$

where the dielectric constant is an isotropic scalar either real or complex, and the permeability tensor above is formulated for the case when a material is biased along the height of the waveguide or in the y-direction. The variables δ and μ are complex numbers: $\delta = \delta' + j\delta''$ and $\mu_g = \mu_g' + j\mu_g''$. The expressions for δ and μ are given by

$$\delta = \frac{f f_m}{f^2 - f_0^2} \tag{3.3}$$

and

$$\mu = \left(1 - \frac{f_0 f_m}{f^2 - f_0^2}\right). \tag{3.4}$$

In (3.3) and (3.4), f is the operating frequency, the saturation magnetic resonance frequency $f_m = 2.8 \times 10^6 \times (4\pi M_s)$, and the magnetic resonance frequency $f_o = 2.8 \times 10^6 \times \left(H_0 + j\frac{\Delta H}{2}\right)$. Here H_0 is the strength of the internal static biasing magnetic field in Oersted (Oe), which can be determined from the expression $H_0 = H_a + NM_s$, where N is the demagnetization factor, H_a is the external magnetic field, and $4\pi M_s$ is the saturation magnetization in gauss (G) that defines the external field magnitude above which all the spins of unpaired electrons in the ferrite are aligned in the same direction. When the external static magnetic field is parallel to a thin layer of ferrite, the demagnetization factor N becomes 0, which results in $H_0 = H_a$. The magnetic losses inherent in the magnetic materials is also included as the linewidth ΔH. With the equations above it is possible to determine the effect of the magnetic resonance on the value of permeability at different frequencies.

The permeability dyadic has a dependence on biasing magnetic field and frequency. The diagonal term μ was plotted under different magnetic fields over frequency to help visualize the dependance. Consider a gyromagnetic material with $4\pi M_s = 1000$ G and linewidth $\Delta H = 25$. It is seen from Figure 3.1 that the magnetic resonance frequency occurs around 2.8 GHz with the internal magnetic biasing field of 1000 Oe. As H_0 increases to 1500 Oe, it is seen from Figure 3.2 that the magnetic resonance rises to 4.2 GHz. The occurrence of the magnetic resonance in the frequency range of interest may cause the extraction procedure to be more difficult due to the drastic variation of the relative material parameters. The ideal biasing field strength should bring a magnetic resonance slightly above the frequency band of interest, which keeps the permeability above zero while also maintaining a smooth variation across the frequency band. In Figure 3.3, for a magnetic field of 1800 Oe, where the magnetic resonance is at 5 GHz, the permeability value varies from 2 to 2.5 for the frequency

range of 2.6-4 GHz which is the frequency band interested in this work. By manipulating the magnetic biasing field, one could obtain the desired permeability properties at the frequency of interest. This unique property is appealing for developing new engineered material and methodologies of characterizing this type of material are investigated. The behavior of the off-diagonal term δ under the same magnetic field strength is also shown in Figure 3.4. It can be seen both real and imaginary parts of δ are close to 0 within the frequency band of interest.

3.2.2 Modal analysis of the gyromagnetic material in a partially-filled waveguide

To compute the S-parameters of a rectangular waveguide partially filled by a gyromagnetic material using a mode-matching technique, all the modal fields supported by the guide must be formulated. The waveguide system considered is shown in Figure 3.5, consisting of a rectangular waveguide partially filled with a gyromagnetic material sample biased along the y-axis. Waveguide extensions are attached with lengths chosen to be such that only a single TE_{10} rectangular waveguide mode exists at the measurement port of the transmitting extension ($z < 0$) and the receiving extension ($z > d$). A cross-section view of the waveguide system with sample is shown in Figure 3.6.

A single TE_{10} rectangular waveguide mode is incident on the sample, as shown in Figure 3.7. An infinite number of waveguide modes are reflected into the transmitting extensions, while an infinite number of waveguide modes are transmitted into the sample region, $0 < z < d$. On the next interface at $z = d$, these waveguide modes become incident, and thus a spectrum of waveguide modes is reflected into the sample region and transmitted into the receiving end of the empty waveguide extensions. Since the TE_{10} mode is invariant in the y-direction and even about x=a/2 and the gyromagnetic material is magnetized along the y-axis in this case, it is assumed that all excited higher order modes are also y-invariant. Therefore, only TE_{n0} modes are taken into account to describe the field distributions in

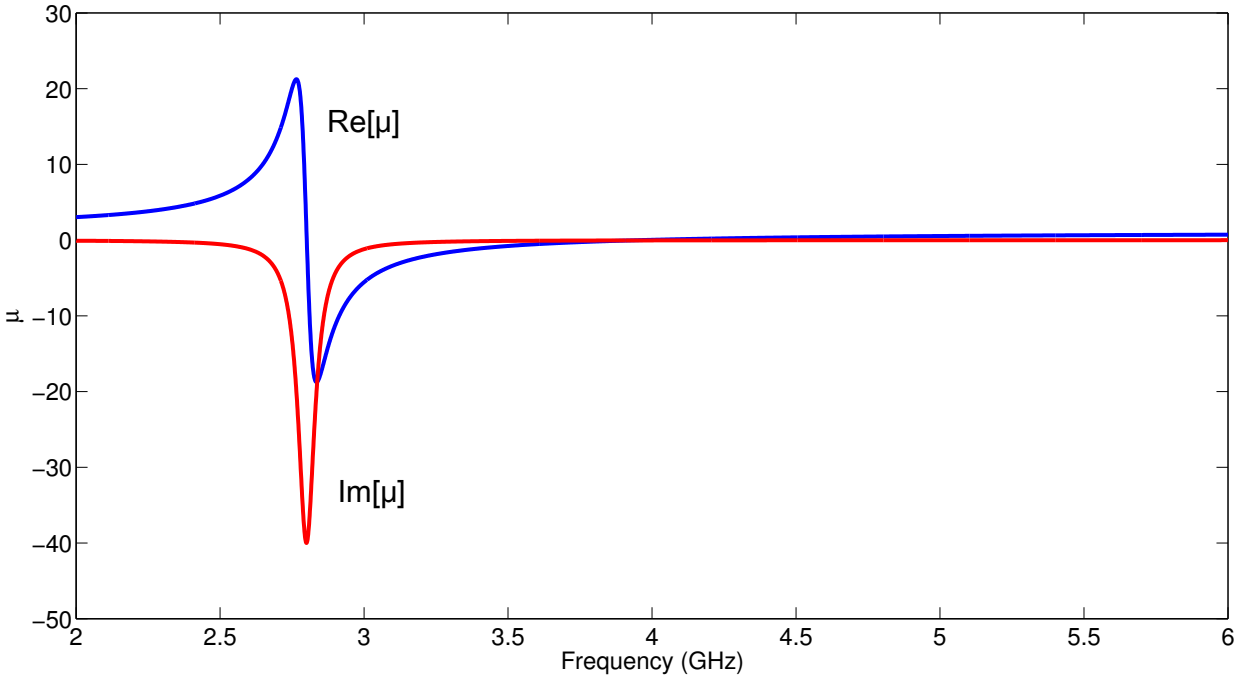

Figure 3.1 Permeability of the gyromagnetic material for $H_0 = 1000$ Oe.

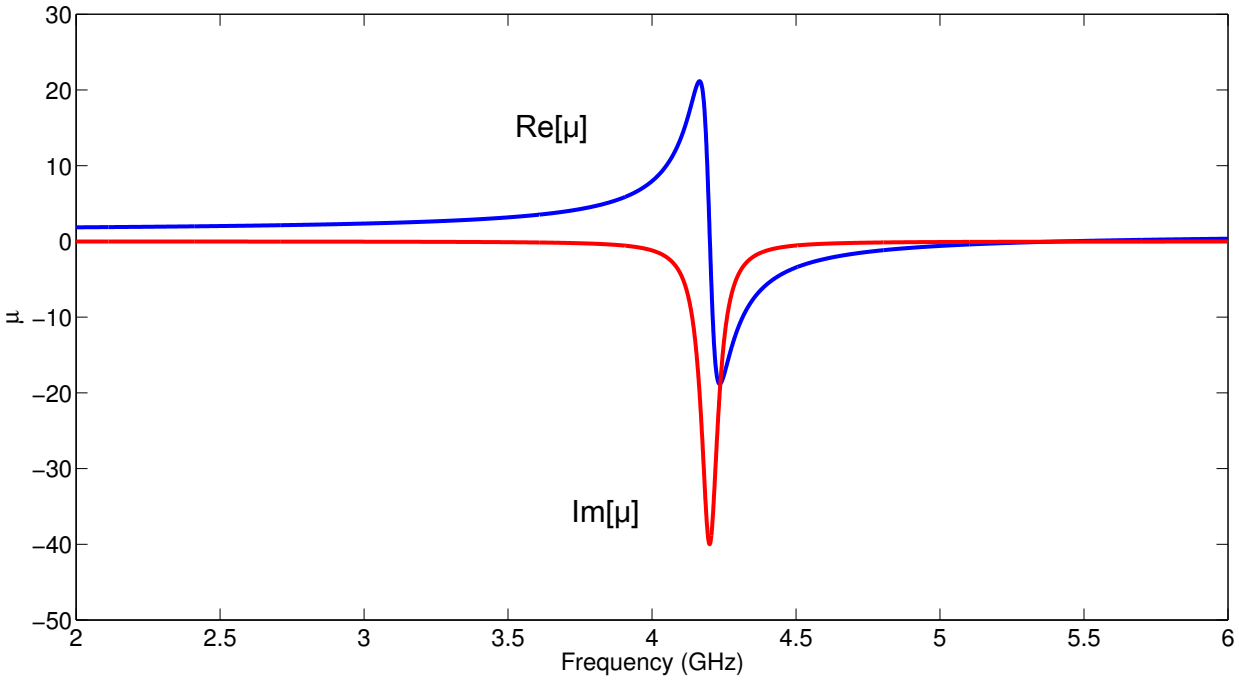

Figure 3.2 Permeability of the gyromagnetic material for $H_0 = 1500$ Oe.

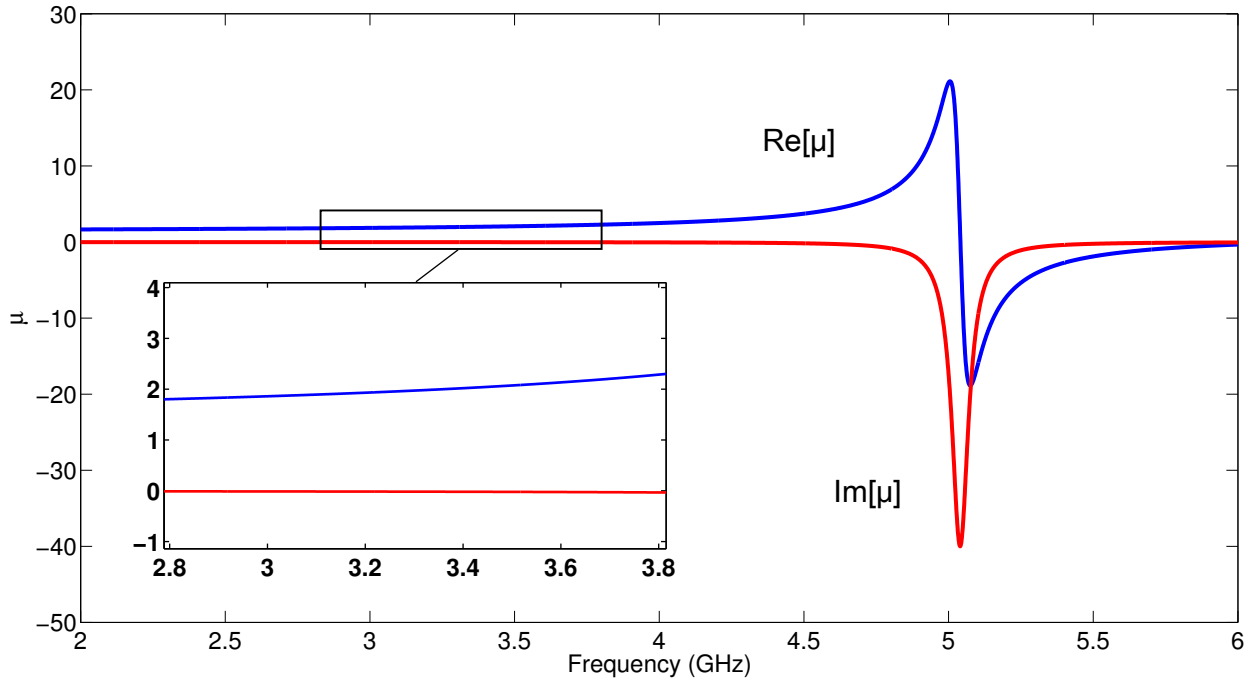

Figure 3.3 Permeability of the gyromagnetic material for $H_0 = 1800$ Oe.

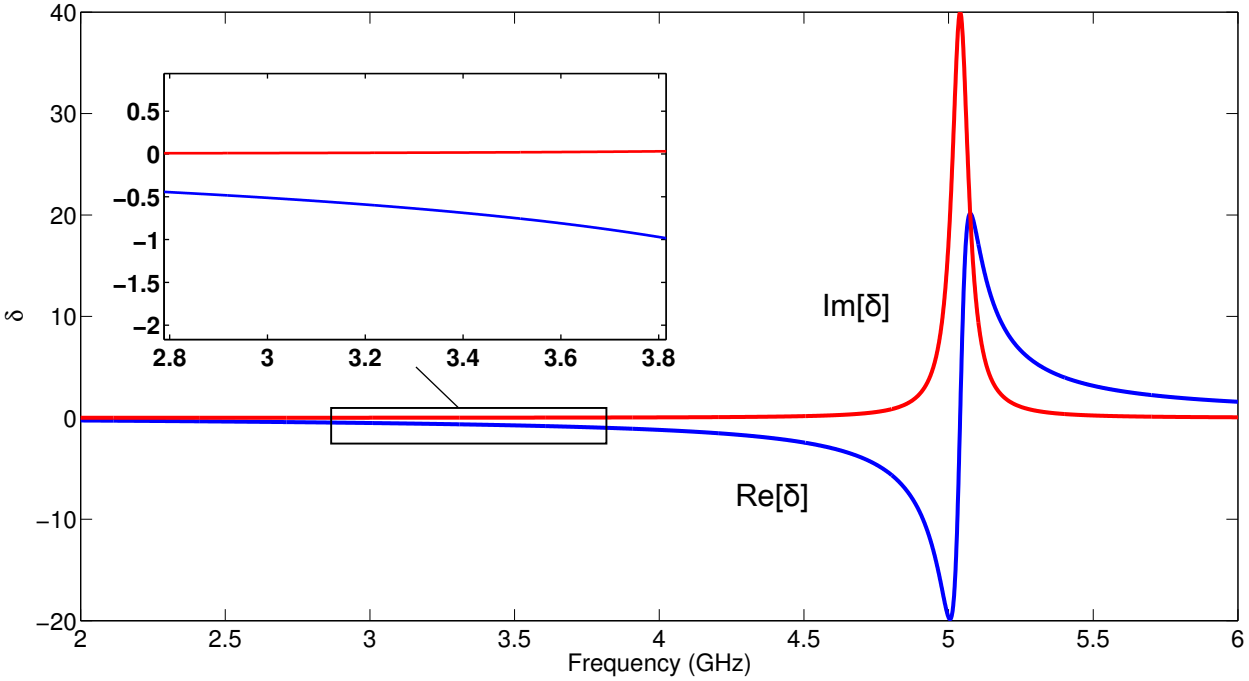

Figure 3.4 Off-diagonal term δ of the permeability dyadic for $H_0 = 1800$ Oe.

each of the empty waveguide regions.

3.2.2.1 Modal behavior inside a rectangular waveguide partially filled with gyromagnetic material

For y-invariant TE_{n0} modes in the empty region of a rectangular waveguide, the wave equation [42] is expressed as

$$\left(\frac{\partial^2}{\partial x^2} + k_c^2\right) E_y = 0, \tag{3.5}$$

where

$$k_c^2 = k_0^2 - \beta^2 \tag{3.6}$$

is the cutoff wavenumber and $k_0 = \omega^2 \mu_0 \epsilon_0$ is the free-space wavenumber. The solution to the wave equation is expressed as

$$E_y(x,z) = (A\sin k_C x + B\cos k_C x) e^{\pm j\beta z}. \tag{3.7}$$

Applying the boundary condition $E_y(x = \frac{a}{2}) = 0$, the fields in the empty waveguide where only TE_{n0} modes are excited are given by

$$E_y(x,z) = A\sin\left[k_C(x + \frac{a}{2})\right] e^{\pm j\beta z} \tag{3.8}$$

$$H_z(x,z) = A\frac{jk_C}{\omega\mu_O}\cos\left[k_C(x + \frac{a}{2})\right] e^{\pm j\beta z}. \tag{3.9}$$

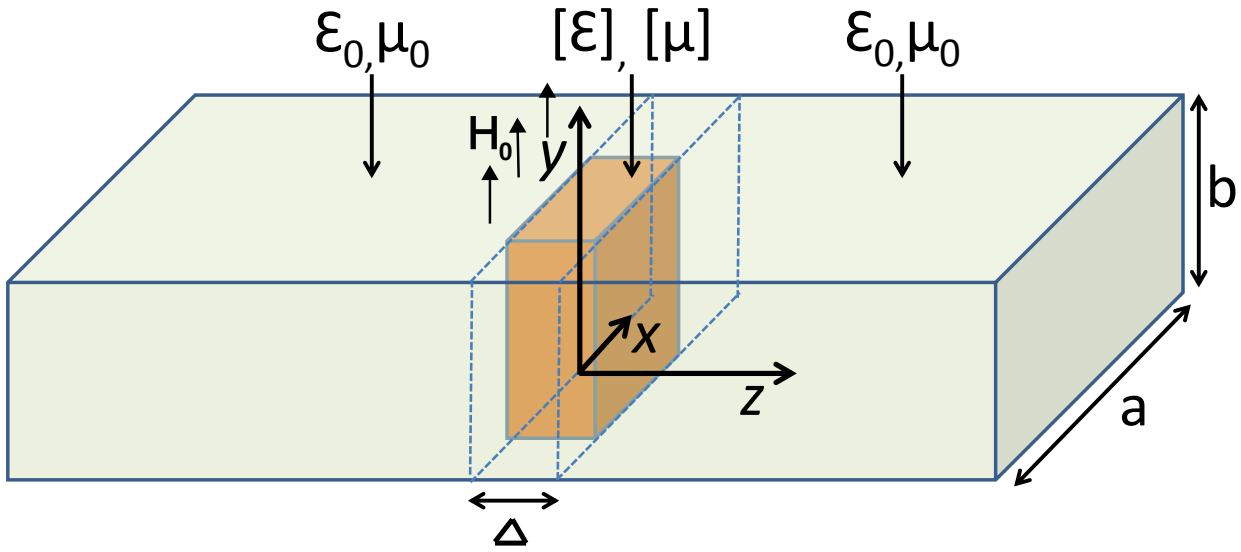

Figure 3.5 Waveguide partially filled with a gyromagnetic sample.

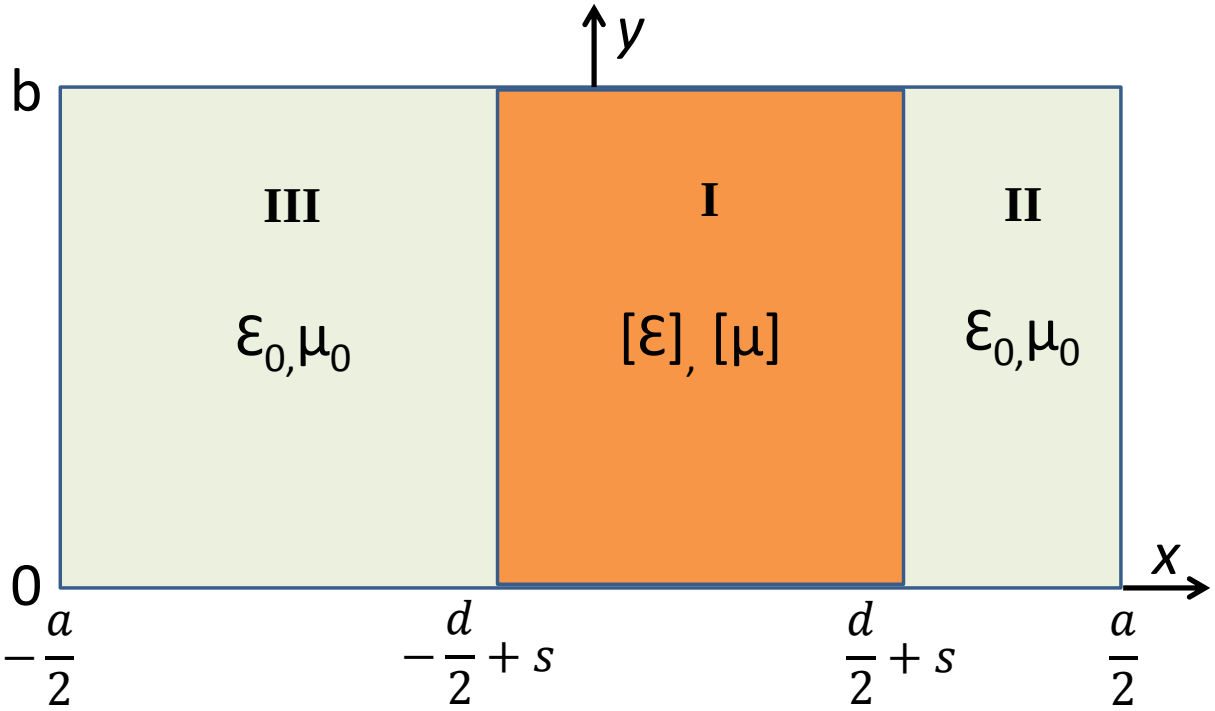

Figure 3.6 Cross-sectional view of a partially filled waveguide.

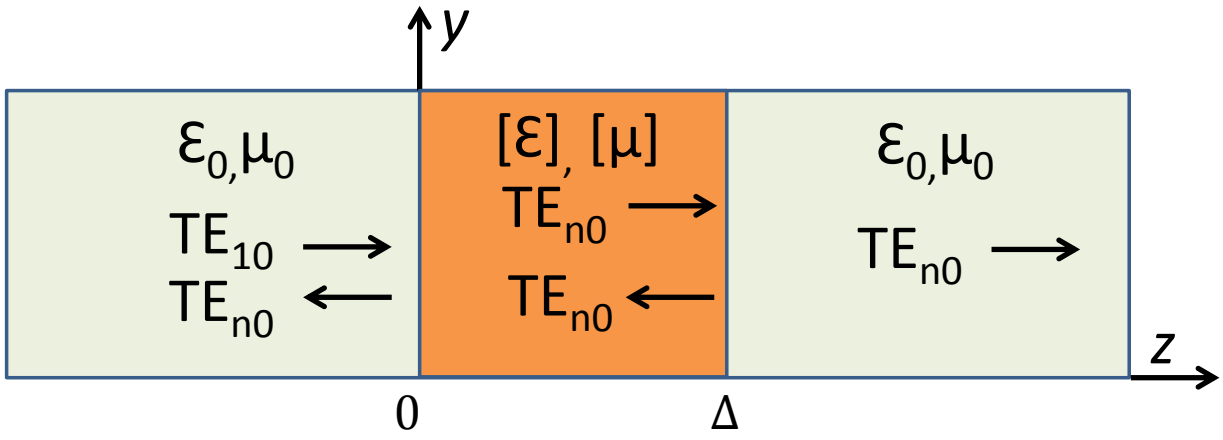

Figure 3.7 Side view of a partially filled waveguide.

In the empty part of the sample region ($\frac{d}{2}+s<x<\frac{a}{2}$), the field in region II of Figure 3.6 can be written as

$$E_y^{II}(x,z)=\left[A^{II}\frac{\sin(k_c^{II}x)}{\cos(k_c^{II}\frac{a-d-2s}{2})}+B^{II}\cos(k_c^{II}x)\frac{\sin(k_c^{II}x)}{\cos(k_c^{II}\frac{a-d-2s}{2})}\right]e^{\pm j\beta z}, \quad (3.10)$$

where

$$k_c^{II}=k_o^2-\beta^2. \quad (3.11)$$

The denominator in (3.10) was chosen for computational purpose to eliminate large values calculated from sinusoidal functions when k_c is complex. Applying the boundary condition $E_y^{II}=0$ at $x=\frac{a}{2}$ yields

$$A^{II}\sin(k_c^{II}\frac{a}{2})+B^{II}\cos(k_c^{II}\frac{a}{2})=0, \quad (3.12)$$

and the field in region II is given by the following equation,

$$E_y^{II}(x,z)=\frac{A^{II}}{\cos(k_c^{II}\frac{a-d-2s}{2})}\left[\sin(k_c^{II}x)-\tan(k_c^{II}\frac{a}{2})\cos(k_c^{II}x)\right]e^{\pm j\beta z}. \quad (3.13)$$

Using 3.13, the fields in region II can be rewritten as

$$E_y^{II}(x,z) = A^{II}\frac{\sin\left[k_c^{II}(x-\frac{a}{2})\right]}{\cos\left[k_c^{II}(\frac{a-d-2s}{2})\right]}e^{\pm j\beta z} \tag{3.14}$$

$$H_z^{II}(x,z) = \frac{j}{\omega\mu_o}\frac{\partial E_y^{II}}{\partial x} = A^{II}\left(\frac{jk_c^{II}}{\omega\mu_o}\right)\frac{\cos\left[k_c^{II}(x-\frac{a}{2})\right]}{\cos\left[k_c^{II}(\frac{a-d-2s}{2})\right]}e^{\pm j\beta z}. \tag{3.15}$$

Similarly, the transverse fields in the other empty part (region III) of the sample region can be found by using

$$E_y^{III}(x,z) = \left[A^{III}\frac{\sin\left(k_c^{III}x\right)}{\cos\left[k_c^{III}(\frac{a-d+2s}{2})\right]} + B^{III}\cos\left(k_c^{III}x\right)\frac{\sin\left(k_c^{III}x\right)}{\cos\left[k_c^{III}(\frac{a-d+2s}{2})\right]}\right]e^{\pm j\beta z}, \tag{3.16}$$

where

$$k_c^{III} = k_c^{II} = \sqrt{k_o^2 - \beta^2}, \tag{3.17}$$

and

$$-A^{III}\sin\left(k_c^{III}\frac{a}{2}\right) + B^{III}\cos\left(k_c^{III}\frac{a}{2}\right) = 0 \tag{3.18}$$

given by the boundary condition $E_y^{III} = 0$ at $x = -\frac{a}{2}$. Thus, the electric field in region III is given by

$$E_y^{III}(x,z) = \frac{A^{III}}{\cos\left[k_c^{II}(\frac{a-d+2s}{2})\right]}\left[\sin\left(k_c^{II}x\right) + \tan\left(k_c^{II}\frac{a}{2}\right)\cos\left(k_c^{II}x\right)\right]e^{\pm j\beta z}. \tag{3.19}$$

Therefore, the fields in region III are expressed by

$$E_y^{III}(x,z) = A^{III}\frac{\sin\left[k_c^{II}(x+\frac{a}{2})\right]}{\cos\left[k_c^{II}\left(\frac{a-d+2s}{2}\right)\right]}e^{\pm j\beta z} \tag{3.20}$$

$$H_z^{III}(x,z) = \frac{j}{\omega\mu_o}\frac{\partial E_y^{II}}{\partial x} = A^{III}\frac{jk_c^{II}}{\omega\mu_o}\frac{\cos\left[k_c^{II}(x+\frac{a}{2})\right]}{\cos\left[k_c^{II}\left(\frac{a-d+2s}{2}\right)\right]}e^{\pm j\beta z}. \tag{3.21}$$

To find the fields in the region I occupied by the sample, first start with the solutions for the wave equation in the sample region (Section 2.2.4 [42])

$$E_y^I(x,z) = \left[A^I\frac{\sin(k_C x)}{\cos\left(k_C\frac{d}{2}\right)} + B^I\frac{\cos(k_C x)}{\cos\left(k_C\frac{d}{2}\right)}\right]e^{\pm j\beta z}, \tag{3.22}$$

and

$$H_z^I(x,z) = -j\frac{u/\omega}{\delta^2-\mu^2}\left(\frac{\partial E_y^I}{\partial x} \mp \frac{\beta\delta}{\mu}E_y^I\right), \tag{3.23}$$

so that

$$\begin{aligned} H_z^I(x,z) = -j\frac{u/\omega}{\delta^2-\mu^2}\Bigg[&A^I k_C\frac{\cos(k_C x)}{\cos\left(k_C\frac{d}{2}\right)} - B^I k_C\frac{\sin(k_C x)}{\cos\left(k_C\frac{d}{2}\right)} \mp \\ &A^I\frac{\beta\delta}{\mu}\frac{\sin(k_C x)}{\cos\left(k_C\frac{d}{2}\right)} \mp B^I\frac{\beta\delta}{\mu}\frac{\cos(k_C x)}{\cos\left(k_C\frac{d}{2}\right)}\Bigg]e^{\pm j\beta z}. \end{aligned} \tag{3.24}$$

where

$$k_c^2 = \omega^2\mu\varepsilon - \omega^2\frac{\delta^2}{\mu^2}\mu\varepsilon - \beta^2 \tag{3.25}$$

is the cutoff wavenumber for region I.

Since E_y and H_z are continuous at the interface between the sample and the empty waveguide, four equations can be established by applying the boundary conditions for both

E_y and H_z. 1) $E_y(\frac{d}{2}+s)$ is continuous

$$\frac{-A^{II}\sin\left[k_C^{II}(\frac{a-d-2s}{2})\right]}{\cos\left[k_C^{II}(\frac{a-d-2s}{2})\right]} = A^I\frac{\sin\left[k_C(\frac{d}{2}+s)\right]}{\cos(k_C\frac{d}{2})} + B^I\frac{\sin\left[k_C(\frac{d}{2}+s)\right]}{\cos(k_C\frac{d}{2})} \tag{3.26}$$

2) $H_z(\frac{d}{2}+s)$ is continuous

$$A^{II}\left(\frac{jk_C^{II}}{\omega\mu_O}\right) = -j\left(\frac{u/\omega}{\delta^2-\mu^2}\right)\left\{A^I k_C\frac{\sin\left[k_C(s+\frac{d}{2})\right]}{\cos(k_C\frac{d}{2})} - B^I k_C\frac{\sin\left[k_C(s+\frac{d}{2})\right]}{\cos(k_C\frac{d}{2})} \mp A^I\left(\frac{\beta\delta}{\mu}\right)\frac{\sin\left[k_C(s+\frac{d}{2})\right]}{\cos(k_C\frac{d}{2})} \mp B^I\left(\frac{\beta\delta}{\mu}\right)\frac{\cos\left[k_C(s+\frac{d}{2})\right]}{\cos(k_C\frac{d}{2})}\right\} \tag{3.27}$$

3) $E_y(-\frac{d}{2}+s)$ is continuous

$$\frac{-A^{III}\sin\left[k_C^{II}(\frac{a-d+2s}{2})\right]}{\cos\left[k_C^{II}(\frac{a-d+2s}{2})\right]} = A^I\frac{\sin\left[k_C(s-\frac{d}{2})\right]}{\cos(k_C\frac{d}{2})} + B^I\frac{\sin\left[k_C(s-\frac{d}{2})\right]}{\cos(k_C\frac{d}{2})} \tag{3.28}$$

4) $H_z(-\frac{d}{2}+s)$ is continuous

$$A^{III}\left(\frac{jk_C^{II}}{\omega\mu_O}\right) = -j\left(\frac{u/\omega}{\delta^2-\mu^2}\right)\left\{A^I k_C\frac{\sin\left[k_C(s-\frac{d}{2})\right]}{\cos(k_C\frac{d}{2})} - B^I k_C\frac{\sin\left[k_C(s-\frac{d}{2})\right]}{\cos(k_C\frac{d}{2})} \mp A^I\left(\frac{\beta\delta}{\mu}\right)\frac{\sin\left[k_C(s-\frac{d}{2})\right]}{\cos(k_C\frac{d}{2})} \mp B^I\left(\frac{\beta\delta}{\mu}\right)\frac{\cos\left[k_C(s-\frac{d}{2})\right]}{\cos(k_C\frac{d}{2})}\right\} \tag{3.29}$$

Substituting A^{II} in terms of A^I and B^I from (3.26), the expression (3.27) becomes

$$A^I \frac{k_c^{II}(\delta^2-\mu^2)}{\mu\mu_o} \frac{\sin\left[k_c(s+\frac{d}{2})\right]\cot\left[k_c^{II}(\frac{a-d-2s}{2})\right]}{\cos(k_c\frac{d}{2})} +$$
$$B^I \frac{k_c^{II}(\delta^2-\mu^2)}{\mu\mu_o} \frac{\cos\left[k_c(s+\frac{d}{2})\right]\cot\left[k_c^{II}(\frac{a-d-2s}{2})\right]}{\cos(k_c\frac{d}{2})} =$$
$$A^I k_c \frac{\cos\left[k_c(s+\frac{d}{2})\right]}{\cos(k_c\frac{d}{2})} - B^I k_c \frac{\sin\left[k_c(s+\frac{d}{2})\right]}{\cos(k_c\frac{d}{2})} \mp$$
$$A^I \frac{\beta\delta}{\mu} \frac{\sin\left[k_c(s+\frac{d}{2})\right]}{\cos(k_c\frac{d}{2})} \mp B^I \left(\frac{\beta\delta}{\mu}\right) \frac{\cos\left[k_c(s+\frac{d}{2})\right]}{\cos(k_c\frac{d}{2})}. \tag{3.30}$$

The equation above can be written as

$$F_{AA}^{\pm} A^I + F_{AB}^{\pm} B^I = 0, \tag{3.31}$$

where

$$F_{AA}^{\pm} = -\frac{k_c^{II}(\delta^2-\mu^2)}{\mu\mu_o} \frac{\sin\left[k_c(s+\frac{d}{2})\right]\cot\left[k_c^{II}(\frac{a-d-2s}{2})\right]}{\cos(k_c\frac{d}{2})} +$$
$$k_c \frac{\cos\left[k_c(s+\frac{d}{2})\right]}{\cos(k_c\frac{d}{2})} \mp \left(\frac{\beta\delta}{\mu}\right) \frac{\sin\left[k_c(s+\frac{d}{2})\right]}{\cos(k_c\frac{d}{2})} \tag{3.32}$$
$$F_{AB}^{\pm} = -\frac{k_c^{II}(\delta^2-\mu^2)}{\mu\mu_o} \frac{\cos\left[k_c(s+\frac{d}{2})\right]\cot\left[k_c^{II}(\frac{a-d-2s}{2})\right]}{\cos(k_c\frac{d}{2})} -$$
$$k_c \frac{\sin\left[k_c(s+\frac{d}{2})\right]}{\sin(k_c\frac{d}{2})} \mp \left(\frac{\beta\delta}{\mu}\right) \frac{\cos\left[k_c(s+\frac{d}{2})\right]}{\cos(k_c\frac{d}{2})}. \tag{3.33}$$

Similarly, using (3.28), the expression (3.29) becomes

$$A^I \frac{k_c^{II}(\delta^2-\mu^2)}{\mu\mu_o} \frac{\sin\left[k_c(s-\frac{d}{2})\right]\cot\left[k_c^{II}(\frac{a-d+2s}{2})\right]}{\cos(k_c\frac{d}{2})} +$$
$$B^I \frac{k_c^{II}(\delta^2-\mu^2)}{\mu\mu_o} \frac{\cos\left[k_c(s-\frac{d}{2})\right]\cot\left[k_c^{II}(\frac{a-d+2s}{2})\right]}{\cos(k_c\frac{d}{2})}$$
$$+A^I k_c \frac{\cos\left[k_c(s-\frac{d}{2})\right]}{\cos(k_c\frac{d}{2})} - B^I k_c \frac{\sin\left[k_c(s-\frac{d}{2})\right]}{\cos(k_c\frac{d}{2})}$$
$$\mp A^I\left(\frac{\beta\delta}{\mu}\right)\frac{\sin\left[k_c(s-\frac{d}{2})\right]}{\cos(k_c\frac{d}{2})} \mp B^I\left(\frac{\beta\delta}{\mu}\right)\frac{\cos\left[k_c(s-\frac{d}{2})\right]}{\cos(k_c\frac{d}{2})} = 0. \tag{3.34}$$

The equation above can also be written as

$$F_{BA}^{\pm}A^I + F_{BB}^{\pm}B^I = 0, \tag{3.35}$$

where

$$F_{BA}^{\pm} = \frac{k_c^{II}(\delta^2-\mu^2)}{\mu\mu_o} \frac{\sin\left[k_c(s-\frac{d}{2})\right]\cot\left[k_c^{II}(\frac{a-d+2s}{2})\right]}{\cos(k_c\frac{d}{2})} +$$
$$k_c\frac{\cos\left[k_c(s-\frac{d}{2})\right]}{\cos(k_c\frac{d}{2})} \mp \left(\frac{\beta\delta}{\mu}\right)\frac{\sin\left[k_c(s-\frac{d}{2})\right]}{\cos(k_c\frac{d}{2})} \tag{3.36}$$
$$F_{BB}^{\pm} = \frac{k_c^{II}(\delta^2-\mu^2)}{\mu\mu_o} \frac{\cos\left[k_c(s-\frac{d}{2})\right]\cot\left[k_c^{II}(\frac{a-d+2s}{2})\right]}{\cos(k_c\frac{d}{2})} -$$
$$k_c\frac{\sin\left[k_c(s-\frac{d}{2})\right]}{\sin(k_c\frac{d}{2})} \mp \left(\frac{\beta\delta}{\mu}\right)\frac{\cos\left[k_c(s-\frac{d}{2})\right]}{\cos(k_c\frac{d}{2})}. \tag{3.37}$$

Equation (3.31) and (3.35) may be written in matrix form as

$$\begin{bmatrix} F_{AA}^{\pm} & F_{AB}^{\pm} \\ F_{BA}^{\pm} & F_{BB}^{\pm} \end{bmatrix} \begin{bmatrix} A^I \\ B^I \end{bmatrix} = \begin{bmatrix} 0 \\ 0 \end{bmatrix}.$$

The determinant of the 2 x 2 matrix has to be zero for a nontrivial solution for A^I and B^I to exist , which yields

$$F^{\pm}_{AA}F^{\pm}_{BB} - F^{\pm}_{BA}F^{\pm}_{AB} = 0. \tag{3.38}$$

The expressions $F^{\pm}_{AA}, F^{\pm}_{AB}, F^{\pm}_{BA}$, and $F^{\pm}_{BB}$ can be written as

$$\begin{aligned} F^{\pm}_{AA} &= (\Gamma_1 \pm \Delta)SC_1 - CC_1 \quad F^{\pm}_{AB} = (\Gamma_1 \pm \Delta)CC_1 + SC_1 \\ F^{\pm}_{BA} &= (\Gamma_2 \mp \Delta)SC_2 + CC_2 \quad F^{\pm}_{BB} = (\Gamma_2 \mp \Delta)CC_2 + SC_2, \end{aligned} \tag{3.39}$$

where

$$\begin{aligned} \Gamma_1 &= -\frac{k_c^{II}(\delta^2 - \mu^2)}{k_c \mu \mu_o} \cot\left[k_c^{II}(\frac{a-d-2s}{2})\right] \\ \Gamma_2 &= -\frac{k_c^{II}(\delta^2 - \mu^2)}{k_c \mu \mu_o} \cot\left[k_c^{II}(\frac{a-d+2s}{2})\right] \\ SC_1 &= \frac{\sin\left[k_c(s+\frac{d}{2})\right]}{\cos(k_c\frac{d}{2})} \qquad CC_1 = \frac{\cos\left[k_c(s+\frac{d}{2})\right]}{\cos(k_c\frac{d}{2})} \\ SC_2 &= \frac{\sin\left[k_c(\frac{d}{2}-s)\right]}{\cos(k_c\frac{d}{2})} \qquad CC_2 = \frac{\cos\left[k_c(\frac{d}{2}-s)\right]}{\cos(k_c\frac{d}{2})} \\ \Delta &= \frac{\beta\delta}{\mu k_c}. \end{aligned} \tag{3.40}$$

Then (3.38) can be written as

$$[(\Gamma_1 \pm \Delta)SC_1 - CC_1][(\Gamma_2 \mp \Delta)CC_2 + SC_2] - [(\Gamma_1 \pm \Delta)CC_1 + SC_1][(\Gamma_2 \mp \Delta)SC_2 + CC_2] = 0. \tag{3.41}$$

Finally, this equation above can be further simplified into

$$(\Gamma_1 \pm \Delta)(\Gamma_2 \mp \Delta)\sin(k_c d) - (\Gamma_2 \mp \Delta)\cos(k_c d) + (\Gamma_1 \pm \Delta)\cos(k_c d) - \sin(k_c d) = 0, \tag{3.42}$$

and thus the characteristic equation for the modal spectrum of the gyromagnetic material

sample partially placed in the waveguide is given by

$$(\Gamma_1 \pm \Delta)(\Gamma_2 \mp \Delta)\sin(k_C d) - (\Gamma_1 + \Gamma_2)\cos(k_C d) - \sin(k_C d) = 0, \tag{3.43}$$

A special case of the characteristic equation can be obtained when $s = 0$, which means the sample is placed at the center of the cross-section of the waveguide extensions. This situation results in a much simplified characteristic equation

$$(\Gamma + T)(\Gamma T - 1) = \Delta^2 T, \tag{3.44}$$

where

$$\begin{aligned} \Gamma &= -\frac{k_c^{II}(\delta^2 - \mu^2)}{k_C \mu \mu_O} \cot\left[k_c^{II}(\frac{a-d}{2})\right] \\ \Delta &= \frac{\beta\delta}{\mu k_C} \\ T &= \tan\left(k_C \frac{d}{2}\right). \end{aligned} \tag{3.45}$$

3.2.2.2 Modal spectrum dependence on the transverse position of the sample

Based on the characteristic equation derived above, the modal spectrum can be plotted for different transverse positions of the sample in the waveguide to understand the modes in the waveguide. Since the measurements for extraction were performed using an S-band waveguide, the investigation of the modal behavior was carried out in S-band (2.6-3.95 GHz).

Consider a 1.34 inches wide lossless gyromagnetic sample with $4\pi M_S$=1000 G and ϵ_r=14.7 and H_0 of 2800 Oe which is placed at the center of the waveguide cross-section. The propagation constant β can be found by solving (3.44). Of many possible root solving algorithms, the Newton's method is chosen for its simplicity and capability of finding complex roots. Figure 3.8 shows the $\omega - \beta$ diagram for the propagation modes with real values of β. When the sample is centered, more than one propagating mode exists in the sample region, and

the number of propagating modes varies with frequency. Roots with imaginary values are plotted in Figure 3.9. Since an infinite number of evanescent modes can be found, only the first five evanescent modes are shown in the plot. Note that for any root found from (3.44), either real or imaginary, one can always find a second root of the equation by changing the sign of the first root. Therefore, only the roots with positive sign are shown in those two figures.

Figure 3.10 shows all the propagating modes when the sample is shifted by s =0.1 inches. It can be seen that the propagating modes existing in the sample region are close to those in the case where the sample is centered. However, since (3.43) has different signs depending on the direction of wave propagation, two different roots of the same mode at any given frequency can be found, one for each propagating direction. It may appear in some cases that the two roots are very close, but as long as $s \neq 0$, two roots should be different. The upper half of Figure 3.10 shows the propagating modes for the wave propagating along +z direction, while the lower half shows the modes for the −z direction. The signs of the roots found in the −z direction are chosen to be minus for clear graphical demonstration since any real root with both signs still satisfies the characteristic equation.

When $s \neq 0$, purely imaginary roots cannot satisfy (3.44). Instead of evanescent modes, complex roots are found. These roots are found in complex conjugate pairs. For instance, for any complex root of a+jb (a and b are real numbers), one is able to find that a-jb is also a valid root. Complex modes have been studied by many researchers and they are observed in circular waveguides [44]-[45], dielectric waveguides [46]-[48] or structures with high-permittivity inhomogeneity [49]. The physical existence of complex modes in waveguides does not violate the principle of conservation of energy as long as both roots of each pair are included, as is discussed in [50]. The first 5 complex modes for $s = 0.1$ inches are shown in Figure 3.11. The red curve shows the imaginary part of the complex root and the black curve shows the real part. It can be noticed that the imaginary parts of the roots are very close to the purely imaginary roots found for the center case (Figure

3.9), which indicates a similar rate of attenuation. Also, it can be seen that the real parts of the complex roots are much smaller than the imaginary parts. Similar modal behavior can be observed in Figures 3.12-3.15 when the sample is shifted by 0.3 and 0.75 inches. The number of propagating modes may vary as the shift increases; for example, the number of propagating modes changes from four to three as the shift goes from 0.3 inches to 0.75 inches.

To further investigate the impact of sample shift on the modes, the computed roots β are plotted as a function of the shift. Figures 3.16-3.21 show the relationship between β and s at three different frequencies. The variation of the roots for the propagating modes is less than 10% when the shift is between 0 and 0.4 inches. However, once the shift is larger than 0.4 inches, a noticeable change can be observed in the roots, especially for the low order modes. In any cases, the variation of s does not cause the complex modes to change dramatically. It can be seen that both the real and imaginary parts of the complex roots stay within a certain range, and the real part remains a relatively small number as the sample location is changed.

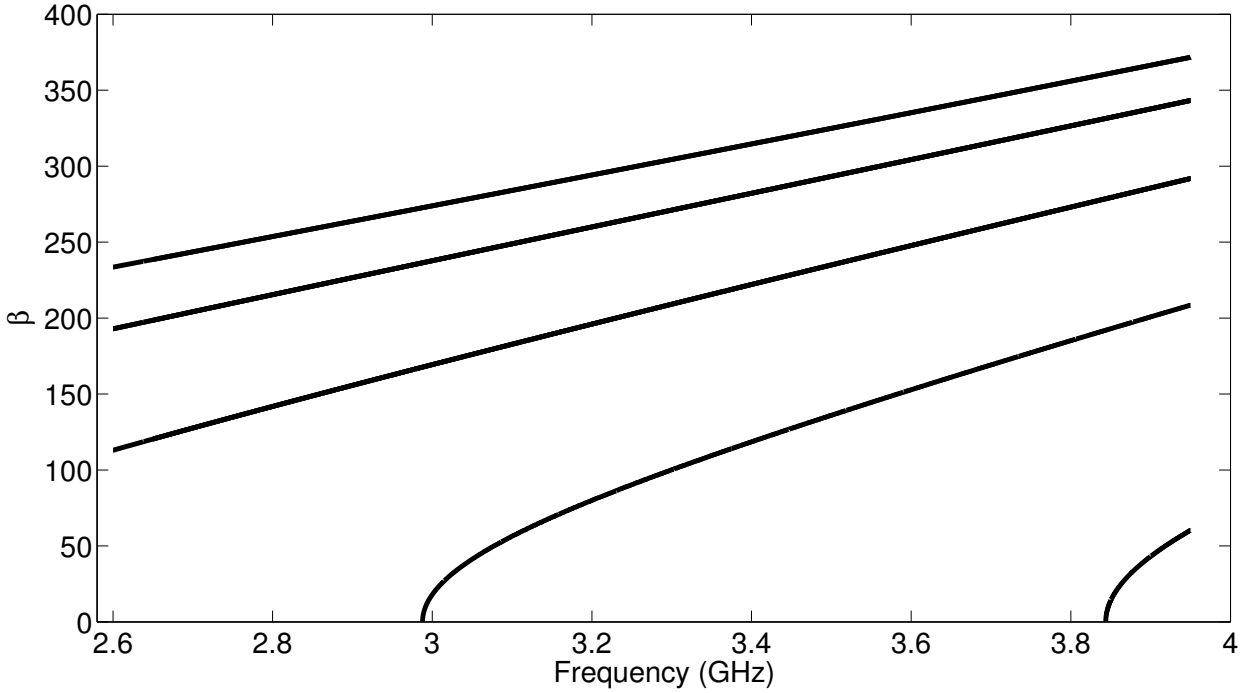

Figure 3.8 Modal spectrum of the propagating modes for a centered sample.

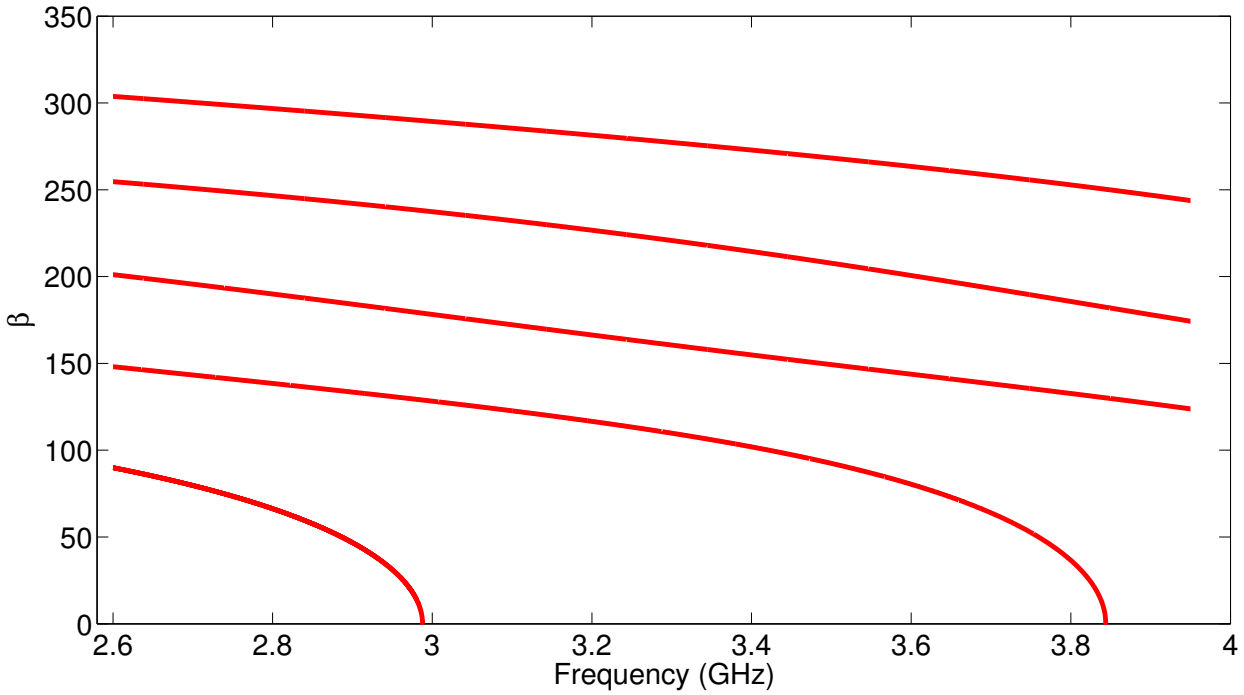

Figure 3.9 Modal spectrum of the evanescent modes for a centered sample.

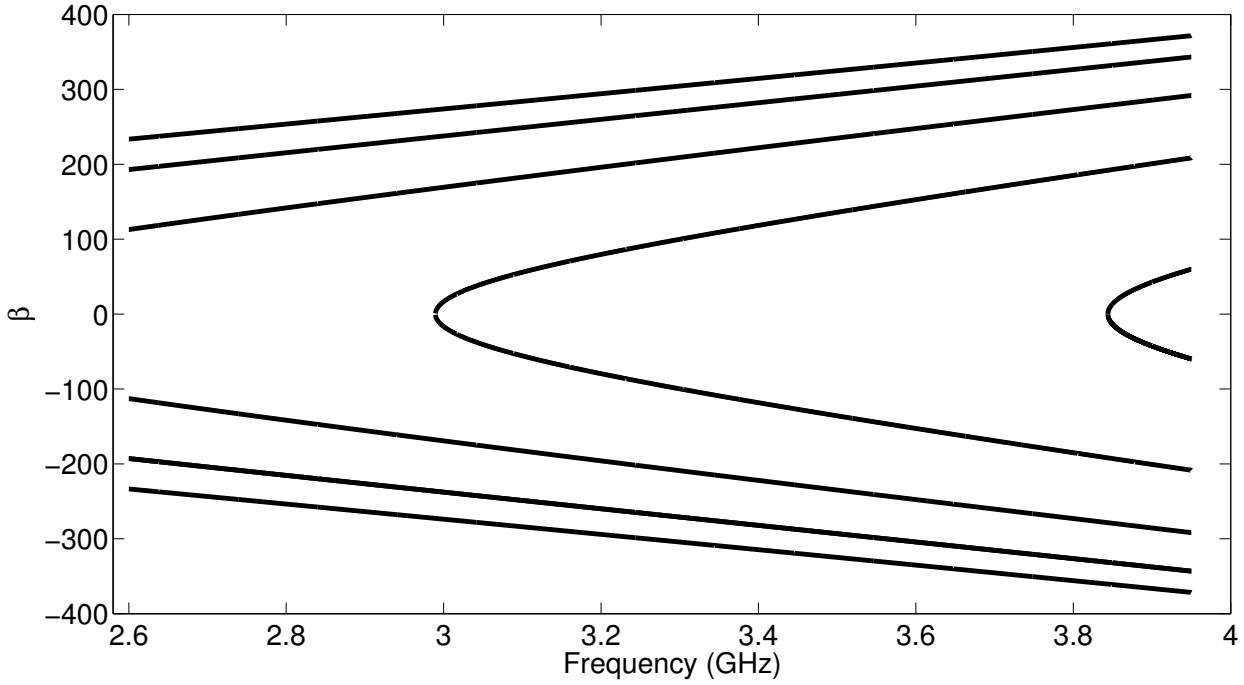

Figure 3.10 Modal spectrum of the propagating modes for sample shift s=0.1 inches.

3.2.3 Fields in the Waveguide

Different modes existing in the waveguide with gyromagnetic sample can be found through solving the characteristic equation (3.43). As a result, the fields in the sample region ($0 <$

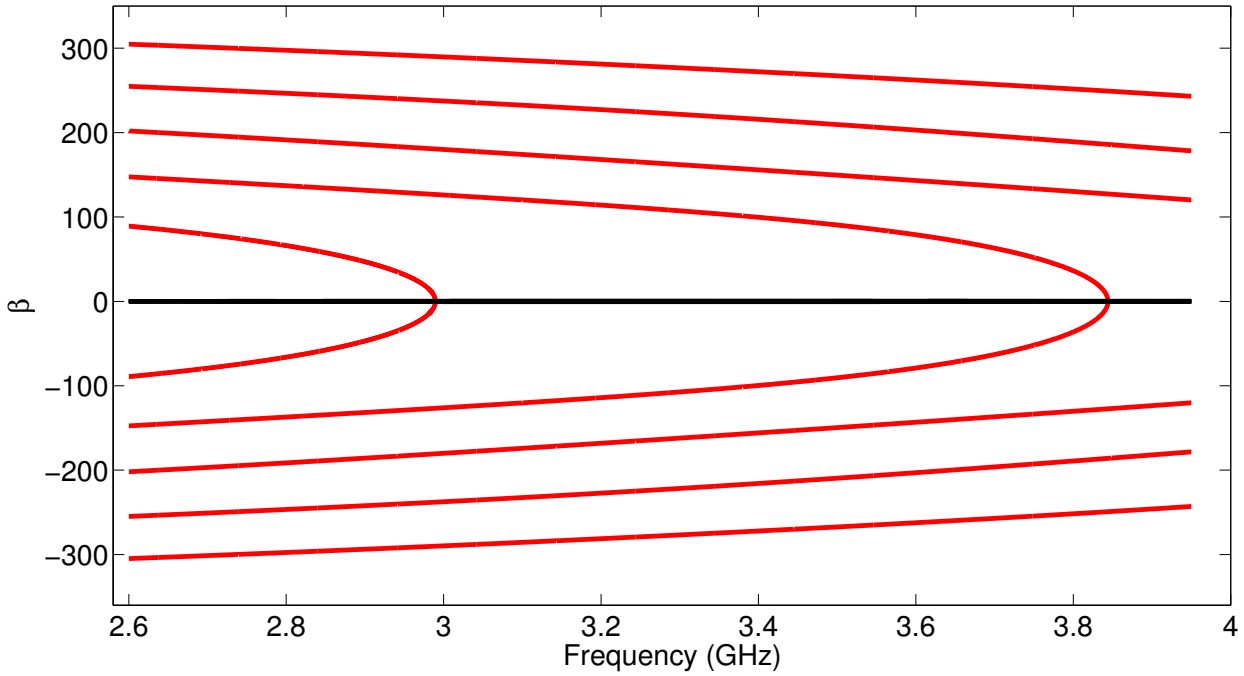

Figure 3.11 Modal spectrum of the complex modes for sample shift s=0.1 inches.

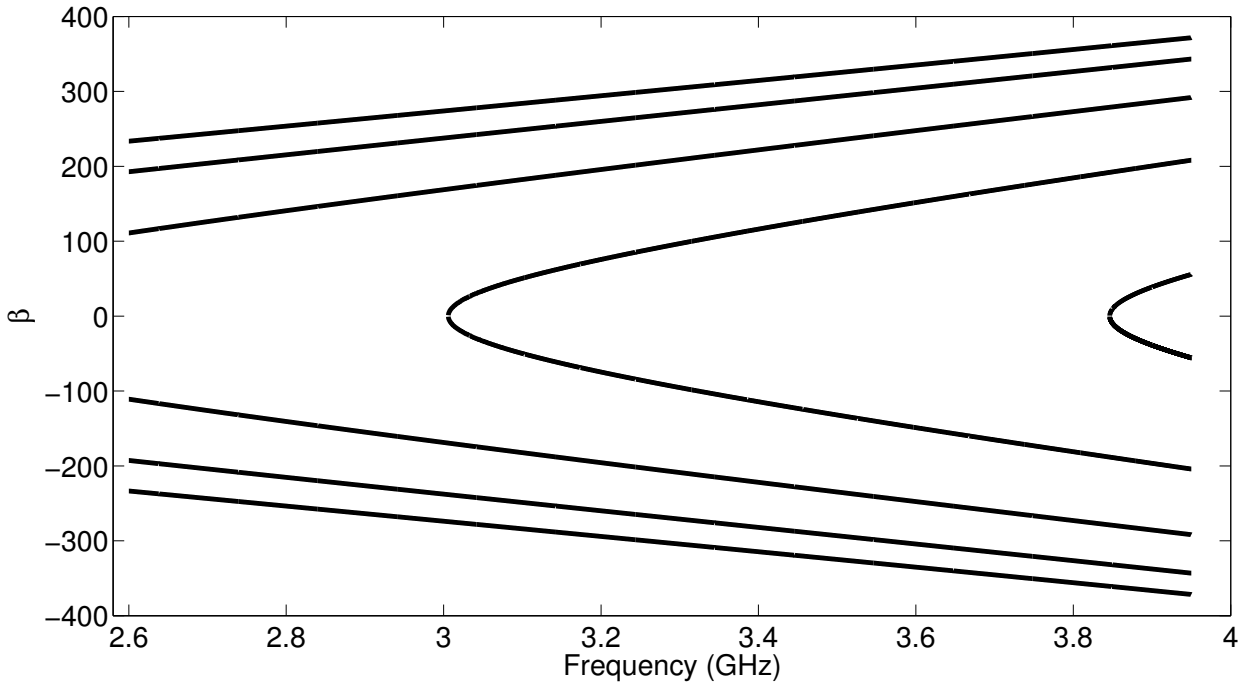

Figure 3.12 Modal spectrum of the propagating modes for sample shift s=0.3 inches.

$x < d$) can be plotted and the modes found can be validated. To obtain the expression for

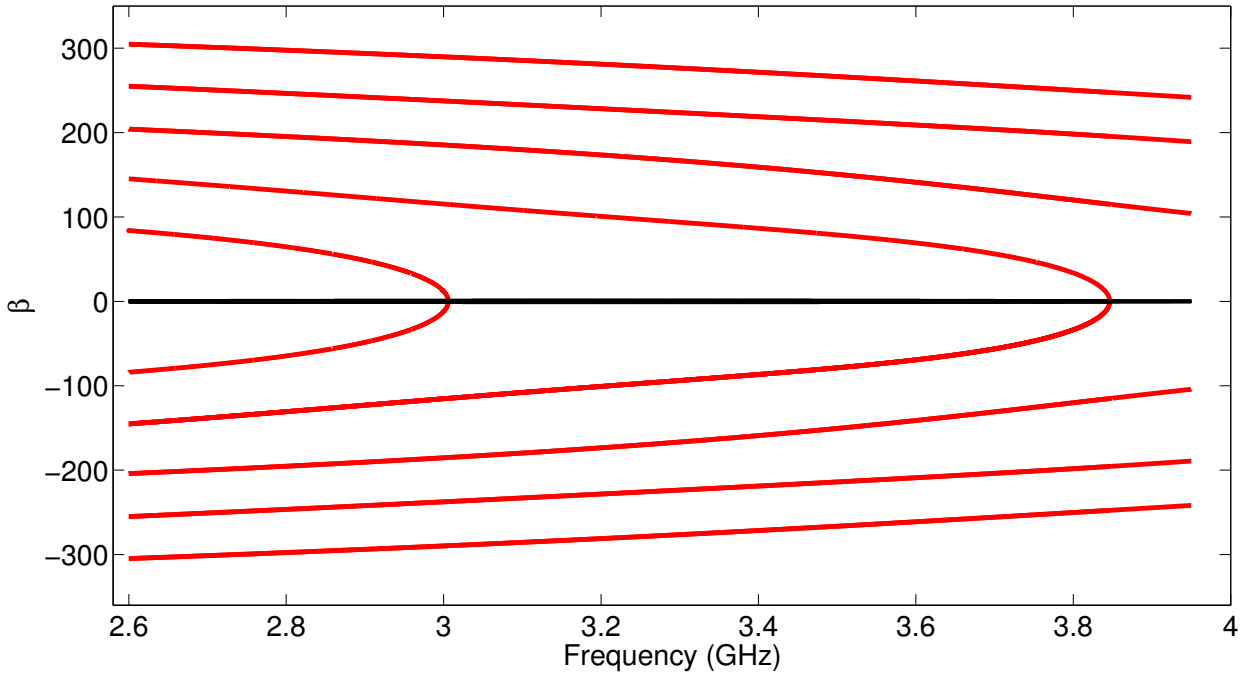

Figure 3.13 Modal spectrum of the complex modes for sample shift s=0.3 inches.

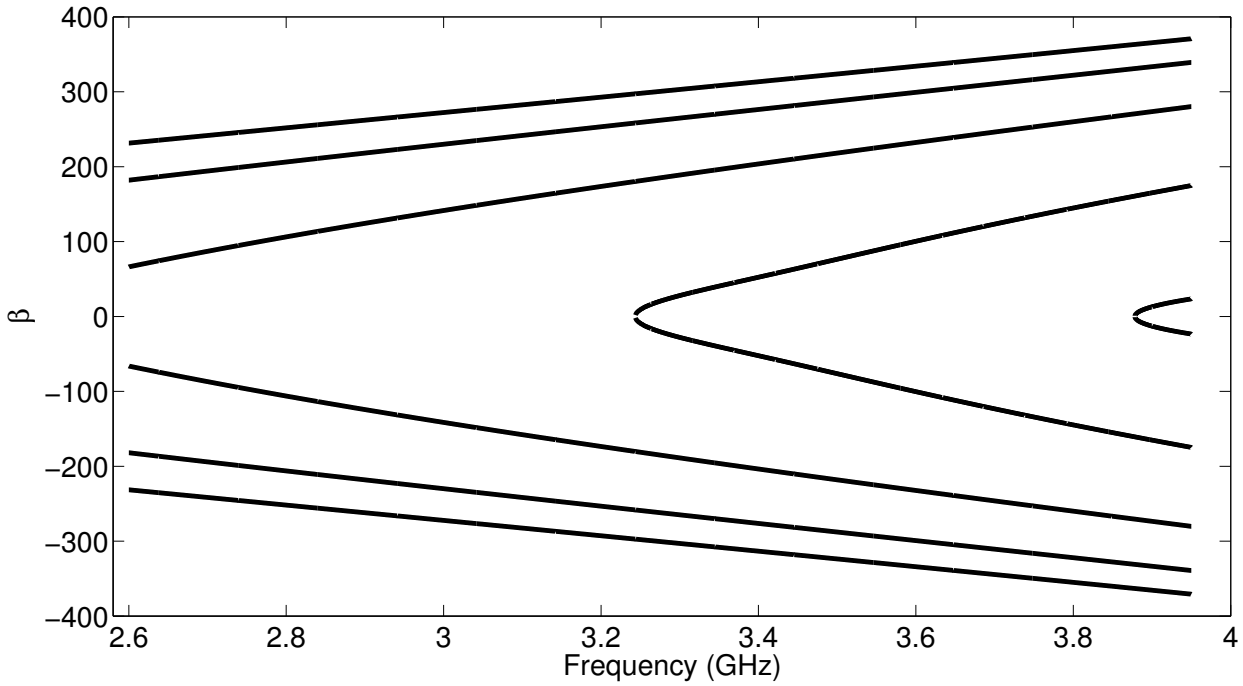

Figure 3.14 Modal spectrum of the propagating modes for sample shift s=0.75 inches.

the fields in the sample region, use (3.35) to obtain

$$B^I = -A^I \frac{F^{\pm}_{BA}}{F^{\pm}_{BB}}. \tag{3.46}$$

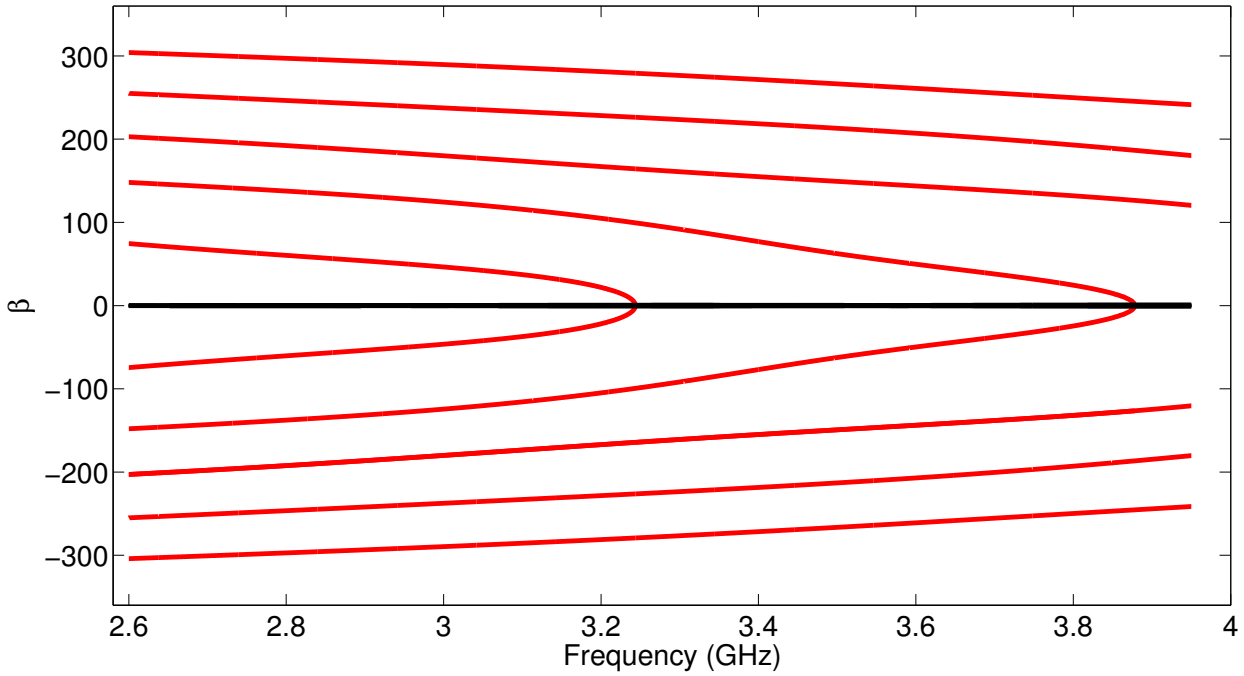

Figure 3.15 Modal spectrum of the complex modes for sample shift s=0.75 inches.

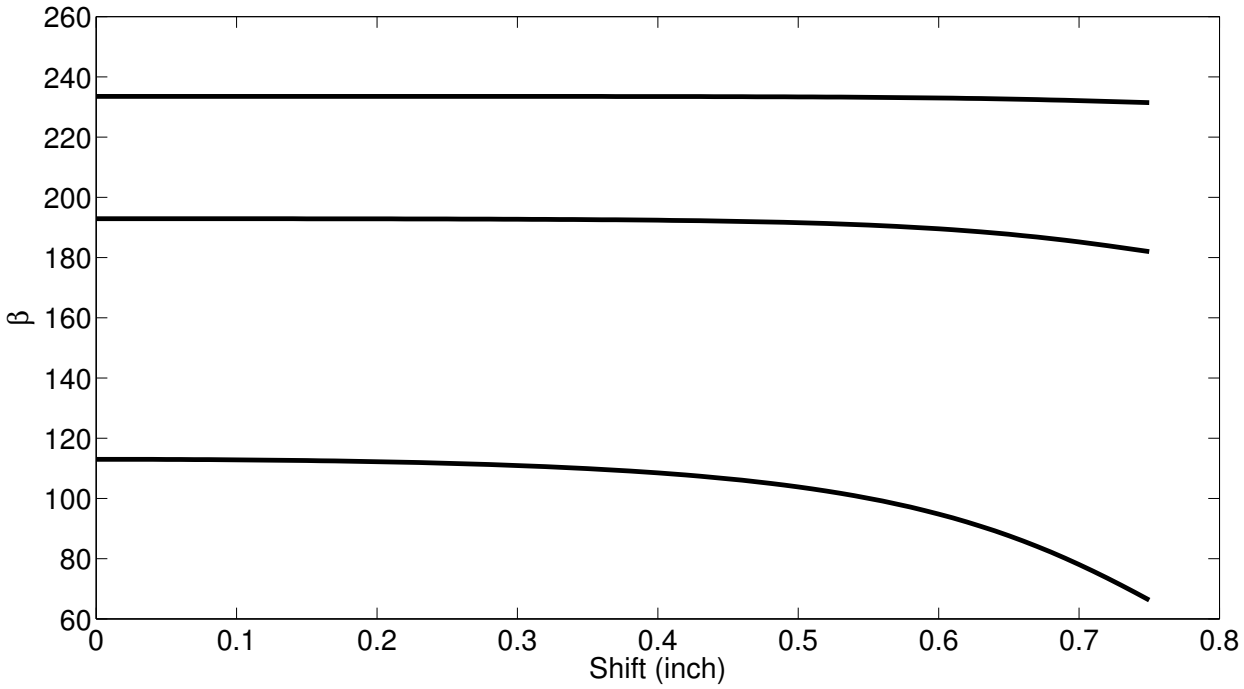

Figure 3.16 Propagation constants (propagating modes) for various sample shift (s) at 2.6 GHz.

This equation can be written as

$$B^I = -A^I G^{\pm}, \tag{3.47}$$

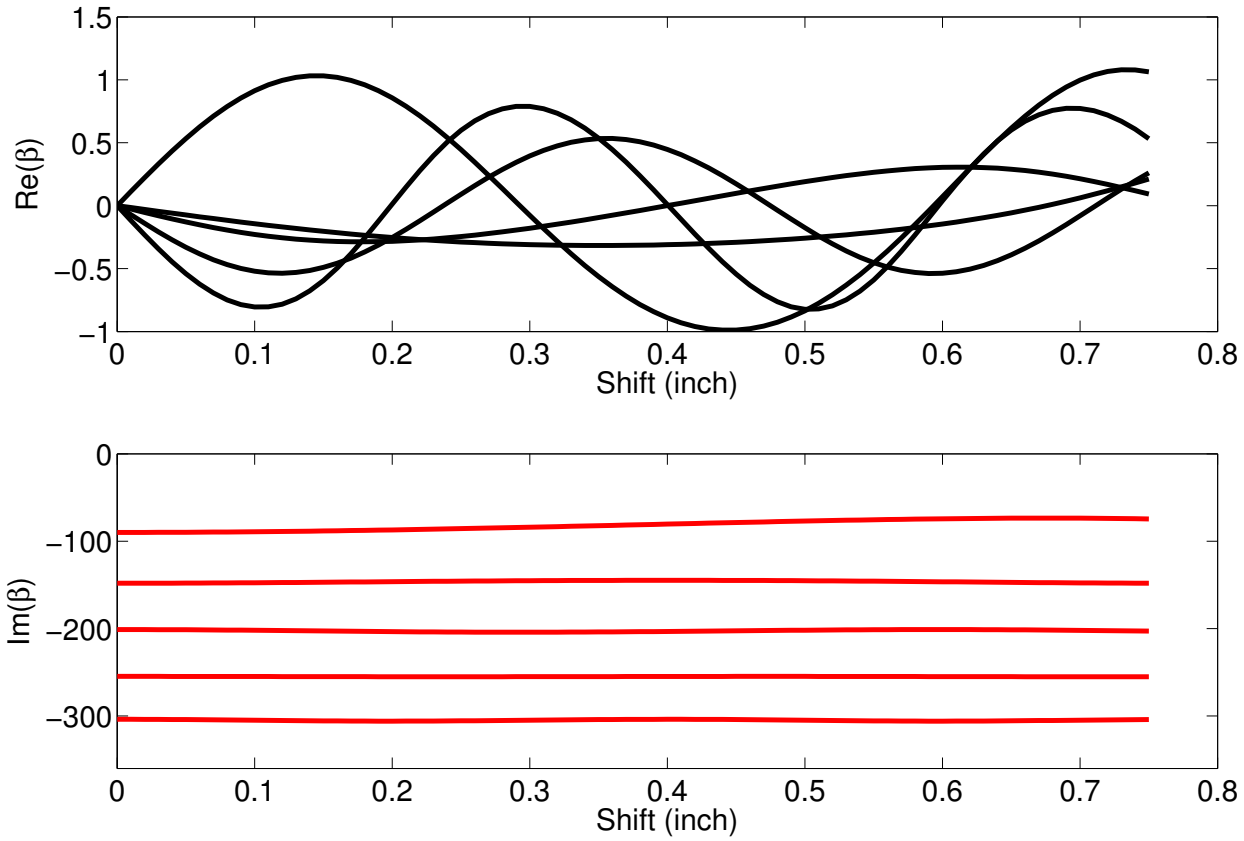

Figure 3.17 Propagation constants (complex modes) for various sample shift (s) at 2.6 GHz.

where

$$G^{\pm} = \frac{F^{\pm}_{BA}}{F^{\pm}_{BB}} = \frac{(\Gamma_2 \mp \Delta)\sin\left[k_C(s-\frac{d}{2})\right] + \cos\left[k_C(s-\frac{d}{2})\right]}{(\Gamma_2 \mp \Delta)\cos\left[k_C(s-\frac{d}{2})\right] - \sin\left[k_C(s-\frac{d}{2})\right]}. \tag{3.48}$$

For (3.26) and (3.28), substitute B^I with (3.47) to give

$$-A^{II}\tan\left[k_C^{II}(\frac{a-d-2s}{2})\right] = A^I\frac{\sin\left[k_C(\frac{d}{2}+s)\right]}{\cos(k_C\frac{d}{2})} - A^I G^{\pm}\frac{\cos\left[k_C(\frac{d}{2}+s)\right]}{\cos(k_C\frac{d}{2})} \tag{3.49}$$

$$A^{III}\tan\left[k_C^{III}(\frac{a-d+2s}{2})\right] = A^I\frac{\sin\left[k_C(s-\frac{d}{2})\right]}{\cos(k_C\frac{d}{2})} - A^I G^{\pm}\frac{\cos\left[k_C(s-\frac{d}{2})\right]}{\cos(k_C\frac{d}{2})}. \tag{3.50}$$

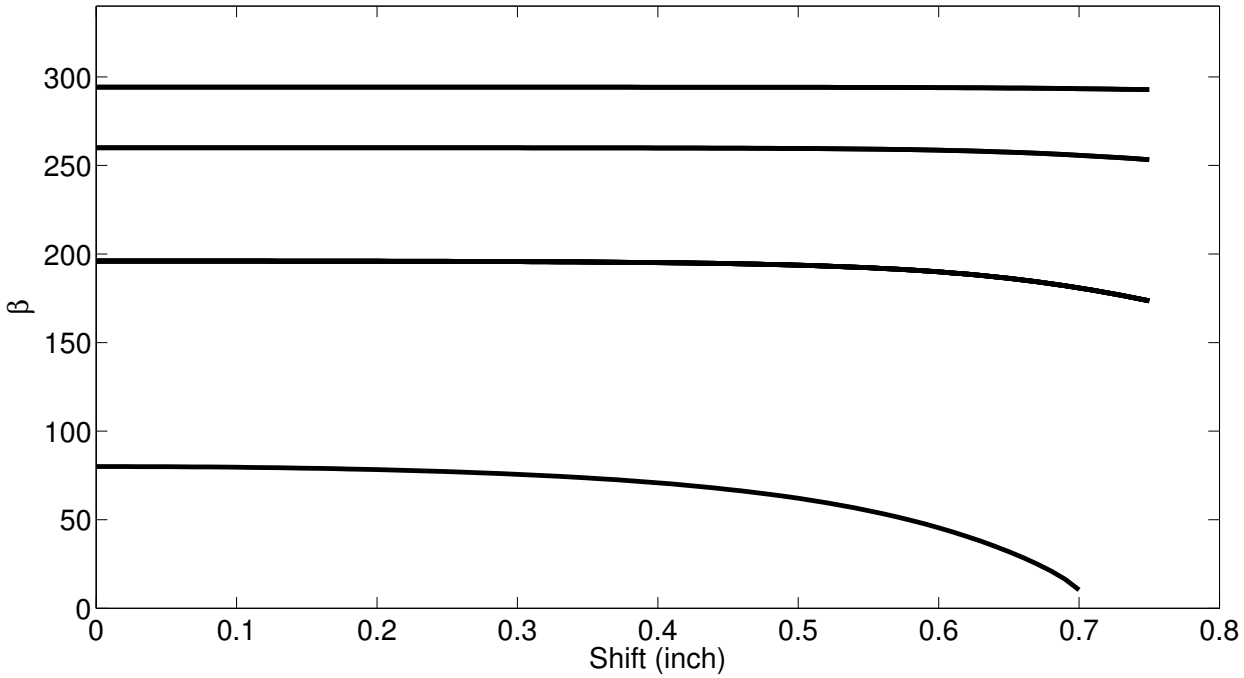

Figure 3.18 Propagation constants (propagating modes) for various sample shift (s) at 3.2 GHz.

Based on this, the relationship between A^I, A^{II} and A^{III} can be obtained as

$$A^{II} = A^I W^{\pm} \tag{3.51}$$

$$A^{III} = A^I U^{\pm}, \tag{3.52}$$

where

$$W^{\pm} = \left\{ G^{\pm} \frac{\cos\left[k_C(\frac{d}{2}+s)\right]}{\cos(k_C\frac{d}{2})} - \frac{\sin\left[k_C(\frac{d}{2}+s)\right]}{\cos(k_C\frac{d}{2})} \right\} \cot\left[k_C^{II}(\frac{a-d-2s}{2})\right] \tag{3.53}$$

$$U^{\pm} = \left\{ -\frac{\sin\left[k_C(\frac{d}{2}-s)\right]}{\cos(k_C\frac{d}{2})} - G^{\pm} \frac{\cos\left[k_C(s-\frac{d}{2})\right]}{\cos(k_C\frac{d}{2})} \right\} \cot\left[k_C^{II}(\frac{a-d+2s}{2})\right]. \tag{3.54}$$

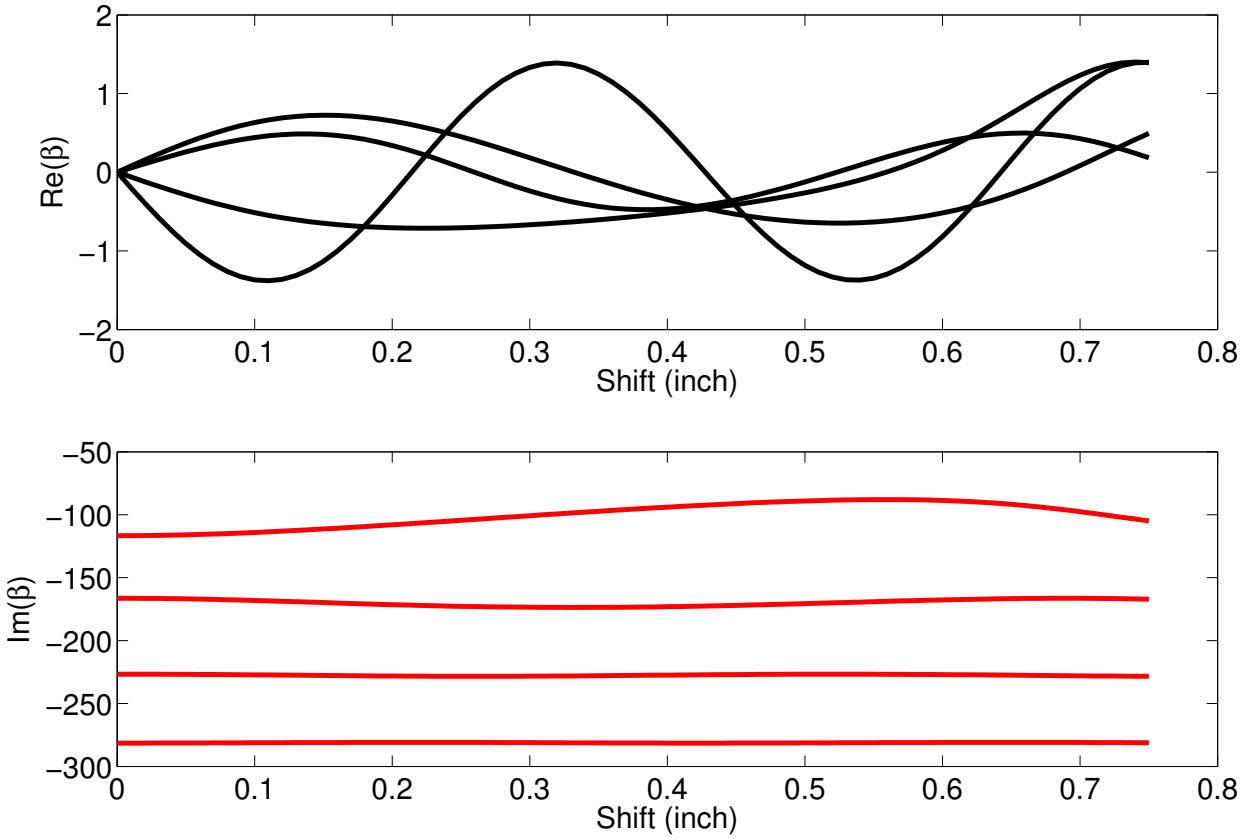

Figure 3.19 Propagation constants (complex modes) for various sample shift (s) at 3.2 GHz.

Now E_y and H_x within the empty part of the material region (region II and III) can be written as

$$E_y^{II}(x,z) = W^{\pm}\frac{\sin\left[k_c^{II}(x-\frac{a}{2})\right]}{\cos\left[k_c^{II}(\frac{a-d-2s}{2})\right]}e^{\pm j\beta z} \tag{3.55}$$

$$H_x^{II}(x,z) = \pm W^{\pm}\left(\frac{\beta}{\omega\mu_o}\right)\frac{\sin\left[k_c^{II}(x-\frac{a}{2})\right]}{\cos\left[k_c^{II}(\frac{a-d-2s}{2})\right]}e^{\pm j\beta z} \tag{3.56}$$

$$E_y^{III}(x,z) = U^{\pm}\frac{\sin\left[k_c^{II}(x+\frac{a}{2})\right]}{\cos\left[k_c^{II}(\frac{a-d+2s}{2})\right]}e^{\pm j\beta z} \tag{3.57}$$

$$H_x^{III}(x,z) = \pm A^I U^{\pm}\left(\frac{\beta}{\omega\mu_o}\right)\frac{\sin\left[k_c^{II}(x+\frac{a}{2})\right]}{\cos\left[k_c^{II}(\frac{a-d+2s}{2})\right]}e^{\pm j\beta z}, \tag{3.58}$$

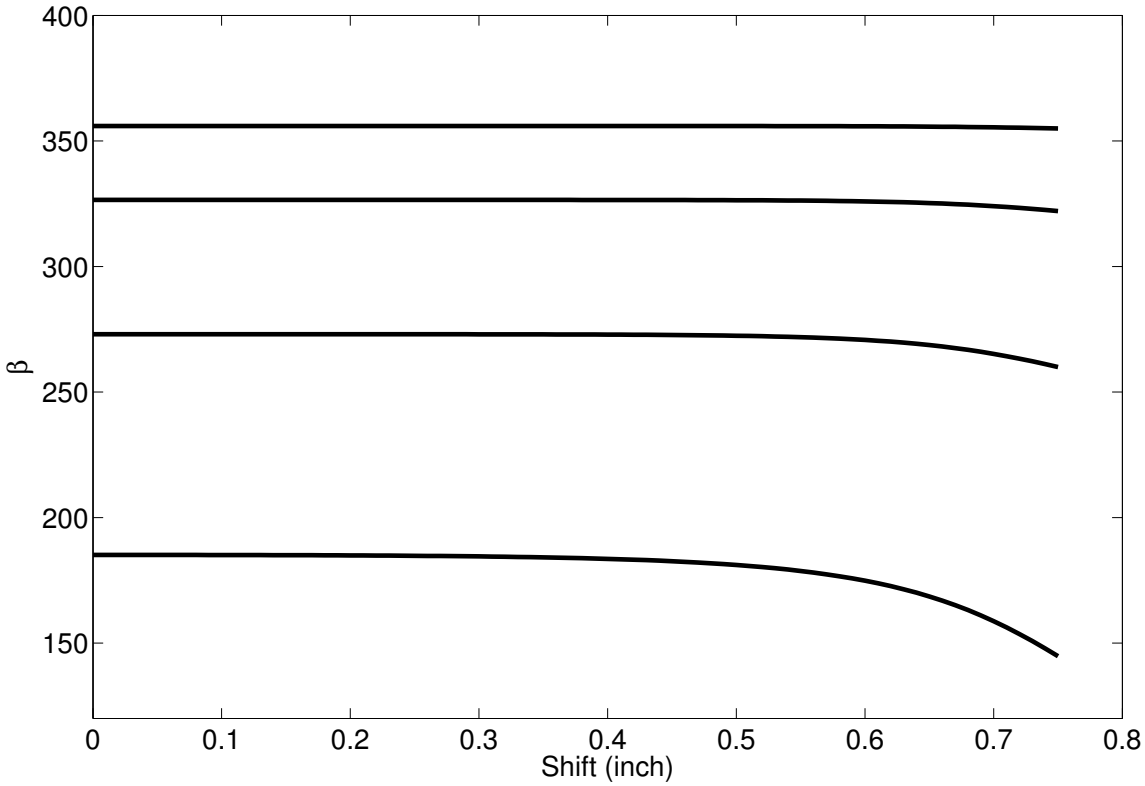

Figure 3.20 Propagation constants (propagating modes) for various sample shift (s) at 3.8 GHz.

and the fields inside the material (region I) can be expressed as

$$E_y^I(x,z) = A^I \left[\frac{\sin(k_C x)}{\cos(k_C \frac{d}{2})} - G^{\pm} \frac{\cos(k_C x)}{\cos(k_C \frac{d}{2})} \right] e^{\pm j\beta z} \quad (3.59)$$

$$H_x^I(x,z) = \left(\frac{\delta/\omega}{\delta^2 - \mu^2} \right) A^I \left[\frac{\sin(k_C x)}{\cos(k_C \frac{d}{2})} (k_C G^{\pm} \mp \frac{\beta\mu}{\delta}) + \frac{\cos(k_C x)}{\cos(k_C \frac{d}{2})} (k_C \pm G^{\pm} \frac{\beta\mu}{\delta}) \right] e^{\pm j\beta z} \quad (3.60)$$

To summarize, the fields in the partially-filled waveguide are described as

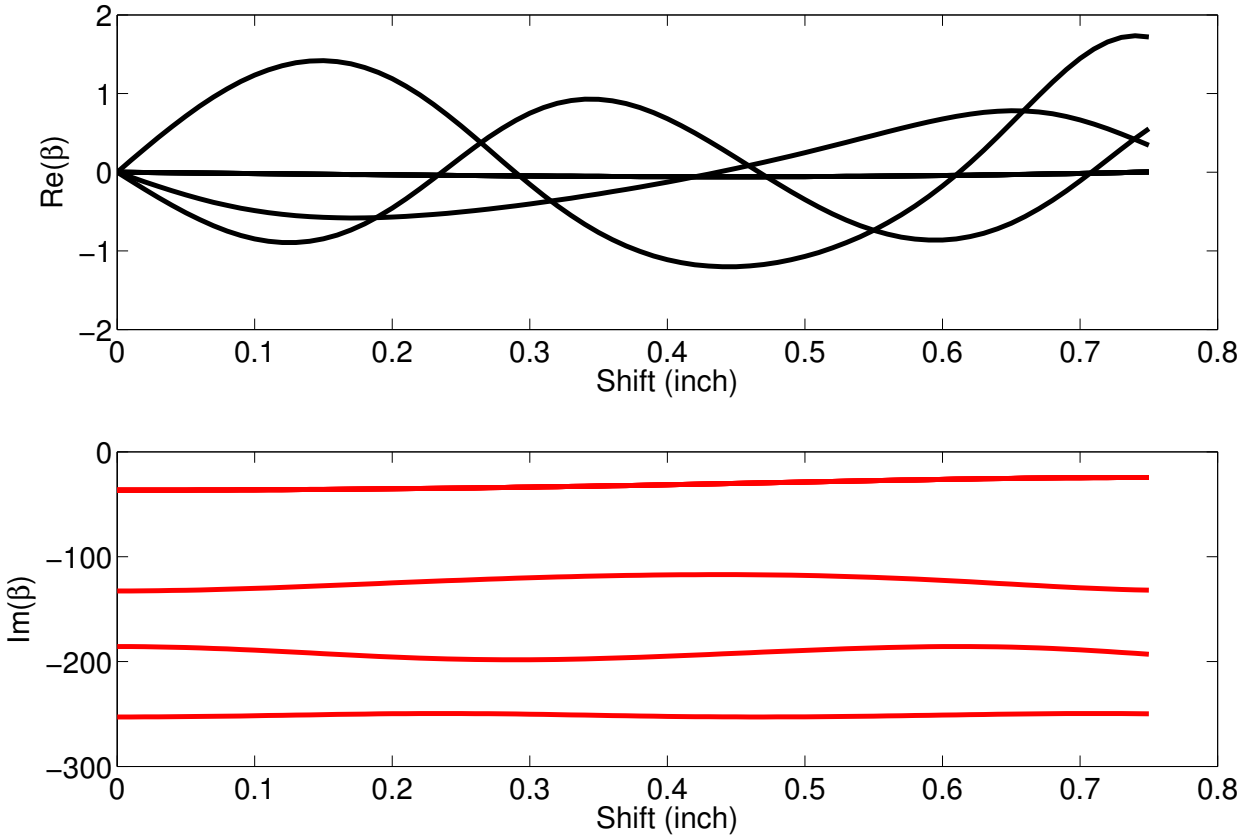

Figure 3.21 Propagation constants (complex modes) for various sample shift (s) at 3.8 GHz.

$$E(x,z)^{\pm} = \begin{cases} W^{\pm}\dfrac{\sin\left[k_c^{II}(x-\frac{a}{2})\right]}{\cos\left[k_c^{II}(\frac{a-d-2s}{2})\right]}e^{\pm j\beta z} & \frac{d}{2}+s \leqslant x \leqslant \frac{a}{2} \\ \left[\dfrac{\sin(k_C x)}{\cos(k_C\frac{d}{2})} - G^{\pm}\dfrac{\cos(k_C x)}{\cos(k_C\frac{d}{2})}\right]e^{\pm j\beta z} & -\frac{d}{2}+s \leqslant x \leqslant \frac{d}{2}+s \\ U^{\pm}\dfrac{\sin\left[k_c^{II}(x+\frac{a}{2})\right]}{\cos\left[k_c^{II}(\frac{a-d+2s}{2})\right]}e^{\pm j\beta z} & -\frac{a}{2} \leqslant x \leqslant -\frac{d}{2}+s, \end{cases} \tag{3.61}$$

and

$$H(x,z)^{\pm} = \begin{cases} \pm W^{\pm}\frac{\beta}{\omega\mu_o}\,\dfrac{\sin\left[k_c^{II}(x-\frac{a}{2})\right]}{\cos\left[k_c^{II}(\frac{a-d-2s}{2})\right]}\,e^{\pm j\beta z} & \frac{d}{2}+s \leqslant x \leqslant \frac{a}{2} \\ \dfrac{\delta/\omega}{\delta^2-\mu^2}\left[\dfrac{\sin(k_C x)}{\cos(k_C\frac{d}{2})}(k_C G^{\pm} \mp \frac{\beta\mu}{\delta})+\right. & \\ \left.\dfrac{\cos(k_C x)}{\cos(k_C\frac{d}{2})}(k_C \pm G^{\pm}\frac{\beta\mu}{\delta})\right]e^{\pm j\beta z} & -\frac{d}{2}+s \leqslant x \leqslant \frac{d}{2}+s \\ \pm U^{\pm}\frac{\beta}{\omega\mu_o}\,\dfrac{\sin\left[k_c^{III}(x+\frac{a}{2})\right]}{\cos\left[k_c^{II}(\frac{a-d+2s}{2})\right]}\,e^{\pm j\beta z} & -\frac{a}{2} \leqslant x \leqslant -\frac{d}{2}+s. \end{cases} \tag{3.62}$$

The fields for the special case where the sample is placed at the center of the waveguide can be found by setting s to 0, and thus $G^{\pm}$, $W^{\pm}$ and $U^{\pm}$ can be further simplified into

$$G^{\pm} = \frac{-(\Gamma \mp \Delta)\tan(k_C\frac{d}{2})+1}{(\Gamma \mp \Delta)+\tan(k_C\frac{d}{2})} \tag{3.63}$$

$$W^{\pm} = \left[G^{\pm} - \tan\left(k_C\frac{d}{2}\right)\right]\cot\left[k_c^{II}(\frac{a-d}{2})\right] \tag{3.64}$$

$$U^{\pm} = \left[-G^{\pm} - \tan\left(k_C\frac{d}{2}\right)\right]\cot\left[k_c^{II}(\frac{a-d}{2})\right], \tag{3.65}$$

where Γ is shown in (3.45). Finally, the fields for the special case are found to be

$$E(x,z)^{\pm} = \begin{cases} W^{\pm}\dfrac{\sin\left[k_c^{II}(x-\frac{a}{2})\right]}{\cos\left[k_c^{II}(\frac{a-d-2s}{2})\right]}e^{\pm j\beta z} & \frac{d}{2}+s \leqslant x \leqslant \frac{a}{2} \\ \left[\dfrac{\sin(k_C x)}{\cos(k_C\frac{d}{2})} - G^{\pm}\dfrac{\cos(k_C x)}{\cos(k_C\frac{d}{2})}\right]e^{\pm j\beta z} & -\frac{d}{2}+s \leqslant x \leqslant \frac{d}{2}+s \\ U^{\pm}\dfrac{\sin\left[k_c^{II}(x+\frac{a}{2})\right]}{\cos\left[k_c^{II}(\frac{a-d+2s}{2})\right]}e^{\pm j\beta z} & -\frac{a}{2} \leqslant x \leqslant -\frac{d}{2}+s, \end{cases} \tag{3.66}$$

and

$$H(x,z)^{\pm} = \begin{cases} \pm W^{\pm}\frac{\beta}{\omega\mu_o}\,\frac{\sin\left[k_c^{II}(x-\frac{a}{2})\right]}{\cos\left[k_c^{II}(\frac{a-d-2s}{2})\right]}\,e^{\pm j\beta z} & \frac{d}{2}+s \leqslant x \leqslant \frac{a}{2} \\ \frac{\delta/\omega}{\delta^2-\mu^2}\left[\frac{\sin(k_c x)}{\cos(k_c\frac{d}{2})}(k_c G^{\pm} \mp \frac{\beta\mu}{\delta})+\right. & \\ \left.\frac{\cos(k_c x)}{\cos(k_c\frac{d}{2})}(k_c \pm G^{\pm}\frac{\beta\mu}{\delta})\right]e^{\pm j\beta z} & -\frac{d}{2}+s \leqslant x \leqslant \frac{d}{2}+s \\ \pm U^{\pm}\frac{\beta}{\omega\mu_o}\,\frac{\sin\left[k_c^{III}(x+\frac{a}{2})\right]}{\cos\left[k_c^{II}(\frac{a-d+2s}{2})\right]}\,e^{\pm j\beta z} & -\frac{a}{2} \leqslant x \leqslant -\frac{d}{2}+s. \end{cases} \tag{3.67}$$

Also, the fields inside an empty waveguide are given by

$$E_m(x) = -\frac{j\omega\mu_o}{k_{cm}}\sin\left[k_{cm}(x-\frac{a}{2})\right] \tag{3.68}$$
$$H_x(x) = \frac{E_m}{Z_m},$$

where

$$k_{cm} = \frac{m\pi}{a},\ m = 1,2,3\cdots$$
$$Z_m = \frac{\omega\mu_o}{\beta_m}.$$

The fields in the waveguide can be plotted to validate the boundary condition. Considering the same material parameters used in Section 3.2.2.2, the propagation constant β of the first order propagating mode is computed under different conditions. For modes propagating in both the +z and -z directions, Figures 3.22-3.25 show the normalized fields of E_y,H_x and H_z at two frequencies with s=0 and s=0.2 inches. It is obvious that E_y and H_z are always continuous at the boundary of the sample, which satisfies the imposed boundary conditions. As the sample is shifted by 0.2 inches, one can see that the field confined in the material is also shifted as expected. At 3.6 GHz, a similar trend can be seen while the field distribu-

tion is different from that at 2.6 GHz. With the validation of the modes, a mode matching technique can be developed to compute the reflection and transmission coefficients.

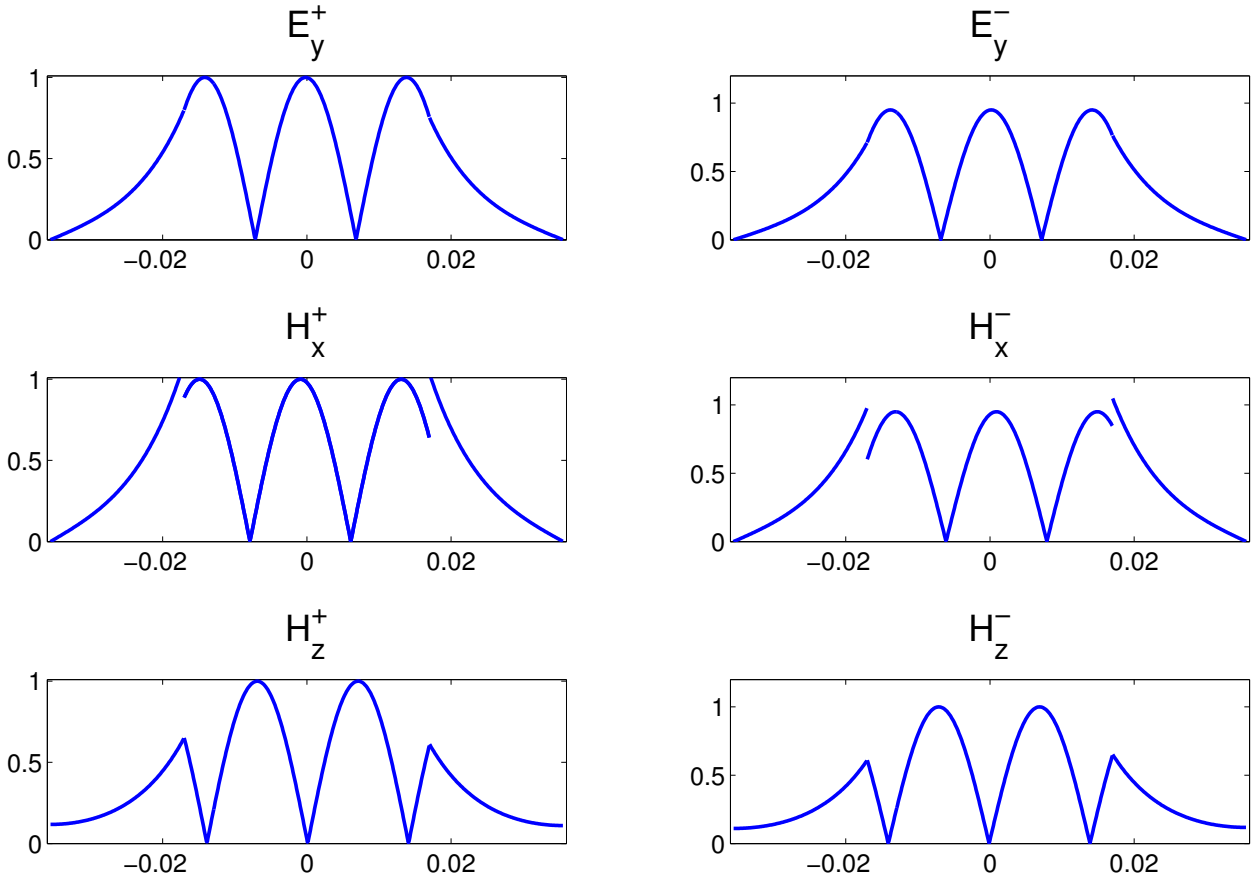

Figure 3.22 Field distribution of the first propagating mode for a sample shift of s=0 at 2.8 GHz.

3.2.4 Mode Matching

Now the transverse fields in the material region and empty region of the waveguide are known and can be expressed as an infinite summation of modal fields. The next step is to determine the modal amplitudes by applying different boundary conditions. From Figure 3.7, it can be

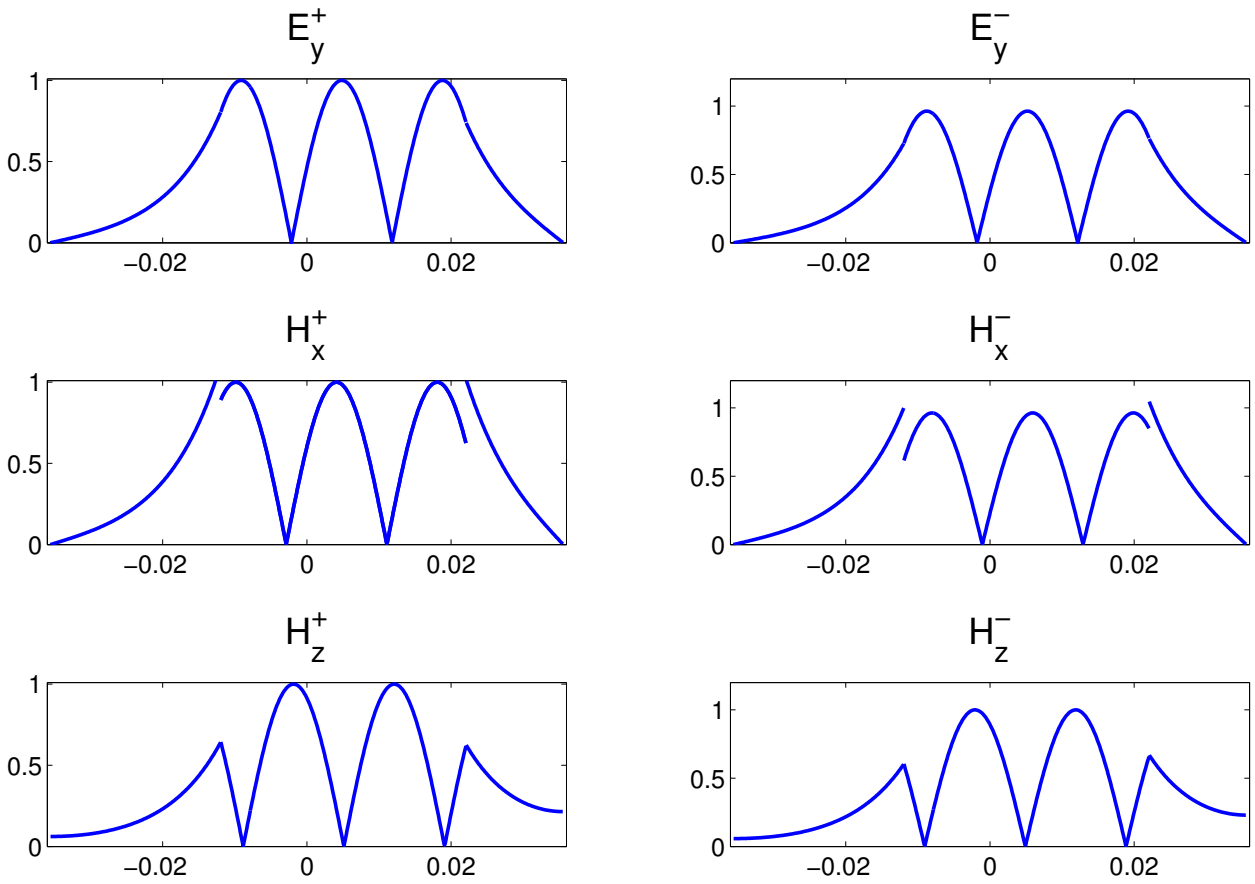

Figure 3.23 Field distribution of the first propagating mode for a sample shift of s=0.2 inches at 2.8 GHz.

seen that for the empty waveguide region $z < 0$,

$$E_y(x,z) = a_1^i \overline{E}_1^-(x) e^{-j\overline{\beta}1z} + \sum_{n=1}^{N} a_n^r \overline{E}_n^+(x) e^{j\overline{\beta}nz} \tag{3.69}$$

$$H_x(x,z) = a_1^i \overline{H}_1^-(x) e^{-j\overline{\beta}1z} + \sum_{n=1}^{N} a_n^r \overline{H}_n^+(x) e^{j\overline{\beta}nz} \tag{3.70}$$

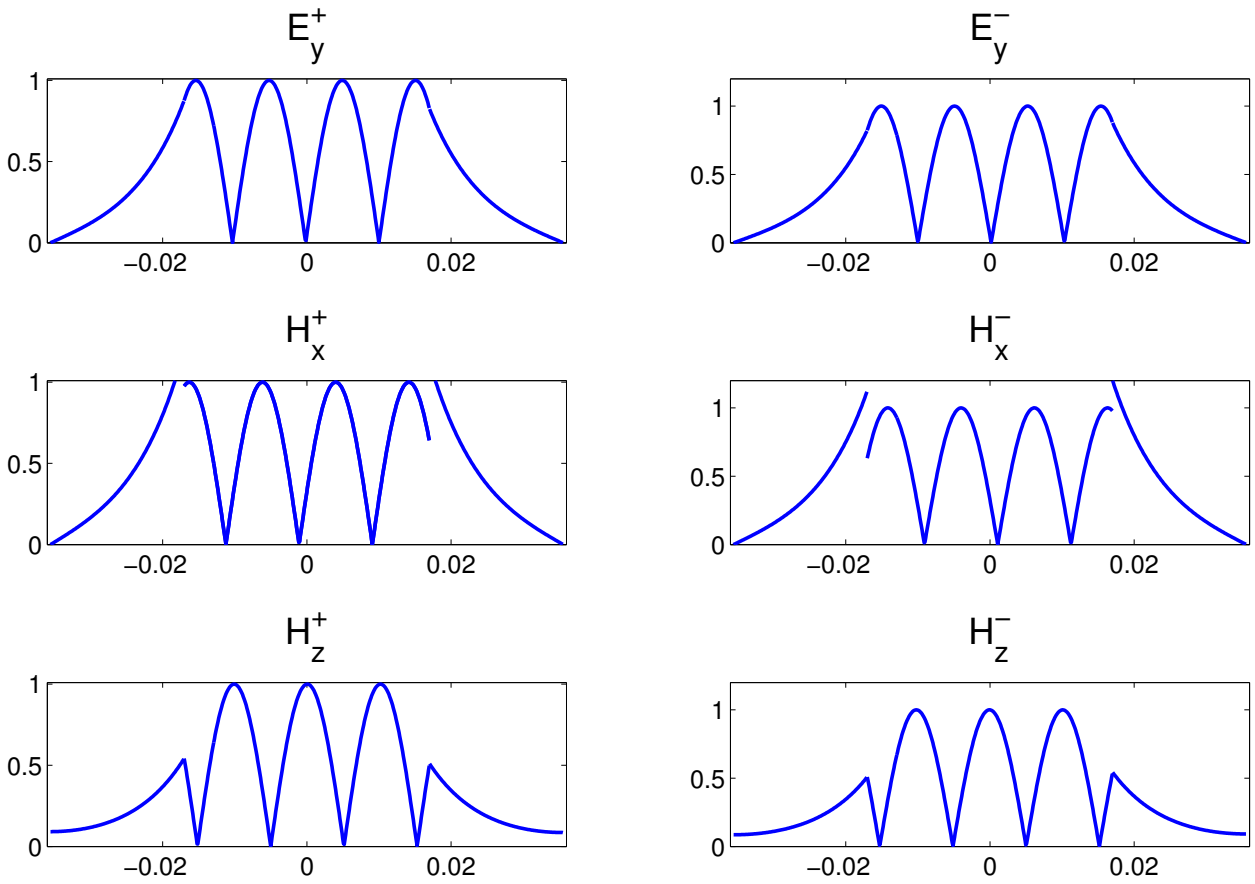

Figure 3.24 Field distribution of the first propagating mode for a sample shift of s=0 at 3.6 GHz.

The coefficient a_1^i is the amplitude of the incident TE_{10} wave, which is supposed to be known. In the material region $0 < z < \Delta$, the transverse fields are expressed as

$$E_y(x,z) = \sum_{n=1}^{N} a_n^- E_n^-(x) e^{-j\beta n z} + \sum_{n=1}^{N} a_n^+ E_n^+(x) e^{j\beta n (z-\Delta)} \tag{3.71}$$

$$H_x(x,z) = \sum_{n=1}^{N} a_n^- H_n^-(x) e^{-j\beta n z} + \sum_{n=1}^{N} a_n^+ H_n^+(x) e^{j\beta n (z-\Delta)}. \tag{3.72}$$

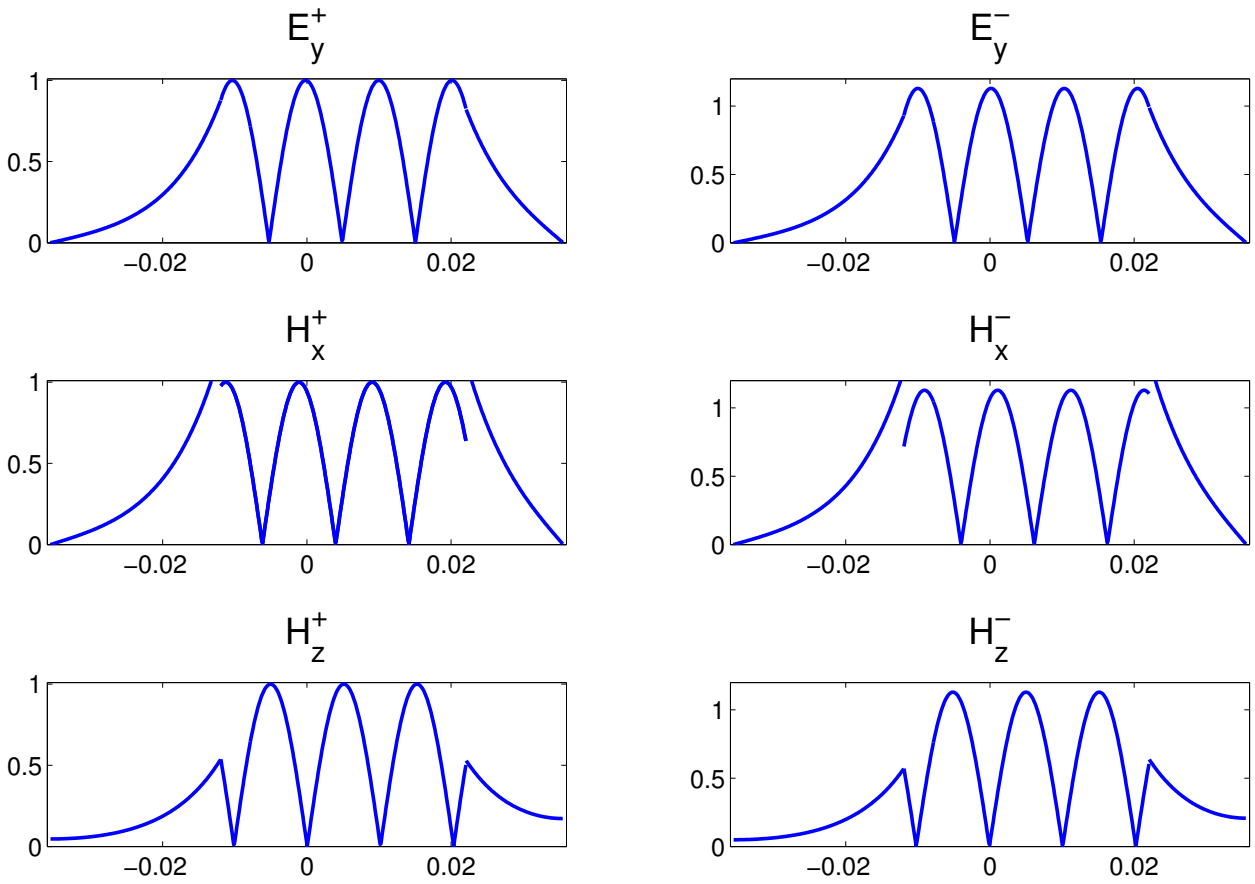

Figure 3.25 Field distribution of the first propagating mode for a sample shift of s=0.2 inches at 3.6 GHz.

The fields in the empty waveguide region $z > \Delta$ are

$$E_y(x,z) = \sum_{n=1}^{N} a_n^t E_n^-(x) e^{-j\beta n(z-\Delta)} \tag{3.73}$$

$$H_x(x,z) = \sum_{n=1}^{N} a_n^t H_n^-(x) e^{-j\beta n(z-\Delta)}. \tag{3.74}$$

The modal amplitude can be determined by applying the boundary conditions on E_y and H_x at the interfaces at z=0 and $z = \Delta$. The continuity of E_y at z=0 gives

$$a_1^i \overline{E}_1^-(x) + \sum_{n=1}^{N} a_n^r \overline{E}_n^+(x) = \sum_{n=1}^{N} a_n^- E_n^-(x) + \sum_{n=1}^{N} a_n^+ E_n^+(x) e^{-j\beta n\Delta}. \tag{3.75}$$

The continuity of H_x at z=0 gives

$$a_1^i \overline{H}_1^-(x) + \sum_{n=1}^{N} a_n^r \overline{H}_n^+(x) = \sum_{n=1}^{N} a_n^- H_n^-(x) + \sum_{n=1}^{N} a_n^+ H_n^+(x) e^{-j\beta n\Delta}. \tag{3.76}$$

The continuity of E_y at $z = \Delta$ gives

$$\sum_{n=1}^{N} a_n^- E_n^-(x) e^{-j\beta n\Delta} + \sum_{n=1}^{N} a_n^+ E_n^+(x) = \sum_{n=1}^{N} a_n^t E_n^-(x). \tag{3.77}$$

The continuity of H_x at $z = \Delta$ gives

$$\sum_{n=1}^{N} a_n^- H_n^-(x) e^{-j\beta n\Delta} + \sum_{n=1}^{N} a_n^+ H_n^+(x) e^{j\beta n(z-\Delta)} = \sum_{n=1}^{N} a_n^t H_n^-(x). \tag{3.78}$$

To convert the set of equations (3.75) - (3.78) into a set of linear equations, the testing operations of empty waveguide modes using (3.69) are applied to the four equations and yield,

$$\begin{aligned}
&\mathrm{a}_1^i \overbrace{\int_{-\frac{a}{2}}^{\frac{a}{2}} \overline{E}_1^-(x)\overline{E}_m^+(x)dx}^{C_{m1}^-} + \textstyle\sum_{n=1}^{N} a_n^r \overbrace{\int_{-\frac{a}{2}}^{\frac{a}{2}} \overline{E}_n^+(x)\overline{E}_m^+(x)dx}^{C_{mn}^+} \\
&= \textstyle\sum_{n=1}^{N} a_n^- \overbrace{\int_{-\frac{a}{2}}^{\frac{a}{2}} E_n^-(x)\overline{E}_m^+(x)dx}^{D_{mn}^-} + \sum_{n=1}^{N} a_n^+ \overbrace{\int_{-\frac{a}{2}}^{\frac{a}{2}} E_n^+(x)\overline{E}_m^+(x)dx}^{D_{mn}^+} e^{-j\beta n\Delta} \\
&\mathrm{a}_1^i \overbrace{\int_{-\frac{a}{2}}^{\frac{a}{2}} \overline{H}_1^-(x)\overline{H}_m^+(x)dx}^{E_{m1}^-} + \textstyle\sum_{n=1}^{N} a_n^r \overbrace{\int_{-\frac{a}{2}}^{\frac{a}{2}} \overline{H}_n^+(x)\overline{H}_m^+(x)dx}^{E_{mn}^+}
\end{aligned} \tag{3.79}$$

$$=\sum_{n=1}^{N} a_n^- \overbrace{\int_{-\frac{a}{2}}^{\frac{a}{2}} H_n^-(x)\overline{H}_m^+(x)dx}^{F_{mn}^-} + \sum_{n=1}^{N} a_n^+ e^{-j\beta n\Delta} \overbrace{\int_{-\frac{a}{2}}^{\frac{a}{2}} H_n^+(x)\overline{H}_m^+(x)dx}^{F_{mn}^+} \quad (3.80)$$

$$\sum_{n=1}^{N} a_n^- e^{-j\beta n\Delta} \overbrace{\int_{-\frac{a}{2}}^{\frac{a}{2}} E_n^-(x)\overline{E}_m^+(x)dx}^{D_{mn}^-} + \sum_{n=1}^{N} a_n^+ \overbrace{\int_{-\frac{a}{2}}^{\frac{a}{2}} E_n^+(x)\overline{E}_m^+(x)dx}^{D_{mn}^+}$$

$$=\sum_{n=1}^{N} a_n^t \overbrace{\int_{-\frac{a}{2}}^{\frac{a}{2}} E_n^-(x)\overline{E}_m^+(x)dx}^{C_{mn}^-} \quad (3.81)$$

$$\sum_{n=1}^{N} a_n^- e^{-j\beta n\Delta} \overbrace{\int_{-\frac{a}{2}}^{\frac{a}{2}} H_n^-(x)\overline{H}_m^+(x)dx}^{F_{mn}^-} + \sum_{n=1}^{N} a_n^+ e^{j\beta n(z-\Delta)} \overbrace{\int_{-\frac{a}{2}}^{\frac{a}{2}} H_n^+(x)\overline{H}_m^+(x)dx}^{F_{mn}^+}$$

$$=\sum_{n=1}^{N} a_n^t \overbrace{\int_{-\frac{a}{2}}^{\frac{a}{2}} H_n^-(x)\overline{H}_m^+(x)dx}^{E_{mn}^-}. \quad (3.82)$$

This gives the set of linear equations

$$a_1^i C_{m1}^- + \sum_{n=1}^{N} a_n^r C_{mn}^+ = \sum_{n=1}^{N} a_n^- D_{mn}^- + \sum_{n=1}^{N} a_n^+ D_{mn}^+ e^{-j\beta n\Delta} \quad (3.83)$$

$$a_1^i E_{m1}^- + \sum_{n=1}^{N} a_n^r E_{mn}^+ = \sum_{n=1}^{N} a_n^- F_{mn}^- + \sum_{n=1}^{N} a_n^+ F_{mn}^+ e^{-j\beta n\Delta} \quad (3.84)$$

$$\sum_{n=1}^{N} a_n^- D_{mn}^- e^{-j\beta n\Delta} + \sum_{n=1}^{N} a_n^+ D_{mn}^+ = \sum_{n=1}^{N} a_n^t C_{mn}^- \quad (3.85)$$

$$\sum_{n=1}^{N} a_n^- F_{mn}^- e^{-j\beta n\Delta} + \sum_{n=1}^{N} a_n^+ F_{mn}^+ = \sum_{n=1}^{N} a_n^t E_{mn}^-. \quad (3.86)$$

Let $e_N = e^{-j\beta n\Delta}$, The linear equation can be expressed as a 4×4 block matrix equation where each block is $N \times N$

$$\begin{bmatrix} -C^+ & D^- & e_N D^+ & 0 \\ -E^+ & F^- & e_N F^+ & 0 \\ 0 & e_N D^- & D^+ & -C^- \\ 0 & e_N F^- & F^+ & -E^- \end{bmatrix} \begin{bmatrix} a^r \\ a^- \\ a^+ \\ a^t \end{bmatrix} = \begin{bmatrix} a_1^i f^- \\ a_1^i g^- \\ 0 \\ 0 \end{bmatrix} \tag{3.87}$$

where $f_m^- = C_{m1}^-$ and $g_m^- = E_{m1}^-$. Finally, the S parameters can be obtained from

$$S_{11} = \frac{a_1^r}{a_1^i} \tag{3.88}$$

$$S_{21} = \frac{a_1^t}{a_1^i} \tag{3.89}$$

The matrix entries can be determined by calculating the corresponding integrals. Begin with

$$C_{mn}^{\pm} = \int_{-\frac{a}{2}}^{\frac{a}{2}} \overline{E}_1^{\pm}(x)\overline{E}_m^{+}(x)dx \tag{3.90}$$

$$= \int_{-\frac{a}{2}}^{\frac{a}{2}} \sin\frac{n\pi}{a}(x-\frac{a}{2})\sin\frac{m\pi}{a}(x-\frac{a}{2})dx \tag{3.91}$$

$$if\ m = n,\ C_{mn}^{\pm} = \frac{a}{2}.\ if m \neq n,\ C_{mn}^{\pm} = 0. \tag{3.92}$$

or

$$C_{mn}^{\pm} = \frac{a}{2}\delta_{mn} \tag{3.93}$$

Similarly

$$E_{mn}^{\pm} = \int_{-\frac{a}{2}}^{\frac{a}{2}} \overline{H}_1^{\pm}(x)\overline{H}_m^{+}(x)dx \tag{3.94}$$

$$= \pm\frac{1}{\overline{z}_m\overline{z}_n}\int_{-\frac{a}{2}}^{\frac{a}{2}} \overline{E}_1^{\pm}(x)\overline{E}_m^{+}(x)dx = \pm\frac{1}{(\overline{Z}_m)^2}\frac{a}{2}\delta_{mn}, \tag{3.95}$$

where

$$\overline{Z}_m = \frac{\omega\mu_o}{\overline{\beta}_n}. \tag{3.96}$$

Next, $D^{\pm}_{mn}$ can be expressed as

$$\begin{aligned} D^{\pm}_{mn} &= \int_{-\frac{a}{2}}^{\frac{a}{2}} E^{\pm}_n(x)\overline{E}^{+}_m(x)dx \\ &= \int_{-\frac{a}{2}}^{-\frac{d}{2}+s} U^{\pm}\sin\overline{k}_{cm}(x-\frac{a}{2})\,\frac{\sin k_c^{II}(x+\frac{a}{2})}{\cos k_c^{II}\frac{a-d+2s}{2}}dx \\ &+ \int_{-\frac{d}{2}+s}^{\frac{d}{2}+s} \sin\overline{k}_{cm}(x-\frac{a}{2})\left(\frac{\sin k_c x}{\cos k_c\frac{d}{2}} - G^{\pm}\frac{\cos k_c x}{\cos k_c\frac{d}{2}}\right)dx \\ &+ \int_{\frac{d}{2}+s}^{\frac{a}{2}} W^{\pm}\sin\overline{k}_{cm}(x-\frac{a}{2})\,\frac{\sin k_c^{II}(x-\frac{a}{2})}{\cos k_c^{II}\frac{a-d-2s}{2}}dx. \end{aligned} \tag{3.97}$$

This can be rewritten as

$$D^{\pm}_{mn} = \frac{U^{\pm}_n}{\cos k_c^{III}\frac{a-d+2s}{2}}I^A_{mn} + \frac{1}{\cos k_{cn}\frac{d}{2}}I^B_{mn} + \frac{G^{\pm}_n}{\cos k_{cn}\frac{d}{2}}I^C_{mn} + \frac{W^{\pm}_n}{\cos k_c^{II}\frac{a-d-2s}{2}}I^D_{mn}, \tag{3.98}$$

and each of the coefficients I_{mn} can be obtained by calculating the corresponding integrals.

Here

$$I^A_{mn} = \int_{-\frac{a}{2}}^{-\frac{d}{2}+s} \sin\overline{k}_{cm}(x-\frac{a}{2})\sin k^{III}_c(x+\frac{a}{2})dx$$

$$= \int_0^{\frac{a-d}{2}+s} \sin\overline{k}_{cm}(u-a)\sin k^{III}_c u du$$

$$= \frac{1}{2}(-1)^m\left[\frac{\sin(\overline{k}_{cm}-k^{III}_c)\frac{a-d+2s}{2}}{\overline{k}_{cm}-k^{III}_c} - \frac{\sin(\overline{k}_{cm}+k^{III}_c)\frac{a-d+2s}{2}}{\overline{k}_{cm}+k^{III}_c}\right] \tag{3.99}$$

$$I^B_{mn} = \int_{-\frac{d}{2}+s}^{\frac{d}{2}+s} \sin\overline{k}_{cm}(x-\frac{a}{2})\sin k_{cn}x dx$$

$$= \frac{\sin[\frac{ak_{cm}}{2}-(\overline{k}_{cm}+k_{cn})(s+\frac{d}{2})]}{2(\overline{k}_{cm}+k_{cn})} - \frac{\sin\left[\frac{ak_{cm}}{2}+(k_{cn}-\overline{k}_{cm})(s+\frac{d}{2})\right]}{2(\overline{k}_{cm}-k_{cn})}$$

$$-\frac{\sin[\frac{ak_{cm}}{2}-(\overline{k}_{cm}+k_{cn})(s-\frac{d}{2})]}{2(\overline{k}_{cm}+k_{cn})} + \frac{\sin\left[\frac{ak_{cm}}{2}+(k_{cn}-\overline{k}_{cm})(s-\frac{d}{2})\right]}{2(\overline{k}_{cm}-k_{cn})} \tag{3.100}$$

$$I^C_{mn} = \int_{-\frac{d}{2}+s}^{\frac{d}{2}+s} \sin\overline{k}_{cm}(x-\frac{a}{2})\cos k_{cn}x dx$$

$$= -\frac{\cos[\frac{ak_{cm}}{2}+(k_{cn}-\overline{k}_{cm})(s+\frac{d}{2})]}{2(\overline{k}_{cm}-k_{cn})} - \frac{\cos\left[\frac{ak_{cm}}{2}-(k_{cn}+\overline{k}_{cm})(s+\frac{d}{2})\right]}{2(\overline{k}_{cm}+k_{cn})}$$

$$+\frac{\cos[\frac{ak_{cm}}{2}+(k_{cn}-\overline{k}_{cm})(s-\frac{d}{2})]}{2(\overline{k}_{cm}-k_{cn})} + \frac{\cos\left[\frac{ak_{cm}}{2}-(k_{cn}+\overline{k}_{cm})(s-\frac{d}{2})\right]}{2(\overline{k}_{cm}+k_{cn})} \tag{3.101}$$

$$I^D_{mn} = \int_{\frac{d}{2}+s}^{\frac{a}{2}} \sin\overline{k}_{cm}(x-\frac{a}{2})\sin k^{II}_c(x-+\frac{a}{2})dx$$

$$= \int_0^{\frac{a-d}{2}-s} \sin\overline{k}_{cm}(u-a)\sin k^{II}_c u du$$

$$= \frac{1}{2}\left[\frac{\sin(\overline{k}_{cm}-k^{II}_c)\frac{a-d-2s}{2}}{\overline{k}_{cm}-k^{II}_c} - \frac{\sin(\overline{k}_{cm}+k^{II}_c)\frac{a-d-2s}{2}}{\overline{k}_{cm}+k^{II}_c}\right]. \tag{3.102}$$

Similarly, $F_{mn}^{\pm}$ can be expressed as

$$F_{mn}^{\pm} = \frac{\pm U_n^{\pm}\frac{\beta_n}{\omega\mu_o}}{\cos k_c^{III}\frac{a-d+2s}{2}}\frac{I_{mn}^A}{\overline{z}_m} + \frac{\delta/\omega}{\delta^2-\mu^2}\frac{k_c G^{\pm} \mp \frac{\beta_n\mu}{\delta}}{\cos k_c\frac{d}{2}}\frac{I_{mn}^B}{\overline{z}_m} + \frac{\delta/\omega}{\delta^2-\mu^2}\frac{k_c \pm G^{\pm}\frac{\beta_n\mu}{\delta}}{\cos k_c\frac{d}{2}}\frac{I_{mn}^C}{\overline{z}_m} + \frac{\pm W_n^{\pm}\frac{\beta_n}{\omega\mu_o}}{\cos k_c^{III}\frac{a-d-2s}{2}}\frac{I_{mn}^D}{\overline{z}_m}, \tag{3.103}$$

where all the coefficients I_{mn}^A, I_{mn}^B, I_{mn}^C and I_{mn}^D are the same as those in the D_{mn} case.

When the material is placed at the center of the waveguide, where s=0, the expressions of the integrals can be further simplified into,

$$\begin{aligned} I_{mn}^A &= \int_{-\frac{a}{2}}^{-\frac{d}{2}} \sin\overline{k}_{cm}(x-\frac{a}{2})\sin k_c^{III}(x+\frac{a}{2})dx \\ &= \int_0^{\frac{a-d}{2}} \sin\overline{k}_{cm}(u-a)\sin k_c^{III}u du \\ &= \frac{1}{2}(-1)^m\left[\frac{\sin(\overline{k}_{cm}-k_c^{III})\frac{a-d}{2}}{\overline{k}_{cm}-k_c^{III}} - \frac{\sin(\overline{k}_{cm}+k_c^{III})\frac{a-d}{2}}{\overline{k}_{cm}+k_c^{III}}\right] \end{aligned} \tag{3.104}$$

$$\begin{aligned} I_{mn}^B &= \int_{-\frac{d}{2}}^{\frac{d}{2}} \sin\overline{k}_{cm}(x-\frac{a}{2})\sin k_{cn}x dx \\ &= \cos\frac{m\pi}{2}\left[\frac{\sin[(\overline{k}_{cm}+k_{cn})\frac{d}{2}]}{(\overline{k}_{cm}-k_{cn})} - \frac{\sin(k_{cn}+\overline{k}_{cm})\frac{d}{2}}{(\overline{k}_{cm}+k_{cn})}\right] \end{aligned} \tag{3.105}$$

$$\begin{aligned} I_{mn}^C &= \int_{-\frac{d}{2}}^{\frac{d}{2}} \sin\overline{k}_{cm}(x-\frac{a}{2})\cos k_{cn}x dx \\ &= -\sin\frac{m\pi}{2}\left[\frac{\sin[(\overline{k}_{cm}-k_{cn})\frac{d}{2}]}{(\overline{k}_{cm}-k_{cn})} + \frac{\sin(k_{cn}+\overline{k}_{cm})\frac{d}{2}}{(\overline{k}_{cm}+k_{cn})}\right] \end{aligned} \tag{3.106}$$

$$\begin{aligned} I_{mn}^D &= \int_{\frac{d}{2}}^{\frac{a}{2}} \sin\overline{k}_{cm}(x-\frac{a}{2})\sin k_c^{II}(x-+\frac{a}{2})dx \\ &= \int_0^{\frac{a-d}{2}} \sin\overline{k}_{cm}(u-a)\sin k_c^{II}u du \\ &= \frac{1}{2}\left[\frac{\sin(\overline{k}_{cm}-k_c^{II})\frac{a-d}{2}}{\overline{k}_{cm}-k_c^{II}} - \frac{\sin(\overline{k}_{cm}+k_c^{II})\frac{a-d}{2}}{\overline{k}_{cm}+k_c^{II}}\right]. \end{aligned} \tag{3.107}$$

It is very important to mention that since the propagation constant (β) is different along the two propagating directions when $s \neq 0$, appropriate β values should be used to calculate the matrix entries. For instance, to compute the entries of D^- and $e_N D^+$, the β determined for +z direction should be used to compute D^-, while the β value for the $-$z direction should be used to compute both e_N and D^+. However, for the special case where the sample is centered, it is not necessary to follow this rule since both values of β for the two propagating directions for any mode are the same.

3.2.5 Validation of Theoretical Analysis

Since HFSS does not support assigning permeability tensors of a material with off-diagonal terms, an in-house FEM code wrote by Dr. Tuncer was used as an alternative method to validate the mode matching technique. For a fictitious gyromagnetic sample of d=1.4 inches wide and Δ=0.4 inches thick, with ϵ_r=14.7, $4\pi M_s$=1000 G, H_O=900 Oe and linewidth ΔH=0, this sample is simulated within a L-band (1.12-1.7 GHz) waveguide with the sample positioned at the center of the guide. To obtain a convergence to the third decimal place, the number of unknowns or meshing elements used in the FEM code is 60000. The number of modes used in the mode matching technique is chosen 20 and to achieve an accuracy of 0.1$\circ$ in phase and 0.01 dB in magnitude. The calculated S-parameters are compared in Figure 3.28 and 3.29. Similarly, the same fictitious sample is simulated within a S-band (2.6-3.95 GHz) waveguide with a shift s=1 inch and H_O=2800 Oe. The calculated S-parameters are shown in Figure **??** and **??**. Good agreement is achieved between the two methods, which validate the proposed mode matching technique.

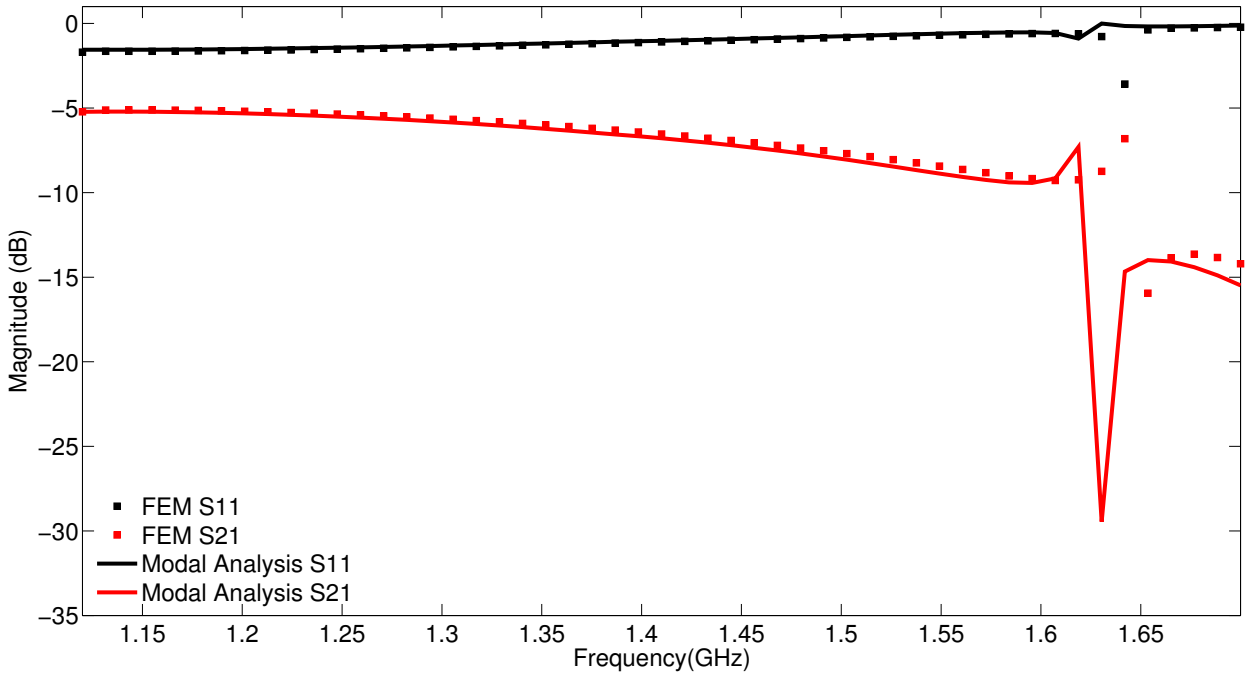

Figure 3.26 Magnitude of the S-parameters simulated using proposed mode-matching technique and FEM method under L-band (sample centered).

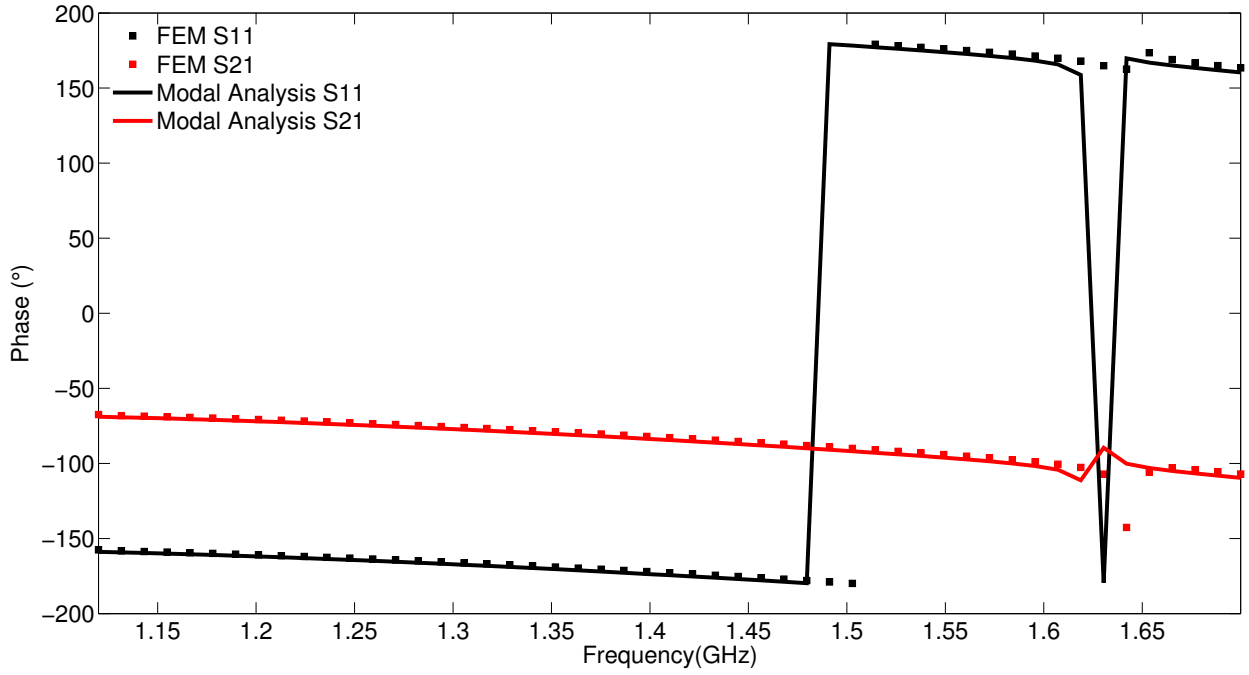

Figure 3.27 Phase of the S-parameters simulated using proposed mode-matching technique and FEM method under L-band (sample centered).

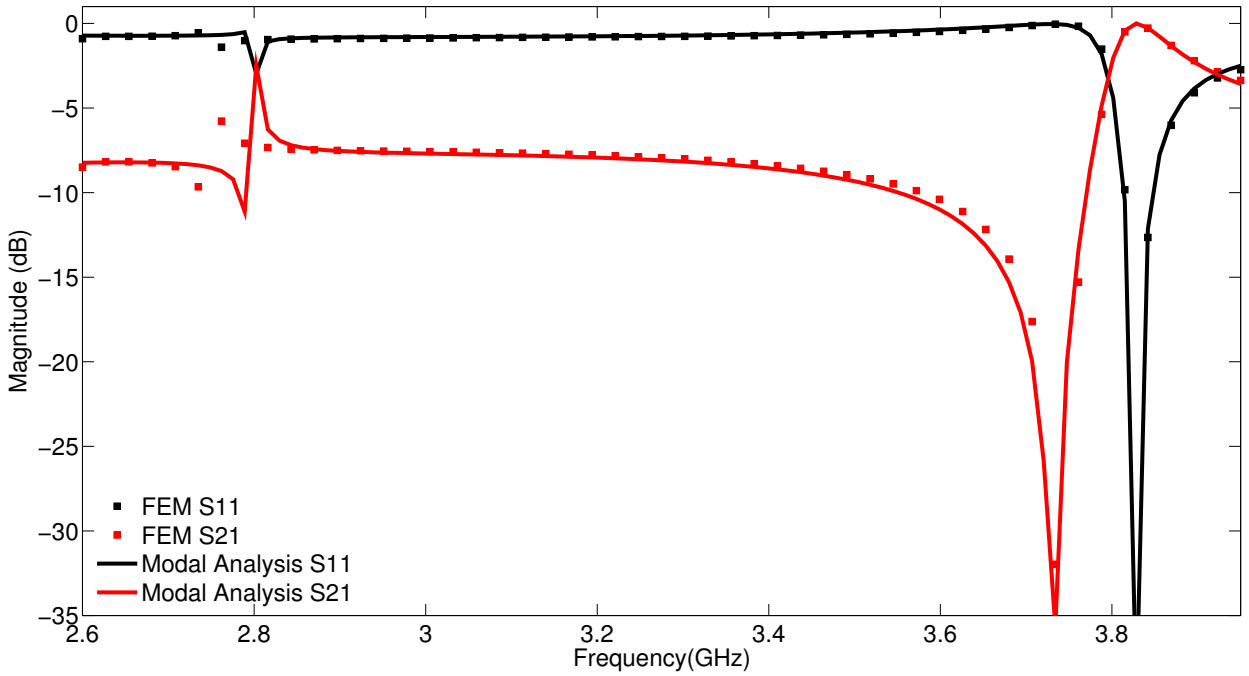

Figure 3.28 Magnitude of the S-parameters simulated using proposed mode-matching technique and FEM method under S-band (1 inch shift).

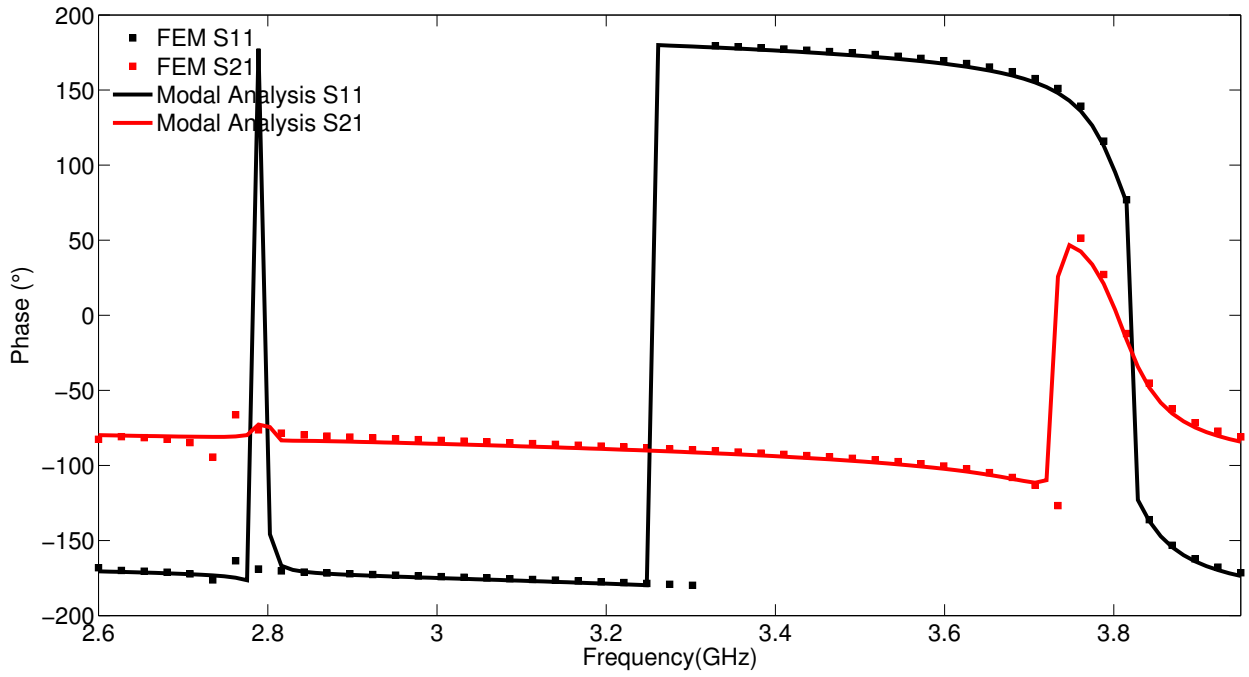

Figure 3.29 Phase of the S-parameters simulated using proposed mode-matching technique and FEM method under S-band (1 inch shift).

3.3 Summary

A mode matching technique is developed for computing the S-parameters of gyromagnetic materials partially filling a rectangular waveguide. This method can be adopted to develop an extraction process which eliminates the need for a large sample required by standard waveguide techniques in which a sample completely fills the rectangular waveguide cross section. The mode matching technique is validated using an in-house FEM code and a special case where the material is placed at the center is also discussed and analyzed. An inverse problem which extracts the material parameters from measured or theoretical S-parameters is introduced in the following chapter.

CHAPTER 4

Extraction Process for Gyromagnetic Material Properties Using a Partially-Filled Waveguide Technique

4.1 Introduction

This chapter presents a method for characterizing gyromagnetic materials using two complex measurements (S_{11} and S_{21}). The material parameters are obtained through a nonlinear least square method that minimizes the difference between the measured and the theoretical reflection and transmission coefficients. This procedure is implemented by utilizing optimization algorithms in Matlab. The adopted optimization algorithms in Matlab are described, and an error analysis using these optimization algorithms with different sample configurations is considered to show that the proposed characterization technique is very robust to measurement error. In addition, an extraction process which employs a series of measured S-parameters under different magnetic biasing fields to extract a single set of material parameters is introduced.

4.2 Least Square Method for Extraction

The three complex constitutive parameters (μ_g, κ, and ϵ_r) describing a gyromagnetic material can be extracted using a frequency by frequency characterization. However, since each measurement contains only two complex measured quantities (S_{11} and S_{21}), this results in an underdetermined system. Alternatively, based on the fact that the value of ϵ_r'' of the gyromagnetic samples of interest is typically very small, a frequency by frequency characterization of four real physical parameters ($4\pi M_s$, H_0, ΔH, and ϵ_r') can be achieved by using four real measurements ($S_{11,r}$, $S_{11,i}$, $S_{21,r}$ and $S_{21,i}$). In this work, the extraction process is considered to be frequency-independent since three of the physical parameters $4\pi M_s$, H_0, and ΔH are frequency-independent, and the permittivity varies little over the measurement band. Therefore, the frequency-independent assumption is sufficient for accurate characterization. A nonlinear least-square inversion method is adopted to extract the frequency-independent parameters using measured and theoretical values of S_{11} and S_{21} at a number of frequencies.

The root squared error between theoretical and measured S-parameters is given as

$$Error = \sqrt{\sum_{j=1}^{N_f} \left[\left| S_{11,r}^{meas}(f_j) - S_{11,r}^{thy}(f_j) \right|^2 + \left| S_{11,i}^{meas}(f_j) - S_{11,i}^{thy}(f_j) \right|^2 \right]} + \sqrt{\sum_{j=1}^{N_f} \left[\left| S_{21,r}^{meas}(f_j) - S_{21,r}^{thy}(f_j) \right|^2 + \left| S_{21,i}^{meas}(f_j) - S_{21,i}^{thy}(f_j) \right|^2 \right]}, \tag{4.1}$$

where S^{thy} are the theoretical S-parameters, and S^{meas} are the measured (or simulated) data, f_j is the j^{th} frequency point, and r and i denote the real and imaginary parts of the S-parameters, respectively. Due to the complexity of the inverse problem that requires extraction of multiple parameters, traditional methods such as Newton's method often have

difficulty finding the global minimum. Matlab provides a variety of multi-variables optimization algorithms which are easy to implement. Therefore, in this work, optimization algorithms included in the Matlab optimization tool box are utilized to find accurate approximations of the target material parameters.

4.2.1 Extraction Process Using Matlab Optimization Algorithms

To test the feasibility of the extraction method, theoretical S-parameters are used as a substitute for measured S-parameters. By reducing the root squared error to zero, the extracted parameters should match the parameters used to generate the theoretical S-parameters exactly. At the present, the inversion procedure does not consider characterization of ΔH, since the theoretical implementation assumes lossless permeability. Therefore, a method that can accurately find the three physical parameters ($4\pi M_S$, H_0,and ϵ_r') is sought.

In this work, the extraction procedure is based on the integration of the compiled forward problem with the optimization solvers included in the Matlab optimization toolbox. The optimization toolbox provides solvers for finding parameters that minimize or maximize objective functions which can either contain a single variable or multiple variables. The toolbox includes various solvers such as linear programming, quadratic programming, nonlinear optimization, and multi-objective optimization, that can offer different domain searching algorithms for a variety of problems which can be either continuous or discrete, and constrained or unconstrained. As a result, the solution of an inverse problem can be obtained by choosing an appropriate solver.

To solve the inverse problem which requires minimizing the root squared error shown in (4.4), the behavior of the problem must be investigated so that proper searching algorithms can be chosen for extracting the three parameters. One way to achieve this is to plot the root squared error against different material parameters. Due to the number of the variables involved, which makes it difficult to graphically demonstrate the relationship between the error and all of the parameters simultaneously, the errors are compared with two variables at

a time so that a 3-D surface plot can be used. The theoretical S-parameters of a gyromagnetic sample with $4\pi M_S = 1000$ G, $H_0 = 3000$ Oe, and $\epsilon_r' = 14.7$ were generated and substituted for the measured S-parameters. Figure 4.1 shows the error as a function of $4\pi M_S$ and ϵ_r' when H_0 is set to 3000 G. It can be seen that the surface plot forms a valley where the bottom dark regions represent small error between the measured data and theoretical data. Figure 4.2 shows the same surface plot of the errors but rotated at a different angle. It is noticed that a minimum can be achieved for a $4\pi M_S$ value of around 1000 and an ϵ_r' of 14.7 where the total error is expected to be zero. Similar behavior can be noticed for the errors corresponding to different H_0 and ϵ_r' in Figures 4.3 and 4.4. A minimum can also be be seen at the bottom of the valley where the variables reach the values used to generate the "measured" S-parameters. Several local minima can be seen around the global minimum which emphasizes the need for an solver to find the global minimum in a short period of time.

The Matlab version used for solving the inverse problem was version 7.14/R2012a, which operates under a Windows 64-bit environment. The optimization toolbox included in this release is version 6.2. A new release of the toolbox can be installed to obtain an enhancement of the optimization solvers or to obtain more solvers. However, this version of the toolbox is sufficient for users to take advantage of multiple solvers for different optimization problems. Though the use of this toolbox will be discussed in this section, it is still highly recommended for users to read the description of the optimization toolbox in the help menu before proceeding to actual problems.

There are two ways to access to the optimization toolbox. One is to use the commands in the Matlab prompt directly where the options can be set through different commands, while the other is to use the graphical user interface (GUI) with which one can have access to all the information and resources in a single page. To activate the toolbox, one can either type `optimtool` in the command window or open it from the directory "**Start - Toolboxes - Optimization - Optimization Tools**" at the main user interface. In this section, the

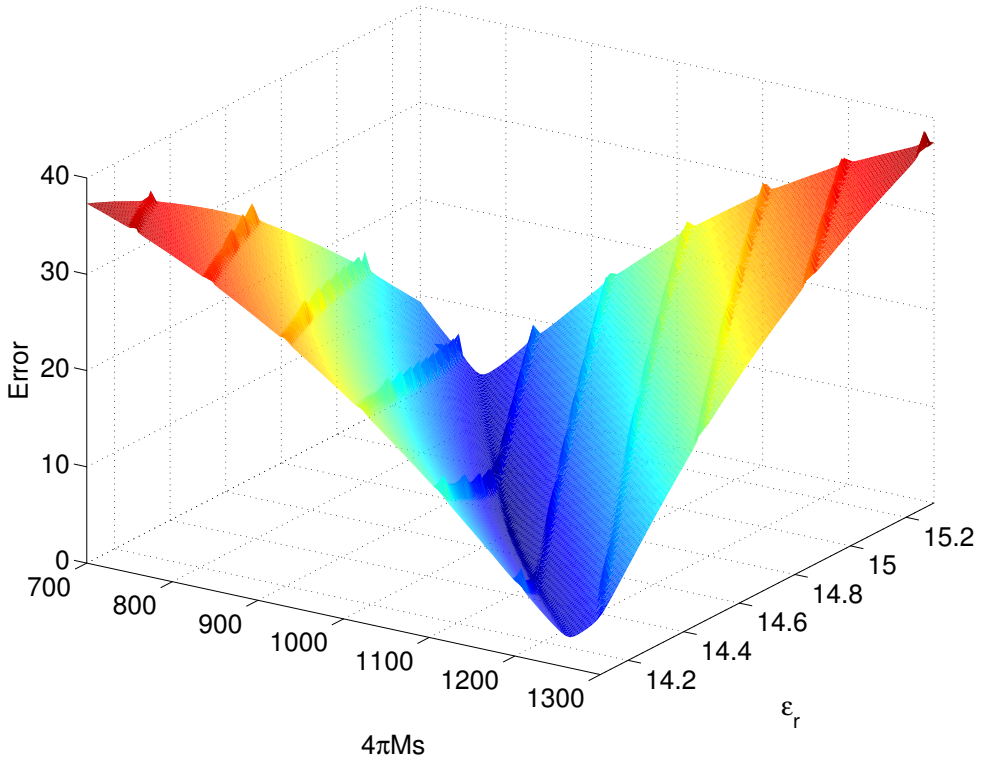

Figure 4.1 3-D surface plot of the root squared error for different $4\pi M_s$ and ϵ_r' with H_0 set to 3000 gauss.

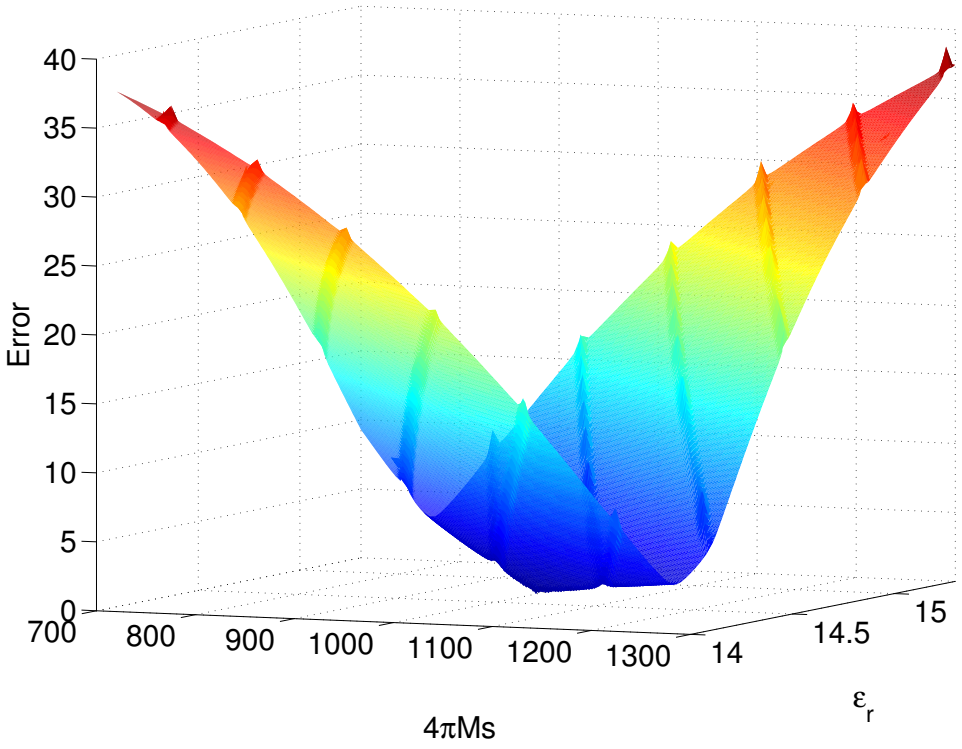

Figure 4.2 3-D surface plot of the root squared error for different $4\pi M_s$ and ϵ_r' with H_0 set to 3000 gauss.

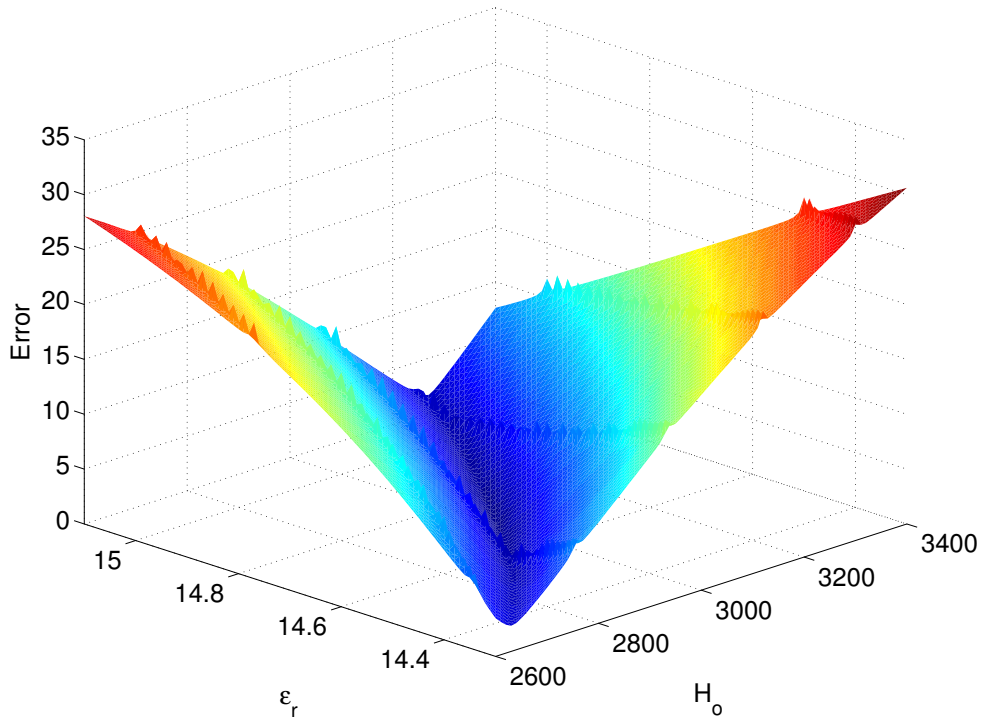

Figure 4.3 3-D surface plot of the root squared error for different H_0 and ϵ_r' with $4\pi M_s$ set to 1000 gauss.

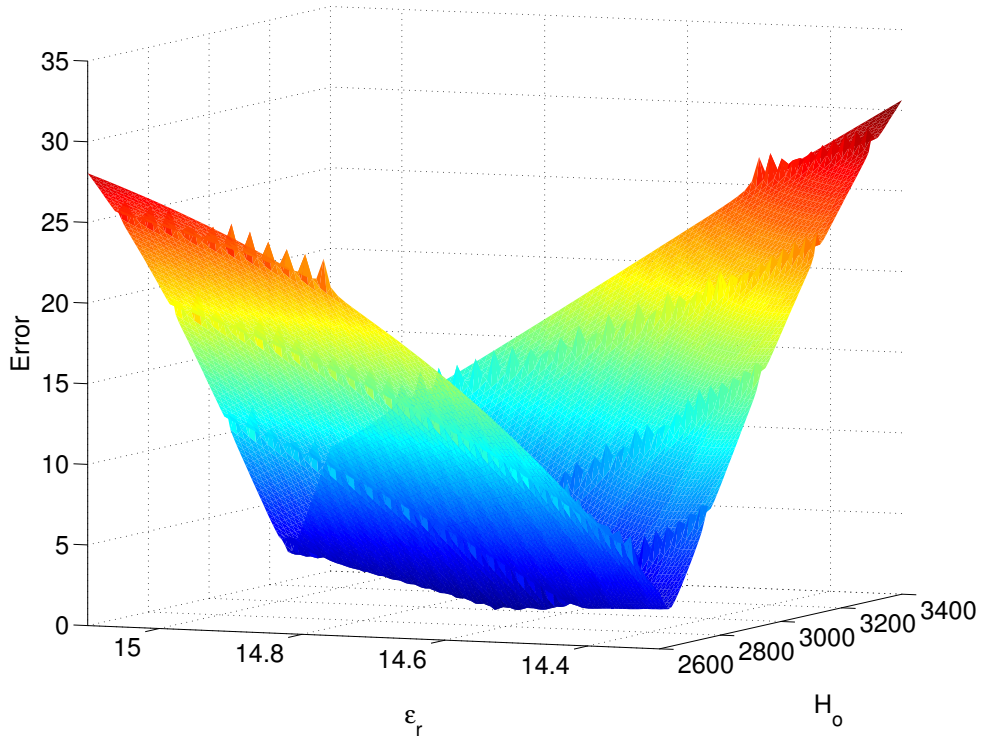

Figure 4.4 3-D surface plot of the root squared error for different H_0 and ϵ_r' with $4\pi M_s$ set to 1000 gauss.

access to the toolbox is implemented through the GUI where the settings can be seen and modified easily. The use of built-in commands will be discussed in the following sections.

The use of the appropriate solver must be ensured to eliminate the possibility of finding local minimum. Additionally, the computational cost should be considered for those solvers that satisfy the goal. For this problem, as was previously shown in the 3D surface plot, the goal is to minimize the root squared error which demonstrates a nonlinear relationship with three variables. Many algorithms are able to optimize for a nonlinear problem, such as genetic algorithm (GA) which is very useful for problems that are highly nonlinear, pattern search (PS) algorithms that find local minima using pattern searches, and simulated annealing (SA) which periodically reset the searching radius to find the global minimum. There are other algorithms for nonlinear problems in which constraints can be defined or excluded. Common unconstrained algorithms in Matlab are `fminunc` and `fminsearch`, while the constrained options are `fmincon, fminbnd` and `fseminf`. Note that most optimization solvers are only local solvers, and different solvers take different time durations to find the solutions. An accurate solver that can reduce the process time significantly is preferred. Studies [51] have been done to compare the time cost of each algorithm to find the solution for Rastrigin's function with default settings. It has been shown that the nonlinear algorithms `fminsearch` and `fmincon` tend to cost less time to find the solution than PS, SA and GA. Among all the solvers mentioned above, GA has been found to be the least efficient costing the most amount of time and iterations. To test the performance of different solvers, the measured S-parameters were substituted in for the theoretical ones, it was found out that either `fminsearch` or `fmincon` was able to find the solution in a short period of time. In this problem which uses theoretical S-parameters as the measured data, the `fminsearch` was used as an unconstrained solver to demonstrate that the solution can be found quickly for an unbounded region even with poor initial guesses. The `fminsearch` function finds the minimum of a unconstrained scalar function with multiple variables based on the Nelder-Mead method. The Nelder-Mead method is a technique for minimizing a multi-dimensional

objective function for which derivatives may not be known. The method uses the idea of forming $N+1$ vertices in N dimensions to approximate a local optimum with an assumption that the function varies smoothly. In this problem, since there are three variables, a tetrahedron in three-dimensional space will be used to find the local optimum. Results found using this solver are described in the following section.

4.2.2 Validation of the Extraction Using Matlab Optimization Functions

To implement the inverse problem, the GUI of the optimization tool is initialized by following the initializing steps mentioned previously. There are three panels displayed in the toolbox GUI. The first panel is the problem setup and results panel which is shown in Figure 4.5. One can call any of the solvers in the toolbox and assign constraints for the objective function. The second panel shown in Figure 4.6 is the options panel where the control parameters such as tolerances can be set for the algorithm. The third one is the quick reference panel that allows users access to help documents and examples using the chosen algorithm. This panel is not displayed in this section.

To initialize the optimization for the inverse problem which minimize the difference between theoretical S-paramters and actual measured S-paramters, the `fminsearch` solver was selected. Two entries in the the problem setup and results panel were required to be specified. As can be seen from Figure 4.5 the first entry to be specified is the name of the objective function. In this case, the name of the function that computes the root squared error in (4.4) was entered with the "@" sign as a prefix. The second entry is the initial guess for the objective function. As was described previously, the selected solver is a local optimization algorithm with no constraints. Therefore, it is important to specify a reasonable initial guess so that a minimum can be found successfully. One of the initial guesses that was used to initialize the optimization was $[2800, 14.5, 1060]$ with the format of a vector. In the options panel, the stopping criteria were chosen to be the default, where the termination tolerance

for both the function value and variables is 10^{-4}. The function value was clicked in the plot function sub-panel to display the iterative function values. Also, the level of display is selected to be iterative in the display sub-panel. Once all the parameters were set up, the optimization could be launched by clicking the start button.

During the optimization procedure, the computed root squared error was plotted for each iteration. Once the the optimization is completed by reaching the stopping criteria, one is able to see that plot with the final results. The function values over different iterations with the initial guess mentioned earlier is shown in Figure 4.7. Notice that the error decreases as the number of iterations increases, and the computed error ends up as 2.8×10^{-8} which indicates that the difference between the theoretical S-parameters and measured S-parameters is insignificant. The final results for the three variables were displayed in the problem setup and results panel once the optimization was over. The returned results match the theoretical values for the three parameters to the fifth decimal place. Therefore, this solver has shown its ability to optimize this inverse problem.

As was stated earlier, a reasonable initial guess is required for local solvers, and different random initial guesses alter the optimization time and results, thus a test of the employed solver with different initial guesses was conducted to understand their impact on the results. Table 4.1 shows the number of iterations required to find the solution. The first column shows five different initial guesses used to start the optimization. It can be seen that different guesses lead to different numbers of iterations to complete the optimization, and generally a closer guess to the correct solution may reduce the number of iterations significantly. For instance, the cost in terms of iterations for a guess of $[3700, 15.2, 1230]$ is more than double that of the one with $[2800, 14.5, 1060]$, which implies the optimization time consumption can be dependent on the starting guess. Furthermore, varying the tolerances in the optimization option panel can also alter the number of iterations. It is obvious that the number of iterations reduced as the tolerances were changed from the default setting (10^{-4}) to 10^{-2}. An average of 22% in iteration reduction is achieved for these five trials. Therefore, increasing

the tolerances will speed up the optimization.

Table 4.1 Number of iterations for different initial guesses.

Initial Guess	Number of Iteration ($Tols$=10^{-4})	Number of Iteration ($Tols$=10^{-2})
$[2500, 14, 1260]$	261	148
$[2800, 14.5, 1060]$	154	133
$[2900, 14.9, 1030]$	227	165
$[3500, 13.6, 860]$	245	206
$[3700, 15.2, 1230]$	324	297

4.3 Error and Sensitivity Analysis

As is described in Section 2.4, a Monte Carlo technique was used to evaluate effects on the propagation of the random measurement error inherent to the VNA. Random measurement errors of the VNA can be attributed to many factors such as temperature or humidity of the operating environment. The uncertainties of the measured S-parameters from the VNA can be obtained from the manufacturer. Table 4.2 lists the S-parameter uncertainties for an HP8510C network analyzer system using the software package *HP 8510 Specifications & Performance Verification Program* and for an Agilent E5071C ENA using *Agilent E5071C ENA Network Analyzer Data Sheet* [52], which are the two VNA models used in the experiments. The value of the uncertainties for S_{21} are quantified by the manufacturer by performing a "through" measurement 32 times over the full frequency range of the VNA with a cable connected between two ports. Similarly, the uncertainties for S_{11} are obtained by performing a "short" measurement 32 times over the frequency span of the analyzer with the port terminated by a short. Standard deviation of the measured data at each frequency is then calculated and then converted into an uncertainty (noise) level in magnitude and phase. For the HP8510C, statistical variance of S_{11} is indicated linearly in amplitude and logarithmically in phase. Thus the uncertainty for S_{11} ($\sigma_{A_{11}}$) carries no units while all of the rest of the uncertainty levels contain units. It can be noticed that the E5071C demonstrates a

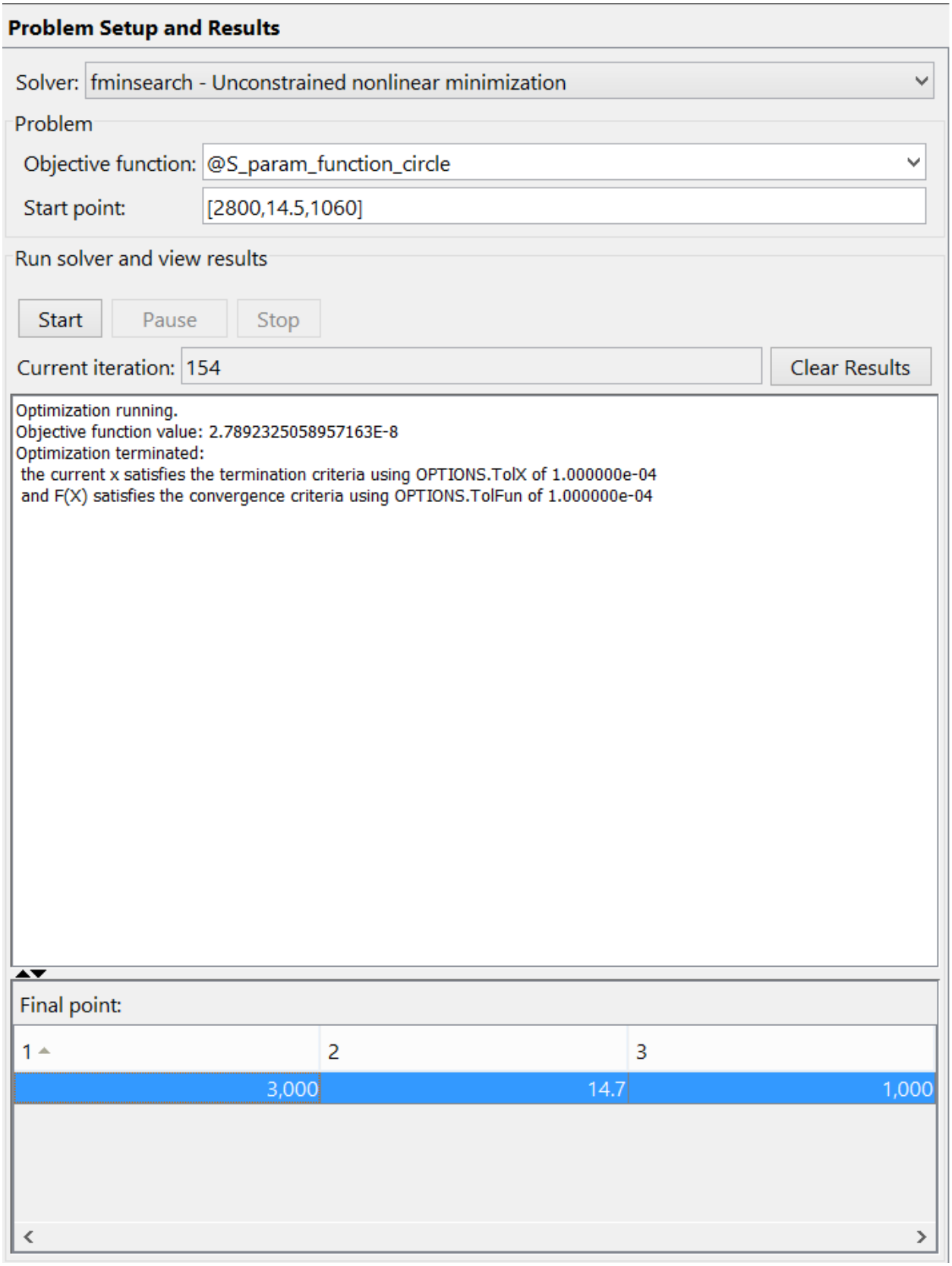

Figure 4.5 Problem setup and results panel of the optimization toolbox GUI.

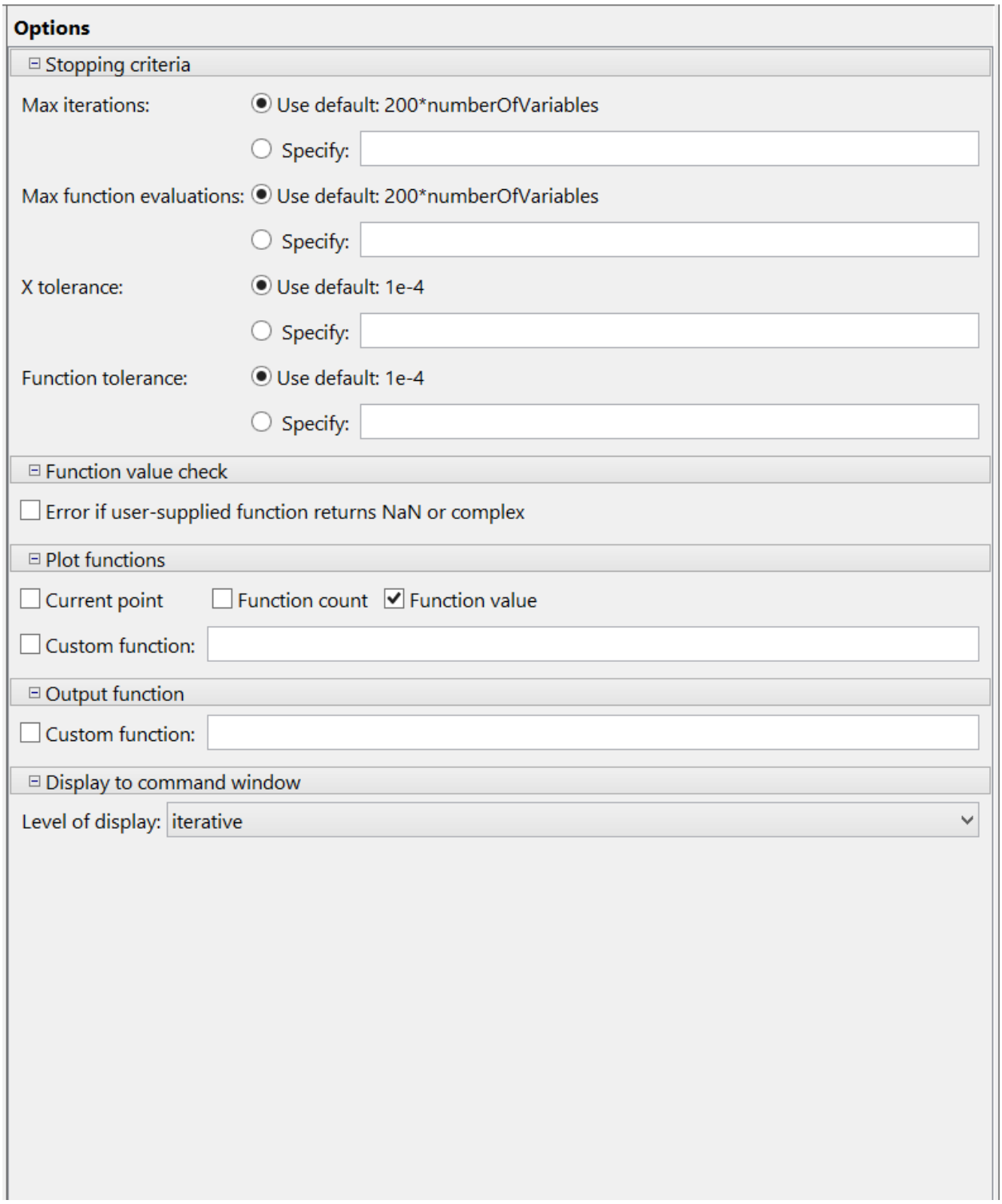

Figure 4.6 Option panel of the optimization toolbox GUI.

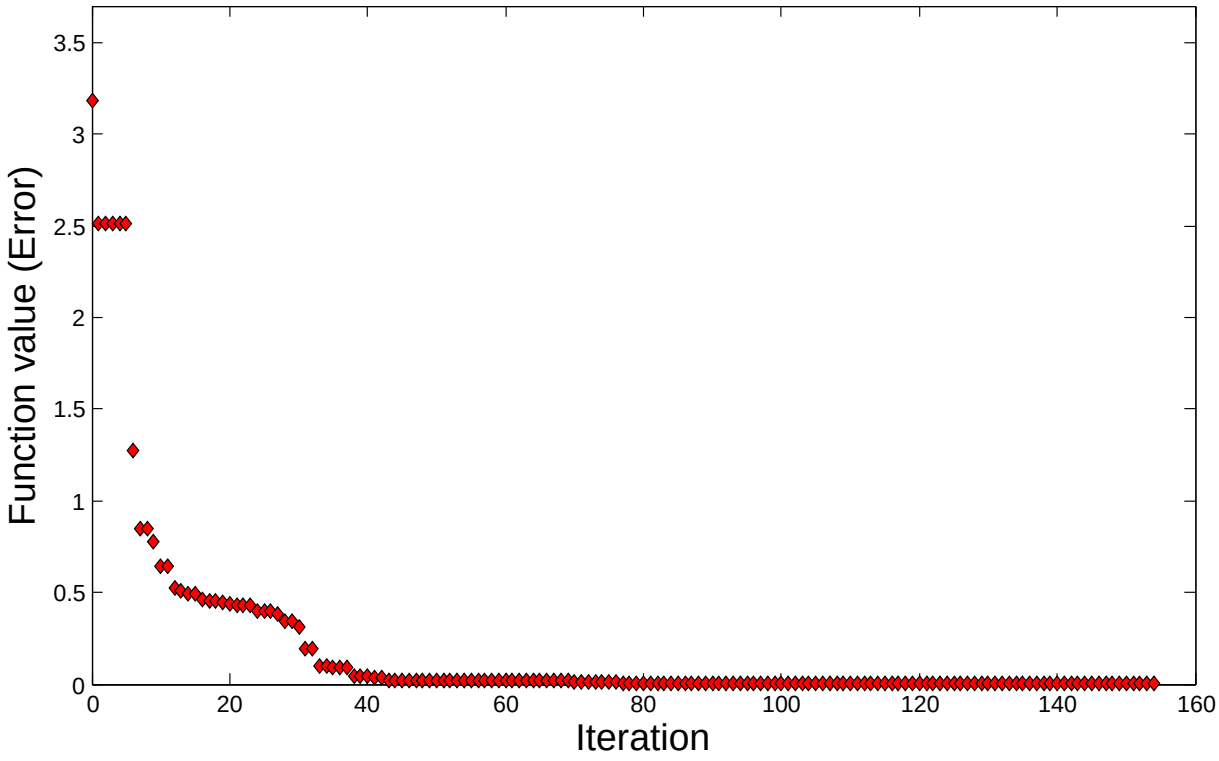

Figure 4.7 Iterative function values during one optimization.

much smaller uncertainty level than the HP8510C. However, to evaluate the impact of the possible maximum measurement error from VNA for extracted parameters, the uncertainty levels from HP8510C were used.

Table 4.2 VNA measurement uncertainties.

	HP8510C network analyzer	Agilent E5071C network analyzer
$\sigma_{A_{11}}$	0.004	0.004 dB
$\sigma_{\phi_{11}}$	0.8°	0.035°
$\sigma_{A_{21}}$	0.04 dB	0.003 dB
$\sigma_{\phi_{21}}$	2.0°	0.035°

The fictitious material described previously with $H_0 = 3000$ Oe, $\epsilon_r' = 14.7$, and $4\pi M_s = 1000$ G was used in the the Monte Carlo analysis of the propagation of VNA uncertainty. The test sample is assumed to have a width of $d = 34$ mm that is the same as the height of the S-band waveguide, and a thickness of 10 mm. The forward problem was computed

with 101 frequency points over the S-band from 2.6 to 3.95 GHz and 20 modes were used to achieve an accuracy of the magnitude less than 0.01 dB and an accuracy of the phase less than 0.1°. White gaussian noise was then added to each of the S-parameter sets, and the noisy data was used to extract the material parameters. The noise levels indicated by the *HP 8510 Specifications & Performance Verification Program* [53] were used. This procedure is described in Section 2.2.5. One hundred and sixty trials were implemented for this Monte Carlo analysis, and the average values of the material parameters using different number of trials were calculated, along with the standard deviations. Figures 4.8 - 4.10 show the extracted parameter values corresponding to different numbers of random trials that were used. The black dots are the average values of the trials and red dots show the average value plus or minus one standard deviation. In these figures, it can be seen that the difference between the average values and the fictitious material parameters are within 1% after a trial number of 110. The standard deviation for H_0 using 160 trials is 34 Oe which is equivalent to 1.1% relative error. Also, the standard deviations for ϵ_r' and $4\pi M_s$ are 0.01 and 15.2G, corresponding to relative errors of 0.7% and 1.5%, respectively. A similar analysis was performed for another test sample with a width of 54 mm and a same thickness of 10 mm. Figures 4.11 - 4.13 show the results of the analysis for a wider sample. It can be seen that the extracted parameters share the same trend of average values as the narrow sample. However, narrower error bars are observed which indicate a reduction in the sensitivity of the extracted parameters to measurement errors. Note that the noise level used in this error analysis is the maximum error that could be introduced into experiments, and the error in the extracted material parameters due to S-parameter noise is still relatively small. Therefore, this extraction technique has shown a robustness to VNA uncertainties.

Monte Carlo analysis of the uncertainties in sample widths were employed to evaluate the impact of inaccurately measured sample width on the extracted parameters. The uncertainty of the sample width was obtained from measuring the actual G1010 sample (Section 5.3.1.1) 20 times and the standard deviation of these measured results were calculated

(0.034 mm). The biasing magnetic field is $H_0 = 3000$ Oe, while the saturation magnetization is $4\pi M_s = 1000$ G. This H_0 results in a FMR occurring at 8.40 GHz. The forward problem was solved at 101 frequency points over the portion of S-band from 2.6 GHz to 3.95 GHz. With the S-parameters computed using altered sample widths, these data was used to extract the material parameters. Two hundred trials were used in the Monte Carlo analysis, and the average values of the material parameters and the standard deviations were calculated. Histograms of different extracted parameters are shown in Figure 4.14-4.16 to provide graphical representations of the distribution of the parameters. Figures 4.20-4.22 show the effects on the permittivity and the permeability characterization. Note that the differences between the theoretical values of G1010 used to generate the S-parameters employed in the Monte Carlo analysis and the average values are within 0.5%. Therefore, the theoretical values of G1010 are not plotted in these figures. Similar procedure was taken to evaluate the impact of inaccurately measured sample thickness on the extracted parameters. The meausured uncertainties of the sample thickness is 0.005 mm. Histograms of different extracted parameters are shown in Figure 4.17-4.19. Figures 4.23-4.25 show the effects on the permittivity and the permeability characterization.

4.4 Extraction of Measured S-parameters

As was shown in the previous section, the `fminsearch` solver was tested to show its capability of finding the correct parameters by using a fictitious material. However, a constrained guess region may be required for processing the measured data not only because accurate initial guesses are usually unavailable before measuring an actual gyromagnetic sample, but also to reduce the optimization time. In this section, three sets of measured data for the same material biased under different external magnetic fields are used to demonstrate the extraction process using measured S-parameters using Matlab optimization function. The details of the measurement procedures are included in the next chapter, and this section only

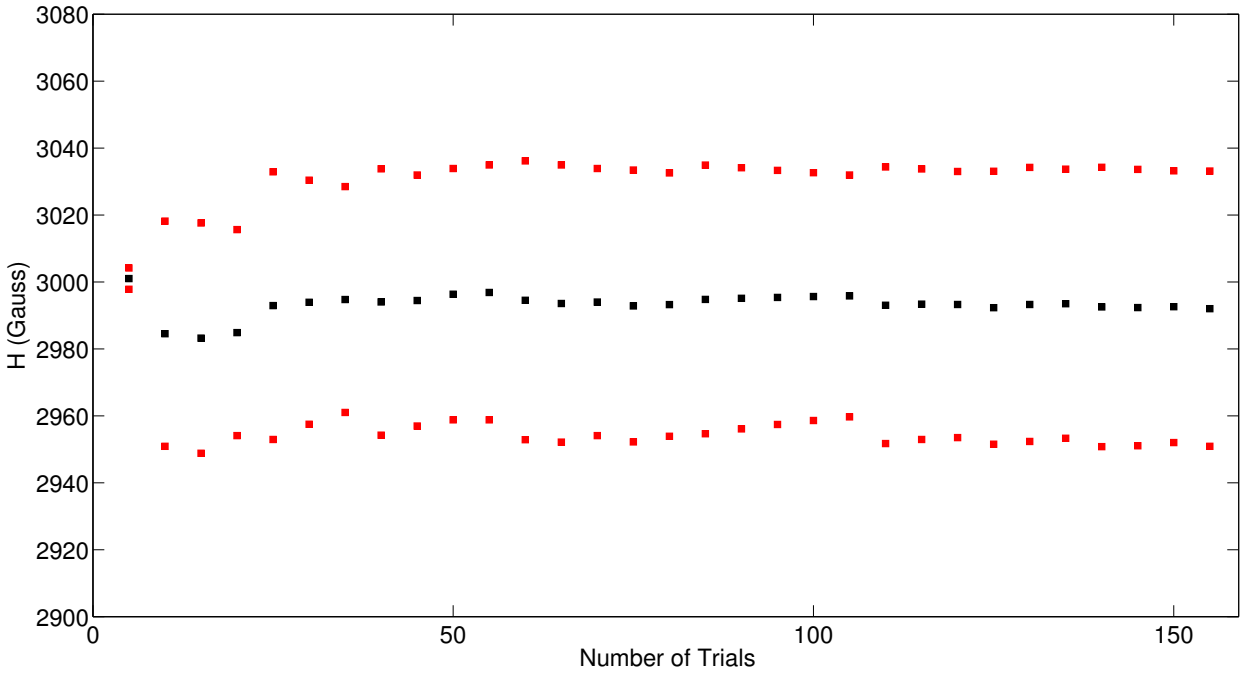

Figure 4.8 Extracted H_0 for a test sample of width d=34 mm under different number of trials. The center dots are the average of the trials. Upper and lower dots show one standard deviation.

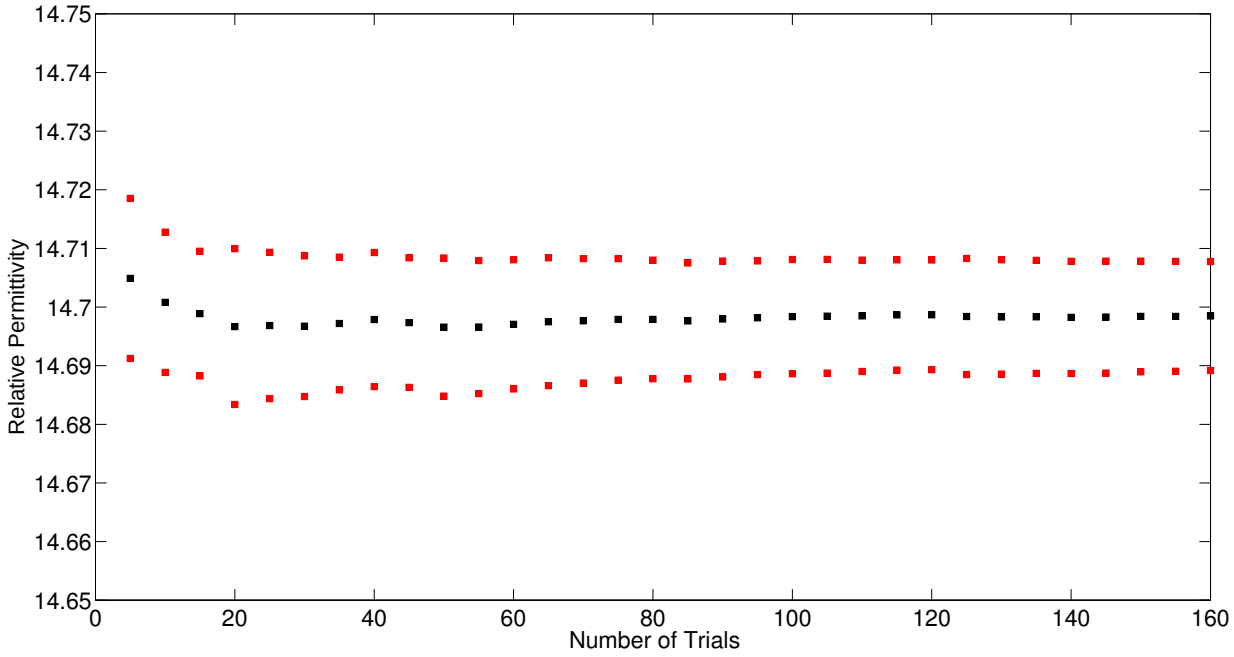

Figure 4.9 Extracted ϵ_r' for a test sample of width d=34 mm under different number of trials. The center dots are the average of the trials. Upper and lower dots show one standard deviation.

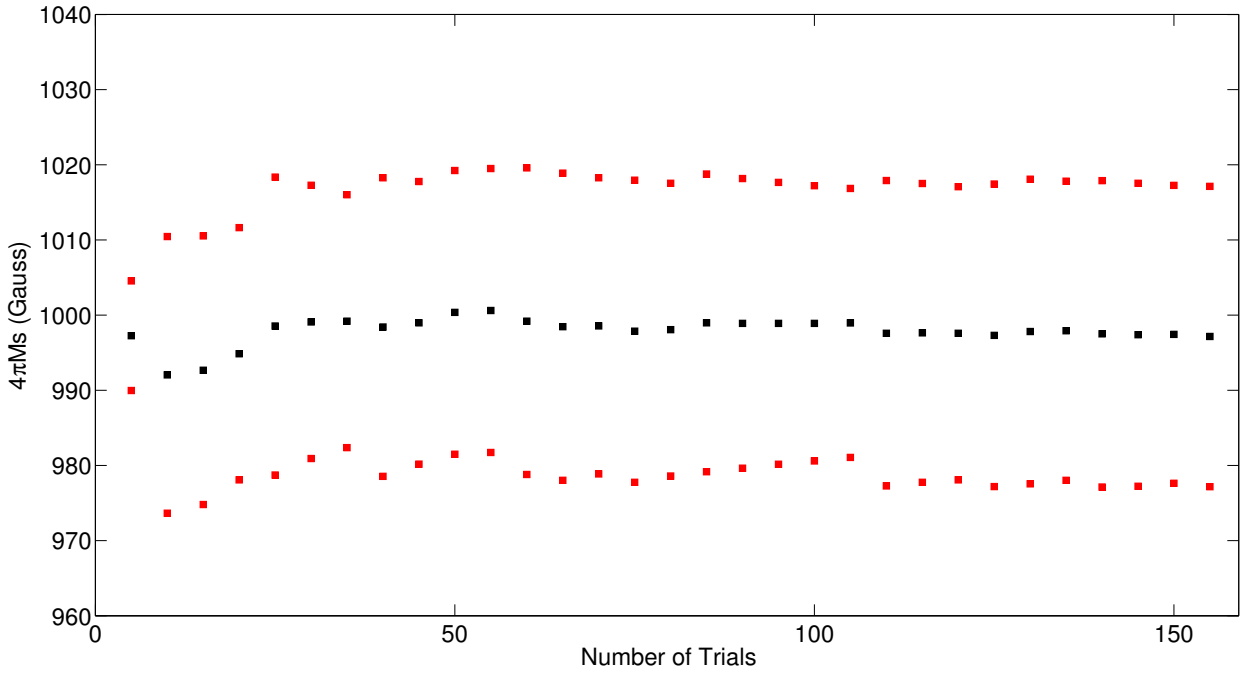

Figure 4.10 Extracted $4\pi M_s$ for a test sample of width d=34 mm under different number of trials. The center dots are the average of the trials. Upper and lower dots show one standard deviation.

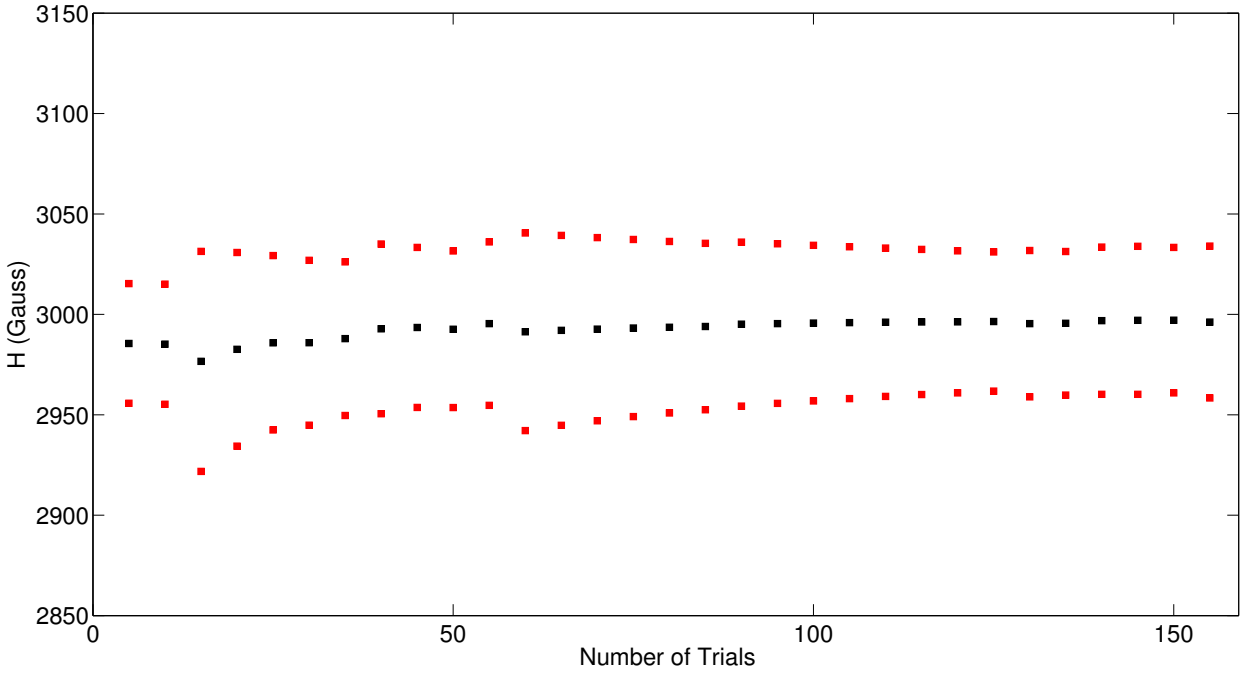

Figure 4.11 Extracted H_0 for a test sample of width d=54 mm under different number of trials. The center dots are the average of the trials. Upper and lower dots show one standard deviation.

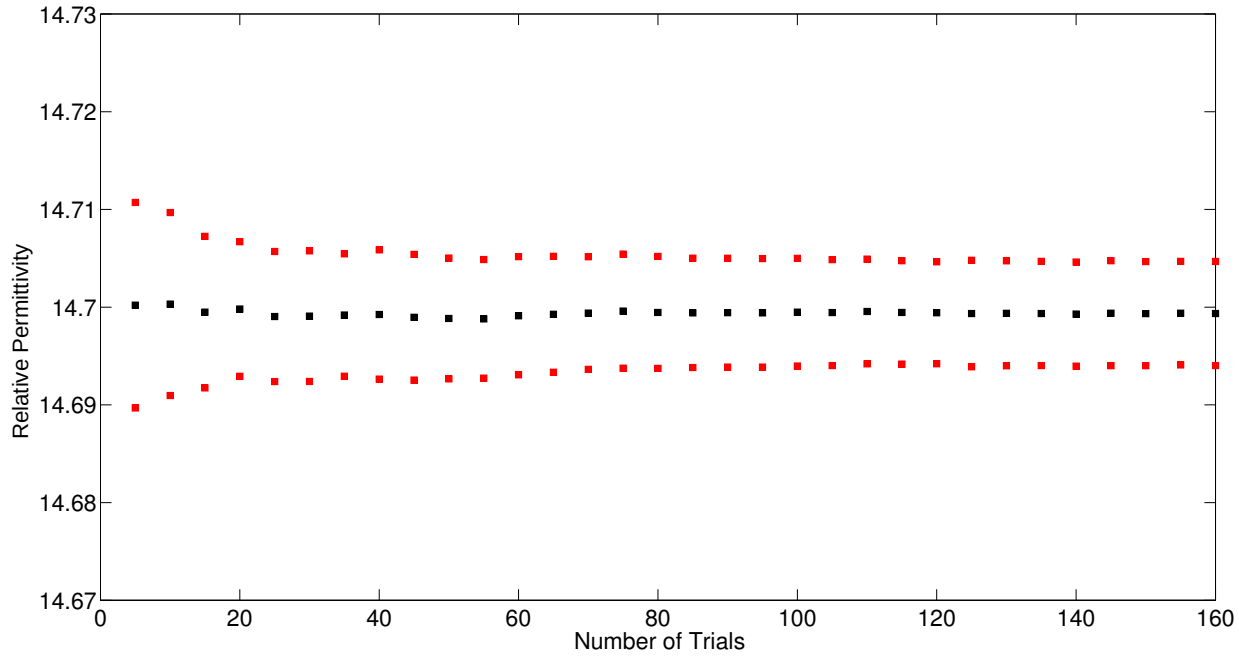

Figure 4.12 Extracted ϵ_r' for a test sample of width d=54 mm under different number of trials. The center dots are the average of the trials. Upper and lower dots show one standard deviation.

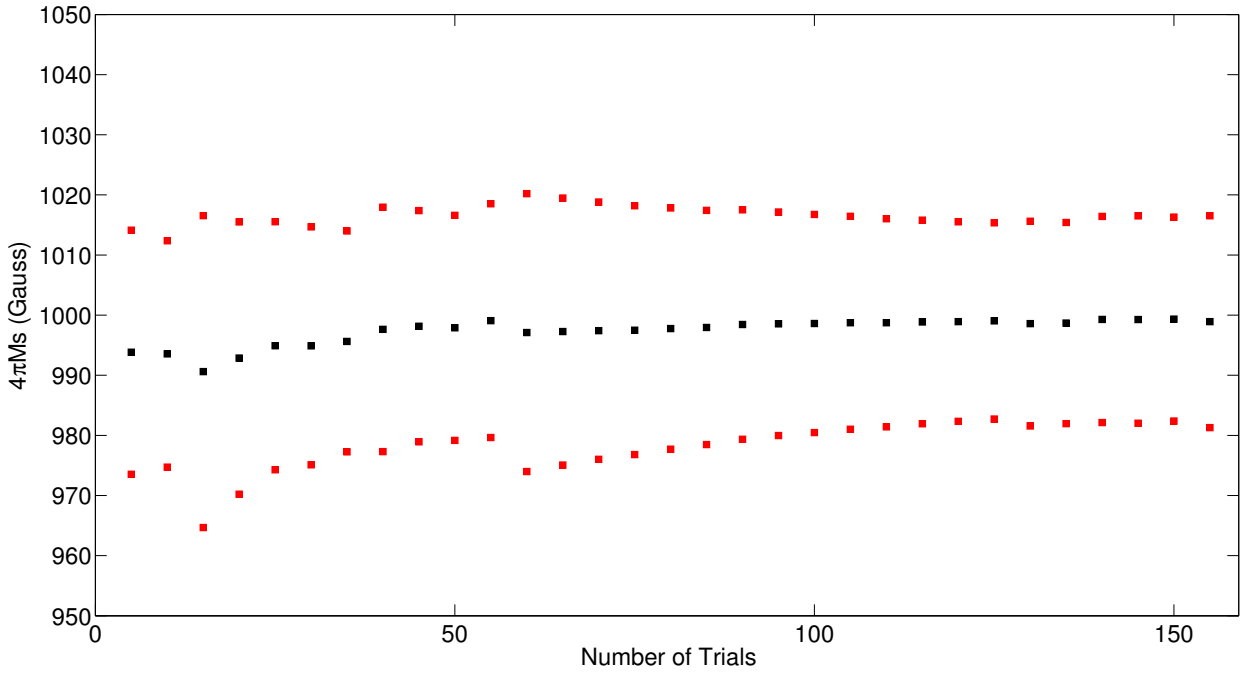

Figure 4.13 Extracted $4\pi M_S$ for a test sample of width d=54 mm under different number of trials. The center dots are the average of the trials. Upper and lower dots show one standard deviation.

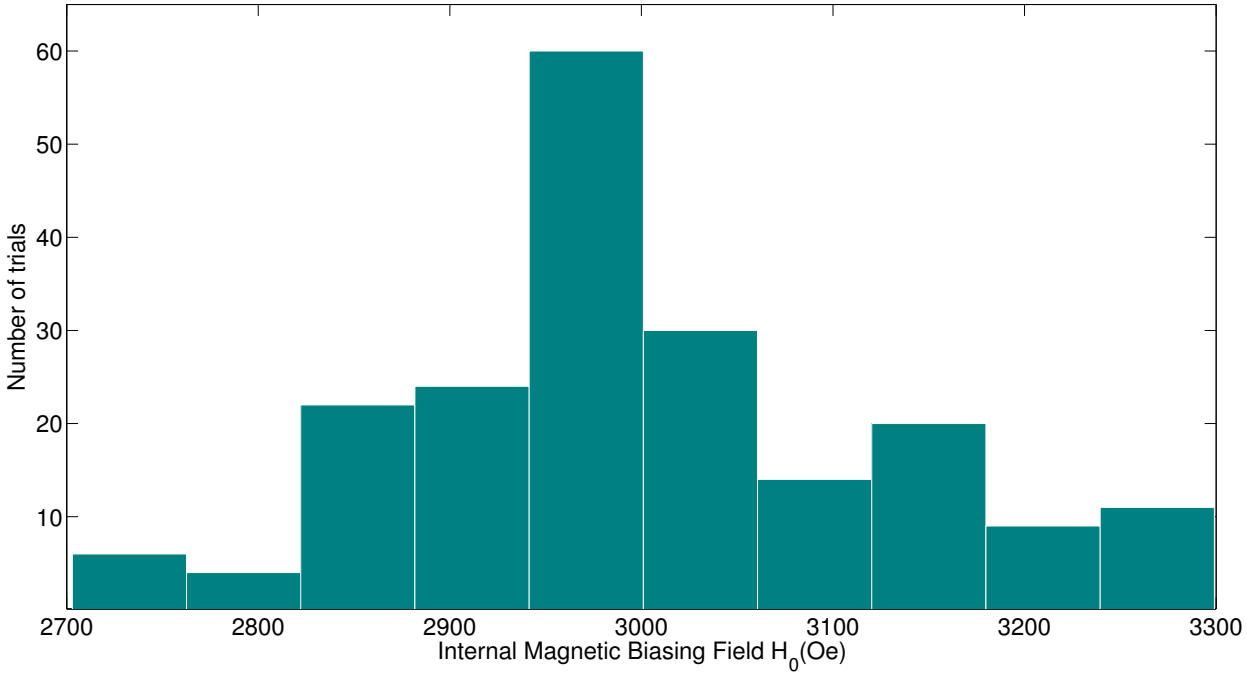

Figure 4.14 Histogram of the H_0 extracted from 200 random trials of simulated S-parameters for a partially filled G1010 sample with various widths.

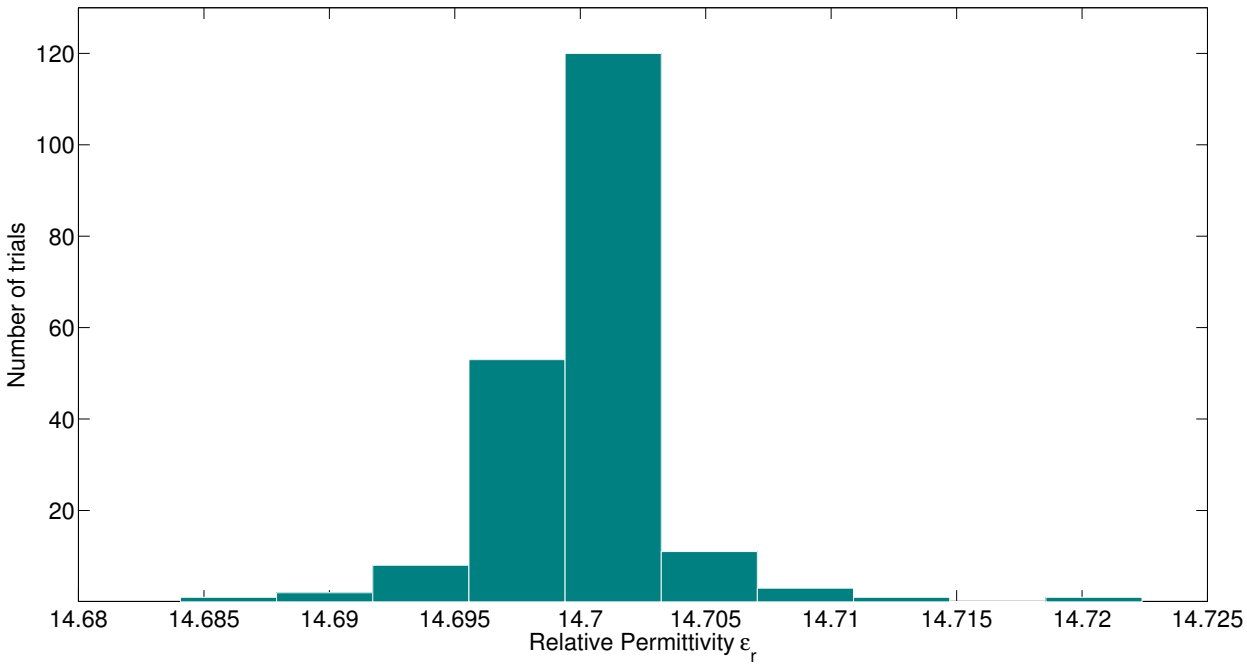

Figure 4.15 Histogram of the relative permittivity extracted from 200 random trials of simulated S-parameters for a partially filled G1010 sample with various widths.

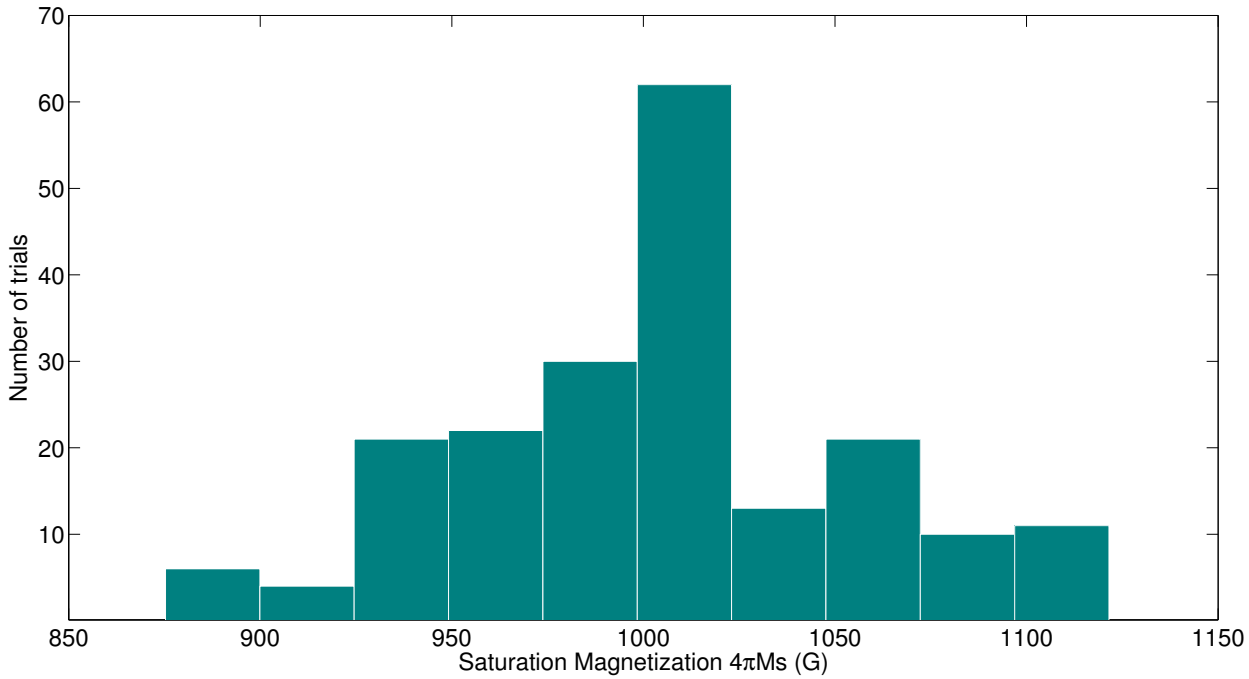

Figure 4.16 Histogram of the $4\pi M_S$ extracted from 200 random trials of simulated S-parameters for a partially filled G1010 sample with various widths.

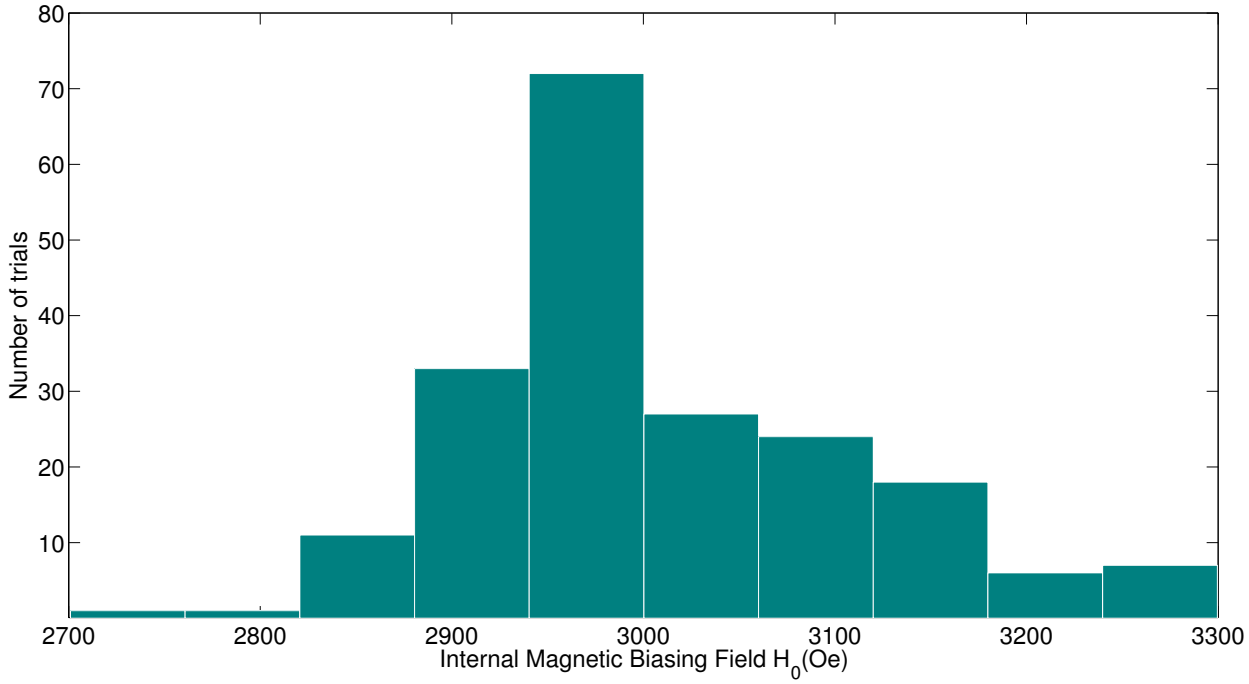

Figure 4.17 Histogram of the H_0 extracted from 200 random trials of simulated S-parameters for a partially filled G1010 sample with various thicknesses.

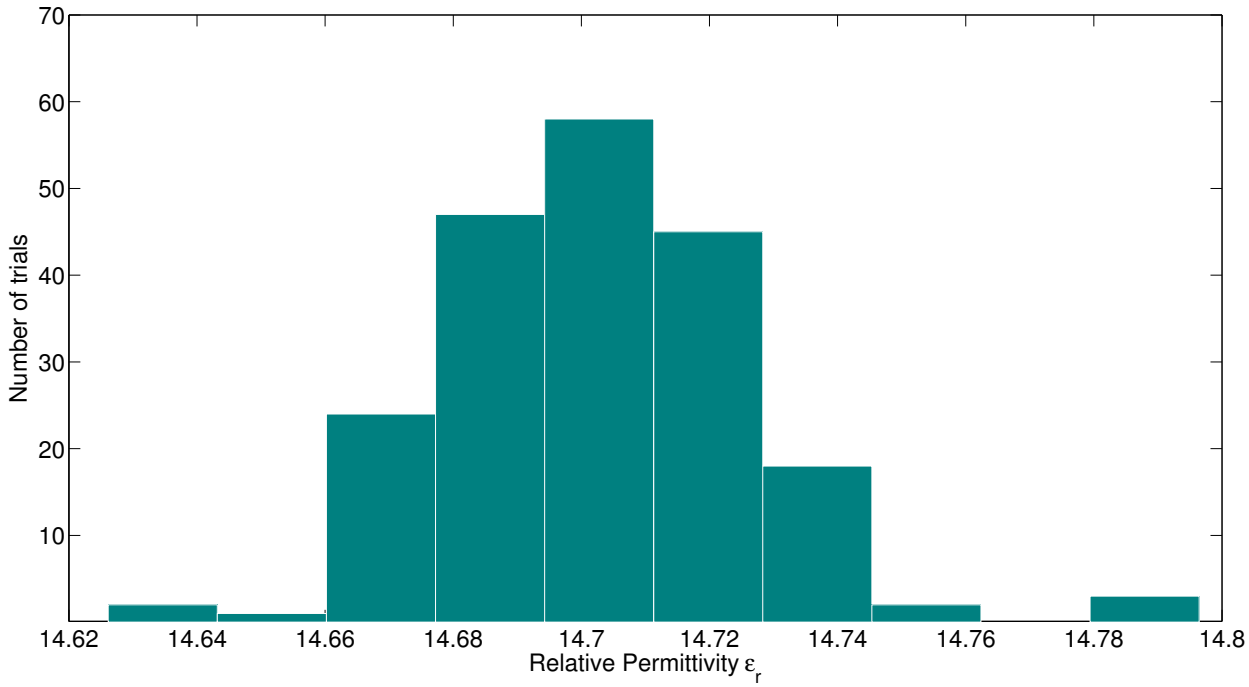

Figure 4.18 Histogram of the relative permittivity extracted from 200 random trials of simulated S-parameters for a partially filled G1010 sample with various thicknesses.

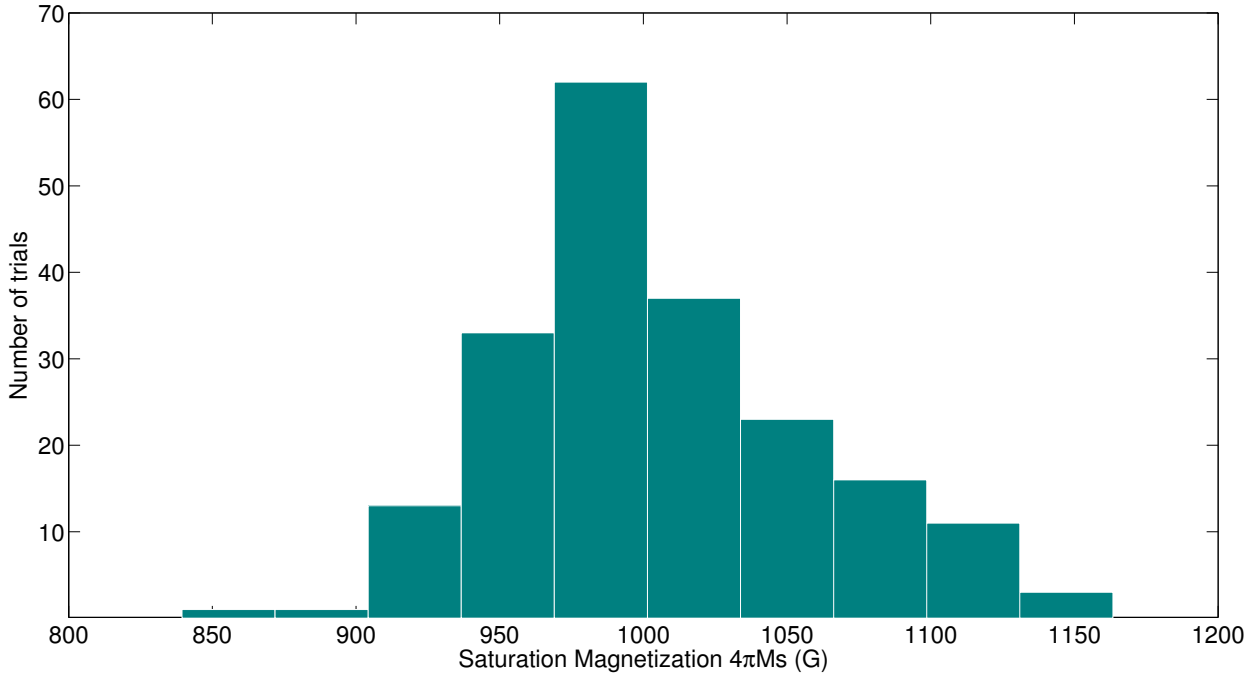

Figure 4.19 Histogram of the $4\pi M_S$ extracted from 200 random trials of simulated S-parameters for a partially filled G1010 sample with various thicknesses.

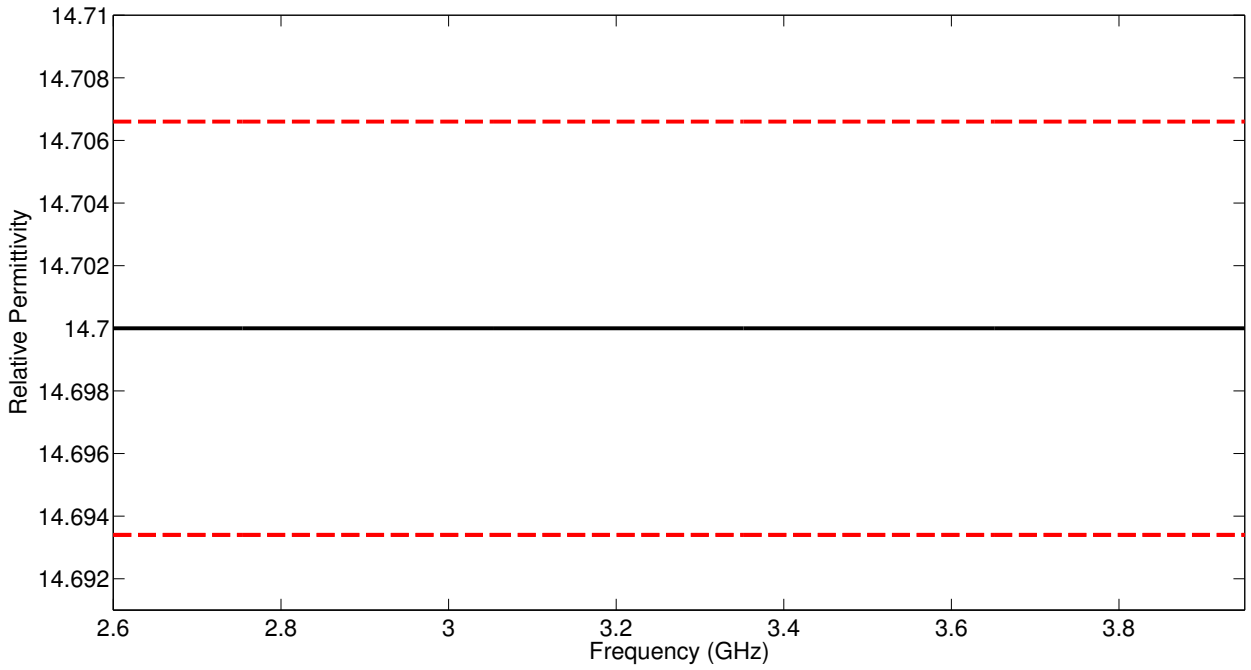

Figure 4.20 Relative permittivity extracted from 200 random trials of simulated S-parameters for a partially filled G1010 sample with various widths. Center black line is the average of the trials. Upper and lower red dashed lines show the 95% confidence interval.

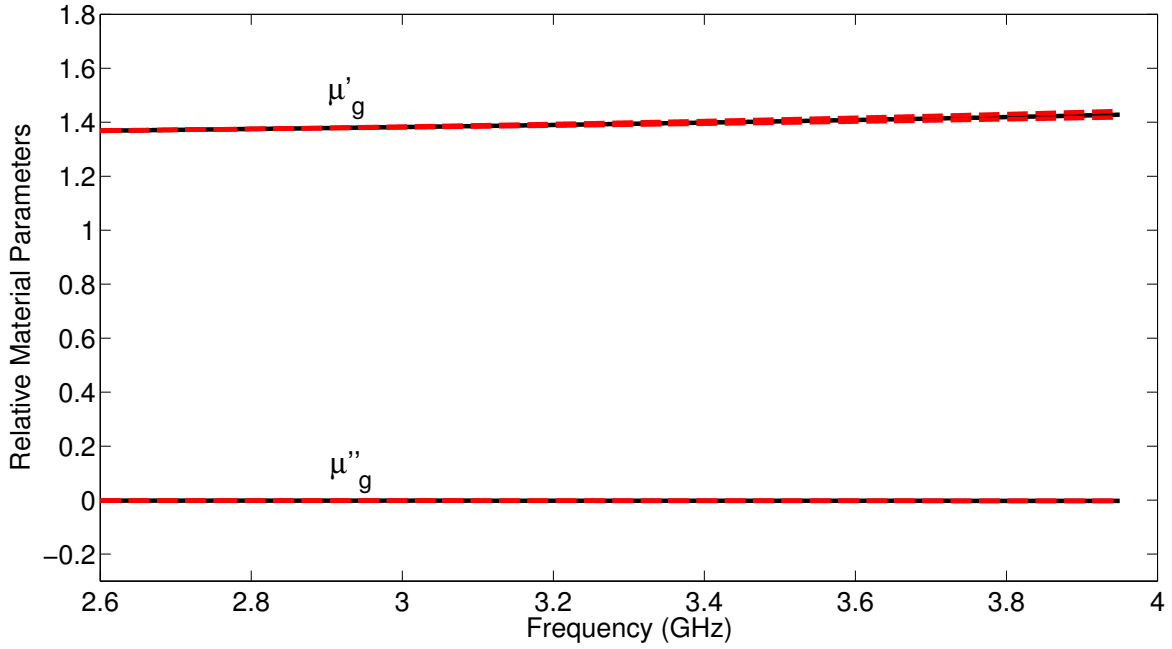

Figure 4.21 Relative permeability values extracted from 200 random trials of simulated S-parameters for a partially filled G1010 sample with various widths. Center black line is the average of the trials. Upper and lower red dashed lines show the 95% confidence interval.

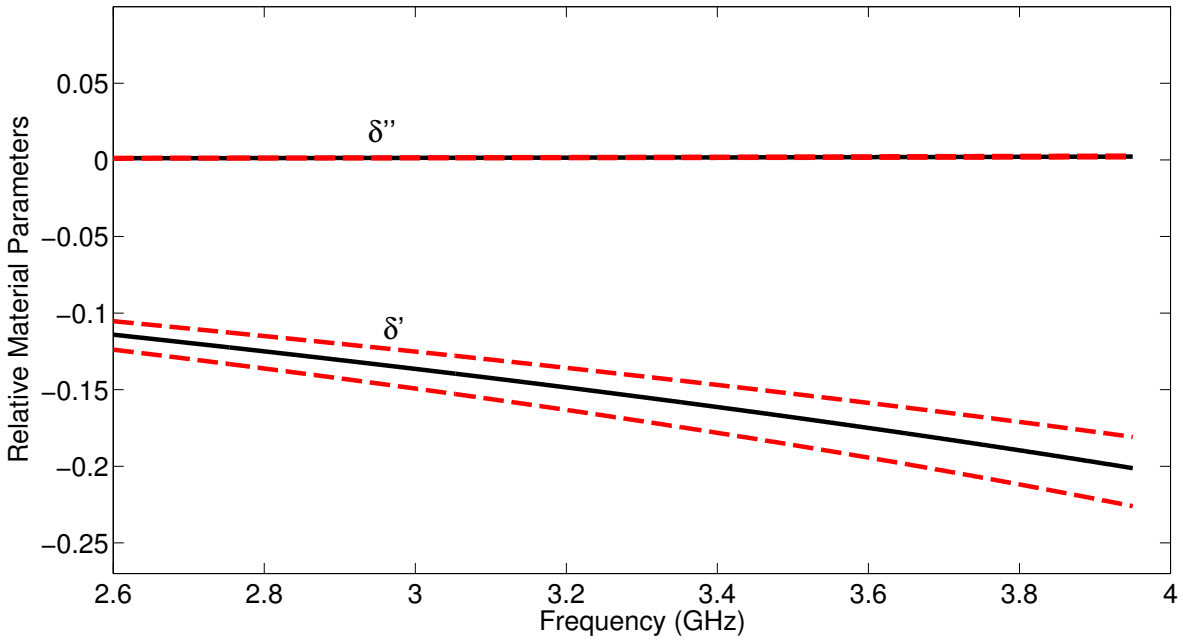

Figure 4.22 Relative permeability values extracted from 200 random trials of simulated S-parameters for a partially filled G1010 sample with various widths. Center black line is the average of the trials. Upper and lower red dashed lines show the 95% confidence interval.

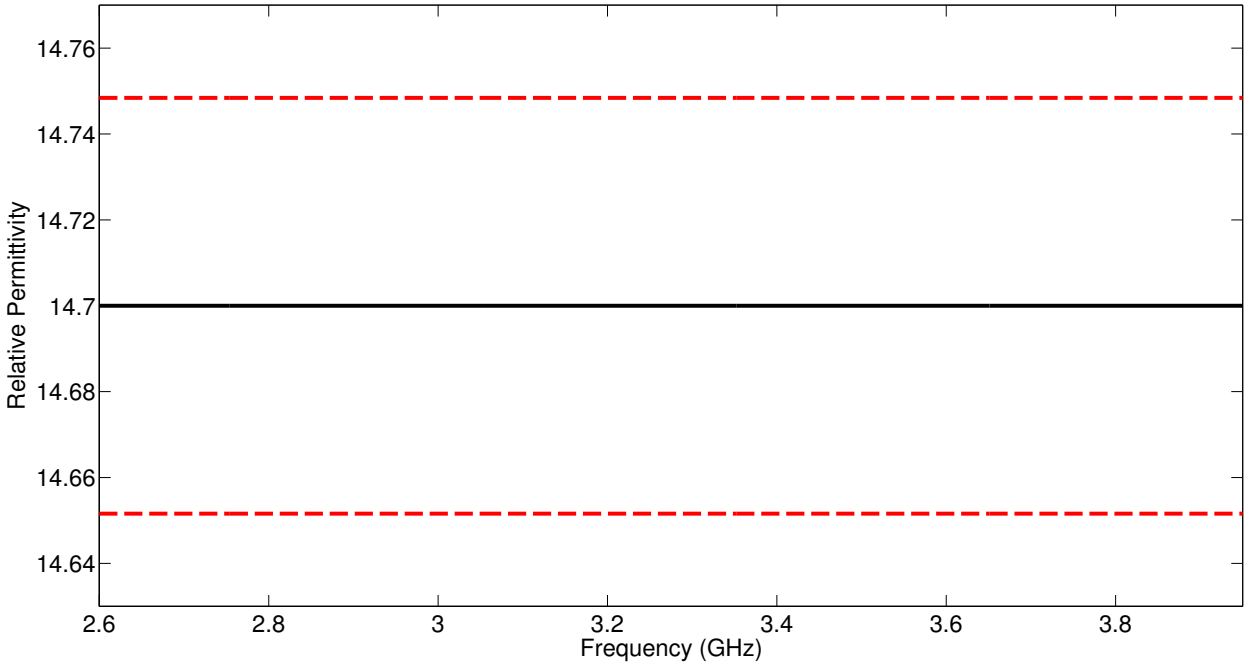

Figure 4.23 Relative permittivity extracted from 200 random trials of simulated S-parameters for a partially filled G1010 sample with various thicknesses. Center black line is the average of the trials. Upper and lower red dashed lines show the 95% confidence interval.

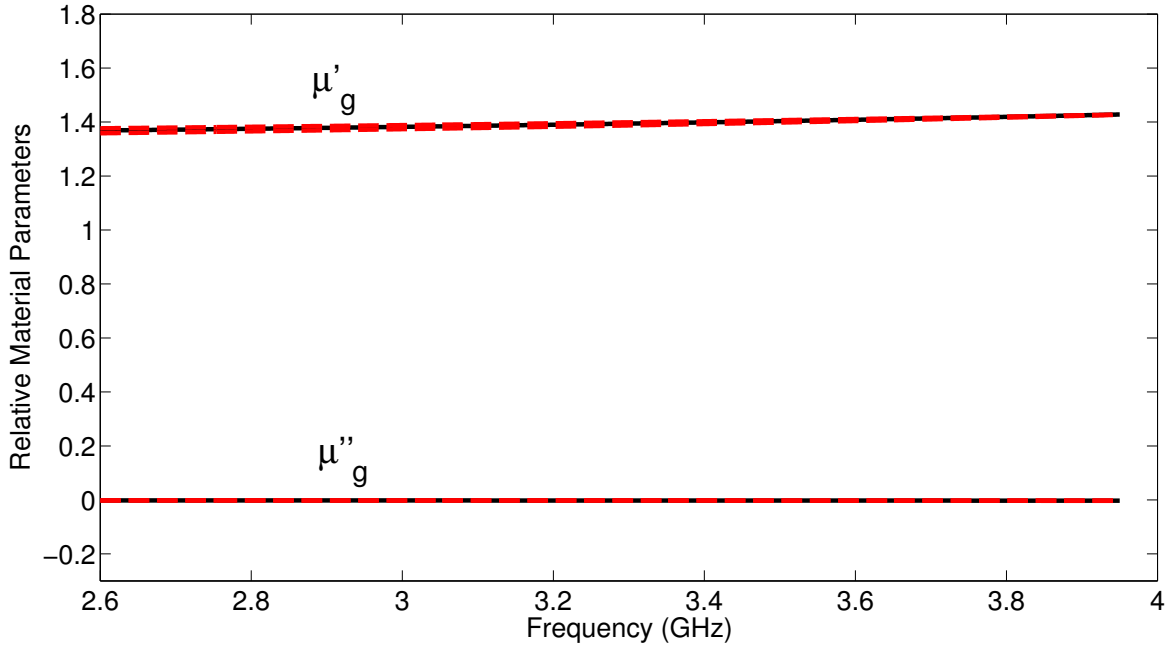

Figure 4.24 Relative permeability values extracted from 200 random trials of simulated S-parameters for a partially filled G1010 sample with various thicknesses. Center black line is the average of the trials. Upper and lower red dashed lines show the 95% confidence interval.

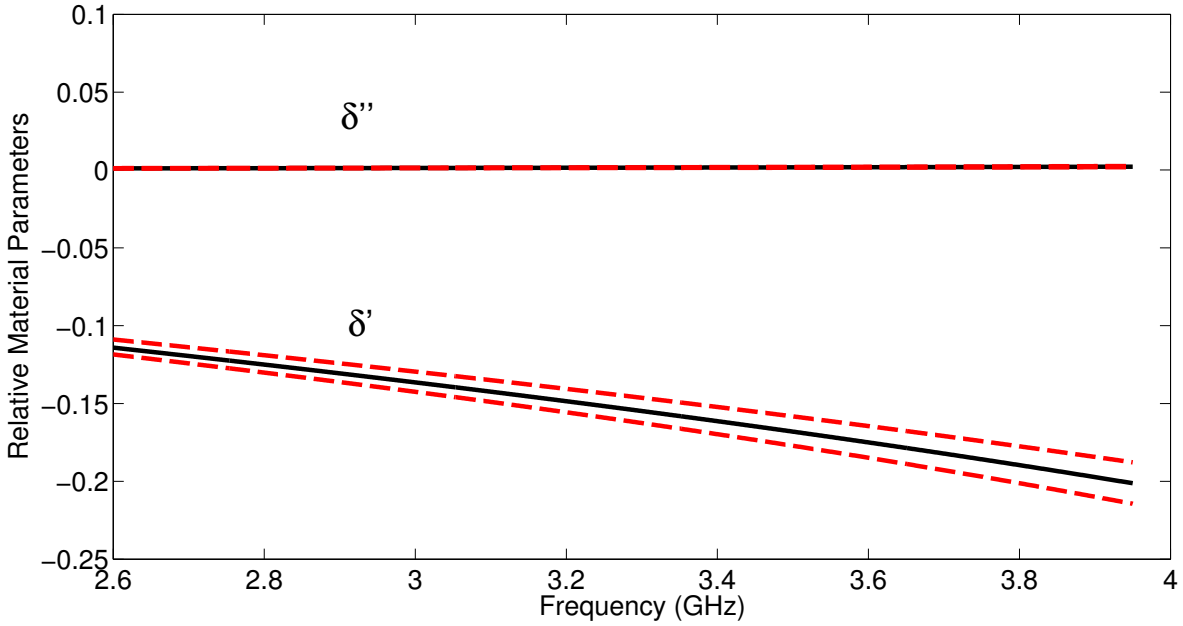

Figure 4.25 Relative permeability values extracted from 200 random trials of simulated S-parameters for a partially filled G1010 sample with various thicknesses. Center black line is the average of the trials. Upper and lower red dashed lines show the 95% confidence interval.

focuses on developing a proper procedure for extraction of measured data using the Matlab optimization functions.

With initial guesses of variables known, `fmincon` is able to determine solutions faster for a bounded region using measured data compared to `fminsearch` which does not require bounds to be assigne. This solver finds the minimum of a constrained nonlinear function with multiple variables based on the gradient method. It requires both the objective function and constraint function to be continuous. Function `fmincon` has four algorithms, with several options for computing Hessians (matrices of second-order partial derivatives of a function): the trust region reflective algorithm, the SPQ algorithm, the active set algorithm, and the interior point algorithm. The trust region reflective algorithm requires a user supplied Hessian or uses a finite-difference approximation for the Hessian. The active set algorithm and SPQ algorithm compute a quasi-Newton approximation of the Hessian matrix. The interior point algorithm uses a combination of the different methods mentioned above to define the Hessian matrix. Appropriate algorithms need to be chosen for specific problems.

Instead of using the graphical user interface (GUI) in the Matlab optimization toolbox as shown in the previous section, the implementation of the optimization using measured data is achieved through Matlab commands, since this method is more convenient for setting up the optimization parameters. Below is an example using `fmincon` with commands for measured data.

```
H0=[2990,14.7,1020];

options = optimset('Algorithm','interior-point','Display','iter','PlotFcns',
@optimplotfval,'TolFun',1e-4,'TolX',1e-5);

A = []; b = []; Aeq=[]; beq=[]; lb=[2600,14.0,640];
ub=[3800,15.2,1360]; nonlcon = [];
```

```
[H_opt,fval] = fmincon(@S_param_function_meas, H0,A,b,Aeq,beq,
lb,ub,nonlcon,options);
```

First, the initial guess was defined as a vector. Second, the optimization options were specified. As it can be seen that in the options, the optimization algorithm chosen for this problem is the interior point algorithm. This hybrid algorithm tends to take less time in optimization; this was demonstrated by comparing it with other algorithms using the same measured data. Also, a plot of the iterative function value can be requested in the options column, which allows the user to see the status of the function value during optimization. Third, the input argument for the objective function was defined. In this problem, only the lower and upper boundary of the initial guess were assigned and they were decided upon based on the reasonable material properties of the sample and estimated magnetic biasing field. In the last step, the optimization was launched by using function `fmincon` with the name of the objective function, which calculates the root squared error between the theoretical data and measured data for this problem. The parameters `H_opt` and `fval` are the returned optimized results and final function value respectively.

Measured data was used to evaluate the performance of this method. A typical measurement contains 801 frequency points, it would be time-consuming to compute the forward problem using so many points. Moreover, the S-parameters are more sensitive to the variations of the material parameters at frequencies near the resonance frequency. Thus, the critical frequency points which are close to the resonance frequencies of the measurement were chosen. However, for some resonance frequencies in the measured data, few frequency points are available to describe that resonance. Therefore, only the frequency points that are near the main resonance frequency are considered for processing. For example, the blue curves in Figure 4.26 show the magnitude and phase of the S-parameters measured under the highest magnetic biasing field. It can be seen that there is a resonance near 2.7 GHz, but it is also not sensitive to the variation of the material parameters. For this measured data, 120 frequency points were chosen from 801 points around the main resonance frequency which

covers a frequency range of $3.62 - 3.82$ GHz. The lower and upper bounds of external magnetic biasing field H_0 are set to be ± 400 of the intial guess. The bounds of ϵ_r' are determined based on the specification sheet offered by the manufacturer of the G1010 sample which are 14 and 15.2. Upper and lower bounds of $4\pi M_s$ are assigned to be 640 and 1360 G. These bounds offer the solver fairly large regions within which reasonable results can be obtained. Note that since only H_0 varies between different measurements, the lower and upper bounds for ϵ_r' and $4\pi M_s$ were kept the same.

The first row in Table 4.3 shows the returned results for the measured data with highest biasing field. Since this chapter only focuses on the extraction procedure, a discussion of the extracted results are included in the chapter 5. Theoretical S-parameters using the extracted parameters were generated and compared with the measured data. It can be seen from Figure 4.26 that good agreement is achieved between the measured S-parameters and theoretical S-parameters calculated using extracted values. Similarly, two other measured data taken under two other different magnetic biasing fields were processed with the same setup to extract the results. However, for these two measured data, some blips around the main resonance frequency can be noticed in Figures 4.27 and 4.28 which may be caused by the air gaps between the sample and waveguide wall. It is found that the best way to eliminate the negative impact of these data on extraction is to avoid these points rather than smoothing them. Thus, 60 frequency points on either side of the main resonance frequency were selected carefully without including the blips. As a result, the same number of the frequency points (120) can still be obtained to process the optimization. The extracted results from these two measurements are shown in the second and third rows of Table 4.3. Good agreement is still achieved between the measured S-parameters and the theoretical S-parameters as shown in Figures 4.27 and 4.28.

Since for the same test sample, ϵ_r' and $4\pi M_s$ should be the same, an alternative extraction process can be established where all the parameters are extracted using all the data measured with various biasing fields. To achieve this, the least-square error, which was optimized for

Table 4.3 Extracted material parameters from measurements with different external magnetic biasing fields.

	H_0 (Oe)	ϵ_r'	$4\pi M_S$ (G)
Measurement 1	3201	14.7371	1049.5
Measurement 2	1889.7	14.9862	1000.3
Measurement 3	1406.4	14.2254	1051.2

a single measurement using (), is minimized using three different measured data. The same number of points were chosen for each set of measured data. Initial guesses for five variables (three different magnetic biasing field strengths for each measurement, ϵ_r' and $4\pi M_S$) were then specified along with the lower and upper bounds. Table 4.4 shows the resulting extracted values of the parameters. The values are reasonably close to the previous values that were extracted from separate data sets. This method may reduce the impact of the experimental errors that are contained in each of the measurements by using three different measured data, thus giving more accurate results.

Table 4.4 Extracted parameters values from one optimization using measurements of different external magnetic biasing fields.

Parameter	Value
H_0 - 1	3024.3
H_0 - 2	1763.8
H_0 - 3	1450.0
ϵ_r'	14.4754
$4\pi M_S$	1061.5

4.5 Summary

A method for characterizing gyromagnetic materials from two complex measurements using Matlab optimization algorithms is introduced. The adopted optimization algorithm in Matlab was validated using a fictitious sample and the performance of the characteriza-

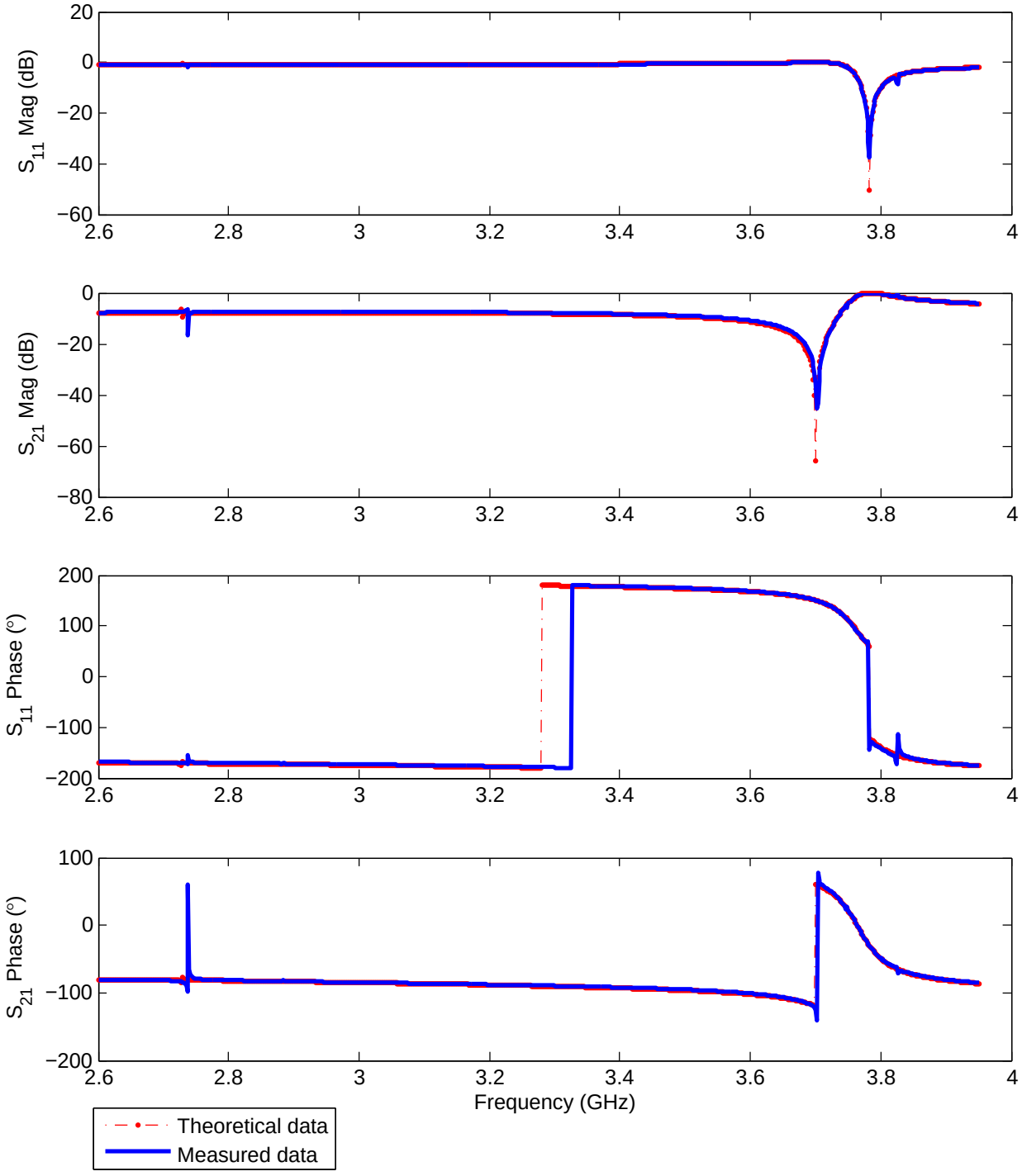

Figure 4.26 Measured S-parameters of the highest biasing field and theoretical S-parameters generated using extracted material parameters.

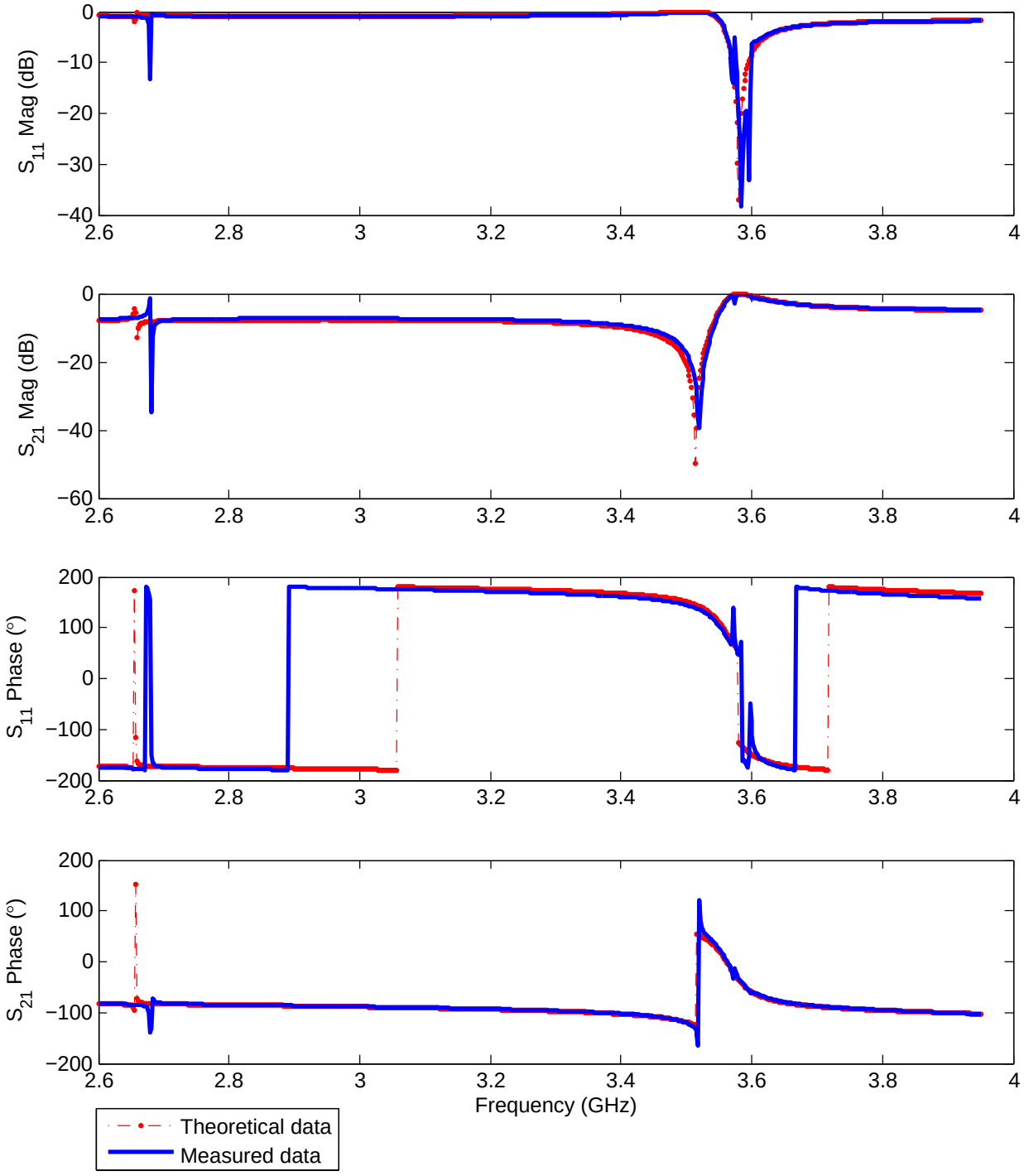

Figure 4.27 Measured S-parameters of the second biasing field and theoretical S-parameters generated using extracted material parameters.

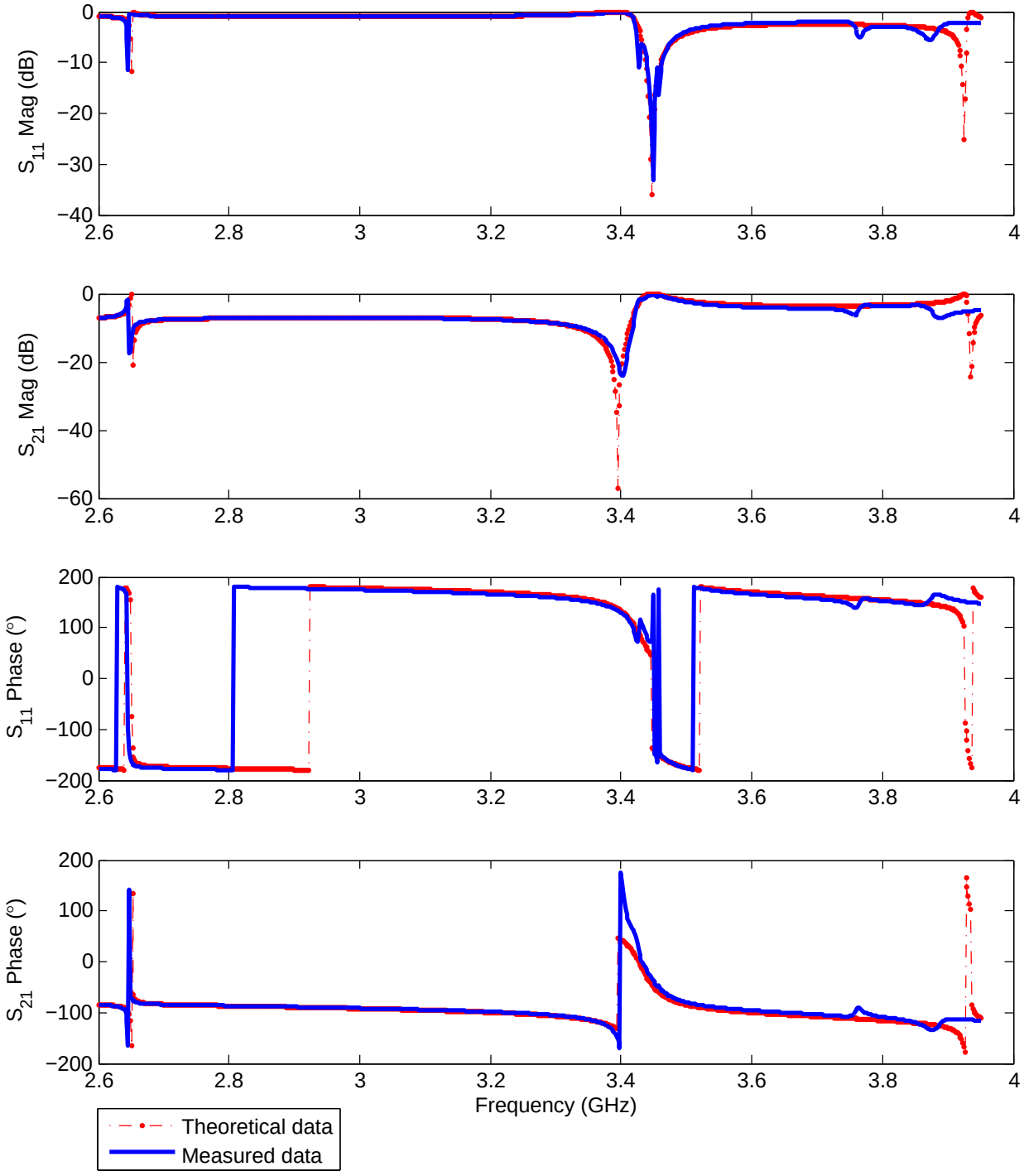

Figure 4.28 Measured S-parameters of the lowest biasing field and theoretical S-parameters generated using extracted material parameters.

tion technique was evaluated using error analysis based on network analyzer uncertainty. It has been found that the technique performs very well for different sample sizes with high VNA uncertainties. Extraction methods for processing measured data are also established to extract material parameters either from a single measurement, or multiple measurements.

CHAPTER 5

EXPERIMENTAL SETUP AND RESULTS

5.1 Introduction

This chapter presents experimental procedures and results for characterizing different anisotropic materials using a partially-filled rectangular waveguide technique. Two types of anisotropic material were constructed and measured at S-band to validate the proposed techniques. The first type is a biaxial material which has different material parameters depending on the incident wave polarization. This type of material can be described using two three by three tensor matrices that each consist of three nonzero entries. To extract all six parameters of the biaxial material, usually three different samples are required to perform three sets of reflection and transmission measurements. However, one can extract all six parameters with the partially filled waveguide technique from one well constructed sample. This extraction method is the three-step approach shown in Section 2.2.4 which requires three reflection and transmission measurements of a cubical sample at different orientations. A simplified extraction approach for a uniaxial material which is a special case of a biaxial material is also developed and shown in Section 2.2.4. Since two parameters in the tensors are identical, with

$\epsilon_A = \epsilon_C$ and $\mu_A = \mu_C$, only four unknown parameters exist. The number of measurements required to complete the extraction for this material is reduced to two.

The second type of the material is the gyromagnetic material which can be described by an isotropic complex permittivity and a three by three permeability tensor with off-diagonal terms which vary with different magnetic biasing conditions. Due to manufacturing difficulties, these material often come with a limited size which makes using the filled aperture extraction method unfeasible for them. This can be solved by using a partially filled waveguide technique where the properly machined sample partially fills the waveguide aperture. The extraction process can be achieved by either using a single measurement or multiple measurements with different experimental configurations, such as with different magnetic biasing fields or sample locations. Matlab optimization algorithms were used in the inverse problem which minimizes the difference between theoretical and measured S-parameters to expedite the extraction process. This is described in Section 4.4.

5.2 Characterization of Biaxial/Uniaxial Material

To experimentally validate the technique of extracting biaxial material and uniaxial material parameters, two samples were built and measured in an S-band waveguide system. The construction of the material sample and the details for setting up the waveguide system are discussed in the following section. The repeatability of the measurements and error analysis of the measured results are also assessed.

5.2.1 Sample Construction

Two samples were built to implement the extraction process using experimental results. The first sample is a cube which was constructed using layers of alternating dielectrics. This produces a material with unixial electric properties, but isotropic magnetic properties. Due to the unavailability of the commercial anisotropic dielectric and anisotropic magnetic

material, this unixial dielectric sample was measured as a biaxial sample to validate the feasibility of the three-step approach. This sample was built by gluing layers of Rogers RO3010 and Rogers RT/druroid 5870 circuit boards together using super glue from Loctite. The manufactured cubic sample is shown in Figure 5.1 where the light color layers are Rogers RO3010. The RO3010 board has a dielectric constant of $\epsilon'_{r1} = 10.2$ and a loss tangent of $\tan\delta_1 = 0.0022$ with a thickness of 1.27 mm. The RT/druroid 5870 board has a dielectric constant of $\epsilon'_{r2} = 2.33$ and a loss tangent of $tan\delta_2 = 0.0012$ with a thickness of 3.4 mm.

The second sample was built by gluing layers of Rogers RT/druroid 5870 with a thickness of 1.27 mm and Eccosorb FGM-125 together, where the designation 125 represents the thickness of the substrate (125 mils). This produces a sample with both unixial electric properties, and uniaxial magnetic properties. The manufactured sample is shown in Figure 5.2 where the thick dark substrate is FGM-125. The reason that the first and last layer of the sample is chosen to be Rogers 5870 is to reduce the sample abrasion from repeated measurements, since FGM-125 is soft and rubbery. This sample was used to evaluate the simplified approach for extracting uniaxial materials.

The ideal side length of the cubes is supposed to be the height of S-band waveguide which is 34.036 mm. However, due to machine error, the final dimensions of the biaxial and uniaxial samples along the direction that the layers inside the sample are horizontal are: 34.05 mm $\times$ 34.11 mm $\times$ 34.09 mm and 34.01 mm $\times$ 34.14 mm $\times$ 33.94 mm, respectively. Note that a perfect sample should be slightly larger than the dimension of the waveguide wall so that the air gap between the sample and waveguide wall can be eliminated. However, it was observed that an air gap of less than 0.2 mm occurred when the uniaxial sample was placed into the waveguide. It is also important to mention that different faces of each sample are marked to give consistent orientation in the measurements.

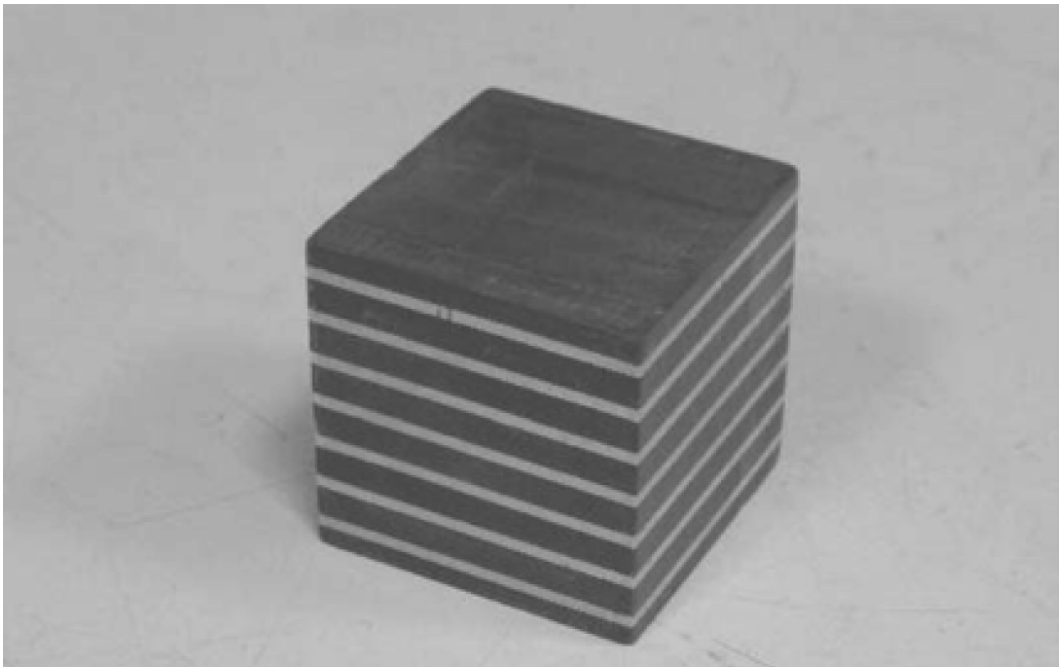

Figure 5.1 Uniaxial electric and isotropic magnetic material sample.

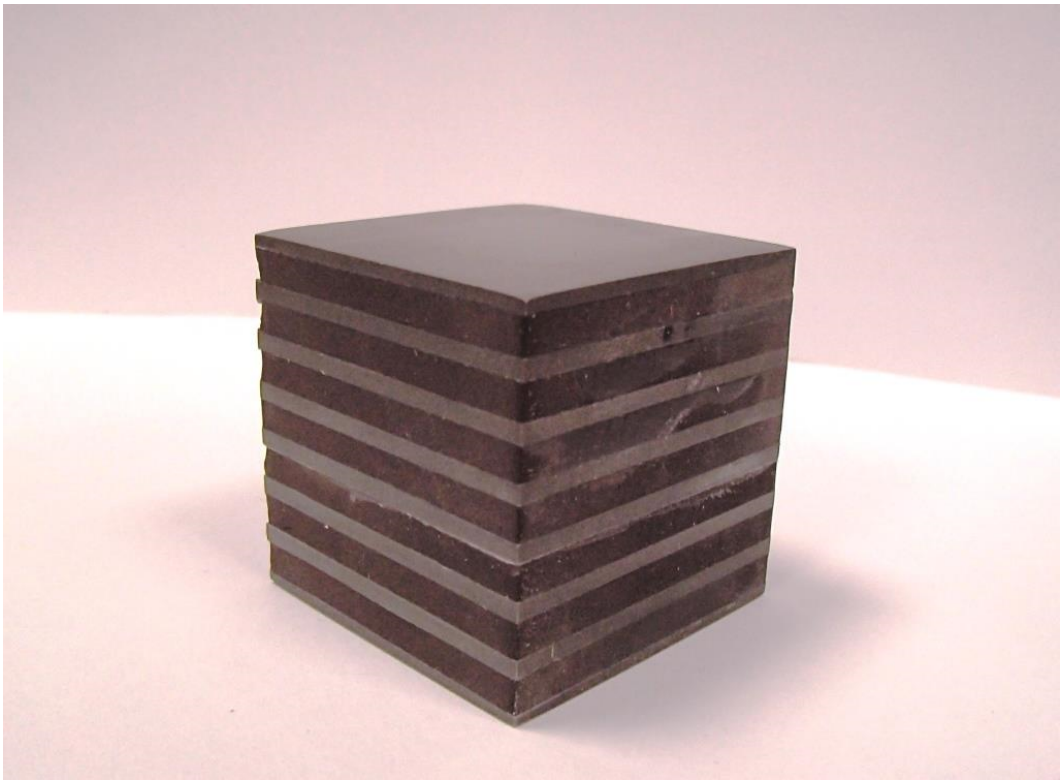

Figure 5.2 Material sample with both uniaxial electric and magnetic properties.

5.2.2 Measurement Techniques

To experimentally validate the proposed technique at S-band, the S-parameters from different samples were measured and the material parameters were extracted. The waveguide system used for the measurements is a S-band calibration kit from Maury Microwave which consists of two 152.4 mm long waveguide section, which acted as extensions, with coaxial transitions attached at the ends. An additional brass plate and a 30.5 mm waveguide section is also included in the calibration kit which is used as short and line respectively during the calibration procedure. The two waveguide extensions were connected to an Aglient E5071C VNA through two 7 mm to 3.5 mm adapters. The whole system is shown in Figure 5.3. The VNA was then calibrated using the calibration kit described above based on a Thru-Reflect-Line (TRL) method with the corresponding algorithm stored in the VNA. The calibration kit consists of two offset shorts and a load. It was found that by performing the TRL calibration method in a certain order, the calibration error can be reduced. For the calibration implemented for the measurements of the cubical samples, the 30.5 mm waveguide section (line) was used first. Then the brass plate was used twice to calibrate each of the ports. Finally, a through measurement was performed to complete the calibration. The typical variation in the value of the magnitude of a through measurement taken right after the calibration is within ± 600 μdB. The reason that the best calibration results can be achieved by following this order might be due to the fact that the error introduced by the misalignment of the waveguide sections can be reduced by performing the through measurement at the end. In addition, a crucial step for achieving consistent calibration and measured results is to have the same configuration for waveguide assembly. To achieve this, an adjustable torque wrench with the torque set to 50 Lb-in was used to tighten the screws used to assemble the waveguide sections or the calibration components. Note that there are 8 holes on the periphery of the waveguide flanges and the calibration components. Two screws on the diagonal were inserted and were tightened using the torque wrench. The next two bolts

were placed so they were not adjacent to the previous bolts. The remaining four bolts were installed in a similar manner. This procedure maintains an even pressure on the waveguide flange and therefore reduces error caused by misalignment. Two wooden holder were built and attached at the end of the waveguide ports to minimize the physical vibration during the calibration process. The measurements were made with VNA settings of -5 dBm source power, 64 averages, 801 frequency points within S-band (2.65 GHz-3.95 GHz), and an IF bandwidth of 70 kHz. Two fixed torque wrenches with torques of 8 lb-in and 12 lb-in were also used to tighten the 3.5 mm and 7 mm adapters respectively, during the calibrations and measurements when each time the waveguide system was dissembled or assembled.

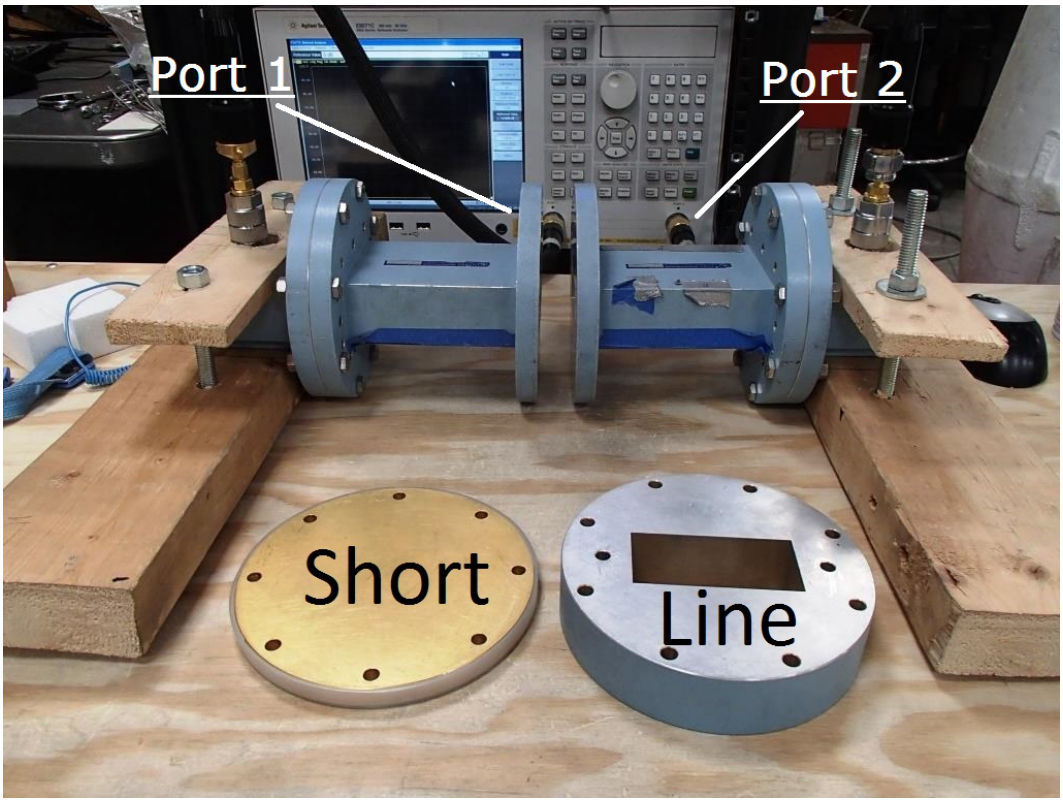

Figure 5.3 Waveguide measurement system.

One advantage of using a partially-filled waveguide technique is that no sample holder is required. Instead, the sample was placed inside the waveguide extension connected to Port 1. The sample was placed at the center of the waveguide using a foam spacer and one surface of the sample must be parallel to the waveguide flange to ensure that the propagation direction

of the incident wave aligns with the sample axis. This latter condition was implemented by making one surface of the sample flush with the waveguide opening. Figure 5.4 shows the unixial sample placed at the center of a waveguide extension at orientation 1 which is described in Section 2.2.4. For the measurements of cubical samples shown in Figure 5.5, the sample is inserted into the waveguide extension attached to port 1. The S-parameters of the sample were measured by the VNA at the calibration plane. However, the extraction method requires using S-parameters referenced to the sample planes z=0 and z=d. Therefore, the measured S-parameters have to be mathematically de-embedded to the sample planes. The S-parameter can be shifted from the calibration plane to the sample planes by multiplying by $e^{-j\beta D}$ in the direction of the wave propagation. Here, β is the propagation constant of the empty waveguide extension which can be found using (2.4), and D is the appropriate distance of the shift. For the measurement of biaxial or uniaxial samples, the shifting can be achieved using the following expressions:

$$S_{21}^{s} = S_{21}^{c} e^{-2j\beta d} \tag{5.1}$$

$$S_{11}^{s} = S_{11}^{c} e^{-j\beta d}, \tag{5.2}$$

where S_{11}^{s} and S_{21}^{s} are the S-parameters referenced to the sample planes while S_{11}^{c} and S_{21}^{c} are the measured S-parameters referenced to the calibration plane. This approach is also described in appendix B. [42].

5.2.3 Experiment Results

The VNA was calibrated ten times using the waveguide calibration kit. Ten sets of measurements for each material sample were conducted and the S-parameters were saved for extraction. For the uniaxial dielectric and isotropic magnetic material (biaxial sample), three orientations for each set of measurement were required to extract all six parameters. For the uniaxial dielectric and uniaxial isotropic magnetic material (uniaxial sample), only two

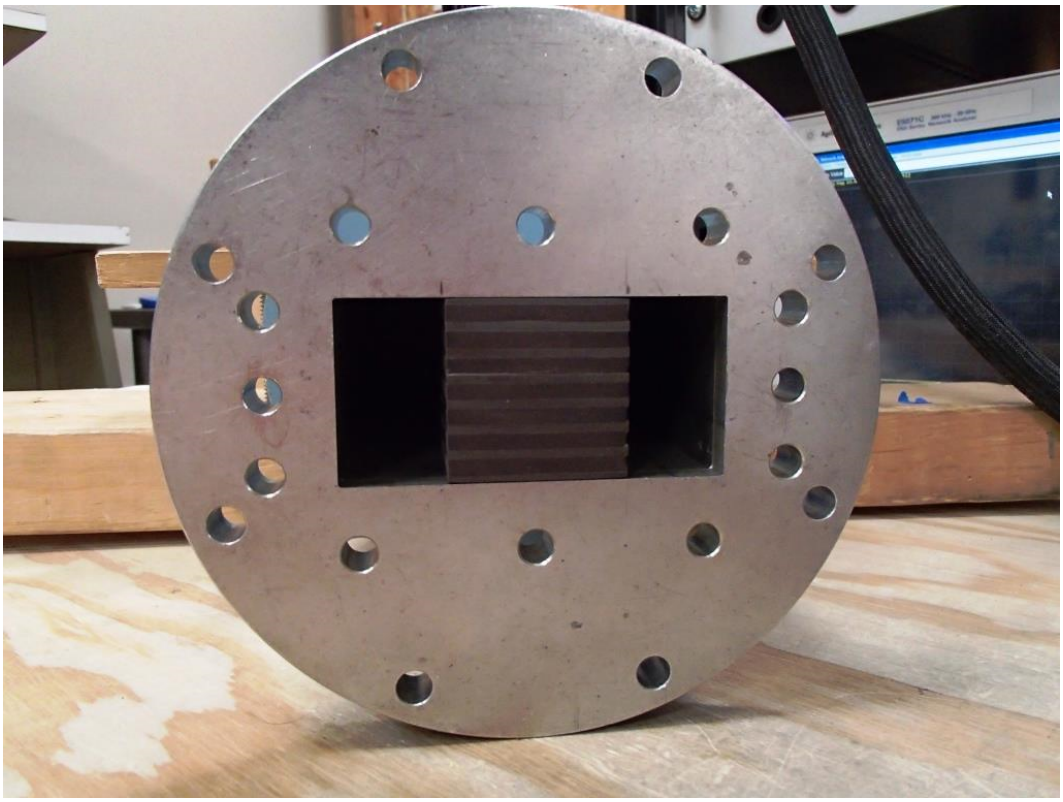

Figure 5.4 Uniaxial material sample placed in the center of the waveguide at orientation 1.

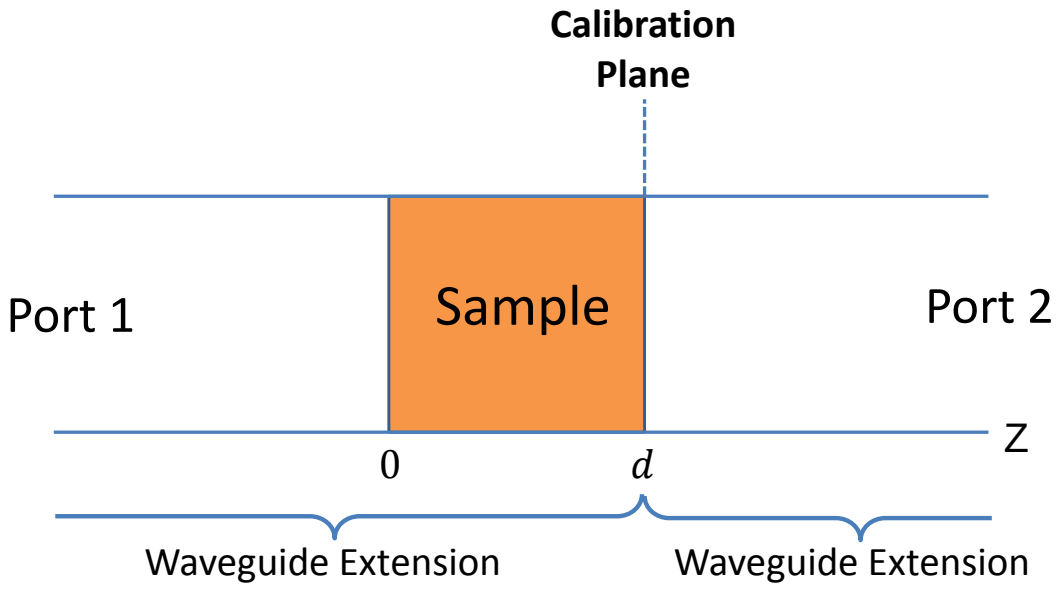

Figure 5.5 Sample inserted into the waveguide extension attached to port 1.

orientations were required since a simplified process was applied to extract the four parameters. Error analysis of both measurement repeatability and extracted material parameters was undertaken.

5.2.3.1 Repeatability Analysis

In Section 2.2.5, a Monte-Carlo technique was used to evaluate the propagation of random error from the VNA. In this section, a statistical analysis of the variance of S_{11} and S_{21} of the measured data was processed to evaluate the repeatability of the experiment.The repeatability error describes the measurement uncertainties. In these experiments, the sources of measurement uncertaities may be attributed to imperfect calibration of the VNA, changes in the environment (temperature, humidity,etc...), misalignment of waveguide sections, and inaccurate sample positioning in the waveguide. A statistical analysis of these errors can help determine the sensitivities of S-parameters to the experimental setup.

Since the experimental setups for both samples are the same, the sources of errors for measuring both samples are identical. The measured S-parameters of the uniaxial sample were chosen for the repeatability analysis because only two measurements were required for each set of measurements and thus it would be more convenient to analyze them. Figures 5.6 - 5.9 show the average S-parameters and the standard deviation generated from 10 repeated measurements of the uniaxial material at the first orientation. In these figures, the two surrounding red lines indicate the 95% confidence interval of ± 2 standard deviations. Note that the two standard deviations of the magnitude of both S_{11} and S_{21} are less than 0.1 dB, which indicates highly consistent measured results. From Figures 5.7 and 5.9, one can see that the confidence interval of S_{11} is approximately 1 degree and that of S_{21} is around 0.5 degree. These values are much larger than the phase uncertainties of the VNA (0.035 degree) . The overall statistical results of the measured S-parameters indicate good consistency of the experimental setup. The same procedure was undertaken for the measured S-parameters of the second orientation which is also described in Section 2.2.4 and the results are shown

in Figures 5.10 - 5.13. The confidence intervals for both of the magnitude of S_{11} and S_{21} are less than 0.04 dB, and confidence interval of the phase is also less than 1 degree. Note that highly consistent results are obtained for the magnitude of the S-parameters from the 10 measurements, while acceptable consistency is shown for the phase. The inconsistency in the phase may due to an unstable sample position in the waveguide which causes a change in the measured phase. A well constructed foam fixture could be used to achieve better measurement consistency. This is left as future work.

5.2.3.2 Extracted Parameters of The Uniaxial Sample

As outlined in Section 5.2.2, a uniaxial dielectric and isotropic magnetic material sample was placed in the cross-section of a waveguide under different orientations and the transmission and reflection coefficients were measured, providing sufficient data for the three-step approach to find both the permittivity and permeability of the sample. An estimation of the material parameters from the sample should be acquired to validate the proposed technique. The following formulas [54] can be used to determine the approximate material parameters

$$\epsilon_B = \left[\frac{1}{\epsilon_{r2}} - \frac{\epsilon_{r1} - \epsilon_{r2}}{\epsilon_{r1}\epsilon_{r2}} \frac{t_1}{t_1 + t_2}\right]^{-1}, \tag{5.3}$$

$$\epsilon_A = \epsilon_C = \epsilon_{2r} + (\epsilon_{r1} - \epsilon_{2r}) \frac{t_1}{t_1 + t_2}, \tag{5.4}$$

where $\epsilon_{r1} = \epsilon'_{r1}(1 - j\tan\delta_1)$, $\epsilon_{r2} = \epsilon'_{r2}(1 - j\tan\delta_2)$ and $(t1,t2)$ are the thicknesses of the substrates. Substituting the variables with the parameters from each substrate gives $\epsilon_B = 2.95 - j0.0038$ and $\epsilon_A = \epsilon_C = 4.47 - j0.0081$. It is expected that the formula for ϵ_B will be less accurate than the formula for ϵ_A and ϵ_C, due to the significant internal reflections within the layers when the cube is oriented such that the interfaces are normal to the wave propagation. It is also expected that ϵ_A would be slightly different from ϵ_C since the commercial boards are slightly anisotropic.

Figures 5.14 and 5.15 show the average values of the permittivity and permeability ex-

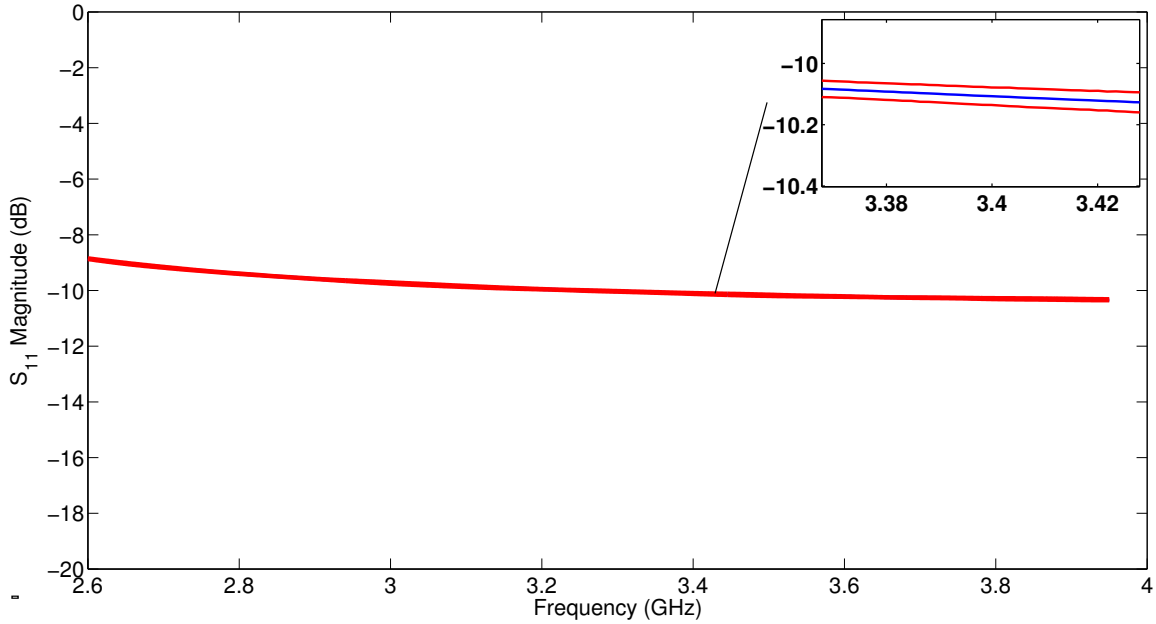

Figure 5.6 Magnitude of S_{11} from the uniaxial sample meausured 10 times at orientation 1. The center blue line is the average value of 10 measurements. The upper and lower lines in red show the 95% confidence interval.

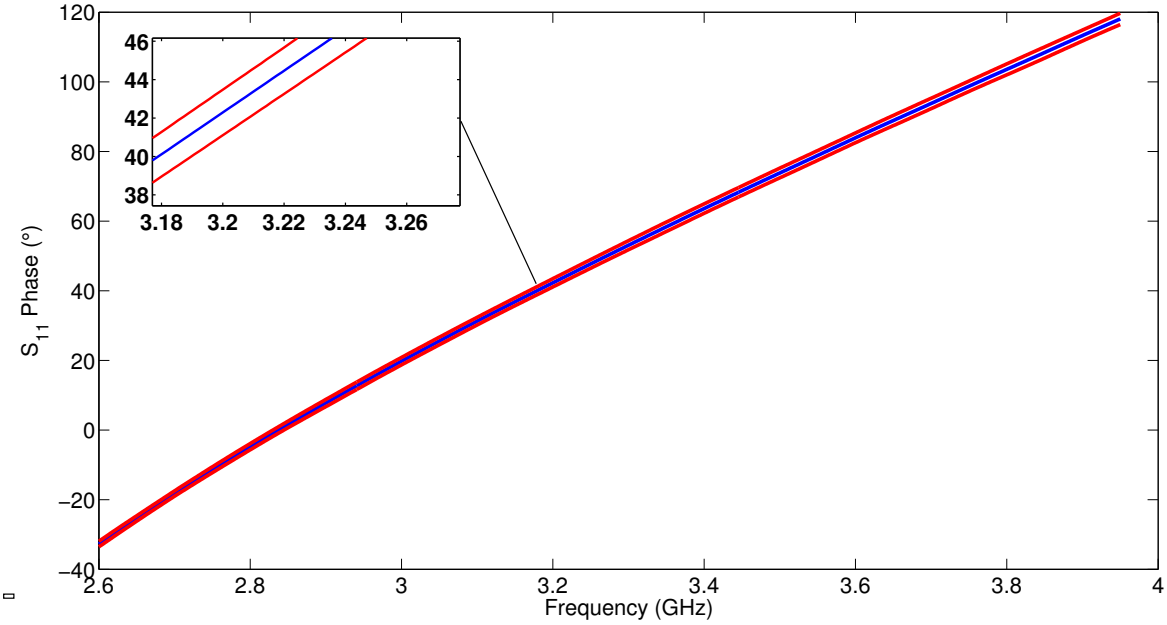

Figure 5.7 Phase of S_{11} from the uniaxial sample meausured 10 times at orientation 1. The center blue line is the average value of 10 measurements. The upper and lower lines in red show the 95% confidence interval.

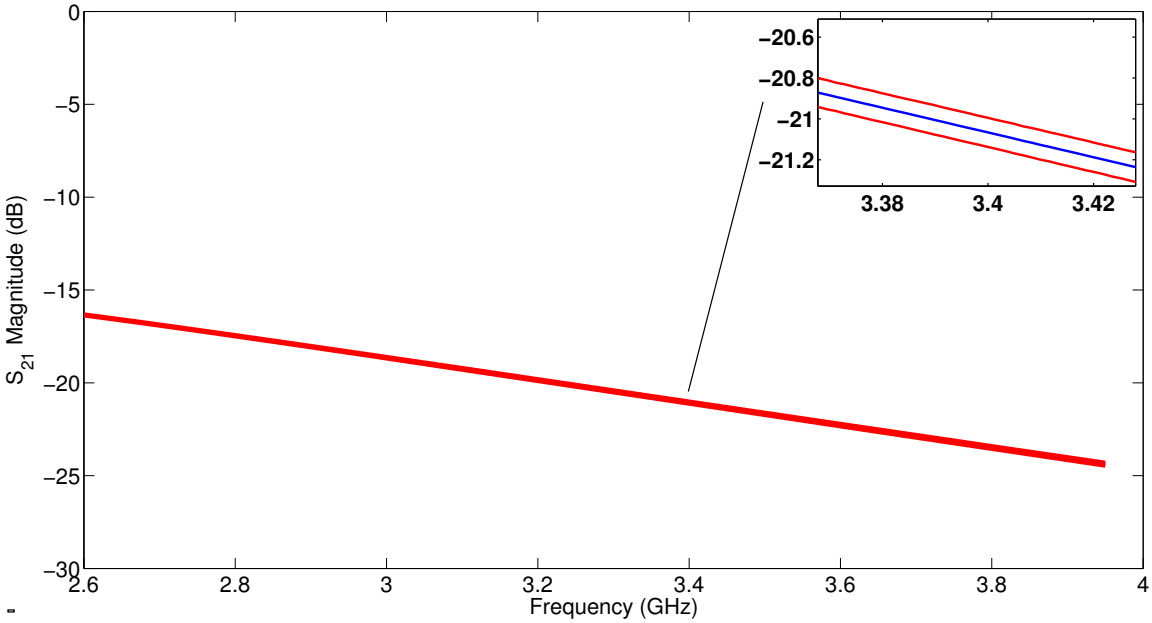

Figure 5.8 Magnitude of S_{21} from the uniaxial sample meausured 10 times at orientation 1. The center blue line is the average value of 10 measurements. The upper and lower lines in red show the 95% confidence interval.

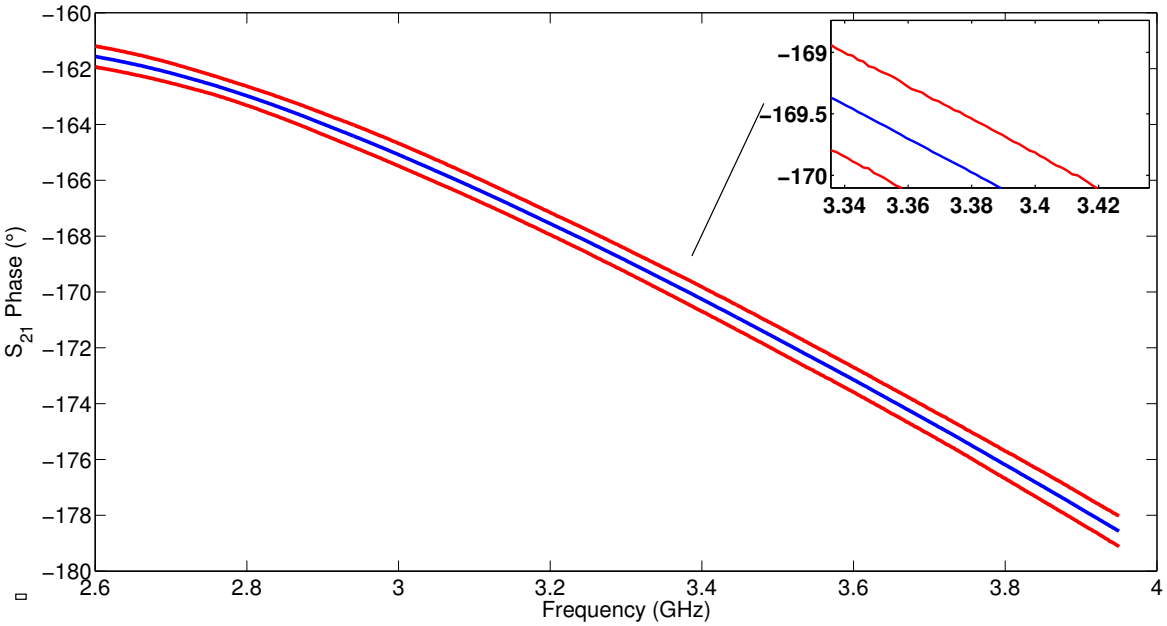

Figure 5.9 Phase of S_{21} from the uniaxial sample meausured 10 times at orientation 1. The center blue line is the average value of 10 measurements. The upper and lower lines in red show the 95% confidence interval.

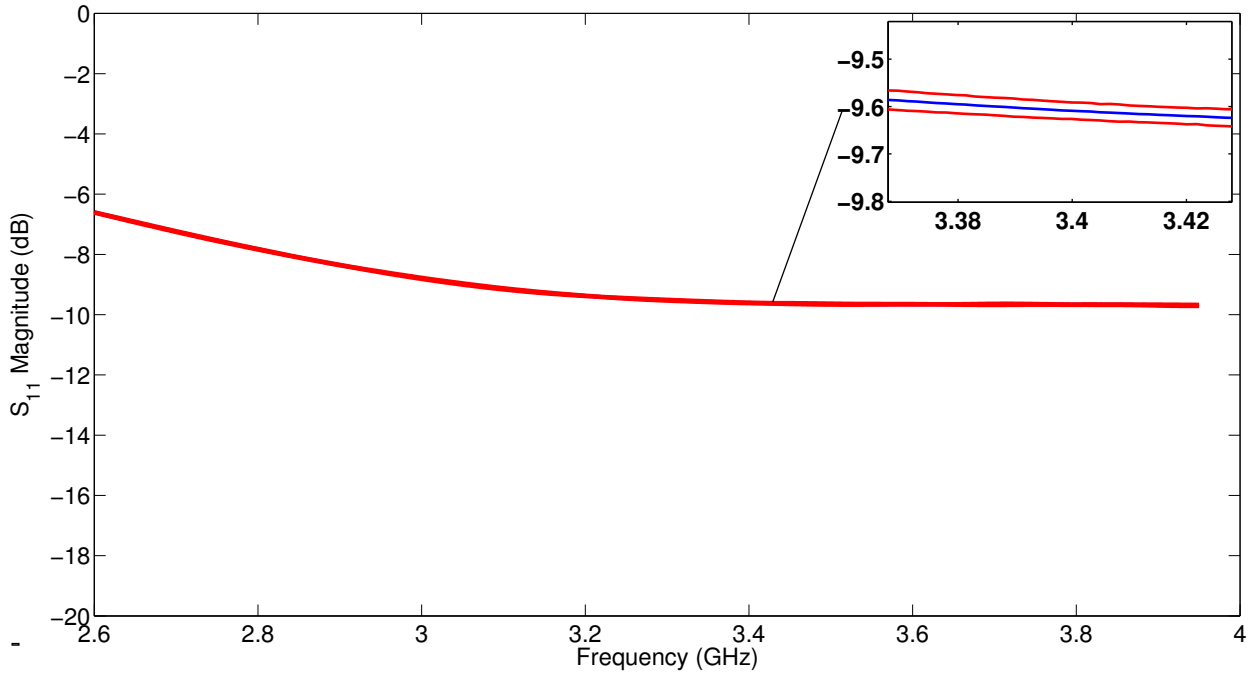

Figure 5.10 Magnitude of S_{11} from the uniaxial sample meausured 10 times at orientation 2. The center blue line is the average value of 10 measurements. The upper and lower lines in red show the 95% confidence interval.

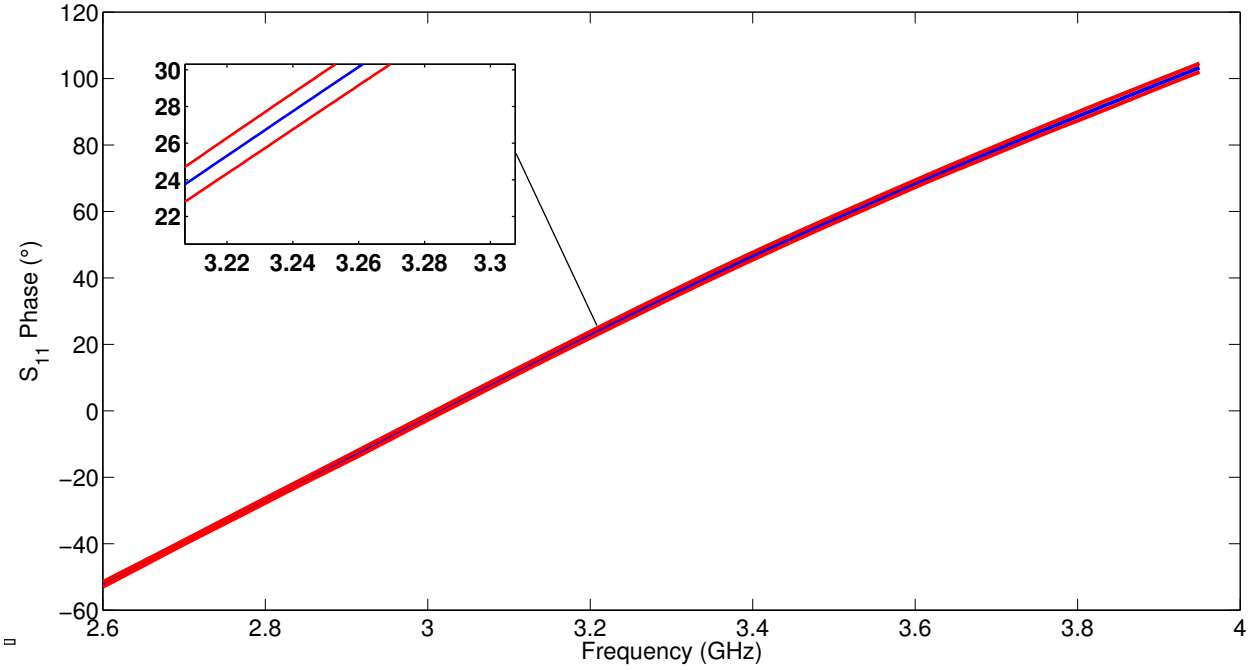

Figure 5.11 Phase of S_{11} from the uniaxial sample meausured 10 times at orientation 2. The center blue line is the average value of 10 measurements. The upper and lower lines in red show the 95% confidence interval.

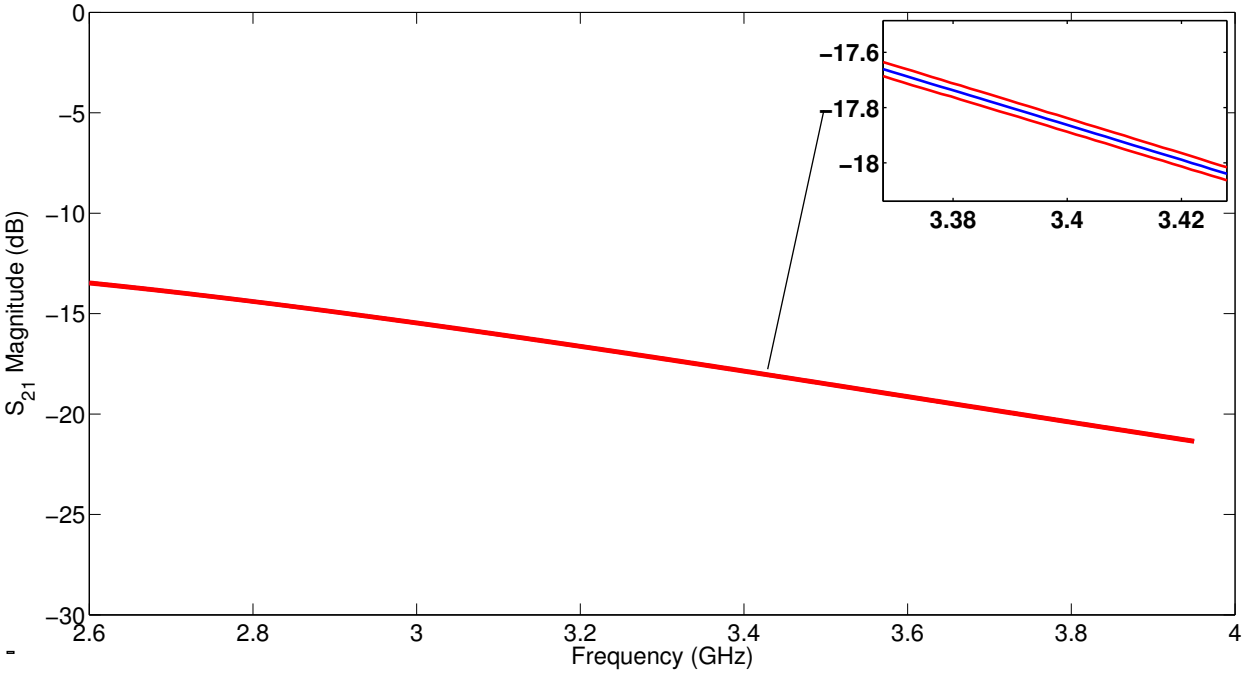

Figure 5.12 Magnitude of S_{21} from the uniaxial sample meausured 10 times at orientation 2. The center blue line is the average value of 10 measurements. The upper and lower lines in red show the 95% confidence interval.

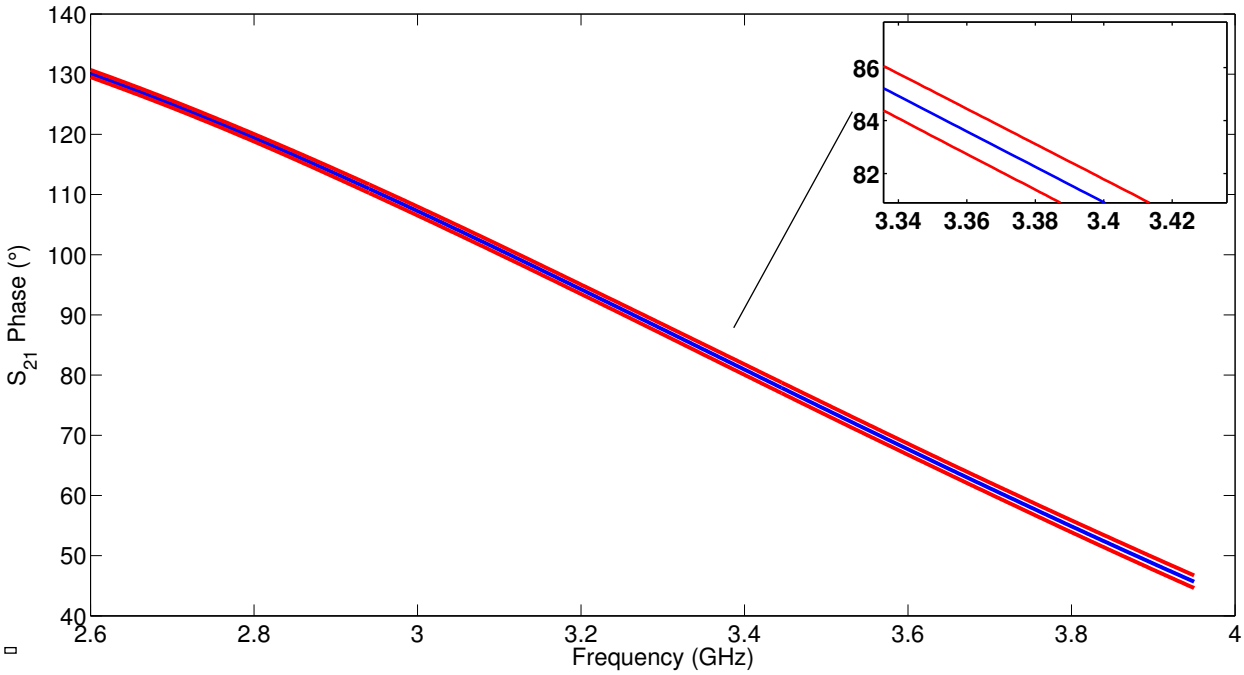

Figure 5.13 Phase of S_{21} from the uniaxial sample meausured 10 times at orientation 2. The center blue line is the average value of the 10 measurements. The upper and lower lines in red show the 95% confidence interval.

tracted from 10 sets of measurements of the uniaxial sample using the extraction approach for biaxial maeterial. The results for ϵ_A and ϵ_C are slightly higher than the estimated values, while ϵ_B is very close to the predicted value. The extracted values of μ_r are all close to unity since the sample is non-magnetic. The smaller insets in the figures show 95% $(2-\sigma)$ confidence intervals for a narrower frequency range. The average value of each parameter is individually shown in Figures 5.18 - 5.23. The narrow confidence intervals over the entire band indicate that noticeable variations in the extracted parameters are due to systematic errors, such as imperfect machining and alignment of the sample layers, or the presence of glue between sample layers, or air gaps between the sample and the waveguide walls. Also, data gaps in the frequency range between 3 and 3.15 GHz caused by ill-conditioning of the extraction process are observed. The data gaps are due to experimental uncertainties that are amplified near frequencies where the sample is a half-wavelength long. This behavior is a drawback of using a cubical sample and it is discussed in Section 2.2.5. For these two figures, extraction within a frequency band approximately ±5% near the half-wavelength frequency is avoided, and so data within that range is not displayed in the figures. Since the material parameters do not vary dramatically with frequency, it is possible to approximate the values within the gap region by interpolation. It is found that a fifth order polynomial fits the data of extracted parameters well over the entire frequency band. Figures 5.16 and 5.17 show the extracted parameters obtained by fitting a fifth-order polynomial to the data across the entire band. It can be seen that a good agreement with the estimated values is achieved.

As is described in Section 2.2 and 2.2.4, the partially-filled waveguide technique has many advantages, such as having no requirement for a sample holder, the reduced impact of air gaps, and faster computational time when compared to the reduced aperture waveguide technique [38]. The material parameters extracted for the same sample using these two techniques are compared and discussed. The average values of each parameter using the partially-filled waveguide are individually shown in Figures 5.18 - 5.23 and are compared

with the results obtained using a reduced-aperture waveguide. Similar results are seen for the parameters ϵ_A, ϵ_C, μ_B, and μ_C. However, for the results of ϵ_B and μ_A, the partially-filed waveguide technique shows more consistent and reasonable results. The values of ϵ_B in Figures 5.19 extracted from a reduced aperture waveguide show more variations, and the imaginary part of ϵ_B is positive over a wide frequency range, which contradicts the fact that the sample is lossy material. Similar behavior is also observed for μ_A in Figure 5.22. Note that the half wavelength difficulties also occur with the reduced-aperture waveguide technique, but due to the different propagation constants of the modes, a different gap range of 3.55-3.75 GHz is seen. Moreover, for ϵ_A and μ_B extracted using a reduced aperture waveguide, a secondary gap near 2.85 GHz is also observed while no extra data gap is observed for the partially-filled waveguide technique. To overcome the problem of data gaps, combining data from both techniques may reduce the impact of half-wavelength difficulties. This is left as future work.

5.2.3.3 Extracted Parameters of Materials with both Uniaxial Electric and Uniaxial Magnetic Properties

As is described in Section 5.2.3.2, a reasonable initial estimation of the material parameters for anisotropic sample can expedite the extraction process. Similarly, an estimation for the uniaxial sample is desired. However, the sample has both uniaxial electric and uniaxial magnetic properties, and no formulas were found to approximate the permeability of the sample. However, formulas (5.3) can still be used to estimate the permittivity of the sample. The electric properties of Eccosorb FGM-125 can be obtained from the manufacturer specification sheet. However, the data sheet published by the manufacturer only shows the material parameters across a wide frequency range of 1-18 GHz with few data points. Thus, more permittivity and permeability data for the FGM-125 in the S-band is needed to estimate the sample parameters.

The material parameters of the FGM-125 were extracted at S-band using the Nicolson-

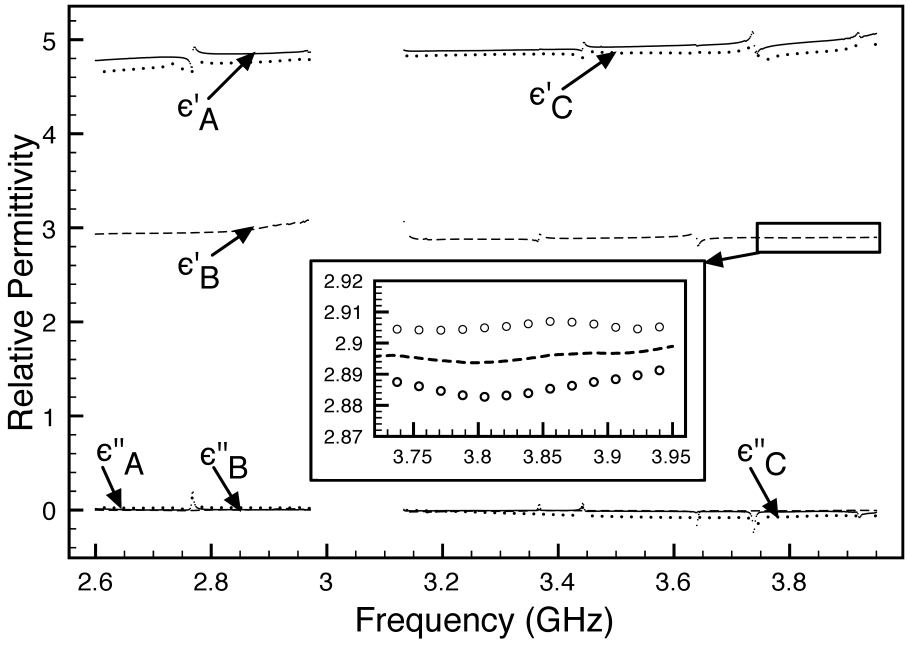

Figure 5.14 Relative permittivities (mean values) of the biaxial sample extracted using 10 measurement sets. Inset shows $2-\sigma$ confidence interval.

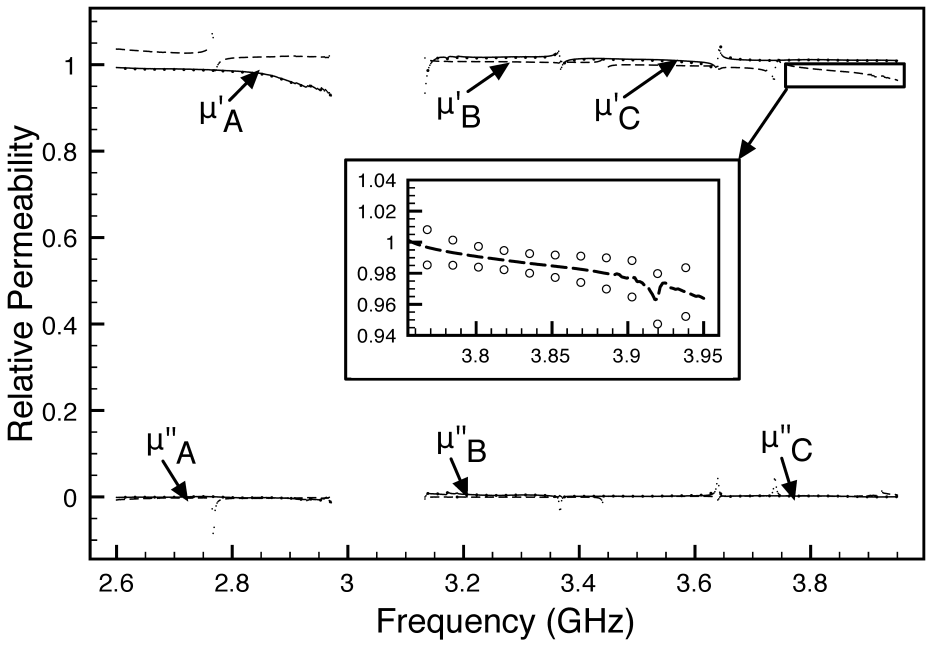

Figure 5.15 Relative permeabilities (mean values) of the biaxial sample extracted using 10 measurement sets. Inset shows $2-\sigma$ confidence interval.

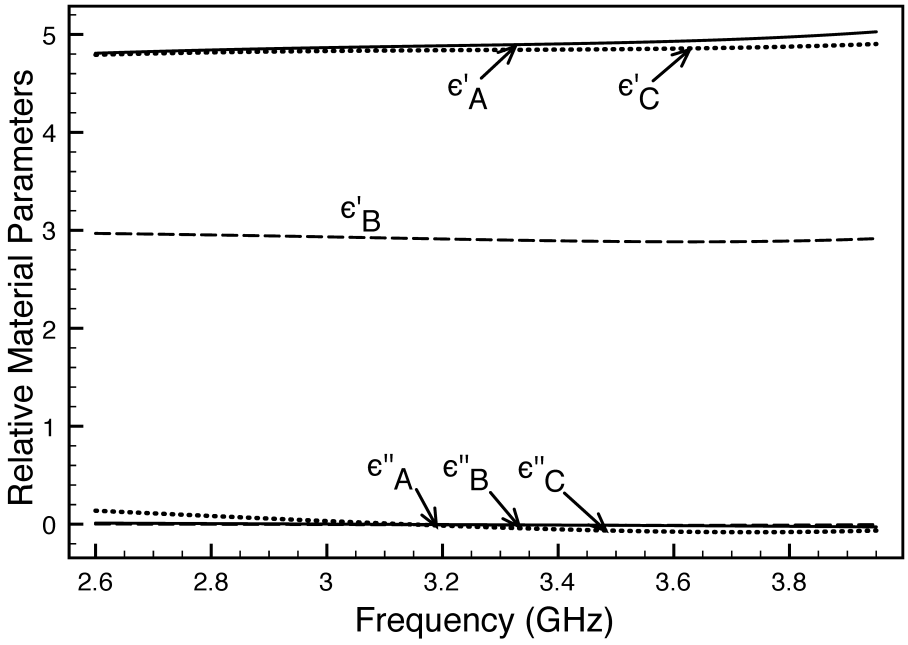

Figure 5.16 Extracted relative permittivities of the biaxial sample fitted to a fifth-order polynomial.

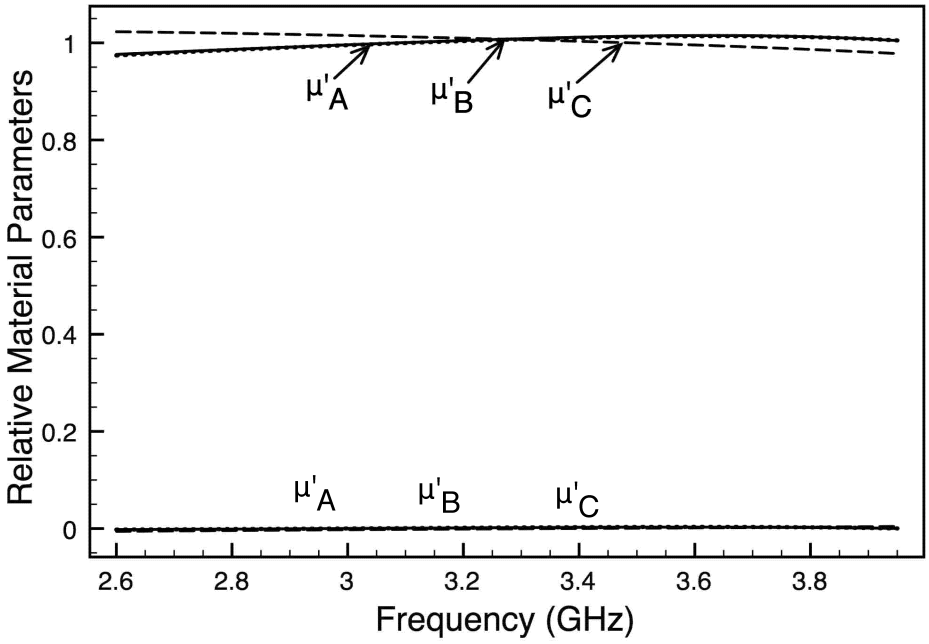

Figure 5.17 Extracted relative permeabilities of the biaxial sample fitted to a fifth-order polynomial.

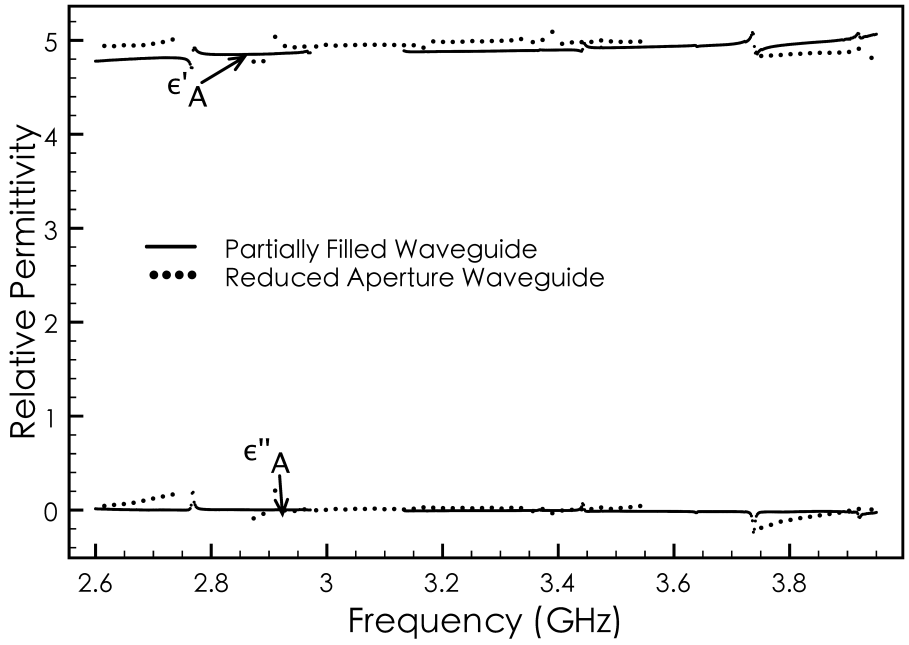

Figure 5.18 Comparison of ϵ_A for the biaxial sample extracted using the partially-filled waveguide technique and the reduced-aperture waveguide technique.

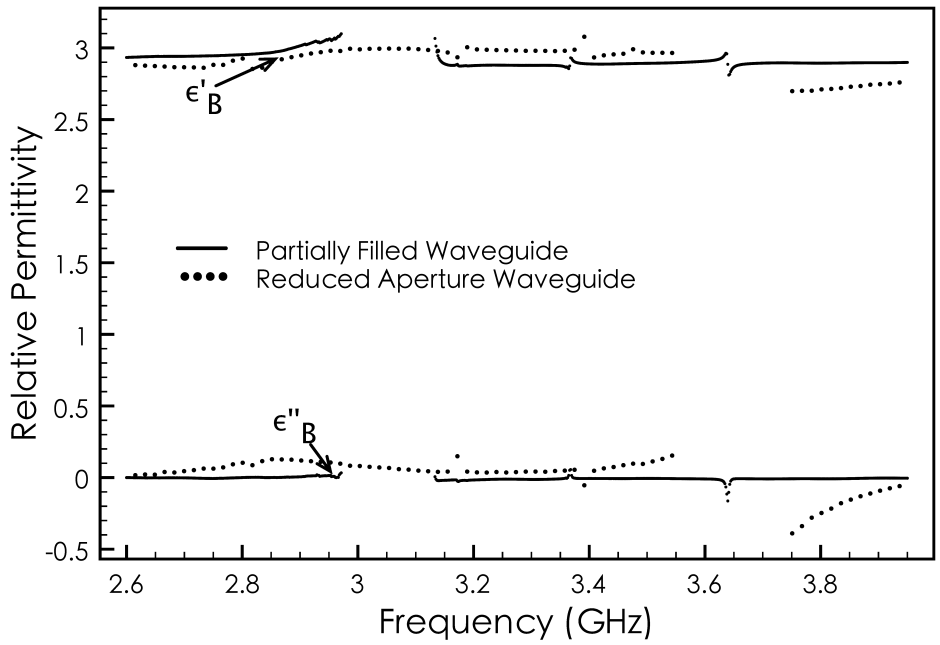

Figure 5.19 Comparison of ϵ_B for the biaxial sample extracted using the partially-filled waveguide technique and the reduced-aperture waveguide technique.

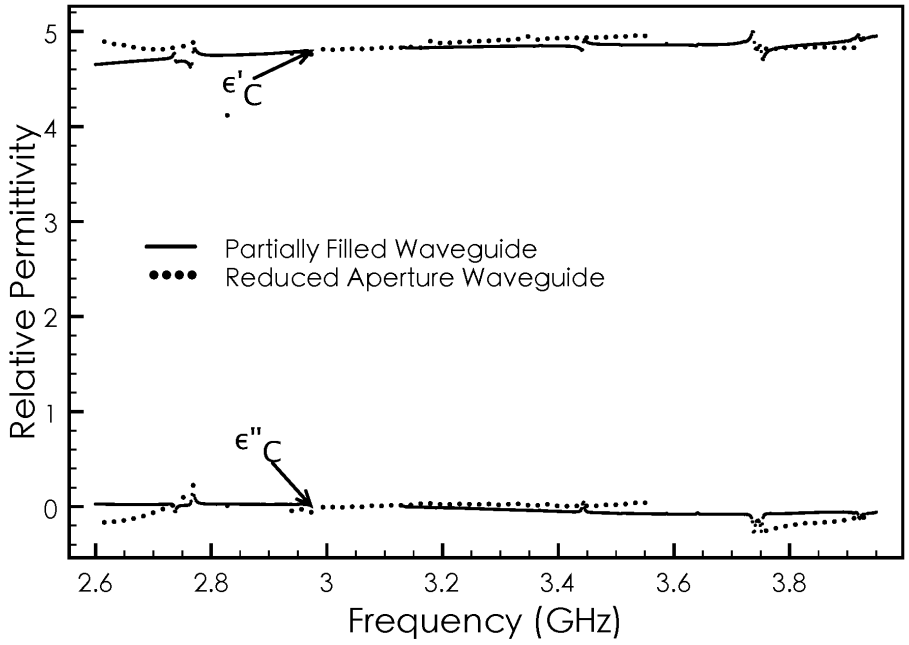

Figure 5.20 Comparison of $_C$ for the biaxial sample extracted using the partially-filled waveguide technique and the reduced-aperture waveguide technique.

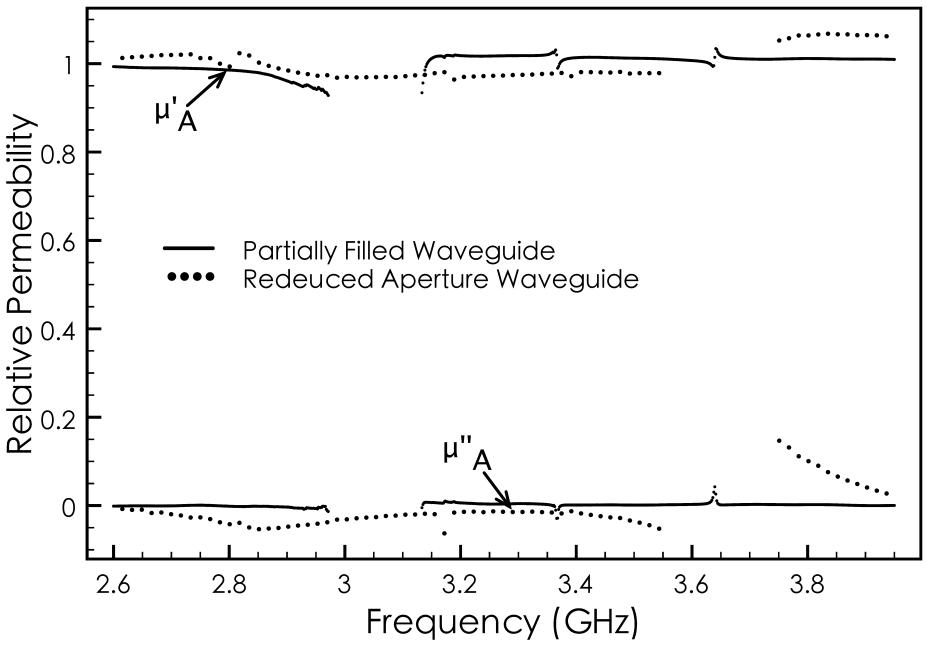

Figure 5.21 Comparison of μ_A for the biaxial sample extracted using the partially-filled waveguide technique and the reduced-aperture waveguide technique.

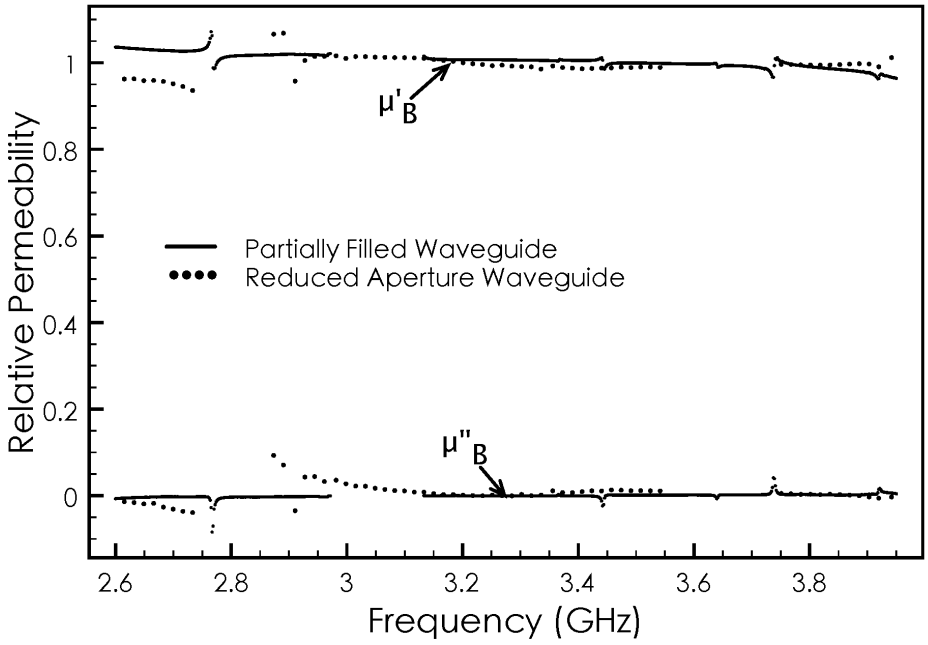

Figure 5.22 Comparison of μ_B for the biaxial sample extracted using the partially-filled waveguide technique and the reduced-aperture waveguide technique.

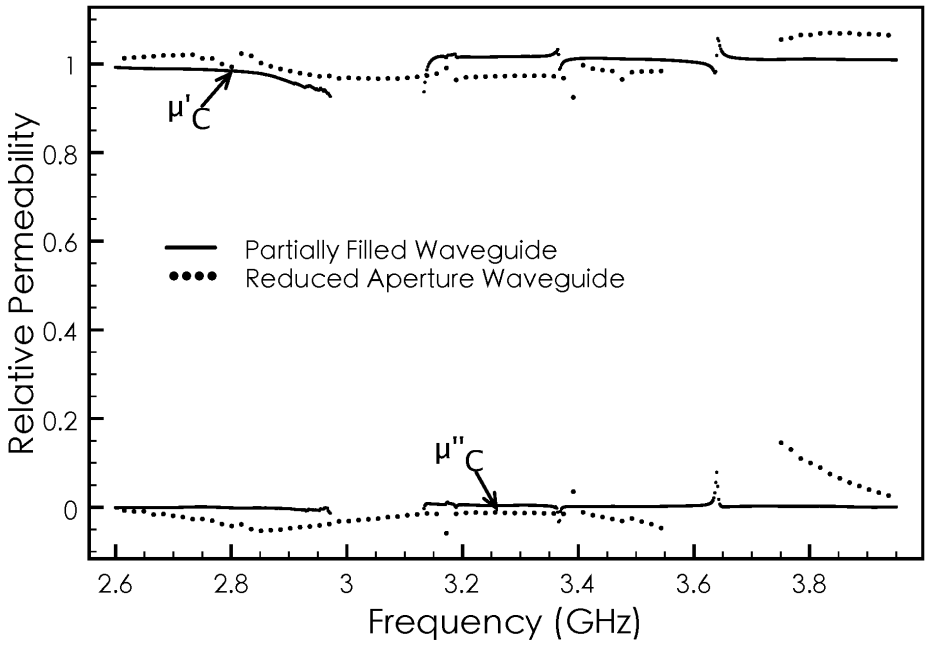

Figure 5.23 Comparison of μ_C for the biaxial sample extracted using the partially-filled waveguide technique and the reduced-aperture waveguide technique.

Ross-Wier closed-form method [28] since this technique is well developed and it is easy to implement both theoretically and experimentally. A piece of FGM-125 having the same size as that used in the S-band waveguide aperture was cut and backed by a foam block to keep it vertically straight in the waveguide extension. The measurement repeatability error was assessed by measuring the FGM-125 sample 5 times, with the VNA calibrated using the S-band waveguide at the start of each set of measurements. A cross-section view of the waveguide completely filled with FGM-125 is shown in 5.24. The permittivity extracted from the 5 measurements is shown in Figure 5.25, while the permeability is shown in Figure 5.26. The center lines in these figures show the average value of the extracted values while the upper and lower solid lines show the 95% confidence levels, or ± 2 standard deviations. It can be seen that the confidence intervals for these parameters are wide and increase at higher frequencies. This might be due to the inconsistent placement of the FGM-125 sheet in the waveguide. It is also observed that the variation of permittivity across the S-band is not significant and dielectric loss is small while the opposite is true for the permeability. With the parameters of the FGM-125 at S-band and the parameters of Rogers 5870, the approximate permittivity of the sample can be determined using (5.3). At 2.6 GHz, the formulas give $\epsilon_B = 4.55 - j0.0326$ and $\epsilon_A = \epsilon_C = 5.91 - j0.0779$.

The measured data from 10 sets of measurement of the second sample were used to extract the material parameters. Each set contains measurements of the sample given at two orientations. The same de-embedding procedure described in (5.9) was used to shift the reference plane from the calibration plane to the sample planes. Figures 5.27 - 5.30 show the average value of the permittivity and permeability extracted from 10 sets of measurements of the sample. The results for ϵ_A and ϵ_B are lower than the estimated value and this may be due to the reduced thickness of the FGM-125 during the sample construction or excessive glue being applied between the layers. The variations in the extracted permittivity are smaller when compared with Figures 5.14 and 5.15 which are obtained using the three-step approach. Also, the overall trend of permeability across the S-band is smoother. However, data gaps

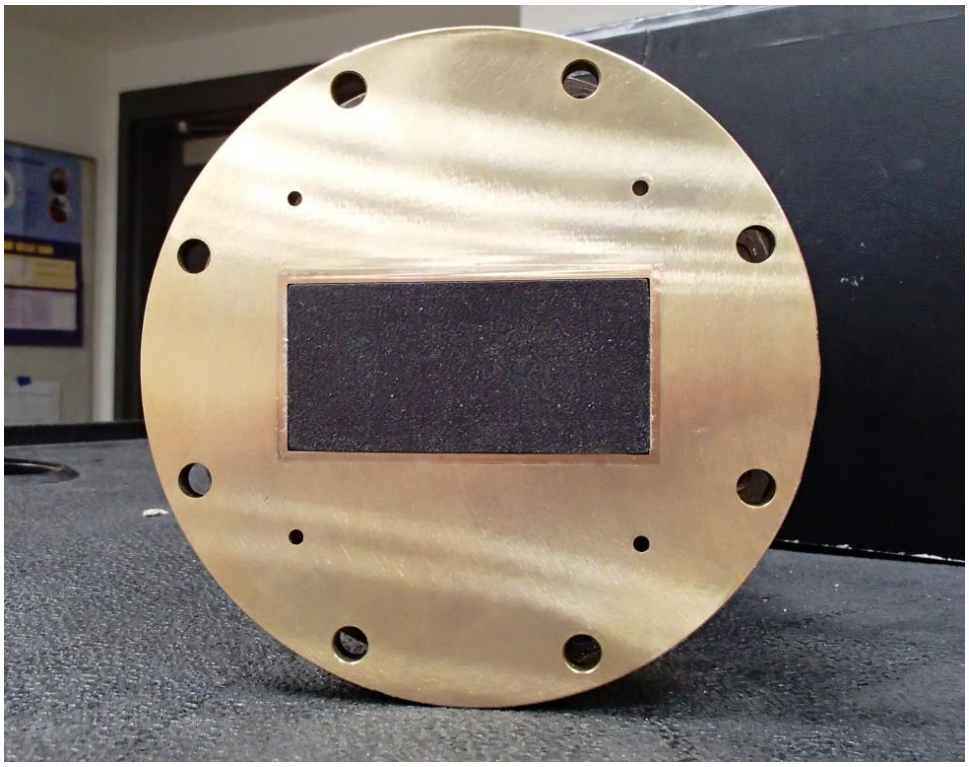

Figure 5.24 FGM125 completely filled in the waveguide.

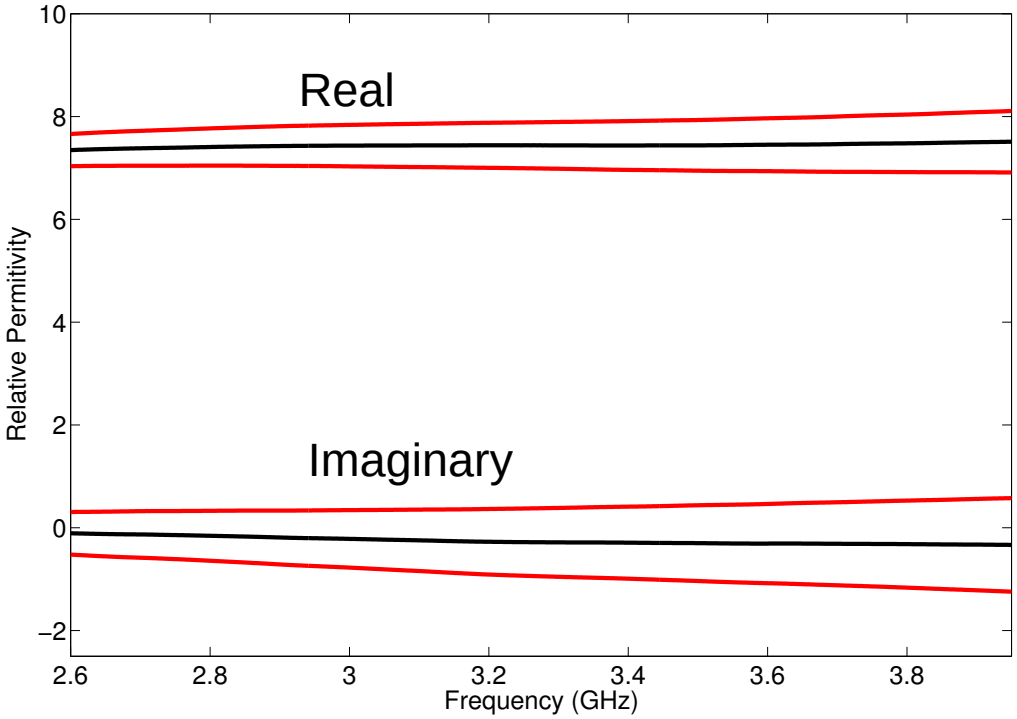

Figure 5.25 Real and imaginary parts of relative permittivity extracted from 5 sets of measurements of FGM-125. Center line is the average of the extracted parameter. Upper and lower lines show the 95% confidence intervals.

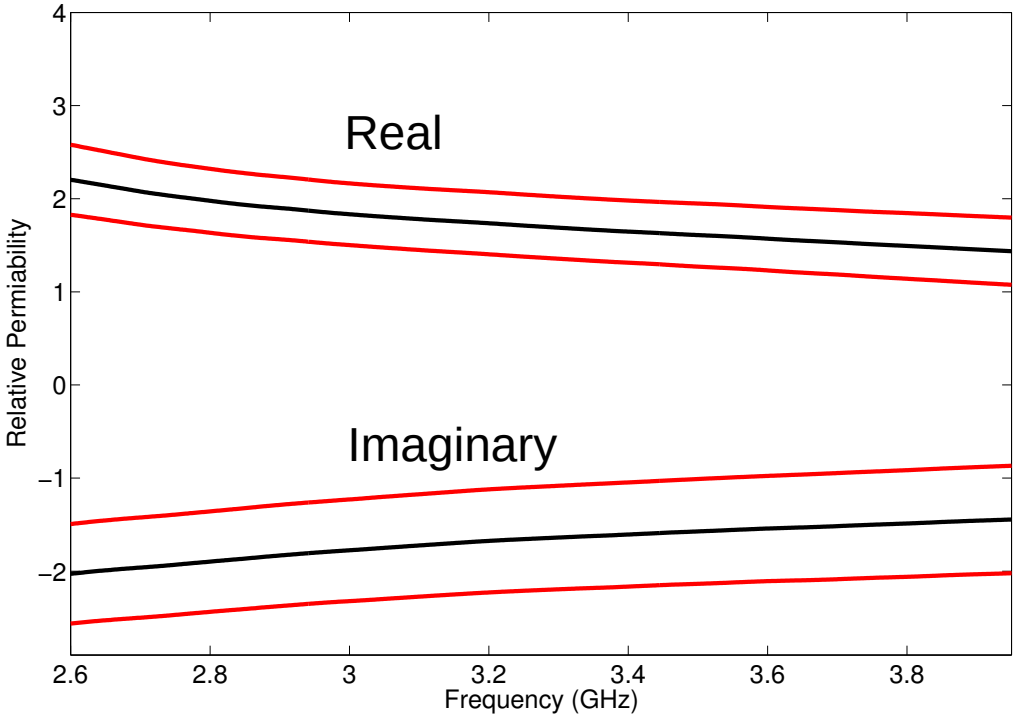

Figure 5.26 Real and imaginary parts of relative permeability extracted from 5 sets of measurements of FGM-125. Center line is the average of the extracted parameter. Upper and lower lines show the 95% confidence intervals.

which are seen in Figures 5.14 and 5.15 still appear in ϵ_A and μ_B. The half wavelength difficulties are experienced when using the three-step approach, but such problems were not seen in the test using a fictitious material sample (Figures 2.15-2.18). Since these gaps only appear in ϵ_A and μ_B which are obtained after the completed extraction of ϵ_B and μ_A (Section 2.2.4), this suggests the gaps are consequences of amplified propagation of experimental uncertainties that lead to a failure for the root-solving algorithm to obtain the parameters. Note that the gap widths vary between each set of measured data, but they all fall into the frequency ranges of 2.96-3.01 GHz and 3.62-3.7 GHz. Therefore, data in those two regions are avoided. The overall results suggest this method can tolerate measurement uncertainties and is useful for extracting parameters from uniaxial samples.

5.3 Characterization of Gyromagnetic Material

This section focuses on the experimental validation of extracting material parameters of a sample of gyromagnetic material using a partilly-filled waveguide technique. The advantages of of this technique are that no special sample holder is required and since typically the size of gyromagnetic sample available on the market is limited, thus this method eliminates the need for the large sample required by standard waveguide techniques in which a sample completely fills the rectangular waveguide cross section. Modal analysis has been carried out to determine the reflection and transmission coefficients of the dominant mode. An optimization algorithm described in Section 4.4 was employed which minimizes the difference between the measured and the theoretical reflection and transmission coefficients to extract the gyromagnetic material parameters and internal magnetic biasing strength.

5.3.1 Experimental System Setup

Since the extraction of all the constitutive parameters of the gyromagnetic material is based on an optimization process which minimizes the difference between the measured and the

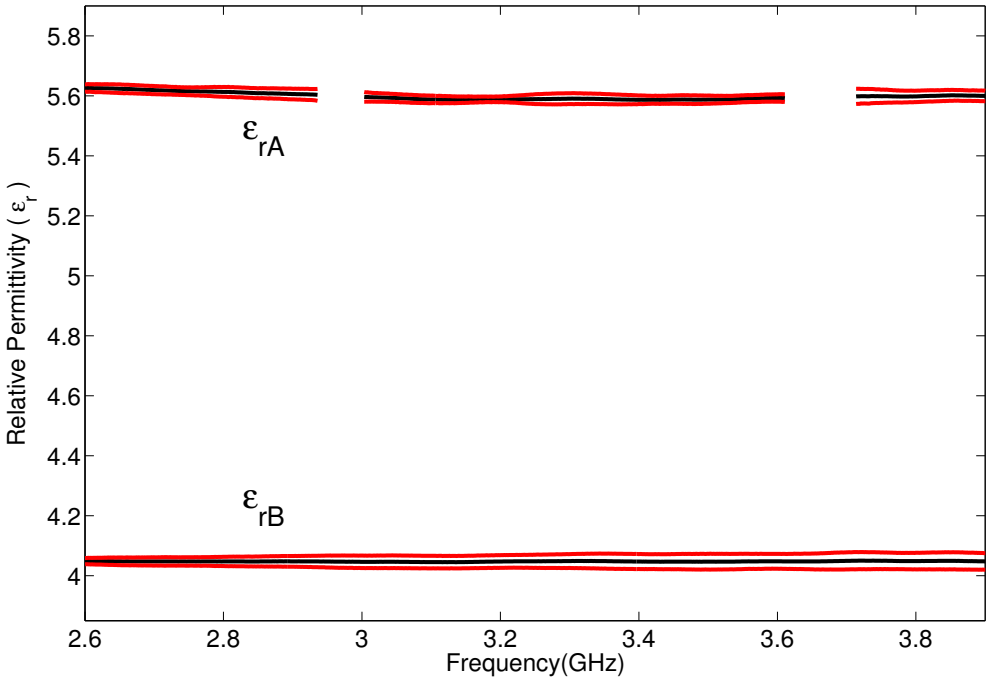

Figure 5.27 Relative permittivities (real part) of the uniaxial sample extracted using 10 sets of measurements. Center line is the average of the extracted parameter. Upper and lower lines show the 95% confidence intervals.

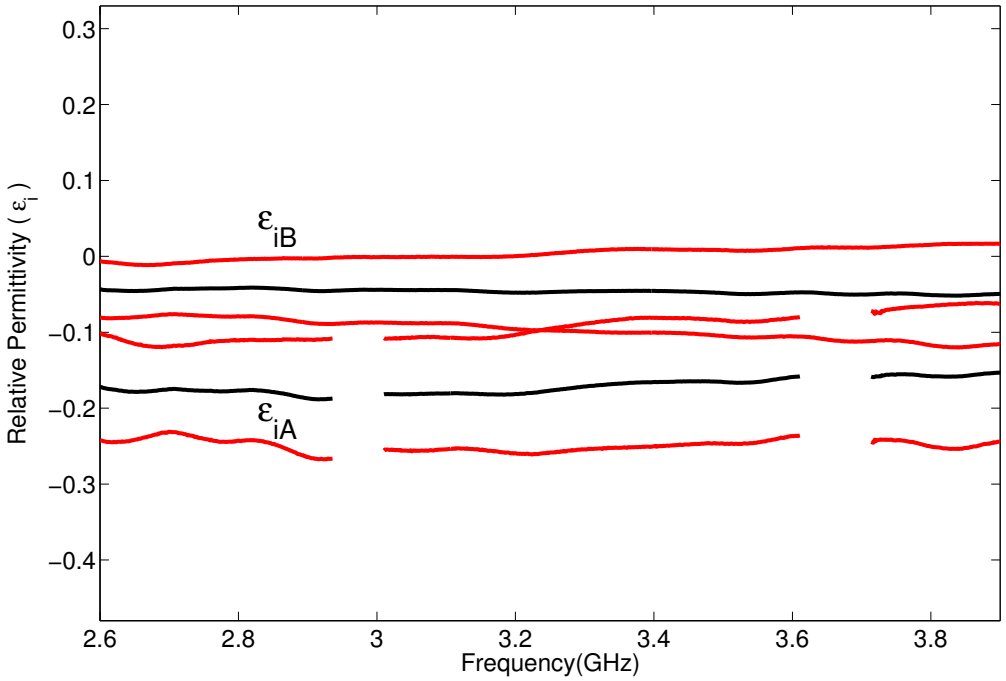

Figure 5.28 Relative permittivities (imaginary part) of the uniaxial sample extracted using 10 sets of measurements. Center line is the average of the extracted parameter. Upper and lower lines show the 95% confidence intervals.

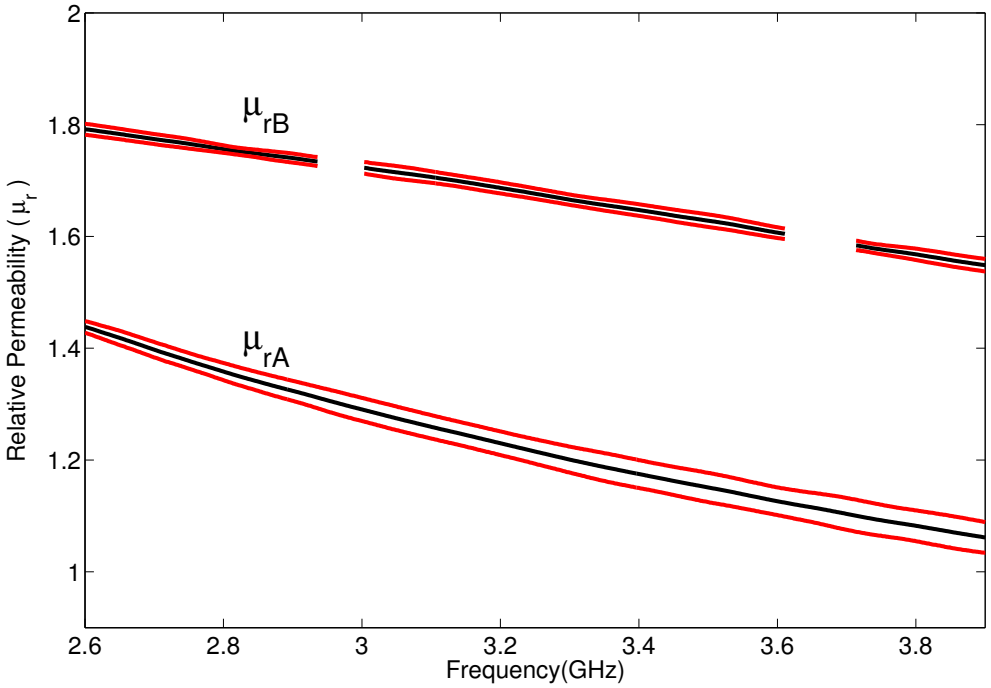

Figure 5.29 Relative permeabilityies (real part) of the uniaxial sample extracted using 10 sets of measurements. Center line is the average of the extracted parameter. Upper and lower lines show the 95% confidence intervals.

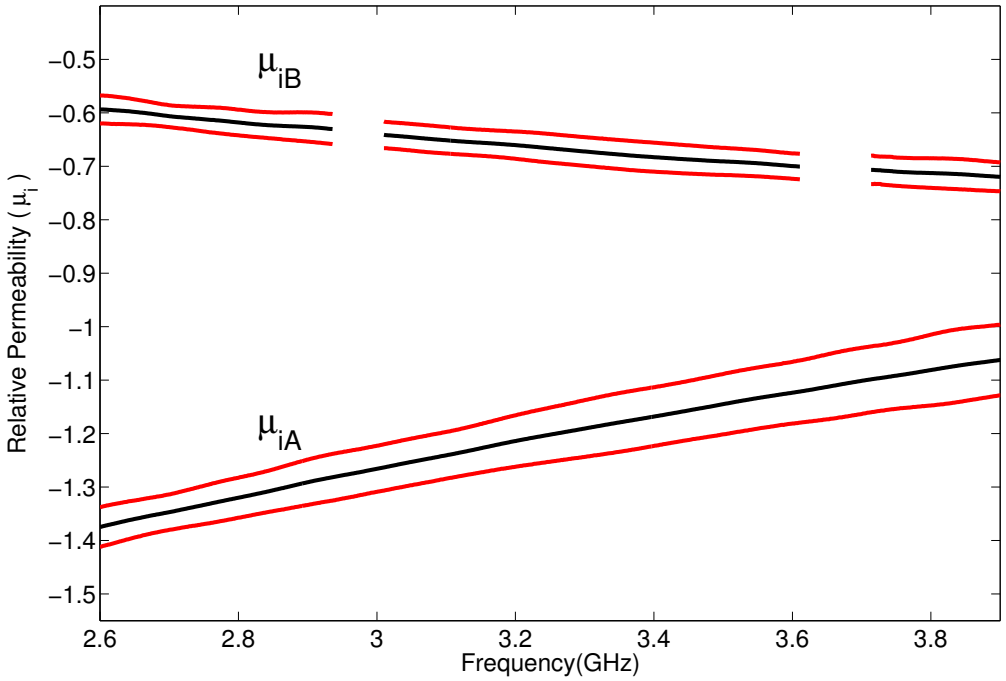

Figure 5.30 Relative permeabilityies (imaginary part) of the uniaxial sample extracted using 10 sets of measurements. Center line is the average of the extracted parameter. Upper and lower lines show the 95% confidence intervals.

theoretical reflection and transmission coefficients, the measurement system should be constructed in a way that best matches the theoretical model under which the S-parameters are predicted. The measurement system consists of waveguide ports and waveguide extensions, and a wooden fixture containing two permanent magnets which are used to produce a consistent but not quiet uniform magnetic biasing field in the area where the sample is located. Different magnetic biasing fields can be obtained by separating the two magnets at certain distance. Multiple S-parameters were taken for the extraction under different magnetic biasing strengths. Details of the experiments including sample preparation and system set-up are presented and discussed.

5.3.1.1 Gyromagnetic Material Sample Specifications

As is shown in Section 3.1.1, the material parameters of gyromagnetic material can be described by tensors

$$\epsilon = \epsilon_0 \begin{bmatrix} \epsilon_r & 0 & 0 \\ 0 & \epsilon_r & 0 \\ 0 & 0 & \epsilon_r \end{bmatrix} \tag{5.5}$$

and

$$\mu = \mu_0 \begin{bmatrix} \mu_g & 0 & -j\delta \\ 0 & 1 & 0 \\ j\delta & 0 & \mu_g \end{bmatrix}, \tag{5.6}$$

where the permeability tensor is formulated when a material is biased along the height of the waveguide or in the y-direction. The variables ϵ_r, δ, and μ_g are complex numbers: $\epsilon_r = \epsilon_r' + j\epsilon_r''$, $\delta = \delta' + j\delta''$ and $\mu_g = \mu_g' + j\mu_g''$. Here the off-diagonal parameter δ and μ_g are given by

$$\delta = \frac{f f_m}{f^2 - f_0^2} \tag{5.7}$$

and

$$\mu_g = \left(1 - \frac{f_0 f_m}{f^2 - f_0^2}\right), \tag{5.8}$$

In (5.7) and (5.8), f is the operating frequency, $f_m = 2.8 \times 10^6 \times 4\pi M_s$, and $f_0 = 2.8 \times 10^6 \times \left(H_0 + j\frac{\triangle H}{2}\right)$. Here H_0 is the strength of the internal static biasing magnetic field in Oersted and M_s the saturation magnetization typically expressed as $4\pi M_s$ in gauss. The magnetic losses inherent in the magnetic materials are also taken account by the linewidth $\triangle H$. The gyromagnetic material empolyed in the measurements is a sample of G1010, a commercial material manufactured by Trans-Tech, Inc [55]. The typical range of the material parameters of the G1010 sample are shown in the sample specification sheet. The dielectric constant ϵ_r' is within the range of 13.97-15.44, the dielectric loss tangent $\tan(\delta_e)$ is within the range of $0 - 0.0002$, the linewidth is within the range of 0-30 Oe and $4\pi M_s$ is within the range of $950 - 1050$ G. Note that the manufacture also provided the tested material parameters of the corresponding purchased sample, in which, ϵ_r' is listed as 14.24, the loss tangent $\tan(\delta_e)$ is 0.0005, the linewidth $\triangle H$ is 19 Oe, and $4\pi M_s$ is 989 G.

Notice that both dielectric and magnetic losses of the G1010 material are small, and since it is seen in Figure 4.14-4.16 that good agreement between the theoretical S-parameters generated from a lossless G1010 sample and measured data, it is assumed that a good approximation of the measured S-parameters can be obtained by only incorporating parameters of ϵ_r', $4\pi M_s$. The extraction of the full properties of the G1010 sample will be carried out in the future and is discussed in the future work section. Furthermore, the extraction of H_0 as a third parameter is also conducted along with the two other parameters. The extracted values of the physical parameters are compared with the values provided by the

manufacture to evaluate the performance of the proposed method, and the extracted internal magnetic biasing field strength H_0 is also compared with the average value obtained using a gaussmeter.

The G1010 sample is a hard ceramic material which cannot be machined by regular CNC milling machine. Therefore, the G1010 sample was purchased from Island Ceramic Grinding, Inc [56] where it was ground into the desired dimensions to fit into the S-band waveguide. The final dimension of the purchased sample is 34.04 mm by 34.04 mm with a thickness of 5 mm. It is very important to mention that this material is very brittle, and thus it should be handled with care to protect the corners from chipping so that multiple measurements can be taken from a sample with the same dimensions. Figure 5.31 shows the final machined G1010 sample.

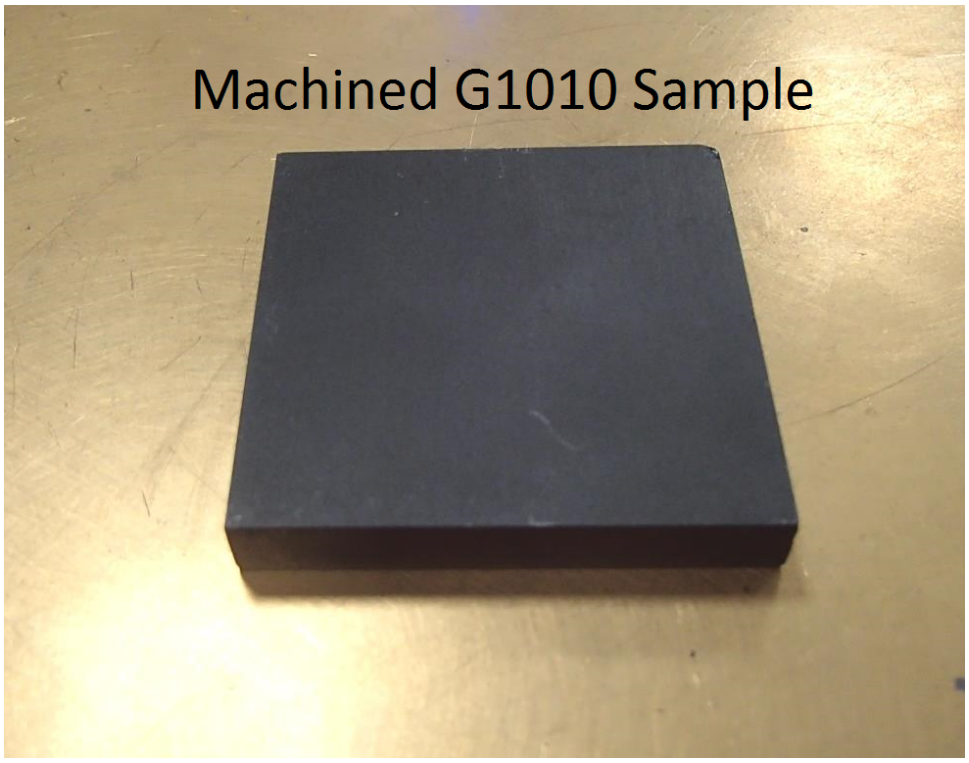

Figure 5.31 Machined G1010 sample.

5.3.1.2 Measured Magnetic Biasing Fields

As is mentioned in Section 3.1.1, when the external static magnetic field is parallel to a thin layer of ferrite sample, the internal magnetic field H_0 is nearly equal to the external magnetic biasing field H_a. In this work, the applied magnetic field is parallel to the broad face of the gyromagnetic sample, and that results in the magnetic field at the surface of the sample being equal to the internal magnetic field. Typically, an external biasing source offers an evenly distributed magnetic field which can be obtained by either a proper solenoid or certain permanent magnets. Permanent magnets are employed here because they are inexpensive and easy to implement. However, few magnets are available on market that can simultaneously meet the need for desired field strength and a large size which have a relatively more even field at the center. In the end, magnets with high field strength and also having a proper size for biasing the sample were purchased from K&J Magnets [**?**]. Two magnets were purchased which are 4 inches $\times$ 1 inch $\times$ 1 inch sized neodymium blocks with magnetization direction through the thickness (1 inch side). A large square magnet would be preferred since a more even magnetic field can be obtained near the center, but the cost will increase tremendously and it could be very dangerous for the experimentalist to use larger magnets since the pulling force may extend to 500 lb. To prevent possible accidents during the experiments and also to create a consistent configuration of the magnetic biasing field, a wooden fixture was built to set the two magnets apart at a desired distance and allow the fixture to be attached to the outside of the waveguide extension. A photo of the fixture is shown in Figure 5.32.

Since the sample is measured inside the waveguide with the magnet fixture attached, it is crucial to understand what the actual external biasing magnetic field for the G1010 sample with the presence of the waveuguide is. A Bell 5070 series guassmeter [58] with a 4 inches probe was used to to measure the magnetic distribution in the cross-section of the waveguide where the sample was placed at. The probe of the gaussmeter was placed at different location in the waveguide and the magnetic field at that point along the y direction (perpendicular to

the broad size of the waveguide) was measured. A total of 84 points were measured for the entire cross-section of the waveuide, and that procedure was repeated three times to obtain the average field distribution inside the waveguide. Figure 5.33 shows the magnetic field strengths inside the waveguide; the average of all measured value is 3346.2 G. It is noticed that a stronger field can be obtained near the surface of the magnets and the magnetic field is strongest near the center of the magnets. Also, as the probe moves away from the surface of the magnet, the measured magnetic field decreases until the probe reaches the center point between the two magnets.

Two pairs of spacers made of rigid polystyrene foam with thicknesses of 5 mm and 9.7 mm were inserted between the waveguide walls and the fixture to increase the separation distance of the magnets in order to obtain a weaker field strength. Figures 5.34 and 5.35 show the magnetic field strengths under these two separations, with average measured fields of 1978.4 and 1647.3 G, respectively. It is obvious that the average magnetic field decreases dramatically with the insertions of thin spacers, and the variations of the field within the guide follow the same trend as when no spacer was added.

5.3.1.3 Experiment Set-up

To prevent the sample from moving in the waveguide during the measurement procedure, sample holders made of polystyrene foam was built to hold the G1010 sample at various positions of the waveguide. The geometry of the holders were designed to facilitate the placement and the removal of the sample. Figure 5.36 shows one waveguide extension containing one sample holder with the magnet fixture attached. Measurements of the S-parameters of the G1010 sample with different biasing field strengths were taken using the Agilent E5071C VNA. The calibration procedure using the S-band waveguide and VNA settings are described in Section 5.2.2. The VNA was calibrated 10 times using the Thru-Reflect-Line (TRL) method and three measurements with different magnetic biasing strengths were taken under each calibration. In the end, a total of 30 measurements were obtained for the case

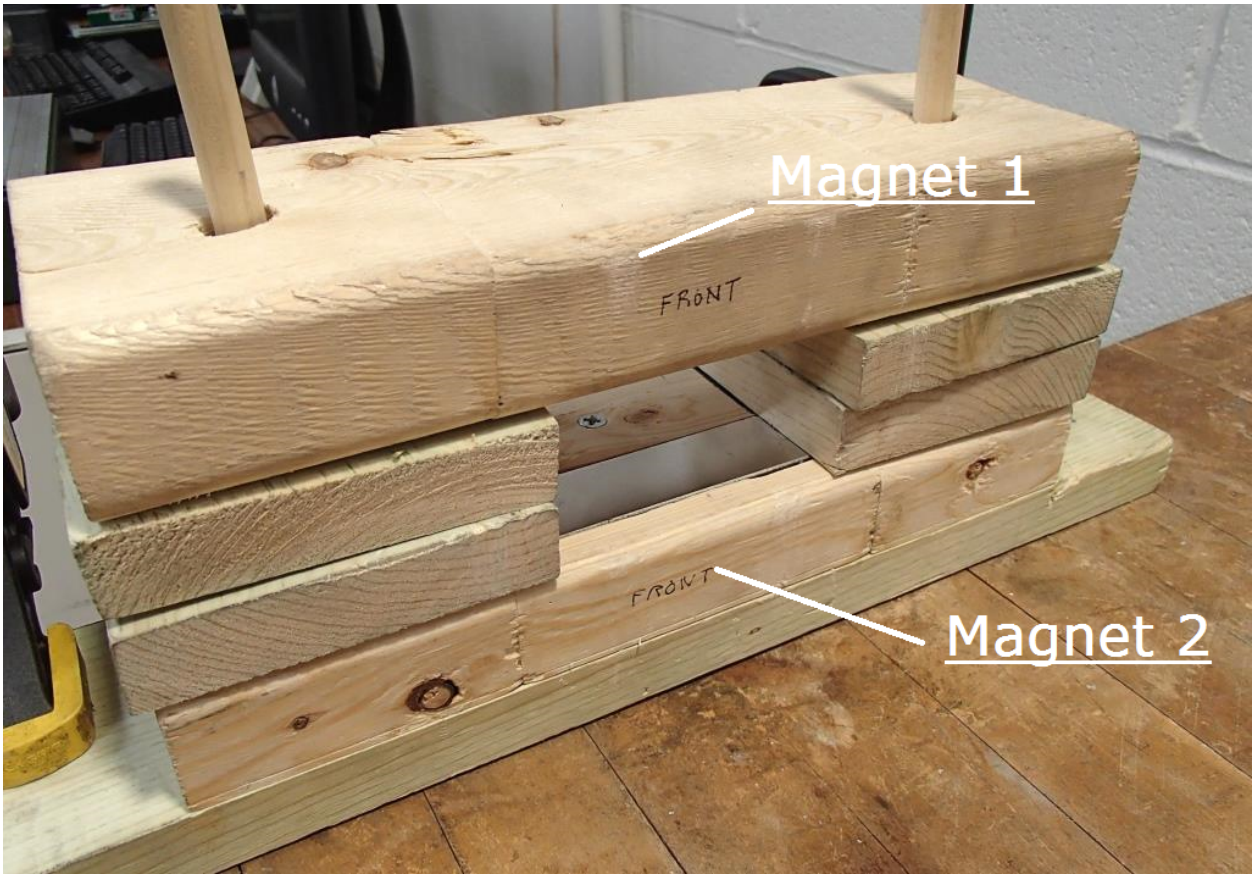

Figure 5.32 Wooden fixture containing two magnets.

where the sample was located at the center of the waveguide.

Like the measurements of cubical uniaxial samples shown in Section 5.2.2, the G1010 sample was inserted into the waveguide extension attached to port 1; the placement of the sample is shown in Figure 5.37. The S-parameters of the sample were measured by the VNA at the calibration plane. However, the extraction method requires using S-parameters referenced to the sample planes z=d+Δ and z=d. Therefore, the measured S-parameters have to be mathematically de-embedded to the sample planes. The S-parameter can be shifted from the calibration plane to the sample planes by multiplying by $e^{-j\beta D}$ in the direction of the wave propagation. Here, β is the propagation constant of the empty waveguide extension, and D is the distance of an appropriately chosen shift, depending on whether S_{11} or S_{21} is corrected. For the measurement of the sample shown in Figure 5.31, the reference plane

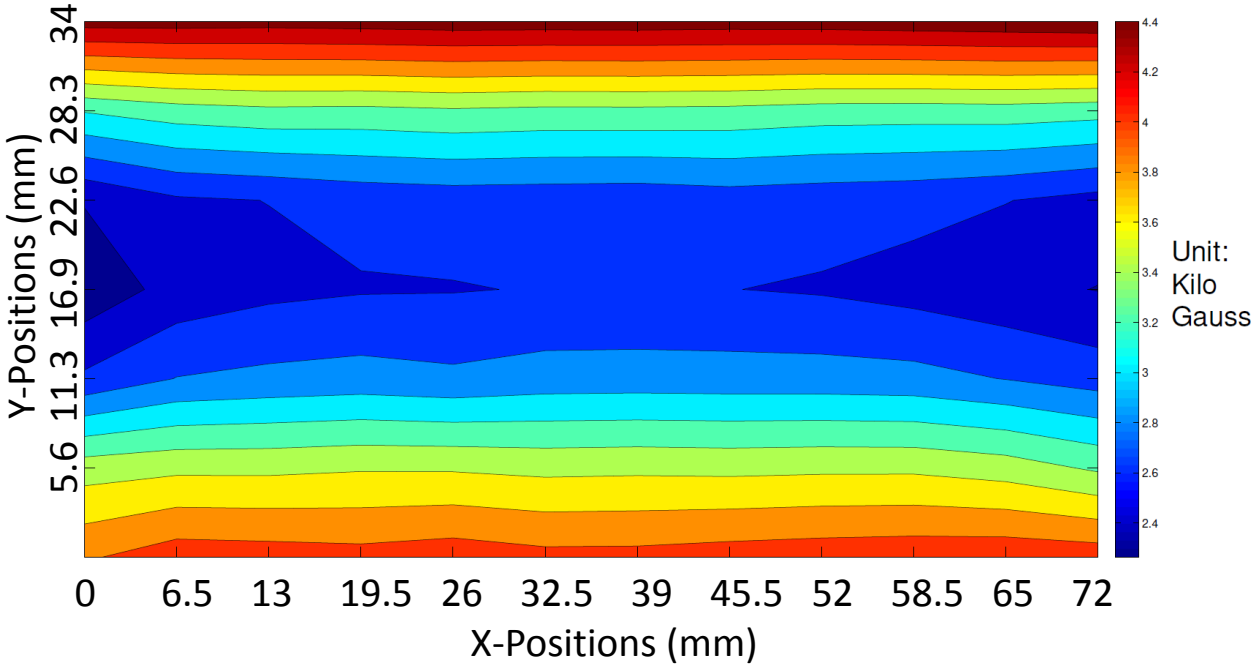

Figure 5.33 Magnetic field strength in the cross-section of the waveguide when no spacer is inserted.

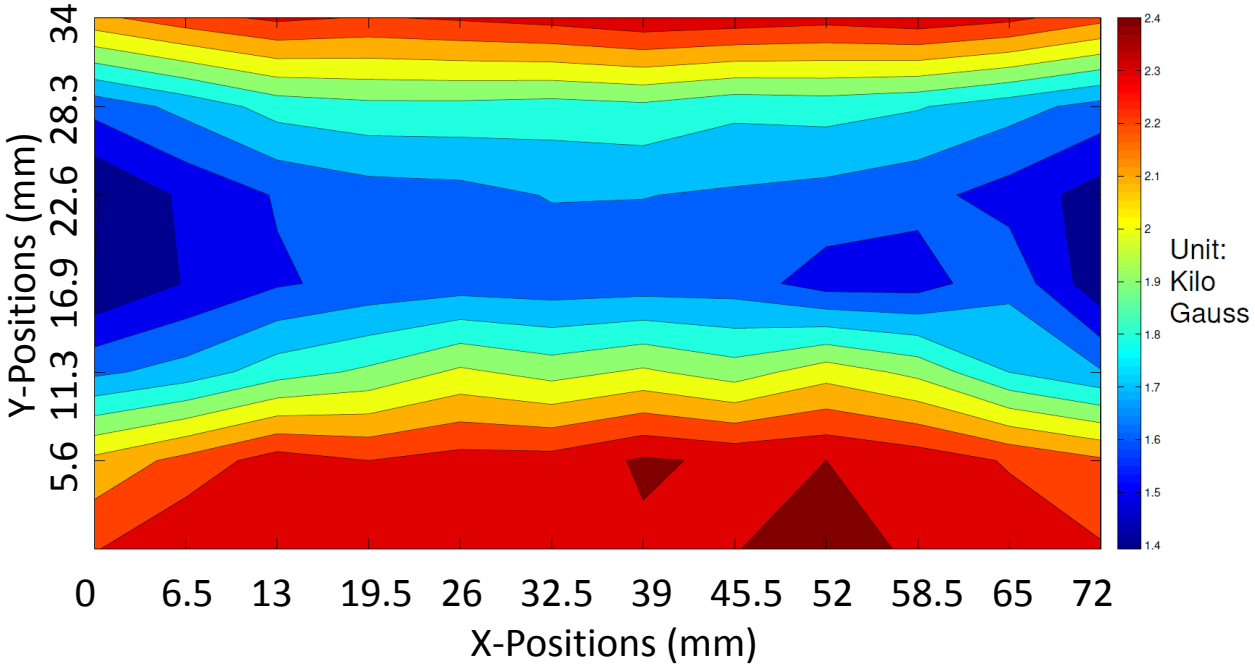

Figure 5.34 Magnetic field strength in the cross-section of the waveguide when the 5 mm spacers is inserted.

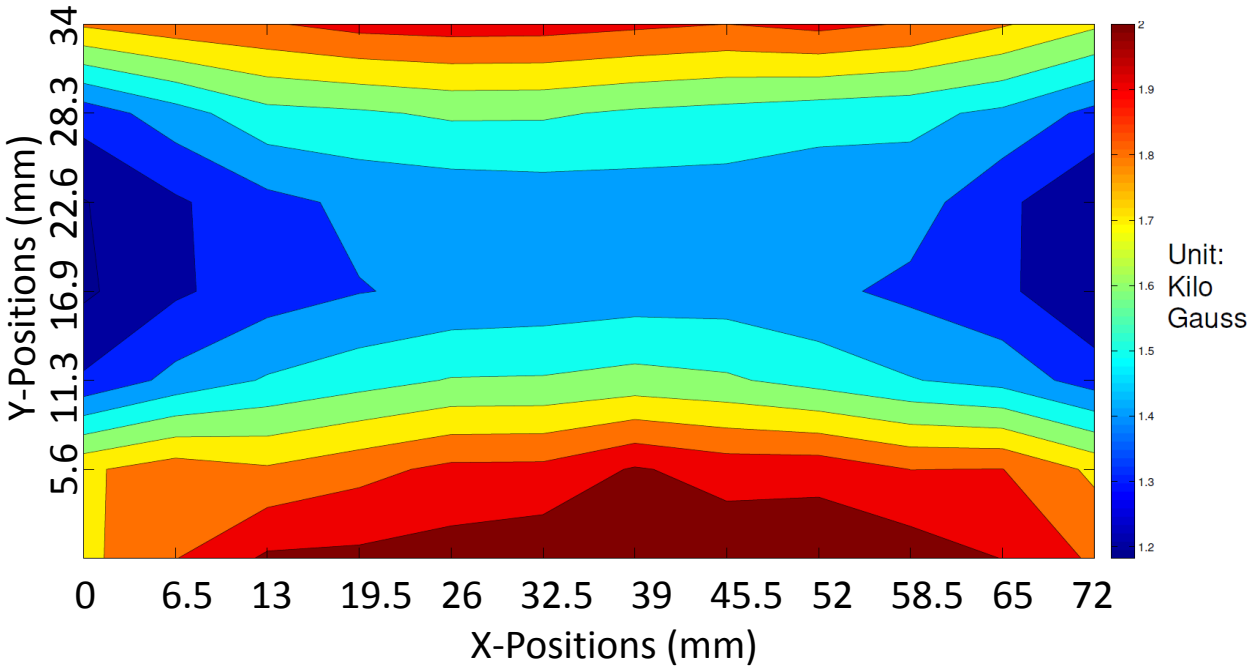

Figure 5.35 Magnetic field strength in the cross-section of the waveguide when the 9.7 mm spacers is inserted.

shift can be achieved using the following expressions:

$$S_{21}^{s} = S_{21}^{c} e^{-2j\beta(d+\Delta)} \tag{5.9}$$

$$S_{11}^{s} = S_{11}^{c} e^{-j\beta d}, \tag{5.10}$$

where S_{11}^{s} and S_{21}^{s} are the S-parameters referenced to the sample planes while S_{11}^{c} and S_{21}^{c} are the measured S-parameters referenced to the calibration plane, and d is the thickness of the sample which is 5 mm and Δ is the inserted distance of the sample which is 45 mm through out the measurements.

5.3.2 Experiment Results

Ten sets of measurements for three different biasing field strengths were conducted and the S-parameters were mathematically de-embedded to the desired sample planes. Measurement repeatability was evaluated and the processed data was used to extract the three frequency

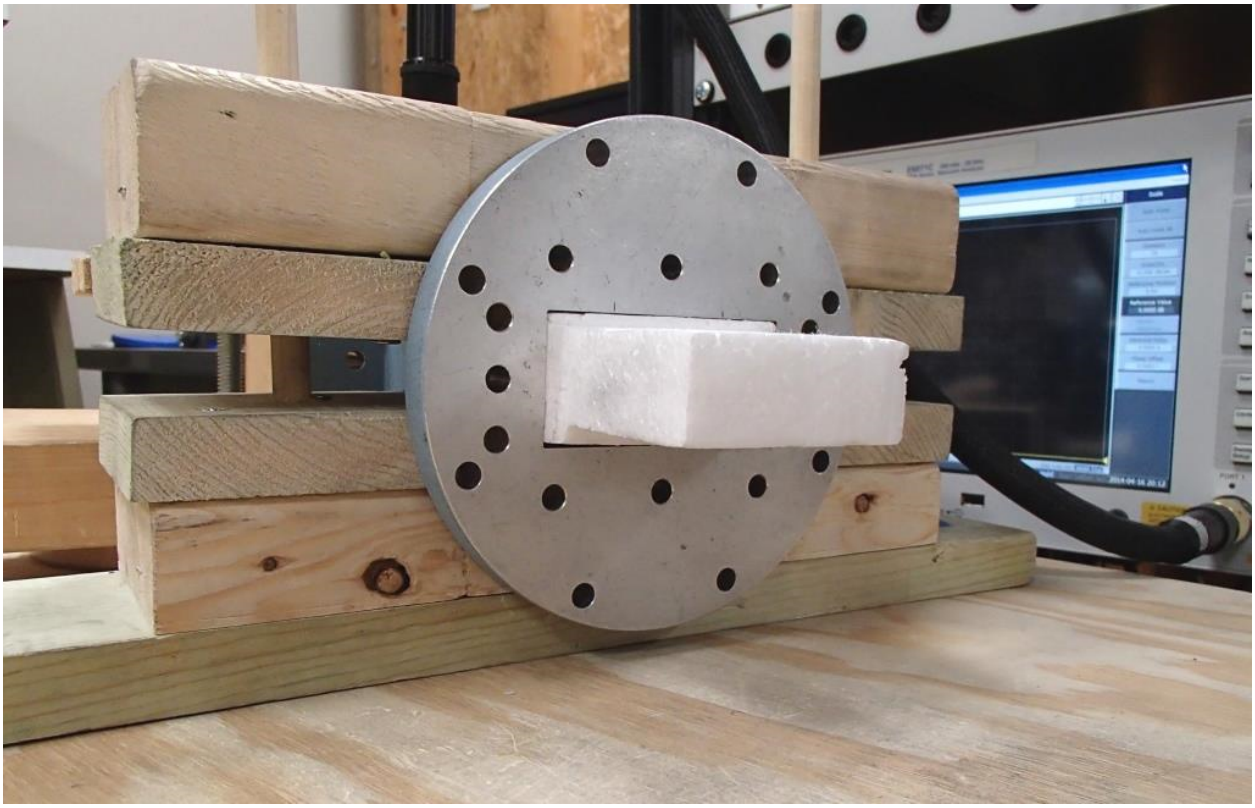

Figure 5.36 Polystyrene foam sample holder inside the waveguide with the magnets fixture attached.

independent parameters.

5.3.2.1 Repeatability Test

As is shown in Section 5.2.2.3, a repeatability test can demonstrate if the designed experimental setup is able to produce consistent measurements. A statistical analysis of the variance of S_{11} and S_{21} of the G1010 sample was processed to evaluate the repeatability of the experiments. Figures 5.38 - 5.41 show the average S-parameters and the standard deviation generated from 10 repeated measurements of the G1010 sample when it was placed at the center of the waveguide with no spacer added to the magnet fixture (highest magnetic field strength). Note that the two standard deviations of the magnitude of both S_{11} and S_{21} are less than 0.1 dB at frequencies away from the resonance frequencies, which indicates consistent measured data near the non-resonance frequencies. However, for the S-parameters near

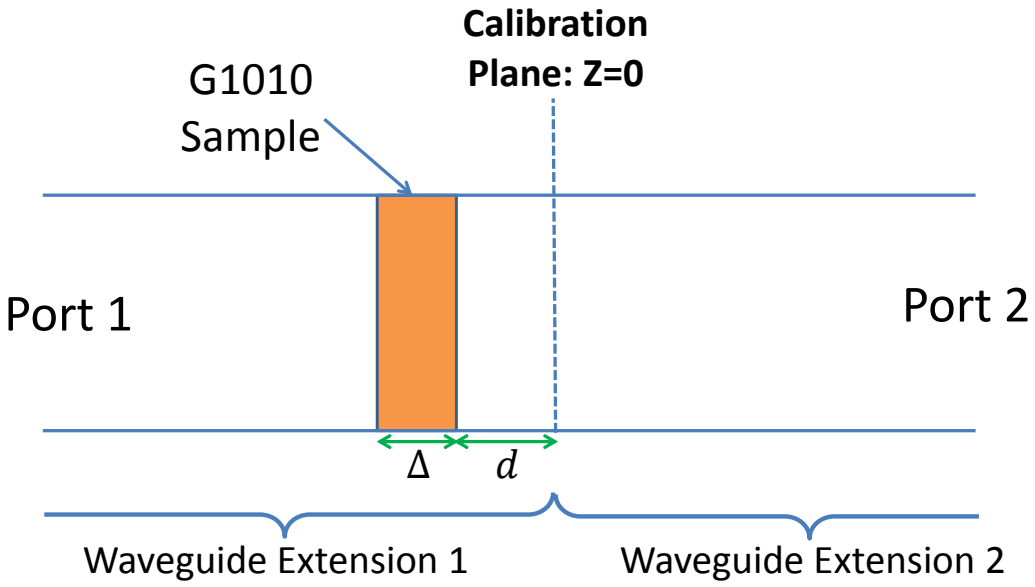

Figure 5.37 G1010 sample inserted into the waveguide extension attached to port 1.

the resonance frequencies, large confidence intervals are observed, which represents poor repeatability of the measured S-parameters and high sensitivity of the S-parameters near those frequencies.

It can be seen that three a secondary dip near the main resonance frequency. This phenomenon was not seen in the first two sets of measurements and it became more noticeable as chips at the edge of the sample began to appear. Therefore, the cause of this unwanted dip is most likely due to the air gap between the sample and the waveguide wall due to the chipped edge of the sample. From Figure 5.39 and 5.41, one can see that the phases of S_{11} and S_{21} have a large confidence intervals, with two standard deviations of approximately 6 degrees for S_{11} and 0.5 degrees for S_{21}. For the phase near the resonance frequencies, larger confidence intervals are seen which also show the high sensitivity of the measured data near these frequencies. A dip caused by air gaps is also seen in these two figures. To avoid having these dips influence the values of the extracted material parameters, the frequencies where

those dips occur are avoided during the extraction process. The overall statistical results of the measured S-parameters indicates acceptable consistency of the experiment set-up. A foam holder with better rigidness may be required to achieve higher consistency of the measured data. It is also very important to keep the sample in good physical condition such that the impact from air gaps can be minimized.

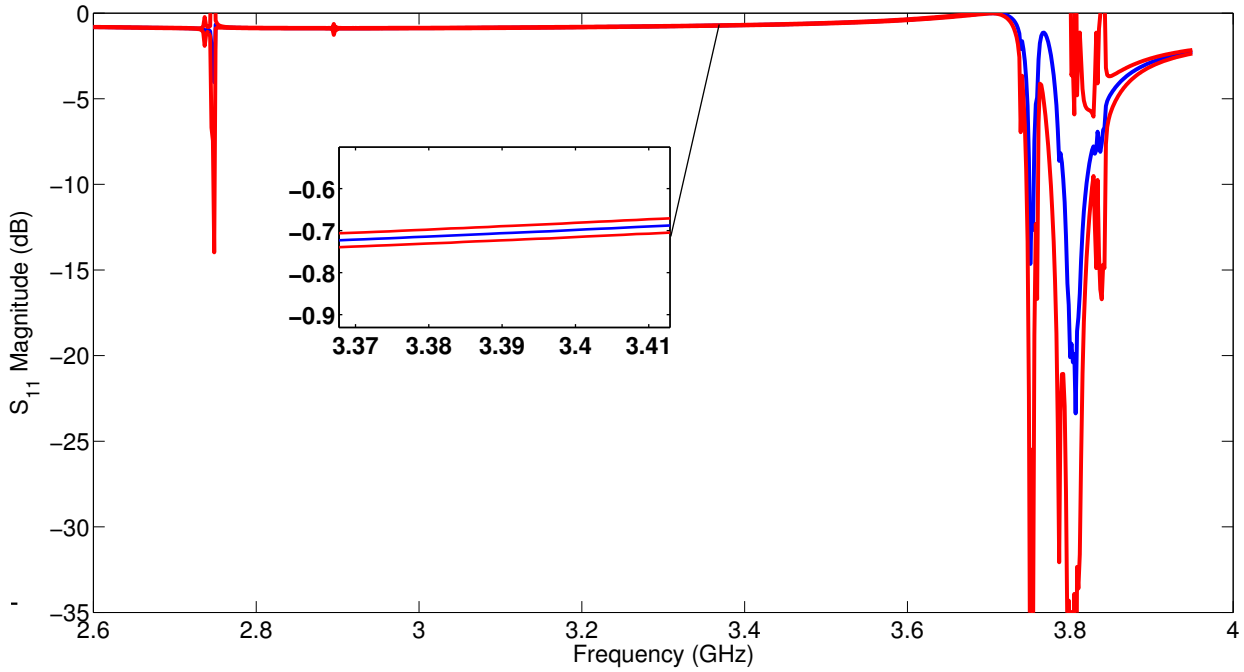

Figure 5.38 Magnitude of S_{11} from the G1010 sample meausured 10 times with the highest magnetic biasing field strength. Center blue line is the average value of 10 measurements. Upper and lower lines in red show the 95% confidence interval (two standard deviations).

5.3.2.2 Extracted Parameters

A Matlab optimization function was used to process the measured data to extract the desired parameters. The details of the optimization function and its settings and the extraction procedure are described in Section 4.4. For each measurement, 120 frequency points near the main resonance frequency were chosen for the optimization. These points were manually chosen for each measurement to avoid the additional resonance caused by the air gap. To be consistent, 60 collocated points below the resonance frequency and 60 collocated points above the resonance frequency were chosen. Tables 5.1-5.3 show the extracted H_0 and material

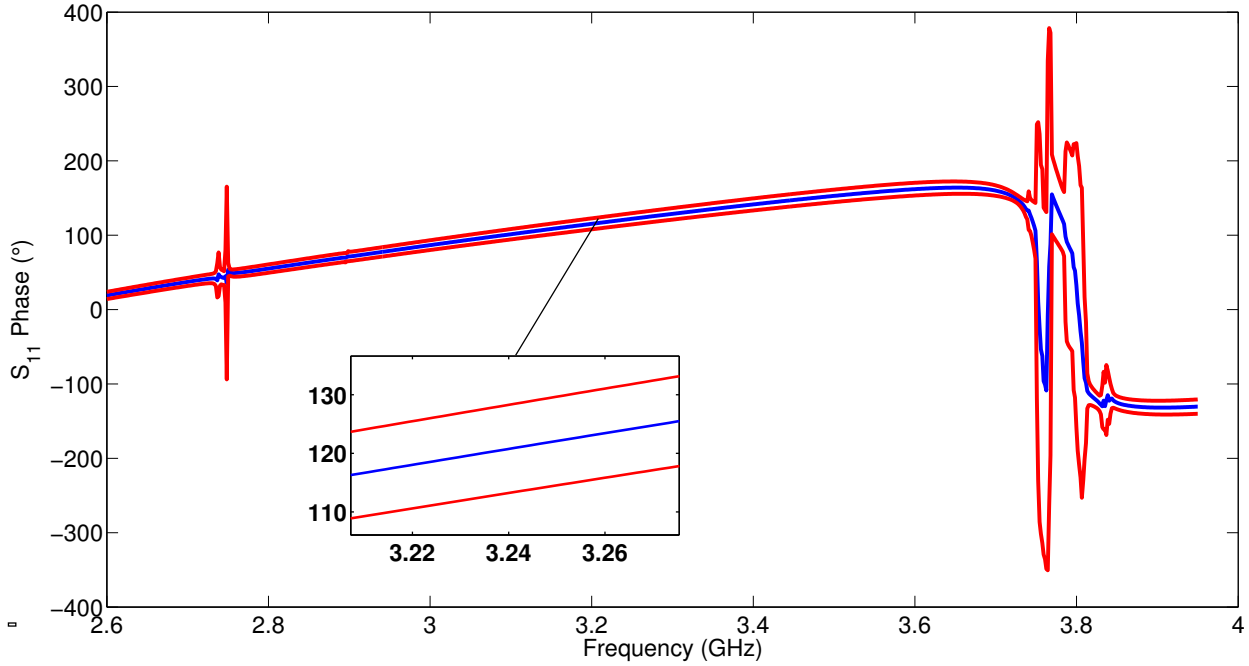

Figure 5.39 Phase of S_{11} from the G1010 sample meausured 10 times with the highest magnetic biasing field strength. Center blue line is the average value of 10 measurements. Upper and lower lines in red show the 95% confidence interval (two standard deviations).

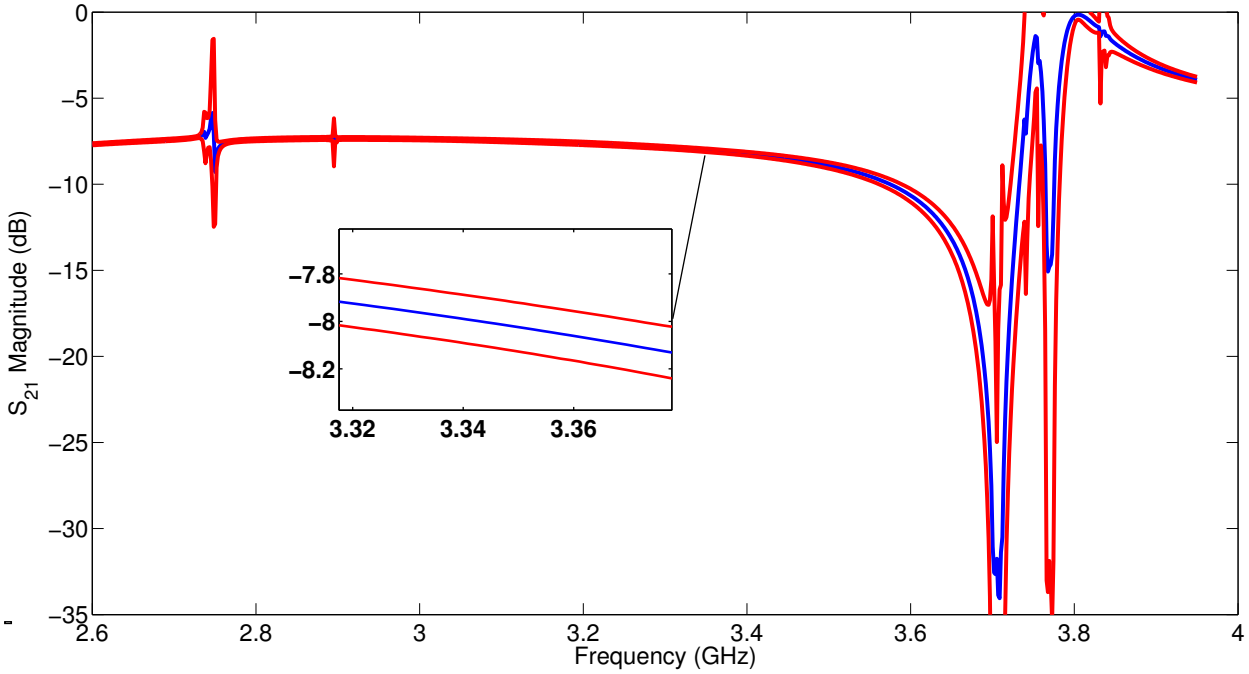

Figure 5.40 Magnitude of S_{21} from the G1010 sample meausured 10 times with the highest magnetic biasing field strength. Center blue line is the average value of 10 measurements. Upper and lower lines in red show the 95% confidence interval (two standard deviations).

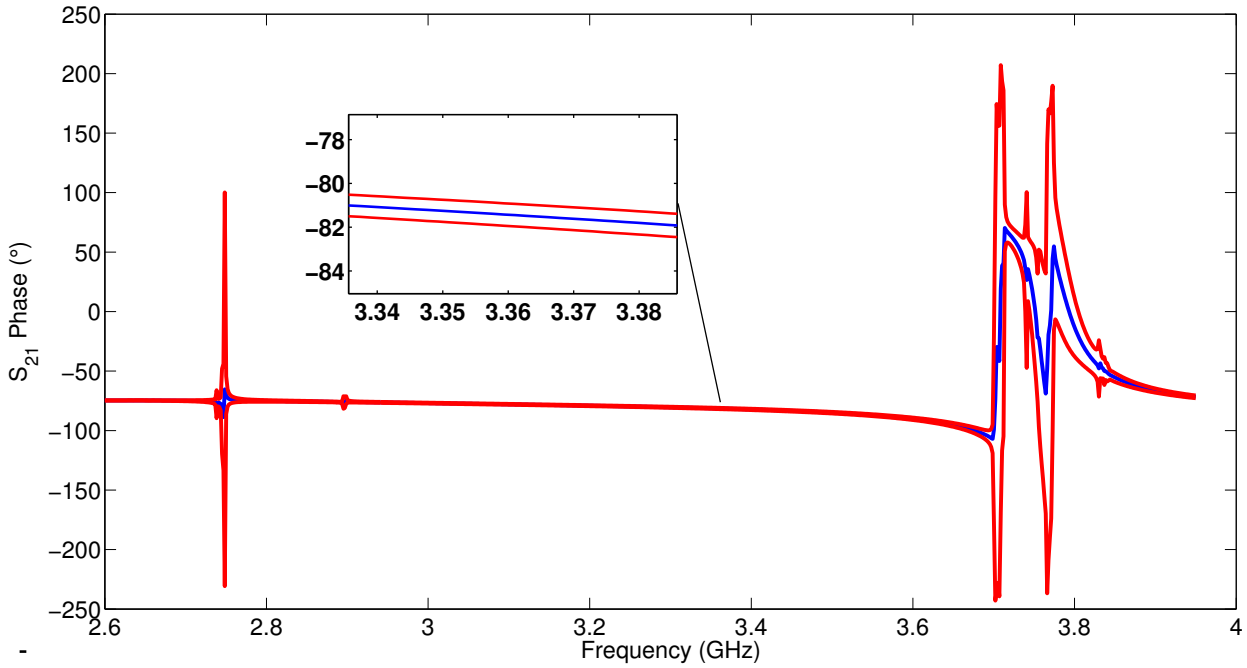

Figure 5.41 Phase of S_{21} from the G1010 sample meausured 10 times with the highest magnetic biasing field strength. Center blue line is the average value of 10 measurements. Upper and lower lines in red show the 95% confidence interval (two standard deviations).

parameters from 10 sets of measurements. The lower and upper bounds of the parameters used in the optimization are also included, and these bounds were chosen to be much larger than that of the range offered by the manufacturer specification sheet in order to evaluate the performance of this extraction method. The same function tolerance (10^{-4}) and variable tolerance (10^{-5}) were used for processing all the measured data. Each extraction process for a single measurement takes approximately 20 minutes on an Intel Core i7 computer with 8 Gb of RAM.

It can be seen from Table 5.1 for the biasing configuration that offers the highest magnetic field strength, the variation of extracted values of H_0, ϵ_r' and $4\pi M_s$ are small. The average value of H_0 from 10 measurements is 3143 Oe which is close to the average measured magnetic field strength 3346 G. The average value of ϵ_r' is 14.68 while the manufacturer specification is 14.24. The average extracted $4\pi M_s$ is 968 G which is also very close to 989 G which is given by the manufacturer. The results for the second biasing configuration are shown in Table 5.2. The average value of the extracted H_0 is 1855.5 Oe which is also slightly lower than the

measured value of 1978 G. The average extracted ϵ_r' and $4\pi M_s$ at this biasing configuration are higher than those found with the highest biasing field. The standard deviation of the extracted H_0 is smaller than the previous case while the standard deviations for ϵ_r' and $4\pi M_s$ are larger. For the third biasing configuration, which produces the lowest magnetic field strength, the average extracted H_0 is 1436.9 while the average measured field strength is 1647 G. Also, the average ϵ_r' and $4\pi M_s$ are close to the previous two cases. It is noticed that the standard deviation of $4\pi M_s$ is significantly reduced. Considering that the Linewidth Δ is not included in the mode matching, the extracted results using different measured data indicate this method is able to extract material parameters that are reasonably close to the expected value.

A second extraction approach using multiple biasing fields was carried out and the results are compared with the extracted values found using a single biasing field. The same frequency points used in the previous extraction were used for this approach, and thus each optimization involves 360 points. In addition, the number of variables used in this approach is 5 since three different H_0 variables are used in the optimization. Table 5.4 shows the extracted values using this approach along with the average values. The obtained average values are compared to the average values using a single biasing field. It can be noticed that the average values are closer to the average values using the highest biasing field than the other two. In addition, the standard deviation of the extracted parameters using this approach is less compared to the results using a single biasing field. This may indicate that this approach is less sensitive to the change of one measurement since three different measured data are used simultaneously.

5.4 Summary

This chapter presents experimental procedures and results for characterizing different anisotropic materials using a partially-filled rectangular waveguide technique. Two types of anisotropic

Table 5.1 Extracted H_0 and material parameters for measurements of the highest external magnetic biasing fields.

	H_0 (Oe)	ϵ_r'	$4\pi M_s$ (G)
Initial guess	3180	14.7	990
Lower bound	2600	14.0	680
Upper bound	3800	15.2	1320
Measurement 1	3201	14.7371	1049.5
Measurement 2	3063.6	14.7921	867.2
Measurement 3	2990	14.4449	1020
Measurement 4	3792.6	14.6992	1180
Measurement 5	2990	14.4169	1019.9
Measurement 6	2990	14.4683	1020
Measurement 7	2990	14.4016	1019.9
Measurement 8	3110.2	14.9589	768.4
Measurement 9	3122.6	15.0485	744.95
Measurement 10	3180	14.7909	990
Average	3143	14.6758	968
Standard Deviation	242.2	0.233	134.4

Table 5.2 Extracted H_0 and material parameters for measurements of the second highest external magnetic biasing fields.

	H_0 (Oe)	ϵ_r'	$4\pi M_s$ (G)
Initial guess	1900	14.7	1020
Lower bound	1600	14.0	680
Upper bound	2400	15.2	1320
Measurement 1	1889.7	14.9862	1000.3
Measurement 2	1903.6	15.1758	1016.6
Measurement 3	1879.7	14.2979	1317.7
Measurement 4	1932.7	15.1469	992.8
Measurement 5	1853.9	14.8553	1062.6
Measurement 6	1831.1	14.6690	1079.9
Measurement 7	1759.3	14.2584	1157.7
Measurement 8	1904.3	15.0163	1016.3
Measurement 9	1704.2	15.1883	715.5
Measurement 10	1896.4	15.1241	1023.3
Average	1855.5	14.8718	1038.3
Standard Deviation	72.1	0.352	150.4

Table 5.3 Extracted H_0 and material parameters for measurements of the lowest external magnetic biasing fields.

	H_0 (Oe)	ϵ_r'	$4\pi M_s$ (G)
Initial guess	1410	14.59	1050
Lower bound	1300	14.0	800
Upper bound	1900	15.2	1200
Measurement 1	1406.4	14.2254	1051.2
Measurement 2	1410.1	14.3933	1020
Measurement 3	1407.7	14.1718	1050.7
Measurement 4	1409.5	14.0098	1020.2
Measurement 5	1544.2	14.9269	998.7
Measurement 6	1410	14.3005	1019.9
Measurement 7	1405.9	14.2385	1051.3
Measurement 8	1410	14.3528	1049.5
Measurement 9	1430.1	14.5105	1019.9
Measurement 10	1535.2	15.1612	991.9
Average	1436.9	14.429	1027.3
Standard Deviation	54.6	0.355	22.3

Table 5.4 Extracted H_0 and material parameters using three biasing fields

	H_0 (Oe) 1st	H_0 (Oe) 2nd	H_0 (Oe) 3rd	ϵ_r'	$4\pi M_s$ (G)
Initial guess	3200	1890	1490	14.2	1020
Lower bound	2600	1600	1300	14.0	680
Upper bound	3400	2400	1900	15.2	1320
Measurement 1	3024.3	1763.8	1450	14.4754	1061.5
Measurement 2	3040.9	1694.1	1425.7	15.0732	796.7
Measurement 3	3028.1	1744.6	1449.9	14.3955	1070.8
Measurement 4	3038.3	1731.8	1449.3	14.4207	1054.5
Measurement 5	3400	1778.1	1511.2	14.6775	1026.5
Measurement 6	3033	1745	1446.6	14.4419	1058.9
Measurement 7	3031.9	1740.6	1431.3	14.3478	1076.6
Measurement 8	3359.6	1699.9	1402.4	15.1998	704.5
Measurement 9	3192.5	1680	1397.9	15.1935	683.9
Measurement 10	3031	1741.9	1462.1	14.577	1057
Average	3147.9	1732	1442.6	14.6802	959.1
Standard Deviation	147.1	31.3	32.1	0.343	162.2

materials were measured at S-band to validate the corresponding extraction techniques. The first type of the characterized material is biaxial. Two cubical samples made of stacked layer substrates were constructed and measured to evaluate the proposed technique which characterize biaxial and unixial materials. It is found that the technique performs very well for characterizing uniaxial material and also for the biaxial material at the frequency band where the electrical length of the sample does not approach a half wavelength. The second type of the material is gyromagnetic. The extraction procedure of this material is based on an optimization algorithm in Matlab and it was validated by laboratory measurements of a gyromagnetic test sample. Extracted material parameters from different experimental configurations or different extraction approaches show good agreement with the values measured or supplied by the manufacturer.

CHAPTER 6

Conclusions and Future Works

In this dissertation, A partially-filled waveguide characterization technique is introduced for two types of materials: biaxial and gyromagnetic. The extraction of the full tensors of a biaxial sample can be achieved using a single sample that is partially filled in a waveguide. This method eliminates many drawback of the previous works which were developed to characterize biaxial materials. The theoretical reflection and transmission coefficients are determined using a closed form solution. The inverse problem is to minimize the difference between the theoretical reflection and transmission coefficients and the measured S-parameters using an iterative solver. A simplified characterization approach is described for the extraction of uniaxial materials. The sensitivity analysis for VNA uncertainties is demonstrated. Two cubical samples made of stacked layer substrates were constructed and measured to validate the proposed technique. To overcome the half-wavelength difficulties mentioned in 5.2.3.2, investigations of new extraction approaches will be carried out in the future, such as combining data produced from reduced aperture waveguide techniques and from the technique proposed in this work.

A method for characterizing gyromagnetic materials partially filled in a guide is also described. The extraction procedure of this material is based on optimization algorithms in Matlab and sensitivity analysis for VNA uncertainties and uncertainties of the sample

dimensions demonstrates promising performance of this method. Multiple measured data with various applied biasing fields was obtained from a gyromagnetic sample. Extracted material parameters from different experimental configurations or different extraction approaches show good agreement with the values measured or supplied by the manufacturer. The extraction of the full properties of the gyromagnetic sample will be carried out in the future along with the extraction from measurements of various sample positions.

BIBLIOGRAPHY

BIBLIOGRAPHY

[1] J. B. Pendry, A. J. Holden, D. J. Robbins, and W. J. Stewart, "Low frequency plasmons in thin-wire structures," *J. Conds. Mat.*, vol. 10, pp. 4785–4809, 1998.

[2] J. B. Pendry, D. Schurig, and D. R. Smith, "Controlling electromagnetic fields," *Science*, vol. 312 no. 5781 pp. 17801782, 2006.

[3] D. Schurig, J. J. Mock, B. J. Justice, S. A. Cummer, J. B. Pendry, A. F. Starr, D. R. Smith, "Metamaterial electromagnetic cloak at microwave frequencies," *Science*, vol. 314, no.5801, pp. 977–980, 2006.

[4] B. Wu, W. Wang, J. Pacheco, X. Chen, J. Lu, T. Grzegorczyk, J. A. Kong, P. Kao, P. A. Theophelakes, and M. J. Hogan, "Anisotropic metamaterials as antenna substrate to enhance directivity," *Micro. Opt. Technol. Lett.*, vol. 48, no. 4, pp. 680–683, Apr. 2006.

[5] Y. Ma, P. Wang, X. Chen, and K. Ong, "Near-field plane-wave-like beam emitting antenna fabricated by anisotropic metamaterial," *Applied Physics Letters*, vol. 94, no. 4, pp. 044107, 2009.

[6] G. Mumcu, K. Sertel, and J. Volakis, "Miniature antennas and arrays embedded within magnetic photonic crystals," *IEEE Antennas and Wireless Propagation Letters*, vol. 5, no. 1, pp. 168-171, Dec. 2006.

[7] E. Decrossas, M. A. EL. Sabbagh, S. M. El. Ghazaly, and V. F. Hanna, "Engineered carbon-nanotubes-based composite material for RF applications," *IEEE Transactions on Electromagnetic Compatibility*, vol. 54, no. 1, pp. 52-59, Jan. 2012.

[8] A. Dimiev, W. Lu, K. Zeller, B. Crowgey, L. C. Kempel, and J. M. Tour, "Low-loss, high-permittivity composites made from graphene nanoribbons," *Applied Materials & Interfaces*, no. 3, pp. 4657–4661, 2011.

[9] Y. Shirakata, N. Hidaka, M. Ishitsuka, A. Teramoto, and T. Ohmi, "High permeability and low loss Ni-Fe composite material for high-frequency applications," *IEEE Trans. Magn.*, vol. 44, no. 9, pp. 2100–2106, Sept. 2008.

[10] L. Yang , L. Martin , D. Staiculescu, C. P. Wong , and M. M. Tentzeris, "A Novel Flexible Magnetic Composite Material for RFID, Wearable RF and Bio-monitoring Applications," *IEEE MTT-S International Microwave Symposium Digest*, pp. 963–966, Jun. 2008.

[11] F. C. Smith, "Effective permittivity of dielectric honeycombs," *IEE Proc. Micro. Antennas Propag.*, vol. 146, no. 1, pp. 55–59, Feb. 1999.

[12] F. C. Smith, F. Scarpa, and B. Chambers, "The electromagnetic properties of re-entrant dielectric honeycombs," *IEEE Microw. Guided Wave Lett.*, vol. 10, no. 11, pp. 451–453, Nov. 2000.

[13] M. Liang, X. Yu, C. Shemelya, D. Roberson, E. MacDonald, R. Wicker, H. Xin, "Electromagnetic materials of artificially controlled properties for 3D printing applications," IEEE Antennas and Propag. Society International Symposium, Memphis, TN, July 6-11, 2014.

[14] G. L. Friedsam, and E. M. Biebl, "A broadband free-space dielectric properties measurement system at millimeter wavelengths," *IEEE Trans. Instrumentation and Measurement*, vol. 46, no. 2, pp. 515–518, Apr. 1997.

[15] R. G. Nitsche, J. Preissner, and E. M. Biebl, "A free space technique for measuring the complex permittivity and permeability in the millimeter wave range," *Microwave Symposium Digest, IEEE MTT-S International*, vol. 3, pp. 1465–1468, May. 1994.

[16] E. Kemptner, S. Thurner , "Free space material characterization for microwave frequencies," *European Conference on Antennas and Propagation (EUCAP)*, pp. 3513–3515, 2012.

[17] J. B. Jarvis, R. G. Geyer, and P. D. Domich, "A non-linear least squares solution with causality constraints applied to transmission line permittivity and permeability determination," *IEEE Transactions on Instrumentation and Measurements*, vol. 41, no. 5, pp. 646–652, Oct. 1992.

[18] J. B. Jarvis, "Measuring the permittivity and permeability of lossy materials: solids, liquids, building material and negative-Index materials," *NIST Technical Note*, no. 1536, 2005.

[19] L. Chen, C. K. Ong, and B. T. G. Tan, "Amendment of cavity perturbation method for permittivity measurement of extremely low-loss dielectrics," *IEEE Transactions on Instrumentation and Measurements*, vol. 48, no. 6, pp. 1031–1037, Dec. 1999.

[20] E. Li, G. Guo, and Q. Zhang, "Broadband complex permittivity measurement of low loss dielectric disks by cylindrical cavity," *Asia-Pacific Microwave Conference Proceedings*, vol. 5, Dec. 2005.

[21] D. Berube, F. M. Ghannouchi, and P. Savard, "A comparative study of four open-ended coaxial probe models for permittivity measurements of lossy dielectric/biological materials at microwave frequencies," *IEEE Transactions on Microwave Theory and Techniques*, vol. 44, no. 10, pp. 1928–1934, Oct. 1996.

[22] C.-L. Li, and Y. F. Chen, "Determination of electromagnetic properties of materials using flanged open-ended coaxial probe-full-wave analysis," *IEEE Transactions on Instrumentation and Measurements*, vol. 44, no. 1, pp. 19–27, Feb. 1995.

[23] J. C. Henaux, and P. Crozat, "Dimensional correction of high dielectric and magnetic constants determined by S parameters measurements," *Electronics Letters*, vol. 26, no. 15, pp. 1151–1153, Jul. 1990.

[24] M. Arai, J. G. P. Binner, and T. E. Cross, "Correction of errors due to airgaps for microwave complex permittivity measurement using a coaxial line," *Electronics Letters*, vol. 31, no. 2, pp. 114–115, Jan. 1995.

[25] J.- H. Le Gallou, M. Ledieu, and O. Acher, "High temperature coaxial line measurement cell using room temperature calibration," *Precision Electromagnetic Measurements Digest*, pp. 473–474, Jun. 2004.

[26] R. Wang, and W. Cui, "A rapid estimation of the conductor loss in the rectangular waveguide with rough surface," *IEEE International Symposium on Microwave, Antenna, Propagation, and EMC Technologies for Wireless Communications (MAPE)*, pp. 498–500, Nov. 2011.

[27] B. Crowgey, O. Tuncer, E. Rothwell, B. Shanker, and L. Kempel, "Development of numerical techniques for simulated characterization of anisotropic materials," 28th Annual Review of Progress in Applied Computational Electromagnetics (ACES), pp. 553–557, Columbus, Ohio, April. 2012.

[28] A. M. Nicolson and G. F. Ross, "Measurement of the intrinsic properties of materials by time-domain techniques," *IEEE Transaction on Instrumentation and Measurements*, vol. 19, no. 4, pp. 377–382, Nov. 1970.

[29] W. B. Weir, "Automatic measurement of complex dielectric constant and permeability at microwave frequencies," *Proc. IEEE*, vol. 62, no. 1, pp. 3336, Jan. 1974.

[30] M. J. Havrilla and D. P. Nyquist, "Electromagnetic characterization of layered materials via direct and de-embed methods," *IEEE Transaction on Instrumentation and Measurements*, vol. 55, no. 1, pp. 158–163, Feb. 2006.

[31] K. M. Fidanboylu, S. M. Riad, and A. Elshabini-Riad, "An enhanced time-domain approach for dielectric characterization using stripline geometry," *IEEE Transaction on Instrumentation and Measurements*, vol. 41, no. 1, pp. 132–136, Feb. 1992.

[32] S. P. Dorey, M. J. Havrilla, L. L. Frasch, C. Choi, and E. J. Rothwell, "Stepped-waveguide material-characterization technique," *IEEE Antennas Propagation Magazine*, vol. 46, no. 1, pp. 170–175, Feb. 2004.

[33] A. Bogle, "Electromagnetic material characterization of a PEC backed lossy simple media using a rectangular waveguide resonant slot technique," Ph.D. Dissertation, Michigan State University, East Lansing, MI, 2007.

[34] E. Kilic, U. Siart, and T. F. Eibert, "Regularized 1-D dielectric profile inversion in a uniform metallic waveguide by measurement and simulation," *IEEE Transaction on Microwave Theory Technology*, vol. 60, no. 5, May. 2012.

[35] A. Bogle, M. Havrilla, D. Nyquis, L. Kempel, and E. Rothwell, "Electromagnetic material characterization using a partially-filled rectangular waveguide," *Journal of Electromagnetic Waves and Applications*, vol. 19, no. 10, pp. 1291–1306, 2005.

[36] G. Mumcu, K. Sertel, and J. L. Volakis, "A measurement process to characterize natural and engineered low-loss uniaxial dielectric materials at microwave frequencies," *IEEE Transaction on Microwave Theory Technology*, vol. 56, no. 1, pp. 217–223, Jan. 2008.

[37] N. J. Damaskos, R. B. Mack, A. L. Maffett, W. Parmon, and P. L. Uslenghi, "The inverse problem for biaxial materials," *IEEE Transaction on Microwave Theory Technology*, vol. 32, no. 4, pp. 400–405, Apr. 1984.

[38] B. R. Crowgey, O. Tuncer, J. Tang, E. J. Rothwell, B. Shanker, L. C. Kempel, and M. Havrilla, "Characterization of biaxial anisotropic material using a reduced aperture waveguide," *IEEE Transaction on Instrumentation and Measurements*, vol. 62, no. 10, pp. 2739–2750, Jun. 2013.

[39] M. M. Scott, D. L. Faircloth, J. A. Bean, and S. G. Holliday, "Biaxial permittivity determination for electrically small material specimens of complex shape using shorted rectangular waveguide measurements," *IEEE Transaction on Instrumentation and Measurements*, vol. 63, no. 4, pp. 896–903, Nov. 2013.

[40] P. Queffelec, M. Le Floc'h, and P. Gelin, "Non-reciprocal cell for the broad-band measurement of tensorial permeability of magnetized ferrites: Direct problem," *IEEE Transaction on Microwave Theory Technology*, vol. 47, no. 4, pp. 390–397, Apr. 1999.

[41] P. Queffelec, M. Le Floc'h, P. Gelin, "New method for determining the permeability tensor of magnetized ferrites in a wide frequency range," *IEEE Transaction on Microwave Theory Technology*, vol. 48, no. 8, pp. 1344–1351, Aug. 2000.

[42] B. Crowgey, "Rectangular waveguide material characterization: anisotropic property extraction and measurement validation," Ph.D. Dissertation, Michigan State University, East Lansing, MI, 2013.

[43] S. Ramo, J. R. Whinnery, and T. Van Duzer, "Fields and Waves in Communications Electronics," 3rd ed., John Wiley Sons, New York, 1994.

[44] G. Busse and A. F. Jacob, "Complex modes in circular chuowaveguides, *Electronics Letter*, vol. 29, no. 8, pp. 711-713, 1993.

[45] H. Cory, "Wave propagation along a closed rectangular chirowaveguide, *Microwave and Optical Technology Letter*, vol. 6, no. 14, pp. 797-800, 1993.

[46] P. J. B. Clarricoats and K. R. Slinn,"Complex modes of propagation in dielectric-loaded circular waveguide," *Electronics Letter*, vol. 1, no. 5, pp. 145-146, 1965.

[47] U. Crombach,"Complex waves on shielded lossless rectangular dielectric waveguide," *Electronics Letter*, vol. 19, no. 14, pp. 557-558, 1983.

[48] T. F. JablofiskiJ, "Complex modes in open lossless dielectric waveguides," *JOSA A*, vol. 11, no. 4, pp. 1272-1282, 1994.

[49] A. S. Omar and K. F. Schinemann, "Complex and backwardwave modes in inhomogeneously and anisotropically filled waveguides," *IEEE Transaction on Microwave Theory and Technology*, vol. 35, no. 3, pp. 268-275, Mar. 1987.

[50] P. Chorney, "Power and energy relations in bidirectional waveguides," *Mass. Inst. Tech., Res. Lab. of Electronics,* vol. 396, Sept. 1961.

[51] http://www.mathworks.com/help/gads/example-comparing-several-solvers.html

[52] http://www.keysight.com/en/pd-810708-pn-E5071C/ena-series-network-analyzer?cc=USlc=eng

[53] http://www.keysight.com/en/pd-1000002059%3Aepsg%3Apro-pn-8510C/vector-network-analyzer?cc=USlc=eng

[54] R. Collin, "A simple artificial anisotropic dielectric medium," *IRE Transaction on Microwave Theory and Techniques*, pp. 206–209, Apr. 1958.

[55] http://www.trans-techinc.com, 5520 Adamstown Road, Adamstown, MD 21710, US.

[56] http://www.islandceramics.com, 370 Kishimura Dr., Gilroy, CA 95020, US.

[57] https://www.kjmagnetics.com, 18 Appletree Ln, Plumsteadville, PA 18949, US.

[58] http://fwbell.com/downloads/manuals.aspx, 4607 SE International Way, Milwaukie, OR 97222, US.